Statistical Fluctuations and Correlations in Hadronic Equilibrium Systems

Dissertation
zur Erlangung des Doktorgrades
der Naturwissenschaften

vorgelegt beim Fachbereich Physik
der Johann Wolfgang Goethe–Universität
in Frankfurt am Main

von
Michael Hauer
aus München, Deutschland

Frankfurt am Main
2010

(D30)

vom Fachbereich Physik der
Johann Wolfgang Goethe–Universität, Frankfurt am Main,
als Dissertation angenommen.

Dekan: Prof. Dr. Dirk-Hermann Rischke

Gutachter: PD Dr. Elena Bratkovskaya

Datum der Disputation: 17. 6. 2010

Zusammenfassung

Diese Arbeit ist dem Studium von Fluktuationen und Korrelationen zwischen extensiven Observablen in hadronischen Gleichgewichtssystemen gewidmet. Als extensive Observablen bezeichnet man Meßgrößen, die Aufschluß über die „Größe“ des zu beobachtenden Systems geben, wie etwa Teilchenanzahl oder Gesamtenergieinhalt, aber auch (elektrische) Nettoladung. Als Gleichgewichtssysteme bezeichnet man Systeme, die sich in einem Gleichgewichtszustand befinden. Also in einem Zustand, der mit (intensiven) Observablen zu beschreiben ist, die über die Zeit betrachtet, ihren Wert nicht mehr ändern. Hiermit könnte die Temperatur oder die Ladungsdichte des Systems gemeint sein. Unter Hadronen versteht man Teilchen, denen eine gewisse Substruktur zugeschrieben werden kann, die also aus elementaren Bausteinen, den Quarks und Gluonen, aufgebaut sind. In der uns im Alltag vertrauten Welt, in der im Wesentlichen die Hadronenvertreter Neutronen und Protonen vorkommen, spielen diese elementaren Bausteinen jedoch keine eigene Rolle. Zusammen mit den Elektronen aus der Familie der Leptonen bilden diese beiden Hadronenarten die Atome und Moleküle aus den wir und unsere Umgebung bestehen.

Wenn zwei schwere Ionen (also von ihrer Elektronenhülle befreite Atomkerne) kollidiert werden, entsteht für sehr kurze Zeit ein sehr heißes und dichtes, möglicherweise kollektives System. Die Beschreibung dieses Systems ausschließlich mit den uns vertrauten hadronischen (und leptonischen) Freiheitsgraden ist nun nicht mehr möglich. Die Bausteine dieser Urmaterie sind die Quarks und die Feldteilchen der starken Wechselwirkung, die Gluonen. Dieser Zustand kann jedoch im Labor nicht direkt beobachtet werden. Nach einer kurzen, aber heftigen Expansionsphase wird die Teilchendichte zu gering, als dass die Teilchen des Systems noch miteinander wechselwirken könnten. Quarks und Gluonen „hadronisieren“ zurück zu den uns bekannten hadronischen Freiheitsgraden. Aus den Fluktuationen und Korrelationen zwischen den Teilchenanzahlen verschiedener Arten dieser Hadronen, so wird vermutet, können Aussagen über die dynamische Entwicklung, also etwa mögliche Phasenübergänge und die effektiven Freiheitsgrade des System gemacht werden. Aufgrund der offensichtlich kraftvollen Expansion des Systems kann hier wohl kaum von einem Gleichgewichtssystem ausgegangen werden.

Diese Arbeit beschäftigt sich mit trivialen Beiträgen zu Fluktuationen und Korrelationen, wie sie durch globale Erhaltungssätze, eingeschränkte Akzeptanz im Impulsraum, Resonanzzerfall, oder Quantenstatistik erzeugt werden. Diese Ef-

fekte können nicht vernachlässigt werden, da deren Auswirkungen von ähnlicher Größenordnung sind, wie die, die aufgrund von Phasenübergängen oder möglicher kritischer Punkte im Phasendiagramm erwartet werden. Die statistischen Eigenschaften von idealen, relativistischen, hadronischen Gleichgewichtsensembles wurden untersucht. Neben den drei Standard-kanonischen Ensembles wurde auch eine Klasse von Ensembles mit endlichem thermodynamischen Bad eingeführt. Die Abhängkeit statistischer Eigenschaften auf (intensive) thermische Parameter wurde untersucht. Es wurde argumentiert, dass das entstehende Bild zumindest qualitativ auf die Schwerionen-Physik anwendbar ist.

In Kapitel 2 wurden großkanonische multivariate Verteilungen von extensiven Meßgrößen, also Verteilungen von mehr als einer Zufallsvariable, durch Fourierintegration der großkanonische Zustandssumme erhalten. Eine analytische Entwicklungsmethode zur Berechnung der Verteilungsfunktionen von kanonischen sowie von mikrokanonischen Ensembles des idealen relativistischen Hadronen-Resonanz-Gases bei endlichem Volumen wurde vorgestellt. Die Einführung der Temperatur in die mikrokanonischen Zustandssumme, und die von chemischen Potentialen in die kanonische Zustandssumme, haben dazu geführt, dass die großkanonische Zustandssumme mit der charakteristischen Funktion der damit verbundenen großkanonischen multivariaten Wahrscheinlichkeitsverteilung identifiziert werden konnte. Mikrokanonische und kanonische Teilchenanzahlverteilungen konnten somit durch bedingte großkanonische Wahrscheinlichkeitsverteilungen definiert werden. Unter bedingter Wahrscheinlichkeit versteht man die Wahrscheinlichkeit in einem großkanonischen Ensemble etwa eine bestimmte Teilchenanzahl zu beobachten, während andere extensive Meßgrößen, wie etwa globale Ladung oder Gesamtenergie, als fest angenommen werden.

In Kapitel 3 wurden multivariate Verteilungen von extensiven Meßgrößen für Systeme mit endlichem - an Stelle von einem unendlichem - thermodynamischen Bad eingeführt. Hierzu wurde ein mikrokanonisches System konzeptionell in zwei Subsysteme aufgeteilt. Für diese Subsysteme wurde weiter angenommen, dass sie im thermodynamischen Gleichgewicht zueinander stehen. Des weiteren sollen sie gemeinsame Energie-, Impuls- und Ladungserhaltung respektieren. Teilchen können nur in einem der beiden Teilsysteme gemessen werden, während das andere Teilsystem als thermodynamisches Bad fungiert. Wird die Größe des ersten Teilsystems nun als fest angenommen, während die Größe des zweiten variiert werden kann, so kann man die Abhängigkeit der statistischen Eigenschaften eines Ensembles von dem beobachtbaren Anteil des System ermitteln. Das heißt, man untersucht deren Sensitivität auf die Anwendung von globalen Erhaltungssätzen.

Die erzeugten Ensembles sind thermodynamisch äquivalent im dem Sinne, dass Mittelwerte extensiver Observablen im beobachteten Teilsystem unverändert bleiben, wenn die Größe des thermodynamischen Bades variiert wird, sofern das kombinierte System hinreichend groß ist. Die drei Standard-kanonischen Ensembles bleiben dabei spezielle Idealisierungen von physikalischen Systemen. Die allgemeineren Ensembles mit endlichem thermodynamischem Bad sollten daher

ebenfalls von phänomenologischem oder konzeptionellem Interesse sein. Diese ersten beiden Kapitel bilden somit die mathematische Grundlage für die analytischen Berechnungen und Monte Carlo Simulationen, die für diese Arbeit durchgeführt wurden.

Die Analyse von Hadronen-Resonanz-Gas-Ereignissen beginnt mit dem Studium des großkanonischen Ensembles in Kapitel 4. Das großkanonische Ensemble gilt als das am leichtesten zugängliche unter den Standard-kanonischen Ensembles. Aufgrund der Annahme eines unendlichen thermodynamischen Bades, sind die Besetzungszahlen in den einzelnen Impulszuständen der Teilchen miteinander unkorreliert. Somit erscheinen auch die Teilchenanzahlen von je zwei verschiedenen Gruppen von Teilchensorten miteinander unkorreliert. Aufgrund der Annahme von unkorrelierten Besetzungszahlen, ergibt sich, daß alle extensiven Meßgrößen, mit Ausnahme des Volumens von Ereignis zu Ereignis (oder von Mikrozustand zu Mikrozustand) variieren. Der Energieinhalt und die Teilchenanzahl des Systems sind somit stark miteinander korreliert, während die durchschnittliche Energie pro Teilchen mit der Teilchenanzahl unkorreliert ist. Die elektrische Ladung, Baryonenzahl und Seltsamkeit des Systems sind korreliert mit der Hadronenanzahl, weil einige Teilchenarten mehrere dieser Ladungen tragen. Verschiedene Teilchenarten haben verschiedene Quantenzahlkonfigurationen und folgen aufgrund ihrer Masse unterschiedlichen Impulsspektren. Die Korrelation zwischen Baryonenzahl und Seltsamkeit im beobachteten Subsystem hängt dann, wie die Korrelation von Energie und Impuls oder von Energie und Teilchenanzahl, davon ab, welcher Teil des Impulsspektrums der Messung zugänglich ist.

In Kapitel 5 wurden multivariate Wahrscheinlichkeitsverteilungen von extensiven Meßgrößen zu ihren mikrokanonischen Grenzwert extrapoliert. Zu diesem Zweck wurden iterativ Stichproben von Ereignissen erzeugt, und für abnehmende Größe des thermodynamischen Bades analysiert. Die Verteilungsfunktion der extensiven Meßgrößen, die gewichtet wurden, konvergiert zu einer δ-Funktion, während die Positionen der Mittelwerte konstant geblieben sind. Während der Transversalimpuls pro Teilchen und die Teilchenanzahl im großkanonischen Ensemble noch unkorreliert waren, so gilt diese Annahme nicht mehr für Systeme mit endlichem Wärmebad. Durch die sukzessive Konzentration auf Ereignisse in der unmittelbaren Nähe eines gewählten Gleichgewichtswertes zeigen sich die Auswirkungen globaler Erhaltungssätze. Dies verläuft in einer systematischen Weise, so dass die Extrapolation von Observablen von ihren großkanonischen zu ihren mikrokanonischen Grenzwerten möglich wurde. Ein Nachteil ist, dass die statistische Unsicherheit, verbunden mit endlichen Stichproben, wächst, wenn man sich dem (mikro-)kanonischen Grenzwerten nähert.

In Kapitel 6 wurden Teilchenanzahlfluktuationen und Korrelationen für ein neutrales Hadronen-Resonanz-Gas mit begrenzter Teilchenakzeptanz im Impulsraum unter Berücksichtigung der Auswirkungen von Resonanzzerfällen untersucht. Die Extrapolationsmethode wurde angewandt, um kanonische und mikrokanonische Grenzwerte von Beobachtunggrößen zu ermittlen. Ein Vergleich mit

analytischen, asymptotischen Lösungen für primordiale Verteilungen in begrenzter Teilchenakzeptanz zeigen eine sehr gute Übereinstimmung der beiden Methoden. Je größer die Anzahl der zu erhaltenen extensiven Meßgrößen, desto größer ist auch die statistische Unsicherheit, die mit endlichen Stichproben von Ereignissen verbunden ist. Mikrokanonische Effekte jedoch werden durch den Monte Carlo Ansatz korrekt wiedergegeben. Werden Erhaltungssätze eingeschaltet, so werden Teilchenanzahlfluktuationen und Korrelationen modifiziert. Impulsraumeffekte bei Teilchenanzahlfluktuationen und Korrelationen ergeben sich aufgrund von Erhaltungssätzen. Für ein ideales, primordiales, großkanonisches Ensemble in der Boltzmann-Näherung (der Ausgangspunkt), sind die Teilchenanzahlverteilungen unkorrelierte Poissonverteilungen, unabhängig von der gewählten Akzeptanz im Impulsraum, da davon ausgegangen wurde, dass Teilchen unabhängig voneinander produziert werden. Das Erfordernis der Energie-, Impuls- und Ladungserhaltungssätze führt zu unterdrückten Fluktuationen und verstärkten Korrelationen zwischen den Teilchenanzahlen von zwei verschiedenen Gruppen von Teilchen am „oberen“ Ende des Impulspektrums, im Vergleich zum „unteren“ Ende des Impulsspektrum, vorausgesetzt, einen nicht vernachlässigbarer Teil eines isolierten Systems wird beobachtet. Resonanzzerfälle änderen diese Trends nicht.

Kapitel 7 ist dem mikrokanonischen Ensemble gewidmet. Ein vereinfachtes physikalisches System wurde gewählt, um eine einfachere Diskussion zu ermöglichen. Aufgrund der zur Verfügung stehenden analytischen Lösungen, konnten Fermi-Dirac und Bose-Einstein-Effekte in die Analyse miteinbezogen werden. Bose-Einstein-Verstärkung und Fermi-Dirac-Unterdrückung der Teilchenanzahlfluktuationen sind besonders stark in Impulsraumsegmenten, in denen die Besetzungszahlen in den einzelnen Impulszuständen groß sind. Dieser Effekt ist deutlich stärker als der, der in früheren Berechnungen von Fermi-Dirac und Bose-Einstein Effekten auf Teilchenanzahlfluktuationen im vollen Phasenraum ermittelt wurde. Für Systeme in kollektiver Bewegung wurde festgestellt, dass die Rolle, die kinematische Erhaltungssätze spielen, besonders wichtig ist. Fluktuation und Korrelation von Messgrößen sind Lorentz-invariant, sofern Impulserhaltung entlang der kollektiven Bewegungsrichtung berücksichtigt wird. Schließlich wurde festgestellt, daß auch im thermodynamischen Grenzwert Langstreckenkorrelationen zwischen getrennten Regionen im Impulsraum verbleiben. Teilchenanzahlen in unterschiedlichen Intervallen in der Rapidität, im transversalen Impulsraum, oder im Azimut, haben einen nicht verschwindenden Korrelationskoeffizienten.

In Kapitel 8 wurde das Phasendiagramm für das Hadronen-Resonanz-Gas-Modell in seiner Abhängigkeit von Temperatur und baryonchemischem Potential untersucht. Großkanonische Ladungskorrelationen und Fluktuationen sind unterschiedlich in den vier verschiedenen Ecken des Phasendiagramms. Wie in der Akzeptanzanalyse ist die Korrelation zwischen zwei Ladungen stark, wenn Teilchen, die beide Ladungen tragen, reichlich vorhanden sind. Bei niedriger Temperatur und niedrigem baryonchemischem Potential dominieren Mesonen über Baryonen,

bei hoher Temperatur und hohem baryonchemischem Potential hingegen tragen Baryonen einen Großteil der Gesamtentropie des Systems. Diesem Zusammenhang entsprechend verhalten sich Fluktuationen und Korrelationen der Ladungen systematisch. Auch Teilchenanzahlfluktuationen und Korrelationen im kanonischen und mikrokanonischen Ensembles tragen dem Rechnung. Der Einfluss eines bestimmten Erhaltungsatzes auf Teilchenanzahlfluktuationen ist stark, wenn die Teilchen der analysierten Arten reichlich vorhanden sind, und somit einen wesentlichen Teil der Gesamtladung und -energie tragen. Ein Vergleich zwischen Ensembles mit und ohne Energie-, Ladungs- oder Impulserhaltung zeigt subtile Unterschiede, die unter anderem am Beispiel von Resonanzzerfällen in kanonischen und mikrokanonischen Ensembles herausgearbeitet wurden. Resultierende primordialen Teilchenanzahlkorrelationen ergeben sich nicht aufgrund von lokalen Interaktionen zwischen den Bestandteilen, sondern aufgrund von global implementierten Erhaltungssätzen für Energie und Ladungen.

In Kapitel 9 wurden Teilchenanzahlfluktuationen und Korrelationen für thermische Parameter analysiert, die der chemischen Freeze-out Linie zentraler Schwerionenkollisionen folgen. Modellparameter wurden von früheren Hadronen-Resonanz-Gas-Modell-Vergleichen mit experimentellen Messungen von mittleren Hadronproduktionsraten übernommen. Diese Messungen stellen eine Verbindung zwischen den experimentellen Kontrollparametern Kollisionsenergie und Größe der zu kollidierenden Ionen, und der Region im Phasendiagramm, die durch das Experiment sondiert wird, her. Einem ersten Vergleich mit experimentellen Daten zufolge ergibt sich eine gute Übereinstimmung mit Hadronen-Resonanz-Gas-Berechnungen. Insbesondere die mikrokanonischen Formulierung des Modells scheint qualitative und quantitative Eigenschaften der Daten gut zu reproduzieren.

Die hier vorgestellten Berechnungen beschreiben qualitative Auswirkungen auf Teilchenanzahlfluktuationen und Korrelationen. Diese Auswirkungen ergeben sich allein aus den Prinzipien der statistischen Mechanik und aufgrund der Anwendung globaler Erhaltungssätze. Es wird interessant sein, zu sehen, ob diese qualitativen Auswirkungen in weiteren experimentellen Messungen von Fluktuationen und Korrelationen sichtbar werden. Wenn ja, könnten diese Effekte wohl von ähnlicher Größenordnung sein, wie die Signale „neuer“ Physik. Das Trennen von dynamischer Evolution des Systems und statischen Erhaltungssätzen ist dann eine wichtige, wenn auch nicht-triviale Aufgabe. Gleichgewichtskorrelationen sind Restkorrelationen, die zurück bleiben, nachdem das System seine (Entwicklungs) Geschichte „vergessen“ hat. Wenn das System „beobachtet“ oder „gemessen“ wird, bevor es einen Gleichgewichtszustand erreicht hat, dann werden Korrelationen aufgrund der Anfangskonfiguration verbleiben. Aber selbst wenn sich das System während seiner Lebensdauer fern von jedem Gleichgewichtspunkt bewegt, so spielen Korrelationen aufgrund der globalen Erhaltungssätze eine wichtige Rolle.

Acknowledgments

First of all I would like to thank my supervisor Professor Elena Bratkovskaya for her patience and guidance. Most of all for giving me the freedom to pursue every once in a while my own interest. I am also grateful to Professor Mark Gorenstein and Professor Marek Gaździcki for constructive collaboration and many stimulating discussions on, amongst other things, the philosophy of doing science.

I would like to acknowledge my scholarship of the Helmholtz Research School at the University of Frankfurt. In particular I would like to thank our course administrator and coordinator Henner Busching for dedicating so much of his energy to this first generation of Helmholtz-PhD students.

I would like to express my gratitude to the Professors Francesco Becattini, Marcus Bleicher, Christoph Blume, Wojciech Broniowski, Jean Cleymans, Krzysztof Redlich, and Peter Steinberg for always having an open ear or two.

I also would like to thank my collaborators and colleagues Viktor Begun, Volodymir Konchakovski, Benjamin Lungwitz, and Oleg Moroz, and for an enjoyable and fruitful time together.

Special thanks here goes to my friends Lorenzo Ferroni, Stephane Häussler, Torsten Kolleger, Jaakko Manninen, Michael Mitrovski, Sophie Nahrwold, Irina Sagert, Tim Schuster, Giorgio Torrieri, and Sascha Vogel for invaluable feedback, opinions, and (if applicable) beer drinking moments.

I am also grateful to Bruce Becker, Gareth de Vaux, Spencer Wheaton, and many many more of, at, and around the physics department of the University of Cape Town, my second home base. In particular I would like to gratefully acknowledge the financial support I have received for two trips to South Africa, which have been the most productive days of my PhD.

To family and friends, and all of you who have shared the one or the other cigarette with me.

Contents

Chapter 1

Introduction

This thesis is dedictaed to the study of fluctuation and correlation observables of hadronic equilibrium systems. The statistical hadronization model of high energy physics, in its ideal, i.e. non-interacting, gas approximation will be investigated in different ensemble formulations. The hypothesis of thermal and chemical equilibrium in high energy interaction will be tested against qualitative and quantitative predictions.

The statistical hadronization model, first introduced by Fermi [1] and Hagedorn [2], has been surprisingly successful during the last couple of decades in describing fundamental properties of systems created in heavy ion collisions, cosmic rays, and elementary particle reactions. In the context of heavy ion collisions it has been applied to an extensive set of data on hadron production, ranging form the center of mass energies of the experiments at the SIS [3, 4, 5], AGS [6], SPS [7, 8, 9],and most recently, RHIC [10] facilities. Model predictions for the upcoming LHC and future FAIR [11, 12, 13, 14, 15, 16, 17] experiments largely follow these trends. A systematic evolution of thermodynamic parameters, as collision energy (and size of colliding ions) is changed [18, 19, 20, 21, 22], has allowed to establish the 'chemical freeze-out line', which is now a commonly accepted ingredient in the phase diagram of strongly interacting matter. More controversially this model has also been applied to a range of elementary collision systems [23, 24, 25], where only few particles are produced, and the picture of a gas of hadrons can hardly be suitable. The remarkable ability of the statistical model to explain these data has lead to the suggestion [23, 24, 25, 26, 27, 28],

that thermal (or phase space dominated) particle production is a general property of the hadronization process itself, rather than the result of a long sequence of microscopic interactions. This thesis will not argue about possible physical interpretations [29] of the partition function of statistical mechanics. It is, however, noted that in order to apply a semi-classical approximation a volume of $\mathcal{O}(10\ \mathrm{fm}^3)$ seems to be sufficient [30].

Somewhere above this chemical freeze-out line in the phase diagram a phase transition from hadronic degrees of freedom to a phase of deconfined quarks and gluons, generally termed the quark-gluon plasma is conjectured; more specifically, a first order phase transition at low temperature and high baryon chemical potential, and a cross-over at high temperature and low baryon chemical potential. In between, a second order endpoint or a critical point might emerge. For recent reviews see [31, 32, 33, 34, 35, 36, 37, 38]. One of the answers still outstanding in high energy physics is then the one of a possible formation of a deconfined state of matter, and the nature of the transition between phases. The growing interest in the study of event-by-event fluctuations in strong interactions is, thus, motivated by expectations of anomalies in the vicinity of the onset of deconfinement [39, 40, 41, 42, 43] and in the case when the expanding system goes through the transition line between quark-gluon plasma and hadron gas [44, 45, 46]. In particular, a critical point of strongly interacting matter may be accompanied by a characteristic power-law pattern in fluctuations [47, 48, 49]. Recently, it has been suggested that correlations across a large interval of rapidity could also arise from color glass condensate initial conditions [50, 51].

In recent years a wide range of experimental measurements of fluctuations of particle multiplicities [52, 53, 54, 55, 56, 57, 58, 59], transverse momenta [60, 61, 62, 63, 64] and multiplicity correlations in rapidity [65, 66, 67] have been reported, leading to a lively discussion regarding their physical interpretation. The most promising region in the phase diagram for observation of critical phenomena seems to be accessible to the SPS accelerator [68, 69, 70]. A new SPS scan program [71] for different ion sizes as well as center-of-mass energies has been proposed to study strongly interacting systems at different energy and net-baryon densities, and life times. Also a second scan program [72], lowering the RHIC colliding beam energy to probe the same domain of the phase diagram,

is under discussion. This should be as well the main motivation for further investigation of properties of statistical ensembles.

Fluctuations of, and correlations between, various experimental observables are believed to have the potential to reveal new physics. They are amongst the most promising candidates suggested to be suitable for signaling the formation of new states of matter, and transitions between them. For recent reviews here see [41, 42, 43, 44, 46, 47, 48, 49, 73, 74]. In particular, multiplicity and charge fluctuations have been proposed to be a good discriminating tool between quark-gluon plasma and hadron gas [39, 40]. Provided the signal survives the phase transition [75], and subsequent evolution of the system. Hence, in order to properly assess the discriminating power of such observables, one might firstly want to asses the magnitude of 'trivial' physical effects, such as the ones induced by global conservation laws, quantum statistics, resonance decays, kinematical cuts, finite spatial extension, etc. The statistical properties of a sample of events are certainly not solely determined by critical phenomena. To get a reliable indication of new physics, it is therefore important to note that most fluctuation and correlation observables are also sensitive to some 'baseline' contributions that, nevertheless, can have non-trivial behavior.

A rather general observation regarding statistical samples can be made: The statistical properties of a sample of events depend on the rules chosen to select this sample from an even larger sample, and on the degree of completeness of the information available about the sample. In the context of heavy ion collision physics these two aspects roughly translate into centrality class construction and particle acceptance in momentum space.

Centrality selection is discussed first. Two heavy ions collide with relativistic momenta. Being extended objects, they can do so in many different ways. Roughly the following rule should apply (in the average sense): The larger the interaction region, the more particles of each particle species are produced. The problem is now that the initial state of a collision cannot be observed directly. All that can be observed is its final state. From this, one can then infer the likelihood of a certain initial state. Yet, each single possible final state observable will generally suggest a slightly different initial state. Hence, the need to average over centrality classes. The problem is then, within any such centrality

class will be events with rather different initial states, altering the true correlation between two observables. Results will depend, in general, on which trigger was chosen to construct the centrality class or sample of events [76, 77]. Centrality selection, although being a crucial experimental issue, is foreign to the statistical hadronization model, and will not be considered in this thesis.

The second problem is particle acceptance. This term should denote particle identification and momentum measurement. Centrality selection is now ignored and a perfectly prepared initial state is assumed. Two limiting cases can be explored. The first one being the ideal detector. All final state particles are observed. Any correlation is measured to any degree. The opposite limit would be a very bad detector. Capable of only detecting a particle every once in a while. This detector could surely measure the ratios of the occurrence of particles of different species. But it would be completely unable to inform one on how particle species within one event are correlated. Any realistic detector is in between these limits. And, hence, will disagree with either limit, in basically any observable. The statistical hadronization model provides a natural framework for such a discussion.

Strictly speaking the model, at least in the from presented here, is not directly comparable to data of heavy ion collisions. It does certainly no justice to the complexity and the dynamical evolution of the system it seeks to describe. The model exhibits no collective flow, or expansion. The size (or volume) of the system is assumed to be the same for all events. Furthermore, no distinction is made between chemical and kinetic freeze-out. On the other hand, the medium created during the collisions of two heavy ions is rapidly expanding, while the initial state can only be accessed indirectly. Yet, essentially the model seeks to describe properties of many-particle systems, and, here in this thesis, their statistical properties. The statistical hadronization model, might not be a bad place to start such a task.

The purpose of this thesis is the calculation of 'baseline' contributions, on top of which one hopes to find unambiguous signals of a phase transition [44, 45, 46], a critical point [47, 48, 49], or thermal/chemical (local or global) non-equilibrium [78, 79, 80]. I.e. to study these baseline correlations in a limiting case: that of a thermalized relativistic ideal (no inter-particle interactions)

quantum gas, for which we want to assess the importance of globally applied conservation laws, quantum statistics, resonance decays, and kinematical cuts for fluctuation and correlation observables. In this case, all observables are calculable simply using statistical mechanics techniques. Such an approach has a long and distinguished history of calculating particle multiplicities in hadronic collisions [1, 9, 81, 82, 83, 84, 85, 86, 87, 88, 89, 90]. Given its success in describing experimentally measured average hadron yields, and its ability to reproduce low temperature lattice susceptibilities [91], the question arises as to whether fluctuation and correlation observables also follow its main line. Critical phenomena (and many more), however, remain beyond the present study.

Conventionally in statistical mechanics three standard ensembles are discussed; the micro canonical ensemble (MCE), the canonical ensemble (CE), and the grand canonical ensemble (GCE). In the MCE[1] one considers an ensemble of micro states with exactly fixed values of extensive conserved quantities (energy, momentum, electric charge, etc.), with 'a priori equal probabilities' of all micro states (see e.g. [92]). The CE introduces the concept of temperature by introduction of an infinite thermal bath, which can exchange energy (and momentum) with the system. The GCE introduces further chemical potentials by attaching the system under consideration to an infinite charge bath[2]. Only if the experimentally accessible system is just a small fraction of the total, and all parts have had the opportunity to mutually equilibrate, can the appropriate ensemble be the grand canonical ensemble.

The main focus of the past study of the statistical hadronization model has been on the mean multiplicities of produced hadrons. However, there is a qualitative difference in the properties of mean values and event-by-event fluctuations about these mean values in statistical mechanics. In the case of the ensemble averages, results obtained in the GCE, CE, and MCE approach each other in the large volume limit. One refers here to as the thermodynamical equivalence of statistical ensembles. However, even in this limit, these ensembles have different

[1]The term MCE is also often applied to ensembles with energy but not momentum conservation.

[2]Note that a system with many charges can have some charges described via the CE and others via the GCE.

properties with respect to fluctuations and correlations [93, 94, 95]. In the MCE, energy and charge are exactly fixed. In the CE, charge remains fixed, while energy is allowed to fluctuate about some average value. Finally, in the GCE the requirement of exact charge conservation is dropped, too. One may also consider isobaric ensembles [96], or even more general 'extended Gaussian ensembles' [97, 98]. In previous articles [93, 94, 95, 96, 98, 99, 100, 101, 102, 103, 104, 105, 106] it was shown that these differences mean that, in particular, multiplicity fluctuations and correlations are ultimately ensemble specific. I.e. depend on how the system under investigation is prepared.

The observation that fluctuations of certain quantities are constraint by conservation laws is not new, nor restricted to heavy ion physics. The Italian physicist Ugo Fano wrote back in 1947 in the abstract of his article [107] 'Ionization Yield of Radiations. II. The Fluctuations of the Number of Ions':

> *The ionization produced by individual fast charged particles is frequently used as a measure of their initial energy; fluctuation effects set a theoretical limit to the accuracy of this method. Formulas are derived here to estimate the statistical fluctuations of the number of ions produced by constant amounts of radiation energy. The variance of the number of ionizations is found to be two or three times smaller than if this number were governed by a Poisson distribution. An improved understanding is gained of the statistical treatment of fluctuation phenomena.*

So, it has been well understood, already some 60 years ago, that global conservation laws affect the statistical properties of a system. Similar observation was made in the fluctuation of the number of atoms forming a Bose-Einstein condensate. The 'grand canonical fluctuation catastrophe' at the Bose-Einstein condensation point [108] is avoided by a micro canonical formulation [109].

This thesis is organized as follows: In Chapter 2 grand canonical joint distributions of extensive quantities are obtained by Fourier integration of the grand canonical partition function. An analytical expansion method for calculation of distributions at finite volume for the canonical as well as the micro canonical ensembles of the ideal relativistic hadron resonance gas will be presented. In

Chapter 3 joint distributions of extensive quantities are then considered for statistical systems with finite, rather than infinite, thermodynamic bath. These two chapters form the mathematical basis for analytical calculations and Monte Carlo simulations performed in this thesis. The analysis of hadron resonance gas events will start with the study of the grand canonical ensemble in Chapter 4. The grand canonical ensemble is considered to be the most accessible amongst the standard canonical ensembles. In Chapter 5 joint distributions of extensive quantities will be extrapolated to the micro canonical limit. In Chapter 6 multiplicity fluctuations and correlations are studied for a neutral and static hadron resonance gas with limited acceptance in momentum space. The effects of resonance decay will be considered, and the extrapolation scheme will be applied to obtain canonical and micro canonical ensemble limits. Chapter 7 is dedicated to the micro canonical ensemble itself. A simplified physical system is chosen to allow for smoother discussion. Owing to available analytical solutions, Fermi-Dirac and Bose-Einstein effects, as well as collective motion, are included into the analysis. In Chapter 8 the temperature and baryon chemical potential phase diagram of the hadron resonance gas model is explored. Lastly, in Chapter 9, multiplicity fluctuations and correlations will be analyzed for thermal parameter sets following the chemical freeze-out line. A first comparison to available experimental data suggests good agreement with hadrons resonance gas calculations. A summary, Chapter 10, will close the thesis. Further technical details of the calculations and Monte Carlo simulations, are presented in the Appendix.

Chapter 2

Grand Canonical Partition Function

Aim of this chapter is to introduce a technique for calculation of grand canonical probability distributions[1] of various extensive quantities at finite volume. The method is based on Fourier analysis of the grand canonical partition function. Taylor expansion of the generating function is used to separate contributions to the partition function in their power in volume. Laplace's asymptotic expansion is employed to show that any equilibrium distribution of multiplicity, charge, energy, etc. tends to a multivariate normal distribution in the thermodynamic limit. Gram-Charlier expansion allows additionally for calculation of finite volume corrections. Analytical formulas facilitate inclusion of resonance decay (in full acceptance), or inclusion of finite acceptance effects (without resonance decay) directly into the system partition function. Multiplicity distributions in (micro) canonical ensembles can then be defined through conditional grand canonical distributions.

The discussion of equilibrium systems with finite, rather than infinite, thermodynamic bath, in Chapter 3, will provide a description for a Monte Carlo approach, capable of assessing the effects resonance decay in finite acceptance. These two chapters will prepare the mathematical framework for the following discussions of statistical fluctuations and correlations in hadronic equilibrium systems.

[1]The term 'distribution' is used for simplicity, rather than the more correct 'probability density function'.

2.1 Probability Distributions

In textbooks on statistical mechanics (see e.g., Ref.[110, 111, 112]) often first the MCE is introduced, where exact conservation laws for energy-momentum and particle number are imposed on a collection of micro states. Relaxing the constraints for energy and momentum constitutes the CE, while allowing additionally particle number to fluctuate about some mean value introduces the GCE. In a relativistic gas of hadrons quantum numbers (charges), rather than particle numbers, will be the conserved quantities.

Here it will prove to be of considerable advantage to start off with the GCE formulation and imposing exact conservation laws thereafter. Generally, the (micro) canonical partition function is obtained from the grand canonical one by multiplication with Kronecker (or Dirac) δ-functions which pick out a set of micro states consistent with a particular conservation law. It is often more economical to use Fourier representations of δ-functions, rather than the δ-function themselves.

The basic idea is to define the probability of finding the system in a state with a given number of particles N_A of some species A at some fixed value of conserved (electric) charge, Q, i.e. the CE distribution $P_{ce}(N_A)$, in terms of the GCE distributions, $P_{gce}(N_A, Q)$ and $P_{gce}(Q)$. In general one may write for the multiplicity distribution $P_{ce}(N_A)$ of a CE with conserved electric charge Q:

$$P_{ce}(N_A) \;=\; \frac{\text{number of all micro states with } Q \text{ and } N_A}{\text{number of all micro states with } Q} \;. \tag{2.1}$$

Likewise, one can write for the CE joint multiplicity distribution $P_{ce}(N_A, N_B)$ of particle species A and B:

$$P_{ce}(N_A, N_B) \;=\; \frac{\text{number of all micro states with } Q,\ N_A \text{ and } N_B}{\text{number of all micro states with } Q} \;. \tag{2.2}$$

The number of all micro states with electric charge Q, and multiplicities N_A and N_B of a system with temperature $T = \beta^{-1}$ and volume V is given by the CE partition function $Z(V, \beta, Q, N_A, N_B)$. Similarly, $Z(V, \beta, Q)$ denotes the number of micro states with fixed electric charge Q, but arbitrary multiplicities N_A and N_B, for the same physical system.

Throughout this thesis the following conventions are used: Ensembles are to be identified by the arguments of their partition functions. Extensive quantities,

denoted by capital letters in the argument, are to be considered as exactly conserved. Intensive quantities, denoted by small letters in the argument, indicate that the corresponding extensive quantity is conserved only in the average sense. The partition function $Z(V, E, Q)$ denotes a MCE with conserved energy E and electric charge Q. The partition function $Z(V, \beta, Q)$ belongs the a CE with an infinite heat bath at temperature β^{-1}. The energy content of the volume V fluctuates then about some mean value $\langle E \rangle$. Lastly, $Z(V, \beta, \mu)$, is the number of micro states available to a system with an infinite heat and charge bath at temperature β^{-1} and chemical potential μ. All constraints on the micro states are dropped, and a weighted average over all charge and energy configurations is taken.

Particle number is here included in the argument of partition functions, despite the fact that no (non-vanishing) particle number specific chemical potential is introduced. Fourier integrals associated with particle multiplicity are going to be solved along with those associated with conserved quantities. In the next chapter, particle number is deligated to an index of the partition function, as its integrals do not need to be solved for the Monte Carlo approach.

The strategy to calculate joint multiplicity distributions could thus be the following (in principle also valid at finite volume):

$$P_{ce}(N_A, N_B) = \frac{Z(V, \beta, Q, N_A, N_B)}{Z(V, \beta, Q)} , \tag{2.3}$$

$$= \frac{e^{Q\mu\beta}\ Z(V, \beta, Q, N_A, N_B)}{Z(V, \beta, \mu)} \frac{Z(V, \beta, \mu)}{e^{Q\mu\beta}\ Z(V, \beta, Q)} , \tag{2.4}$$

$$= P_{gce}(Q, N_A, N_B)\ P^{-1}_{gce}(Q) = P_{gce}(N_A, N_B|Q) . \tag{2.5}$$

In order to get from Eq.(2.3) to Eq.(2.5) both canonical partition functions $Z(V, \beta, Q, N_A, N_B)$ and $Z(V, \beta, Q)$ are divided by their GCE counterpart $Z(V, \beta, \mu)$ and multiplied by the Boltzmann weight $e^{Q\mu\beta}$. The first term on the right hand side of Eq.(2.4) then equals the GCE joint distribution $P_{gce}(Q, N_A, N_B)$, while the second term is just the inverse of the GCE charge distribution $P_{gce}(Q)$. Their ratio is the (normalized) GCE conditional distribution of particle multiplicities N_A and N_B at fixed electric charge Q, $P_{gce}(N_A, N_B|Q)$, and equals the CE distribution $P_{ce}(N_A, N_B)$ at the same value of Q. This result is independent of the choice of chemical potential μ.

The problem of finding a solution, or a (large volume) approximation, to

the CE distribution $P_{ce}(N_A, N_B)$ is now turned into the problem of finding a solution or approximation to the GCE distribution of multiplicities N_A and N_B, and charge Q, $P_{gce}(Q, N_A, N_B)$.

It is worth noting that Eqs.(2.3-2.5) are as well the basis for any Monte Carlo approach [113, 114]. A sampling distribution, usually taken from a Boltzmann GCE system, is used to generate a $\{N_i\}$-tuple of particle multiplicities of all species i considered. All 'events' consistent with certain constraints, like a set of conserved charges, are accepted, while the rest is rejected. On the basis of this set of all accepted 'events' one constructs an ensemble by using a suitable re-weighting scheme to account for quantum statistics and proper normalization. For the Monte Carlo approach presented in the next chapter an unconstrained, i.e. grand canonical, sample of events, $P_{gce}(Q, \{N_i\})$, is generated. Constrained distributions could then be defined through:

$$P\big(Q, \{N_i\}\big) \;=\; W\big(Q\big)\; P_{gce}\big(Q, \{N_i\}\big)\;, \tag{2.6}$$

where a calculated weight factor $W(Q)$ is employed to project out a set of events in the vicinity of an equilibrium value Q_{eq}.

An immediate consequence of Eqs.(2.3-2.5) is that temperature and chemical potentials appear in this formulation of (micro) canonical distributions (as well as in the Monte Carlo [113, 114], microscopic correlator [99] and saddle point expansion [115] approaches). At first sight this seems to be a serious problem and an unnecessary complication of the initial task of finding a reasonable approximation to CE and MCE partition functions. However, the main technical challenge when numerically integrating the original version of the (micro) canonical partition function arises from a heavily oscillating integrand. Auxiliary parameters β and μ will produce a very smooth function, for which approximation schemes can be used. In taking the ratio, Eq.(2.4), artificially introduced temperature and chemical potential drop out. The quality of the approximation on the other hand will crucially depend on their choice.

In Section 2.2 the generating function of the GCE distribution of extensive quantities is introduced. In Section 2.3 it is shown that the requirement of maximizing the generating function of the charge distribution at some given equilibrium point leads to a unique determination of thermal parameters, and moreover constitutes the optimal choice for the approximation scheme. Emerging thermo-

dynamic relations are discussed in Section 2.4.

2.2 Generating Function of the Charge Distribution

The GCE partition function of an ideal relativistic gas with volume V, local temperature $T = \beta^{-1}$, chemical potentials μ_j and collective four velocity u_μ reads (the system four-temperature [113] is $\beta_\mu = \beta u_\mu$):

$$Z(V, \beta, u_\mu, \mu_j) = \exp\left[V\Psi\left(\beta, u_\mu, \mu_j\right)\right] , \tag{2.7}$$

where $\Psi\left(\beta, u_\mu, \mu_j\right)$ is a sum over the single particle partition functions $\psi_i\left(\beta, u_\mu, \mu_j\right)$ of all particle species i considered in the model:

$$\Psi\left(\beta, u_\mu, \mu_j\right) = \sum_i \psi_i\left(\beta, u_\mu, \mu_j\right) . \tag{2.8}$$

The single particle partition function $\psi_i\left(\beta, u_\mu, \mu_j\right)$ of particle species i is given by a Jüttner distribution:

$$\psi_i\left(\beta, u_\mu, \mu_j\right) = \frac{g_i}{(2\pi)^3} \int d^3p \, \ln\left(1 \pm e^{-\beta \, p_i^\mu \, u_\mu \, + \, \beta \, q_i^j \, \mu_j}\right)^{\pm 1} , \tag{2.9}$$

where p_i^μ are the components of the four momentum, q_i^j are the components of the charge vector, and g_i is the degeneracy factor. The upper sign refers to Fermi-Dirac statistics, while the lower sign refers to Bose-Einstein statistics. The case of Maxwell-Boltzmann statistics is analogous.

For a hadron resonance gas, including hadrons and their resonances up to a mass of about 2.5 GeV, i.e. excluding the charm quark sector, the vector of chemical potentials μ_j and the 'charge' vector q_i^j of particle species i are introduced[2]:

$$\mu_j = (\mu_B, \ \mu_S, \ \mu_Q, \ \mu_{N_A}, \ \mu_{N_B}) \qquad q_i^j = (b_i, \ s_i, \ q_i, \ n_A(\Omega), \ n_B(\Omega)) , \tag{2.10}$$

[2]Finite acceptance effects are discussed here. Modifications to Eqs.(2.9,2.10) which allow for inclusion of resonance decay in full acceptance are presented in Appendix C.

where μ_B, μ_S, and μ_Q are the baryon, strangeness, and electric charge chemical potentials, respectively. The parameters μ_{N_A} and μ_{N_B} are particle-specific chemical potentials, and could denote out of chemical equilibrium multiplicities of species 'A' and 'B', similar to phase space occupancy factors γ_s [116] and γ_q [117, 118]. Throughout this thesis out of equilibrium effects are neglected, and thus $\mu_{N_A} = \mu_{N_B} = 0$.

In addition, b_i, s_i, and q_i are the baryonic charge, the strangeness, and the electric charge of a particle of species i. Ω is the momentum space bin in which one is set to measure particle multiplicity. $n_A(\Omega) = 1$ if the momentum vector of the particle is within the acceptance, $n_A(\Omega) = 0$ if not. The charge vector q_i^j also contains, to maintain a common notation for all particle species considered in Eq.(2.8), the 'quantum' number $n_B(\Omega)$. If one were set to determine the joint distribution of positively versus negatively charged hadrons, for instance, the π^+ particle would have $q_{\pi^+} = (0, 0, 1, 1, 0)$, while the K^- particle would have $q_{K^-} = (0, -1, -1, 0, 1)$, see Chapters 6 and 7.

One may also be interested in correlations of, for instance, the systems net-baryon number B and net-strangeness S, as e.g. in Refs.[74, 91]. In this case, the Λ particle, with $q_\Lambda = (1, -1, 0, 1, -1)$, would be counted in groups A and B, provided the momentum vector is within the acceptance Ω. The Ξ^- particle on the other hand carries two strange quarks and would have $q_{\Xi^-} = (1, -2, -1, 1, -2)$, see Chapters 4 and 5.

The generating function of the charge distribution in the GCE is introduced by the substitutions in Eq.(2.9):

$$\beta\ \mu_j \ \rightarrow \ \beta\ \mu_j \ + \ i\phi_j\ , \tag{2.11}$$

$$\beta\ u_\mu \ \rightarrow \ \beta\ u_\mu \ - \ i\alpha_\mu\ . \tag{2.12}$$

The yet un-normalized joint probability distribution of extensive quantities Q^j, P^μ in the GCE is then given by the Fourier transform of Eq.(2.7) after substitutions

Eqs.(2.11,2.12):

$$\mathcal{Z}^{P^\mu,Q^j}(V,\beta,u_\mu,\mu_j) = \int_{-\pi}^{\pi} \frac{d^J\phi}{(2\pi)^J}\, e^{-iQ^j\phi_j} \int_{-\infty}^{\infty} \frac{d^4\alpha}{(2\pi)^4}\, e^{-iP^\mu\alpha_\mu} \times \exp\left[V\Psi\left(\beta,u_\mu,\mu_j;\alpha_\mu,\phi_j\right)\right] . \tag{2.13}$$

Depending on the system under consideration, the vector of extensive quantities Q^j and corresponding Wick rotated fugacities ϕ_j could read:

$$Q^j = (B,\ S,\ Q, N_A, N_B) \qquad \phi_j = (\phi_B,\ \phi_S,\ \phi_Q,\ \phi_{N_A},\ \phi_{N_B}) . \tag{2.14}$$

Here B is the net-baryon number, S is the net-strangeness, and Q is the electric net-charge of the system. Together with particle numbers N_A and N_B this would be a 5-dimensional distribution in the case of a CE hadron resonance gas. Additionally for four-momentum conservation, yielding a 9-dimensional Fourier transform Eq.(2.13) for a MCE hadron resonance gas, the vectors P^μ and α_μ are introduced:

$$P^\mu = (E,\ P_x,\ P_y,\ P_z) \qquad \alpha_\mu = (\alpha_E,\ \alpha_{P_x},\ \alpha_{P_y},\ \alpha_{P_z}) , \tag{2.15}$$

where E is the energy and P_x, P_y, and P_z are the components of the collective momentum of the system, while α_μ are the corresponding fugacities.

The distinction between discrete (Kronecker δ) and continuous quantities (Dirac δ) is not relevant for the large volume approximation, where particle number is a continuous variable to be integrated over. Proceeding by Taylor expansion of Eq.(2.8), it is convenient to include discrete and continuous quantities into a common vector notation:

$$\mathcal{Q}^l = \left(Q^j,\ P^\mu\right) \qquad \text{and} \qquad \theta_l = (\phi_j,\ \alpha_\mu) . \tag{2.16}$$

The dimensionality of the vector $\mathcal{Q}^l$ is denoted as $L = 2 + 3 + 4 = 9$ for a MCE hadron resonance gas. Now, expanding the cumulant generating func-

tion, $\Psi\left(\beta, u_\mu, \mu_j; \theta_l\right)$, in a Taylor series yields:

$$\Psi\left(\beta, u_\mu, \mu_j; \theta_l\right) \simeq \sum_{n=0}^{\infty} \frac{i^n}{n!} \kappa_n^{l_1,l_2,\ldots,l_n} \theta_{l_1} \theta_{l_2} \ldots \theta_{l_n} , \tag{2.17}$$

where the elements of the cumulant tensor, $\kappa_n^{l_1,l_2,\ldots,l_n}$, are defined by:

$$\kappa_n^{l_1,l_2,\ldots,l_n} = (-i)^n \left. \frac{\partial^n \Psi}{\partial\theta_{l_1}\partial\theta_{l_2}\ldots\partial\theta_{l_n}} \right|_{\theta_l=0_l} . \tag{2.18}$$

Generally cumulants are tensors of dimension L and order n. The first cumulant is then a vector, while the second cumulant is a symmetric $L \times L$ matrix. A good approximation to Eq.(2.13) around the point $\mathcal{Q}_{eq}^l = (Q_{eq}^j, P_{eq}^\mu)$, can be found in terms of a Taylor expansion of Eq.(2.8) in $\theta_l = (\phi_j, \alpha_\mu)$, if (see Section 2.3):

$$\left. \frac{\partial \mathcal{Z}^{\mathcal{Q}^l}(V, \beta, u_\mu, \mu_j)}{\partial \mathcal{Q}^l} \right|_{\mathcal{Q}^l=\mathcal{Q}_{eq}^l} = 0_l . \tag{2.19}$$

Implicitly, Eq.(2.19) does not define chemical potentials μ_j and four-temperature $\beta_\mu = \beta u_\mu$, but corresponding Lagrange multipliers, which maximize the amplitude of the Fourier spectrum $\mathcal{Z}^{\mathcal{Q}^l}(V, \beta, u_\mu, \mu_j)$ of the generating function for a desired value of $\mathcal{Q}_{eq}^l = (Q_{eq}^j, P_{eq}^\mu)$. Their values generally differ from the GCE set (β, u_μ, μ_j), however they coincide in the thermodynamic limit. Lagrange multipliers are relevant for finite volume corrections in Section 2.3. The temperature β and the four-velocity u_μ are not five independent Lagrange multipliers, as the four-velocity vector has unit length $u_\mu u^\mu = 1$. The integrand of Eq.(2.13) is sharply peaked at the origin $\phi_j = \alpha_\mu = 0$ in the thermodynamic limit. The main contribution therefore comes from a very small region [115]. To see this, a second derivative test can be done on the integrand of Eq.(2.13) taking into account the first two terms of Eq.(2.18), see Appendix B.

The cumulant of 0^{th} order, κ_0, is just the logarithm of the GCE partition function divided by the volume, $Z\left(V, \beta, u_\mu, \mu_j\right) \equiv \exp(V\kappa_0)$. Hence, after extending

the limits of integration to $\pm\infty$, which will introduce a negligible error, one finds:

$$\mathcal{Z}^{\mathcal{Q}^l}(V,\beta,u_\mu,\mu_j) \;\simeq\; Z(V,\beta,u_\mu,\mu_j) \int\limits_{-\infty}^{\infty} \frac{d^L\theta}{(2\pi)^L} \exp\Bigg[-i\mathcal{Q}^l\theta_l + V\sum_{n=1}^{\infty}\frac{i^n}{n!}\,\kappa_n^{l_1,l_2,\ldots,l_n}\,\theta_{l_1}\theta_{l_2}\ldots\theta_{l_n}\Bigg] . \tag{2.20}$$

It is worth noting that the parts of the integrand of Eq.(2.13) related to discrete quantities were 2π-periodic, while the integrand of Eq.(2.20) is a superposition of oscillating and decaying modes. Spelling out the first two terms of the summation yields:

$$\mathcal{Z}^{\mathcal{Q}^l}(V,\beta,u_\mu,\mu_j) \;\simeq\; Z(V,\beta,u_\mu,\mu_j) \int\limits_{-\infty}^{\infty} \frac{d^L\theta}{(2\pi)^L} \exp\Bigg[-i\mathcal{Q}^l\theta_l + iV\kappa_1^l\theta_l - V\frac{\kappa_2^{l_1,l_2}}{2!}\theta_{l_1}\theta_{l_2} + V\sum_{n=3}^{\infty}\frac{i^n}{n!}\,\kappa_n^{l_1,l_2,\ldots,l_n}\,\theta_{l_1}\theta_{l_2}\ldots\theta_{l_n}\Bigg]. \tag{2.21}$$

Performing now a change of variables will simplify this integral:

$$\vartheta_l \;=\; \sqrt{V}\;{\sigma_l}^k\;\theta_k\;, \tag{2.22}$$

where ${\sigma_l}^k$ is the square root of the second rank tensor κ_2:

$${\sigma_l}^k \;\equiv\; \left({\kappa_2}^{1/2}\right)_l^{\;k}. \tag{2.23}$$

The new integral measure $d^L\vartheta$ then equals to:

$$d^L\vartheta \;=\; \det\left|\sqrt{V}\;\sigma\right| d^L\theta \;=\; V^{L/2}\;\det|\sigma|\;d^L\theta\;. \tag{2.24}$$

Lastly in terms of this transformation normalized cumulant tensors λ_n with components:

$$\lambda_n^{l_1,l_2,\ldots,l_n} \;\equiv\; \kappa_n^{k_1,k_2,\ldots,k_n}\left(\sigma^{-1}\right)_{k_1}^{\;l_1}\left(\sigma^{-1}\right)_{k_2}^{\;l_2}\ldots\left(\sigma^{-1}\right)_{k_n}^{\;l_n} \tag{2.25}$$

are introduced. The new variable ξ^l will be a measure for the distance of the

actual charge vector $\mathcal{Q}^k$ to the peak $V\kappa_1^k$ of the distribution:

$$\xi^l \;=\; \left(\mathcal{Q}^k - V\kappa_1^k\right)\left(\sigma^{-1}\right)_k^{\ l} V^{-1/2}\ . \tag{2.26}$$

Including above steps at once yields:

$$\begin{aligned}\mathcal{Z}^{\mathcal{Q}^l}(V\beta,u_\mu,\mu_j) \;\simeq\; & \frac{Z(V,\beta,u_\mu,\mu_j)}{V^{L/2}\det|\sigma|}\int_{-\infty}^{\infty}\frac{d^L\vartheta}{(2\pi)^L}\ \exp\left[-i\xi^l\vartheta_l-\frac{\vartheta^l\vartheta_l}{2!}\right.\\ &+\left.\sum_{n=3}^{\infty} i^n V^{-\frac{n}{2}+1}\ \frac{\lambda_n^{l_1,l_2,\ldots,l_n}}{n!}\vartheta_{l_1}\vartheta_{l_2}\ldots\vartheta_{l_n}\right]\ .\end{aligned} \tag{2.27}$$

Eq.(2.27) is the starting point for obtaining an asymptotic solution in this section, as well as for finite volume corrections in Section 2.3. Through coordinate transformation Eq.(2.22) terms were separated in their power in volume. Thus, as system size is increased, influence of higher order normalized cumulants λ_n decreases, allowing for truncation of the summation for sufficiently large volume.

A few words on physical units are in order. Discussion of the canonical ensemble shall suffice. The single particle partition function Eq.(2.9) $\psi_i[\mathrm{fm}^{-3}]$, and therefore all cumulant elements Eq.(2.18) $\kappa_n^{j_1,j_2,\ldots,j_n}$ $[\mathrm{fm}^{-3}]$ in the CE. Consequently entries in Eq.(2.23) are $\sigma_j^{\ k}$ $[\mathrm{fm}^{-3/2}]$. The normalization in Eq.(2.27), $V^{J/2}\det|\sigma|$, for J-dimensional σ, as well as the new variable of integration Eq.(2.22) θ_l, are hence dimensionless. The elements of the inverse sigma tensor are $(\sigma^{-1})_k^{\ j}$ $[\mathrm{fm}^{3/2}]$ and, thus, the elements ξ^j of the vector Eq.(2.26) will be dimensionless. Finally, the elements of the normalized cumulants, Eq.(2.25), are $\lambda_n^{j_1,j_2,\ldots,j_n}[\mathrm{fm}^{-3+3n/2}]$, which is canceled by the factor $V^{-n/2+1}$ in the summation in Eq.(2.27). Thus all terms involved in Eq.(2.27) are dimensionless.

As discussed, for $V\to\infty$ one can discard terms of $V^{-1/2}$ and higher in Eq.(2.27), and consider only the first two cumulants for the asymptotic solution:

$$\mathcal{Z}^{\mathcal{Q}^l}(V\beta,u_\mu,\mu_j) \;\simeq\; \frac{Z(V,\beta,u_\mu,\mu_j)}{V^{L/2}\det|\sigma|}\int_{-\infty}^{\infty}\frac{d^L\vartheta}{(2\pi)^L}\ \exp\left[-i\xi^l\vartheta_l-\frac{\vartheta^l\vartheta_l}{2!}\right]\ . \tag{2.28}$$

This is the characteristic function of a multivariate normal distribution [119].

Completing the square the integral (2.28) can be solved:

$$\mathcal{Z}^{\mathcal{Q}^l}(V,\beta,u_\mu,\mu_j) \;\simeq\; \frac{Z(V,\beta,u_\mu,\mu_j)}{(2\pi V)^{L/2}\det|\sigma|}\;\exp\left[-\frac{1}{2}\,\xi^l\xi_l\right]\;. \tag{2.29}$$

The asymptotic solution of the GCE joint distribution of extensive quantities $\mathcal{Q}^l$ is then given by:

$$P_{gce}(\mathcal{Q}^l) \;=\; \frac{\mathcal{Z}^{\mathcal{Q}^l}(V,\beta,u_\mu,\mu_j)}{Z(V,\beta,u_\mu,\mu_j)} \;\simeq\; \frac{1}{(2\pi V)^{L/2}\det|\sigma|}\;\exp\left[-\frac{1}{2}\,\xi^l\xi_l\right]\;. \tag{2.30}$$

Mean values in the thermodynamic limit are given by the first Taylor expansion terms, $\langle N_A\rangle = V\kappa_1^{N_A}$, $\langle Q\rangle = V\kappa_1^{Q}$, $\langle E\rangle = V\kappa_1^{E}$, etc. and converge to GCE values. To obtain a joint (two-dimensional) particle multiplicity distribution one has to take a two-dimensional slice of the (L dimensional) GCE distribution, Eq.(2.30), around the peak of the extensive quantities which one is considering as exactly fixed. Please note that Eq.(2.29) (albeit in different notation) was used as an assumption in the microscopic correlator approach [99, 100, 101, 102]. More details of the calculation, in particular on the connection between the partition functions $\mathcal{Z}^{P^\mu,Q^j}(V,\beta,u_\mu,\mu_j)$ and the conventional version $Z(V,P^\mu,Q^j)$ [113, 114], can be found in Appendix A. Joint particle multiplicity distributions are constructed from Eq.(2.30) in Appendix D. Details of the cumulant tensor are discussed in Appendix C. A closed formula for the scaled variance of CE or MCE particle multiplicity fluctuations can be found in [105].

2.3 Finite Volume Corrections

In considering finite system size effects on distributions, the region where the thermodynamic limit approximation is valid is left. Chemical potentials μ_j and four-temperature β_μ do not correspond anymore to the physical ones, which would be found in the GCE, but have to be thought of as Lagrange multipliers, used to maximize the partition function for a given (micro) canonical state. First some volume dependent correction terms are derived. A condition is obtained that defines the values of μ_j and β_μ. The correct choice allows to write down the thermodynamical potentials, the Helmholtz free energy F for the CE, and the entropy S for the MCE, in terms of the generalized partition function. Some

general criterion for the validity of the expansion is given. Approximations will be compared to analytical CE and MCE solutions of multiplicity distributions.

2.3.1 Gram-Charlier Expansion

In Section 2.2 it was shown that in the thermodynamic limit any equilibrium distribution can be approximated by a multivariate normal distribution, Eq.(2.29). Further parameters, describing the shape of the distribution, like skewness (κ_3), or excess/kurtosis (κ_4), tend to zero as volume is increased. Returning to Eq.(2.27) with a number L of extensive quantities:

$$\mathcal{Z}^{\mathcal{Q}^l}(V,\beta,u_\mu,\mu_j) \simeq \frac{Z(V,\beta,u_\mu,\mu_j)}{V^{L/2}\det|\sigma|}\int_{-\infty}^{\infty}\frac{d^L\vartheta}{(2\pi)^L}\exp\left[-i\xi^l\vartheta_l-\frac{\vartheta^l\vartheta_l}{2!}+\sum_{n=3}^{\infty}i^n\,V^{-\frac{n}{2}+1}\,\frac{\lambda_n^{l_1,l_2,\ldots,l_n}}{n!}\,\vartheta_{l_1}\vartheta_{l_2}\ldots\vartheta_{l_n}\right]. \quad (2.31)$$

Finite volume corrections will be obtained by Gram-Charlier expansion [120, 121, 122, 123]. The charge vector $\mathcal{Q}^l$ denotes a vector of L Abelian charges, and could read for a hadron resonance gas $\mathcal{Q}^l = (B, S, Q, E, P_x, P_y, P_z)$, but could, in principle, also include particles multiplicities. Expanding the exponential in terms of powers in volume, one finds:

$$\mathcal{Z}^{\mathcal{Q}^l}(V,\beta,u_\mu,\mu_j) \simeq \frac{Z(V,\beta,u_\mu,\mu_j)}{V^{L/2}\det|\sigma|}\int_{-\infty}^{\infty}\frac{d^L\vartheta}{(2\pi)^L}\exp\left[-i\xi^l\vartheta_l-\frac{\vartheta^l\vartheta_l}{2!}\right]\times\left[1+\frac{\lambda_3^{l_1,l_2,l_3}}{3!}\,\frac{i^3\vartheta_{l_1}\vartheta_{l_2}\vartheta_{l_3}}{V^{1/2}}+\frac{\lambda_4^{l_1,l_2,l_3,l_4}}{4!}\,\frac{i^4\vartheta_{l_1}\vartheta_{l_2}\vartheta_{l_3}\vartheta_{l_4}}{V}+\frac{1}{2!}\frac{\lambda_3^{l_1,l_2,l_3}}{3!}\,\frac{\lambda_3^{l_4,l_5,l_6}}{3!}\,\frac{i^6\vartheta_{l_1}\ldots\vartheta_{l_6}}{V}+\mathcal{O}\left(V^{-3/2}\right)\right]. \quad (2.32)$$

Correction terms in Eq. (2.32) can be obtained by differentiation of $\exp\left[-i\xi^l\vartheta_l\right]$ with respect to the elements ξ_l. One can thus reverse the order by first integrating and then again differentiating. Using generalized Hermite polynomials:

$$\left[H_n(\xi)\right]_{l_1,l_2,\ldots,l_n} = (-1)^n\,\exp\left[\frac{\xi^l\xi_l}{2}\right]\,\frac{d^n}{d\xi_{l_1}\,d\xi_{l_2}\ldots d\xi_{l_n}}\,\exp\left[-\frac{\xi^l\xi_l}{2}\right], \quad (2.33)$$

with the adjusted shorthand notation for the contractions:

$$h_3(\xi) = \frac{\lambda_3^{l_1,l_2,l_3}}{3!}\left[H_3(\xi)\right]_{l_1,l_2,l_3}, \tag{2.34}$$

$$h_4(\xi) = \frac{\lambda_4^{l_1,l_2,l_3,l_4}}{4!}\left[H_4(\xi)\right]_{l_1,l_2,l_3,l_4} + \frac{1}{2!}\frac{\lambda_3^{l_1,l_2,l_3}}{3!}\frac{\lambda_3^{l_4,l_5,l_6}}{3!}\left[H_6(\xi)\right]_{l_1,\ldots l_6}, \tag{2.35}$$

$$h_5(\xi) = \frac{\lambda_5^{l_1,\ldots,l_5}}{5!}\left[H_5(\xi)\right]_{l_1,\ldots,l_5} + \frac{\lambda_3^{l_1,l_2,l_3}}{3!}\frac{\lambda_4^{l_1,l_2,l_3,l_4}}{4!}\left[H_7(\xi)\right]_{l_1,\ldots,l_7} + \frac{1}{3!}\frac{\lambda_3^{l_1,l_2,l_3}}{3!}\frac{\lambda_3^{l_4,l_5,l_6}}{3!}\frac{\lambda_3^{l_7,l_8,l_9}}{3!}\left[H_9(\xi)\right]_{l_1,\ldots,l_9}, \tag{2.36}$$

the partition function for finite volume can be approximated by:

$$\mathcal{Z}^{\mathcal{Q}^l}(V,\beta,u_\mu,\mu_j) \simeq \frac{Z(V,\beta,u_\mu,\mu_j)}{(2\pi V)^{L/2}\det|\sigma|}\exp\left[-\frac{\xi^l\xi_l}{2}\right] \times\left[1+\frac{h_3(\xi)}{V^{1/2}}+\frac{h_4(\xi)}{V}+\frac{h_5(\xi)}{V^{3/2}}+\mathcal{O}\left(V^{-2}\right)\right]. \tag{2.37}$$

Considering the simplest case of only one conserved charge, it is evident from Eq.(2.33), that the first order correction term in Eq.(2.37) is a polynomial of order 3 in ξ, while the second order correction term is a polynomial of order 4, etc. Hence for large values of ξ^l, e.g. a charge, energy, momentum, and multiplicity state far from the peak of the distribution will lead to a bad approximation, and even to negative values for $P(\mathcal{Q}^l)$. The validity of this approximation is thus restricted to the central region of the distribution. CE and MCE results will be compared to scenarios which are accessible to analytical methods in Section 2.3.3. In order to distinguish approximations which include corrections up to different orders in volume in Eq.(2.37), the asymptotic solution is denoted as CLT (central limit theorem), including terms up to $\mathcal{O}\left(V^{-1/2}\right)$ as GC3 (Gram-Charlier 3), including terms up to $\mathcal{O}\left(V^{-1}\right)$ as GC4, and including terms up to $\mathcal{O}\left(V^{-3/2}\right)$ as GC5.

2.3.2 Chemical and Thermal Equilibrium

Here the question is addressed of how to choose the optimal values for β_μ and μ_j. The postulate is that a (micro) canonical equilibrium state should be as well the most likely state in the GCE. On the other hand, it is apparent that the expansion works best around the peak of the distribution. Hence β_μ and μ_j are chosen such that the partition function is maximized at some equilibrium point $\mathcal{Q}^l_{eq}$. Taking terms up to $\mathcal{O}(V^{-1/2})$ into account, the first derivative of the partition function Eq.(2.20) reads:

$$\frac{\partial \mathcal{Z}^{\mathcal{Q}^l}(V,\beta,u_\mu,\mu_j)}{\partial \mathcal{Q}^l} = \frac{1}{(2\pi)^{L/2}\, V^{(L+1)/2} \det|\sigma|} \exp\left[-\frac{1}{2}\,\xi^l\xi_l\right] \times \left[\xi_k \left(\sigma^{-1}\right)^{\ k}_{l} + \frac{\lambda_3^{k_1,k_2,k_3}}{3!\sqrt{V}} \left(\sigma^{-1}\right)^{\ k_4}_{l} \Big[H_4(\xi)\Big]_{k_1,k_2,k_3,k_4} + \mathcal{O}\left(V^{-1}\right)\right]. \tag{2.38}$$

Lagrange multipliers (or chemical potentials) should be chosen such that the first derivative Eq.(2.38) of $\mathcal{Z}^{\mathcal{Q}^l}$ with respect to the conserved quantities $\mathcal{Q}^l$ vanishes, hence Eq.(2.37) is maximized at the point $\mathcal{Q}^l_{eq.}$:

$$\left.\frac{\partial \mathcal{Z}^{\mathcal{Q}^l}(V,\beta,u_\mu,\mu_j)}{\partial \mathcal{Q}^l}\right|_{\mathcal{Q}^l_{eq}} = 0_l\ . \tag{2.39}$$

Using only the asymptotic solution, valid in the thermodynamic limit, this condition leads to:

$$\xi_l = \left(\mathcal{Q}_k - V\kappa_{1,k}\right)\left(\sigma^{-1}\right)^{k}_{\ l} = 0_l\ . \tag{2.40}$$

Hence the partition function is maximal at the point $Q_{k,eq} = V\kappa_{1,k}$. Charge and energy density correspond thus to the GCE values, and each component of $\mu^j \to \mu^j_{gce}$, and $\beta^\mu \to \beta^\mu_{gce}$. While, when taking the first finite volume correction term in Eq.(2.38) into account, one obtains:

$$\xi_k \left(\sigma^{-1}\right)^{\ k}_{l} + \frac{\lambda_3^{k_1,k_2,k_3}}{3!\sqrt{V}} \left(\sigma^{-1}\right)^{k_4}_{\ l} \Big[H_4(\xi)\Big]_{k_1,k_2,k_3,k_4} = 0_l\ , \tag{2.41}$$

rather than Eq.(2.40), and $\mu^j \neq \mu^j_{gce}$, and $\beta^\mu \neq \beta^\mu_{gce}$. For calculation of distributions for systems of finite volume one should therefore find chemical potentials that satisfy condition (2.39). A technical comment is in order. From Eq.(2.38)

it is evident that the first order correction term to the derivative of the partition function is a polynomial of order 4 in ξ, while the second one is of order 5, etc. It is therefore crucial to find in numerical calculations the correct maximum.

2.3.3 Quality of Approximation

To test the quality of the approximation for multiplicity distributions at finite volume for (very) small systems, the analytical solution for a classical CE particle-anti-particle gas [94], and a classical MCE (without momentum conservation) ultra-relativistic gas [1, 95] are compared to Eq.(2.37).

Fig.(2.1) shows the multiplicity distribution of positively charged particles for two system sizes in the exact form and in different orders of approximation Eq.(2.37) (*top*), and the ratio of approximation to exact solution (*bottom*). In Fig.(2.2) the same physical system is shown for a (relatively large) positive electric net-charge. Due to a one-to-one correspondence between the distributions of negatively (suppressed) and positively (enhanced) particles one finds the multiplicity distribution $P(N_+)$ generally more narrow than in the case of a neutral system. In particular towards the edge of the body of the distribution the approximation becomes worse. For the MCE massless gas approximations to multiplicity distributions (*top*) and ratios to the exact solution (*bottom*) are again compared in Fig.(2.3) for two system sizes.

A few general comments attempt to summarize. The first observation is that indeed as system size is increased a better description of the central region is found in terms of the asymptotic solution CLT. The second observation is that even for systems with a very small number (in the order of 5) of produced particles one finds a good approximation in terms of Gram-Charlier expansion. In particular GC5 provides a very accurate description of the central region with deviations in the order of a few percent. This is quite remarkable given the fact that multiplicity distributions for such small systems are not smooth and continuous functions of multiplicity, while the approximation Eq.(2.37) is. Furthermore, implicitly the concepts of chemical potential and temperature are introduced for systems with small particle number, which may be in contradiction to the common believe that these parameters can only be meaningful when the number of involved particles becomes very large, i.e. in the thermodynamic limit. The last observation is that, indeed, see bottom rows of Figs.(2.1-2.3), finite volume corrections (given

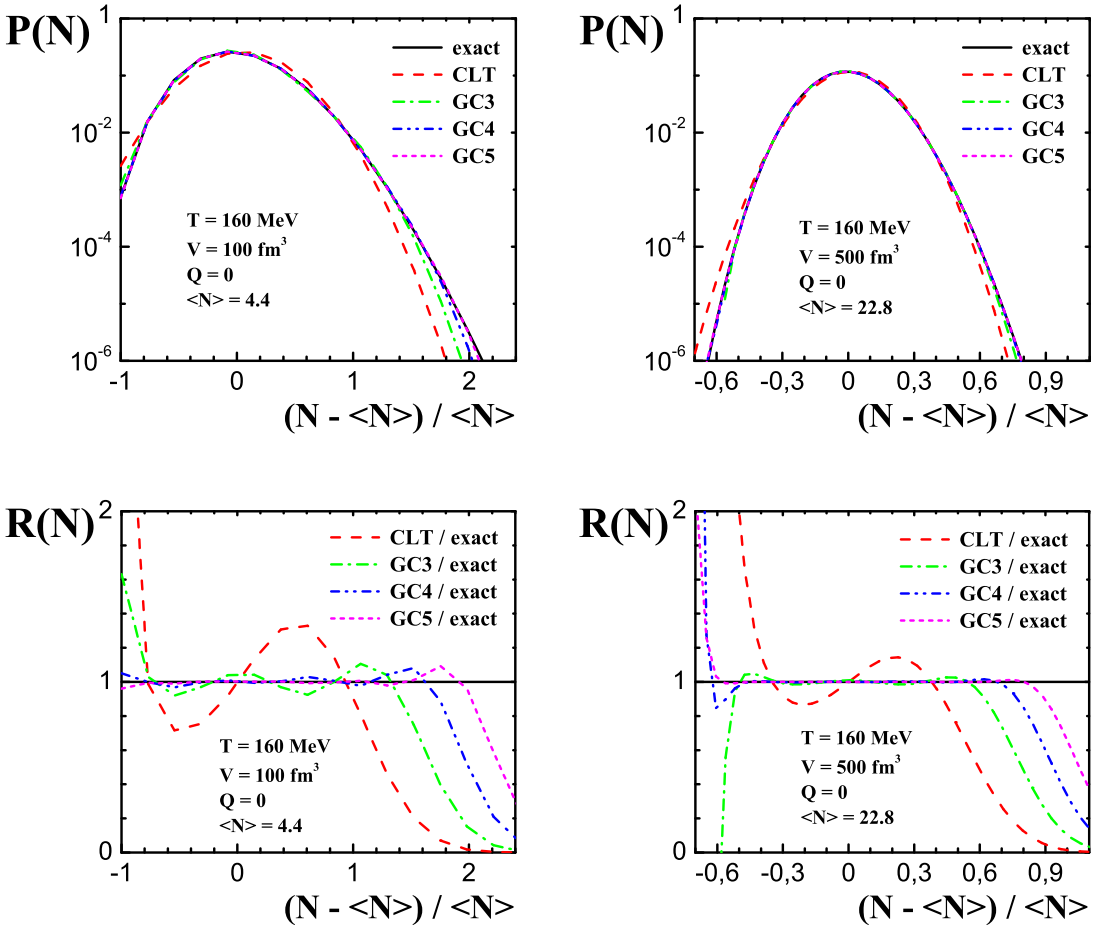

Figure 2.1: (*Top*): The CE π^+ multiplicity distribution in Boltzmann approximation for temperature $T = 160$ MeV, electric net-charge $Q = 0$, and volume $V = 100$ fm^3 (*left*), or volume $V = 500$ fm^3 (*right*). Exact solutions (solid), and various approximations, CLT (dash), GC3 (dash-dot), GC4 (dash-dot-dot), and GC5 (dot) are shown. (*Bottom*): same as (*top*), but the ratios of exact solution to approximations are shown.

in terms of polynomials) lead only to good results for the central region of the distribution.

To give an estimate for a region in which the approximation is reliable, one notes that the finite volume approximation scheme begins to break down when the first expansion term in Eq. (2.37) becomes unity. In the one-dimensional case this would be:

$$\frac{h_3\left(\xi_{max}\right)}{\sqrt{V}} \sim \mathcal{O}\left(1\right) \ . \tag{2.42}$$

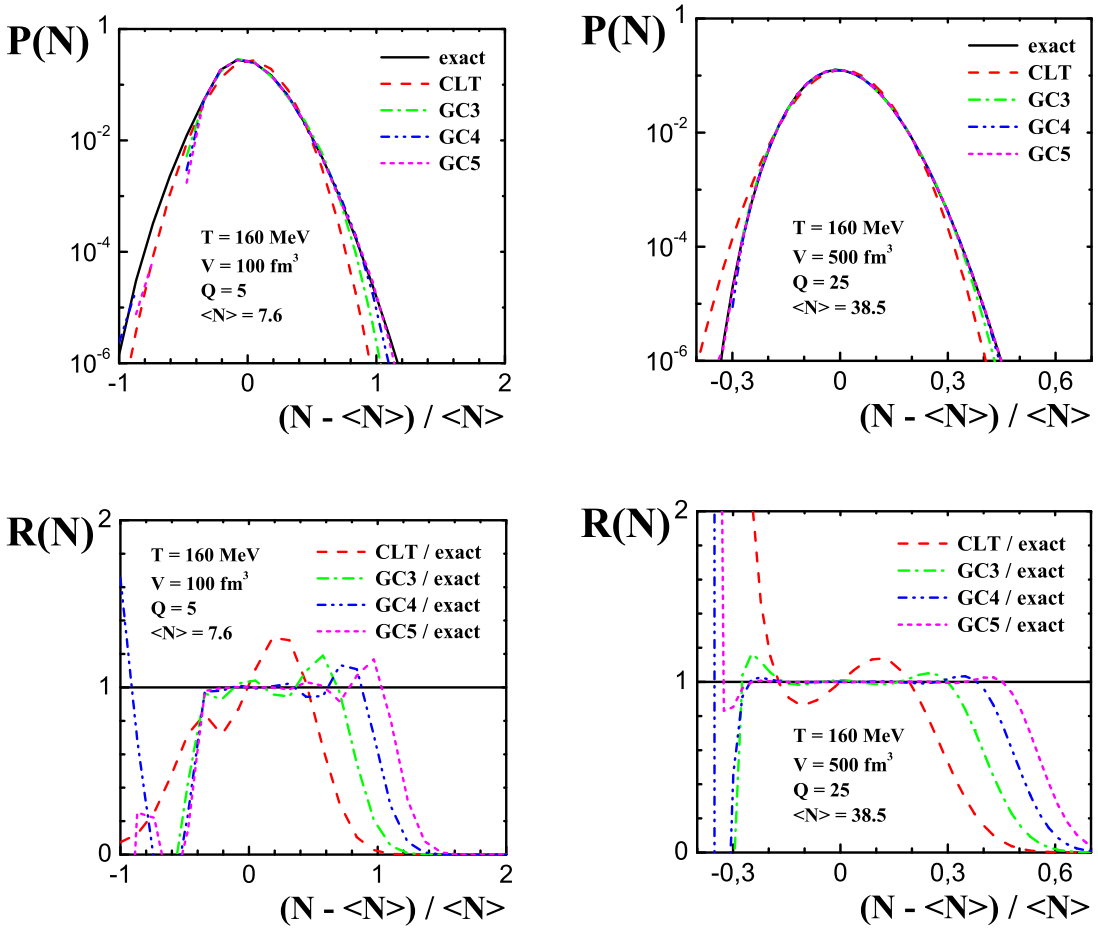

Figure 2.2: Same as Fig.(2.1), but for an electric net-charge of $Q = 5$ (*left*), or an electric net-charge of $Q = 25$ (*right*).

Approximating the Hermite polynomial $H_3 \sim \xi^3$, one can get an estimate for ξ_{max}:

$$\xi_{max} \simeq \left(\frac{3!}{\lambda_3}\right)^{1/3} V^{1/6} \ . \tag{2.43}$$

While, when switching back to the definition of $\xi = \frac{Q - V\kappa_1}{\sigma\sqrt{V}}$, Eq.(2.26), the width of the central region can be estimated by:

$$\frac{|Q - V\kappa_1|_{max}}{\sigma} \simeq \left(\frac{3!}{\lambda_3}\right)^{1/3} V^{2/3} \ . \tag{2.44}$$

Hence the width of the central region scales as $V^{2/3}$, while the width of the dis-

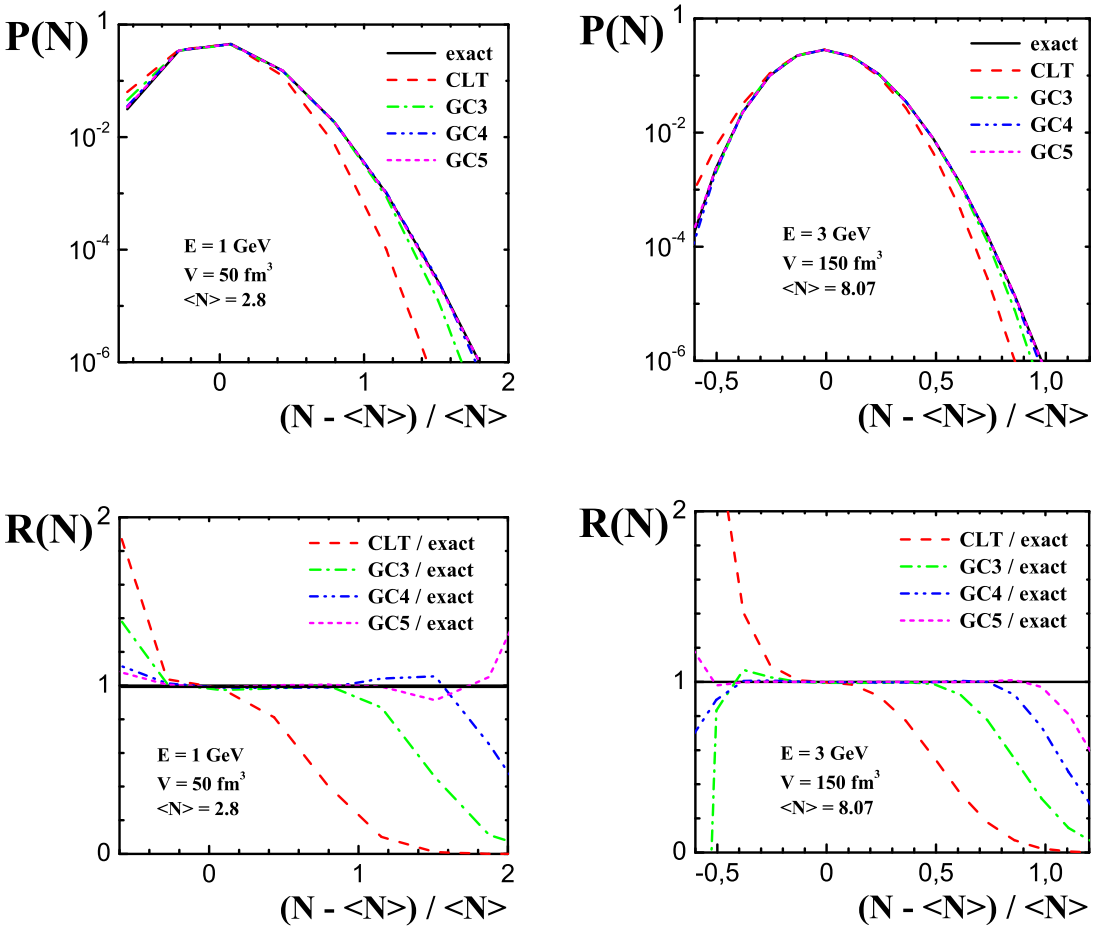

Figure 2.3: (*Top*): MCE multiplicity distribution for an ultra-relativistic gas in Boltzmann approximation. For energy $E = 1$ GeV, and volume $V = 50$ fm^3 (*left*), or for $E = 3$ GeV, and $V = 150$ fm^3 (*right*). Exact solutions (solid), and various approximations, CLT (dash), GC3 (dash-dot), GC4 (dash-dot-dot), and GC5 (dot) are shown. (*Bottom*): same as (*top*), but the ratios of exact solution to approximations are shown.

tribution should scale as $V^{1/2}$ and the approximation should be quite good. Even though larger volumes work better, they will still be sufficiently small enough to allow for calculation of distributions relevant for heavy ion collisions. However, it is stressed that there is no simple criterion for what is a 'small' or a 'large' volume for a particular physical system. Formally the existence and finiteness of (at least) the first three cumulants κ is sufficient for application of the asymptotic solution [120, 121, 122, 123]. Considering the simple case of a

multiplicity distribution of Bose-Einstein particles in the GCE one finds from Eq.(2.9) $\kappa_1^N < \kappa_2^{N,N} < \kappa_3^{N,N,N} < \cdots$. Hence, in particular when finite chemical potentials are involved, cumulants are growing with order, implying that apart from mean value and variance further parameters like skewness and excess (or kurtosis) [119, 124] of the distribution will remain important quantities. For chemical potentials approaching the Bose-Einstein condensation point, one finds for instance the cumulant $\kappa_2^{N,N}$ diverging. The expansion discussed here is hence not valid in this regime.

2.4 Temperature and Chemical Potential

The introduction of chemical potentials in the CE and temperature in the MCE was first and foremost a mathematical trick which allowed to conveniently integrate partition functions for which otherwise no analytical solution could be obtained. However the generalized partition function is self-consistent and not in contradiction to the common definition of temperature and chemical potential. It is shown in the following that the definition of β and μ through Eq.(2.39) coincides with expressions well known from textbooks [110, 111, 112].

Canonical Ensemble

The canonical partition function known from textbooks and the generalized version discussed here are connected as follows:

$$Z\left(V, Q^j, \beta\right) \equiv \mathcal{Z}^{Q^j}\left(V, \beta, \mu_j\right) \; e^{-Q^j \mu_j \beta} \; . \tag{2.45}$$

The Helmholtz free energy F is the thermodynamic potential relevant for CE,

$$F \equiv -T \ln Z^{CE} \; . \tag{2.46}$$

Employing the first law of thermodynamics $dE = TdS - PdV + \mu_j dQ^j$, and using $F = E - TS$ for the free energy, where P is the pressure, and E and S are total energy and entropy, respectively, one can write for the differential of the free energy $dF = -SdT - PdV + \mu_j dQ^j$. The Lagrange multiplier μ_j associated

with conserved charge Q^j is thus defined by:

$$\left(\frac{\partial F}{\partial Q_j}\right)_{V,\beta} = -\beta^{-1} \frac{\frac{\partial \mathcal{Z}^{Q^j}}{\partial Q_j} e^{-Q^j\mu_j\beta} - \mu_j\beta\, \mathcal{Z}^{Q} e^{-Q^j\mu_j\beta}}{\mathcal{Z}^{Q^j} e^{-Q^j\mu_j\beta}} = \mu_j \,, \tag{2.47}$$

where advantage of condition (2.39) was taken. Thus, the correct choice for the effective chemical potential is given by the extremum, $\frac{\partial \mathcal{Z}^{Q^j}}{\partial Q_j} = 0$, of the charge distribution, which coincides with $\mu_j = \left(\frac{\partial F}{\partial Q_j}\right)_{V,\beta}$, Eq.(2.47). In the thermodynamic limit this is equivalent to, Eq.(2.40), $\mu_j \to \mu_{j,gce}$. The subscripts indicate that the derivative with respect to the conserved charge has to be taken at fixed values of V and β. In the non-relativistic case, where particle number N, rather than quantum numbers, is conserved, the corresponding relation to Eq.(2.47) would be $\left(\frac{\partial F}{\partial N}\right)_{V,\beta} = \mu_N$ [110, 111, 112].

Micro Canonical Ensemble

The standard MCE partition function can be obtain by Fourier integration of the generating function of the GCE four-momentum distribution and multiplication with the inverse Boltzmann factor,

$$Z\left(V, P^\mu\right) \equiv \mathcal{Z}^{P^\mu}\left(V, \beta, u_\mu\right) e^{P_\mu u^\mu \beta} \,. \tag{2.48}$$

The relevant thermodynamic potential in the MCE is the entropy S,

$$S \equiv \ln Z\left(V, P^\mu\right) \,. \tag{2.49}$$

The Lagrange multiplier for the temperature is [110, 111, 112, 113, 125, 126]:

$$\left(\frac{\partial S}{\partial P_\mu}\right)_V = \frac{\frac{\partial \mathcal{Z}^{P^\mu}}{\partial P_\mu} e^{P_\mu u^\mu \beta} + u^\mu\beta\, \mathcal{Z}^{P^\mu} e^{P_\mu u^\mu \beta}}{\mathcal{Z}^{P^\mu} e^{P_\mu u^\mu \beta}} = u^\mu\beta \,, \tag{2.50}$$

where again condition (2.39) was employed, $\frac{\partial \mathcal{Z}^{P^\mu}}{\partial P_\mu} = 0$. The subscript in Eq.(2.50) is used to indicate that the derivative with respect to the components of P_μ has to be taken at fixed volume V. Thus Eq.(2.50) resembles the optimal choice of an effective temperature for the approximation scheme. In the thermodynamic limit, $V \to \infty$, one finds $\beta^\mu \to \beta^\mu_{gce}$, due to Eq.(2.40).

Grand Canonical Ensemble

Conventionally, e.g. in textbooks, first the MCE is introduced. Summation over energy - with temperature being a Lagrange multiplier - which is used to maximize the entropy, introduces the CE. Additionally dropping the constraint of exact charge conservation leads to the GCE. Here the chemical potentials μ_j are the Lagrange multipliers. The GCE partition function can be written as:

$$Z(V,\beta,u_\mu,\mu_j) = \sum_{\{Q^j\}} e^{Q^j\mu_j\beta}\; Z(V,\beta,u_\mu,Q^j) \tag{2.51}$$

$$= \sum_{\{Q^j\}}\sum_{\{P^\mu\}} e^{Q^j\mu_j\beta}\; e^{-P_\mu u^\mu\beta}\; Z(V,P^\mu,Q^j)\;. \tag{2.52}$$

While, in the notation used here, this line would read:

$$Z(V,\beta,u_\mu,\mu_j) = \sum_{\{Q^j\}} \mathcal{Z}^{Q^j}(V,\beta,u_\mu,\mu_j) \tag{2.53}$$

$$= \sum_{\{Q^j\}}\sum_{\{P^\mu\}} \mathcal{Z}^{Q^j,P^\mu}(V,\beta,u_\mu,\mu_j)\;. \tag{2.54}$$

The thermodynamic potential for the GCE is the grand potential Ω:

$$\Omega \equiv -T\ln Z(V,\beta,u_\mu,\mu_j) = -T\ln\mathcal{Z}(V,\beta,u_\mu,\mu_j,\theta_l)\Big|_{\theta_l=0_l}\;. \tag{2.55}$$

The relations (2.47) and (2.50) are essentially Legendre transformations from F and S to $Z\,(V,Q^j,\beta)$ and $Z\,(V,P^\mu)$, respectively. The inverse Legendre transformations were obtained in the saddle-point expansion method (see Refs. [113, 114, 115]). Lastly it is emphasized that both methods are complementary from a thermodynamic point of view.

Thus, if exact solutions of the canonical or micro canonical partition functions were available this reversal would not have been necessary. However, this redefinition of the GCE partition function is entirely consistent and simplifies calculations considerably. Whenever an exact solution to the generalized partition function is possible, all relations above would hold exactly. This interpretation of the GCE partition function as the generating (or characteristic) function of a statistical system should be quite useful, even in more general cases than the one presented here.

2.5 Discussion

An analytical expansion method for calculation of distributions at finite volume for the canonical as well as the micro canonical ensembles of the ideal relativistic hadron resonance gas has been presented. The introduction of temperature into the micro canonical partition function and chemical potentials into the canonical partition function have lead to the identification of the grand canonical partition function with the characteristic function of associated joint probability distributions. Micro canonical and canonical multiplicity distributions could, thus, be defined through conditional probability distributions. Hence the probability of finding a certain multiplicity, while other parameters (global charge or energy) were taken to be fixed.

In considering finite volume corrections to the system partition function, thus relaxing the assumption of thermodynamic equivalence of different statistical ensembles, one is lead to demand that the partition function should be maximized for a particular set of conserved charges. It turned out that this requirement is entirely equivalent to the well known textbook definitions of chemical potential in the canonical ensemble as the derivative of Helmholtz free energy with respect to conserved charge and temperature in the micro canonical ensemble through differentiation of entropy with respect to conserved energy.

This method is based on Fourier analysis of the grand canonical partition function. Conventionally one would not introduce chemical potentials and temperature into these calculations. However, one then faces the problem of a heavily oscillating (or even irregular) integrand, making numerical integration unpractical. Artificially introduced temperature and chemical potentials, correctly chosen, produce a very smooth integrand allowing for expansion of the integrand in powers of volume. Analytical solutions to asymptotic distributions could thus be found in terms of Laplace's expansion, while finite volume corrections could be obtained from Gram-Charlier expansion. A comparison with available analytical solutions to simple statistical systems suggests that good results can be expected even for rather small system size. One drawback is that the results can only be applied to the central region of the distribution, owning to the fact that finite volume correction terms appear in the form of Hermite polynomial of low order.

Another, rather practical, drawback is that the effects of resonance decay [101, 103, 105] and limited acceptance [106, 127] are hard to consider simul-

taneously with the approach presented here. This will be solved by the Monte Carlo approach, considered in the next chapter.

Chapter 3

Monte Carlo Approach

A statistical hadronization model Monte Carlo event generator provides the means for studying fluctuation and correlation observables in equilibrium systems. Data analysis can be done in close relation to experimental analysis techniques. Imposing global constraints on a sample is always technically more challenging. Direct sampling of MCE events (or micro states) has only been done in the non-relativistic limit [128, 129]. Sample and reject procedures, suitable for relativistic systems, become rapidly inefficient with increasing system size. However, they have the advantage of being very successful for small system sizes [113, 114, 115].

In this chapter a different approach is taken: the GCE is sampled, events are then re-weighted according to their values of extensive quantities, and the sample-reject limit (MCE) is approached in a controlled manner. In this way one can study the statistical properties of a global equilibrium system in their dependence on the size of its thermodynamic bath. As any of the three standard ensembles remain idealizations of physical systems, one might find these intermediate ensembles to be of phenomenological or conceptual interest too.

In Section 3.1 statistical ensembles with finite thermodynamic bath are discussed. The GCE Monte Carlo sampling procedure is described in Section 3.2.

3.1 Statistical Ensembles with Finite Bath

The starting point taken is similar to the one chosen by Patriha [92], and Challa and Hetherington [97]. However quickly a different route is taken. Two systems, described by their micro canonical partition functions, i.e. the number

of micro states for two separate systems, are assumed. The first system is further assumed to be enclosed in a volume V_1 and to have fixed values of extensive quantities $P_1^\mu = (E_1, P_{x,1}, P_{y,1}, P_{z,1})$, and $Q_1^j = (B_1, S_1, Q_1)$, while the second system is assumed to be enclosed in a volume V_2 and to have fixed values of extensive quantities $P_2^\mu = (E_2, P_{x,2}, P_{y,2}, P_{z,2})$, and $Q_2^j = (B_2, S_2, Q_2)$, where E is the energy of the system, $P_{x,y,z}$ are the components of its three-momentum, and B, S, and Q, are baryon number, strangeness and electric charge, respectively. Thus:

$$Z(V_1, P_1^\mu, Q_1^j) \;=\; \sum_{\{N_1^i\}} Z_{N_1^i}(V_1, P_1^\mu, Q_1^j) \;, \quad \text{and} \quad Z(V_2, P_2^\mu, Q_2^j) \;, \tag{3.1}$$

where $Z_{N_1^i}(V_1, P_1^\mu, Q_1^j)$ denotes the number of micro states of system 1 with additionally fixed multiplicities N_1^i of particles of all species i considered in the model. Supposing that system 1 and system 2 are subject to the following constraints:

$$V_g \;=\; V_1 \;+\; V_2 \;, \tag{3.2}$$

$$P_g^\mu \;=\; P_1^\mu \;+\; P_2^\mu \;, \tag{3.3}$$

$$Q_g^j \;=\; Q_1^j \;+\; Q_2^j \;. \tag{3.4}$$

Then, the partition function $Z(V_g, P_g^\mu, Q_g^j)$ of the joint system is constructed as the sums over all possible charge and energy-momentum split-ups:

$$Z(V_g, P_g^\mu, Q_g^j) = \sum_{\{Q_1^j\}} \sum_{\{P_1^\mu\}} Z(V_g - V_1, P_g^\mu - P_1^\mu, Q_g^j - Q_1^j)\; Z(V_1, P_1^\mu, Q_1^j). \tag{3.5}$$

The distribution of extensive quantities in the subsystem V_1 is given by the ratio of the number of all micro states consistent with a given charge and energy-momentum split-up and a given set of particle multiplicities to the number of all possible configurations:

$$P(P_1^\mu, Q_1^j, N_1^i) \;=\; \frac{Z(V_g - V_1, P_g^\mu - P_1^\mu, Q_g^j - Q_1^j)}{Z(V_g, P_g^\mu, Q_g^j)} \;\; Z_{N_1^i}(V_1, P_1^\mu, Q_1^j) \;. \tag{3.6}$$

Lastly, a weight factor $W(V_1, P_1^\mu, Q_1^j; V_g, P_g^\mu, Q_g^j)$ is defined such that:

$$P(P_1^\mu, Q_1^j, N_1^i) \;=\; W(V_1, P_1^\mu, Q_1^j; V_g, P_g^\mu, Q_g^j) \;\; Z_{N_1^i}(V_1, P_1^\mu, Q_1^j) \;. \tag{3.7}$$

By construction, the first moment of the weight factor is equal to unity:

$$\langle W \rangle \;=\; \sum_{\{Q_1^j\}} \sum_{\{P_1^\mu\}} W(V_1, P_1^\mu, Q_1^j; V_g, P_g^\mu, Q_g^j) \;\; Z_{N_1^i}(V_1, P_1^\mu, Q_1^j) = 1 \;, \quad (3.8)$$

as the distribution is properly normalized.

The weight factor $W(V_1, P_1^\mu, Q_1^j; V_g, P_g^\mu, Q_g^j)$ generates an ensemble with statistical properties different from the limiting cases of vanishing, $V_g \to V_1$ (MCE), and of an infinite thermodynamic bath, $V_g \to \infty$ (GCE). This effectively allows for extrapolation of GCE results to the MCE limit. In principle any other (arbitrary) choice of $W(V_1, P_1^\mu, Q_1^j; V_g, P_g^\mu, Q_g^j)$ could be taken. This thesis confines itself to the situation discussed above. It is worth noting that all micro states consistent with the same set of extensive quantities (P_1^μ, Q_1^j) still have 'a priori equal probabilities'.

In the large volume limit, ensembles are equivalent in the sense that densities are the same. The ensembles defined by Eq.(3.7) and later on by Eq.(3.11) are no exception. If both V_1 and V_g are sufficiently large, then the average densities in both systems will be the same, Q_g^j/V_g and P_g^μ/V_g respectively. The system in V_1 will hence carry on average a certain fraction:

$$\lambda \;\equiv\; V_1/V_g \;, \quad (3.9)$$

of the total charge Q_g^j and four-momentum P_g^μ, i.e.:

$$\langle Q_1^j \rangle \;=\; \lambda \; Q_g^j \;, \qquad \text{and} \qquad \langle P_1^\mu \rangle \;=\; \lambda \; P_g^\mu \;. \quad (3.10)$$

By varying the ratio $\lambda = V_1/V_g$, while keeping $\langle Q_1^j \rangle$ and $\langle P_1^\mu \rangle$ constant, one can thus study a class of systems with the same average charge content and four-momentum, but different statistical properties. In the thermodynamic limit (it is enough to demand that V_1 is sufficiently large) a family of thermodynamically equivalent (same densities) ensembles is generated.

3.1.1 Introducing the Monte Carlo Weight $\mathcal{W}$

Since Eq.(3.7) poses a formidable challenge, both mathematically and numerically, one may write instead:

$$P(P_1^\mu, Q_1^j, N_1^i) \;=\; \mathcal{W}^{P_1^\mu, Q_1^j; P_g^\mu, Q_g^j}(V_1; V_g|\beta, u_\mu, \mu_j) \;\; P_{gce}(P_1^\mu, Q_1^j, N_1^i|\beta, u_\mu, \mu_j) \;, \tag{3.11}$$

where the distribution of extensive quantities P_1^μ, Q_1^j and particle multiplicities N_1^i of a GCE system with temperature $T = \beta^{-1}$, volume V_1, chemical potentials μ_j and collective four-velocity u_μ is given by:

$$P_{gce}(P_1^\mu, Q_1^j, N_1^i|\beta, u_\mu, \mu_j) \;\equiv\; \frac{e^{-P_1^\mu u_\mu \beta}\; e^{Q_1^j \mu_j \beta}}{Z(V_1, \beta, u_\mu, \mu_j)}\; Z_{N_1^i}(V_1, P_1^\mu, Q_1^j) \;, \tag{3.12}$$

where $\mu_j = (\mu_B, \mu_S, \mu_Q)$ summarizes the chemical potentials associated with baryon number, strangeness and electric charge in a vector. The normalization in Eq.(3.12) is given by the GCE partition function $Z(V_1, \beta, u_\mu, \mu_j)$, i.e. the number of all micro states averaged over the Boltzmann weights $e^{-P_1^\mu u_\mu \beta}$ and $e^{Q_1^j \mu_j \beta}$:

$$Z(V_1, \beta, u_\mu, \mu_j) \;=\; \sum_{\{P_1^\mu\}} \sum_{\{Q_1^j\}} \sum_{\{N_1^i\}} e^{-P_1^\mu u_\mu \beta}\; e^{Q_1^j \mu_j \beta}\; Z_{N_1^i}(V_1, P_1^\mu, Q_1^j) \;. \tag{3.13}$$

The new weight factor $\mathcal{W}^{P_1^\mu, Q_1^j; P_g^\mu, Q_g^j}(V_1; V_g|\beta, u_\mu, \mu_j)$ now reads:

$$\begin{aligned} \mathcal{W}^{P_1^\mu, Q_1^j; P_g^\mu, Q_g^j}(V_1; V_g|\beta, u_\mu, \mu_j) \;&=\; Z(V_1, \beta, u_\mu, \mu_j)\; \frac{e^{-(P_g^\mu - P_1^\mu) u_\mu \beta}\; e^{(Q_g^j - Q_1^j)\mu_j \beta}}{e^{-P_g^\mu u_\mu \beta}\; e^{Q_g^j \mu_j \beta}} \\ &\times\; \frac{Z(V_g - V_1, P_g^\mu - P_1^\mu, Q_g^j - Q_1^j)}{Z(V_g, P_g^\mu, Q_g^j)} \;. \end{aligned} \tag{3.14}$$

In the case of an ideal (non-interacting) gas, Eq.(3.14) can be written, see Chapter 2, and Appendix A, as:

$$\begin{aligned} \mathcal{W}^{P_1^\mu, Q_1^j; P_g^\mu, Q_g^j}(V_1; V_g|\beta, u_\mu, \mu_j) \;&=\; Z(V_1, \beta, u_\mu, \mu_j) \\ &\times\; \frac{\mathcal{Z}^{P_g^\mu - P_1^\mu, Q_g^j - Q_1^j}(V_g - V_1, \beta, u_\mu, \mu_j)}{\mathcal{Z}^{P_g^\mu, Q_g^j}(V_g, \beta, u_\mu, \mu_j)} \;. \end{aligned} \tag{3.15}$$

The advantage of Eq.(3.11), compared to Eq.(3.7), is that the distribution $P_{gce}(P_1^\mu, Q_1^j, N_1^i|\beta, u_\mu, \mu_j)$ can easily be sampled for Boltzmann particles, while

a suitable approximation for the weight $\mathcal{W}^{P_1^\mu,Q_1^j;P_g^\mu,Q_g^j}(V_1;V_g|\beta,u_\mu,\mu_j)$ is available. Again, by construction, the first moment of the new weight factor is equal to unity:

$$\langle \mathcal{W} \rangle = \sum_{\{P_1^\mu\}} \sum_{\{Q_1^j\}} \sum_{\{N_1^i\}} \mathcal{W}^{P_1^\mu,Q_1^j;P_g^\mu,Q_g^j}(V_1;V_g|\beta,u_\mu,\mu_j)\, P_{gce}(P_1^\mu,Q_1^j,N_1^i|\beta,u_\mu,\mu_j) = 1\,. \tag{3.16}$$

In principle, Eq.(3.7) and Eq.(3.11) are equivalent. In fact, Eq.(3.7) can be obtained by taking the limit $(\mu_B,\mu_S,\mu_Q)=(0,0,0)$, $u_\mu=(1,0,0,0)$, and $\beta\to 0$ of Eq.(3.11). However, as one can easily see, $\langle \mathcal{W}^n\rangle \neq \langle W^n\rangle$. Higher, and in particular the second, moments of the weight factors W and $\mathcal{W}$ are a measure of the statistical error to be expected for a finite sample of events. The larger the higher moments of the weight factor, the larger the statistical error, and the slower the convergence with sample size. Please see also Appendices F and G.

As GCE and MCE densities are the same in the system V_g, these values are effectively regulated by intensive parameters β, μ_j and u_μ. In order to study a system with average $\langle Q_1^j\rangle$, it is most economical to sample the GCE with $\langle Q_1^j\rangle$ and calculate weights according to Eq.(3.15). This will result in a low statistical error for finite samples (as shown in later sections), and allow for extrapolation to the MCE limit.

Firstly the weight factor Eq.(3.15) will be calculated, and then the relevant limits are taken. With the appropriate choice of β, μ_j and u_μ the calculation of Eq.(3.15) can be done with the method presented in Chapter 2.

3.1.2 Calculating the Monte Carlo Weight $\mathcal{W}$

For the Monte Carlo approach in this chapter, the total number of (potentially) conserved extensive quantities in a hadron resonance gas is $L = J + 4 = 3 + 4 = 7$, where $J = 3$ is the number of charges (B,S,Q) and there are four components of the four-momentum. Particle number integrals are not going to be solved here. Including all extensive quantities into a single vector:

$$\mathcal{Q}^l = (Q^j, P^\mu) = (B,S,Q,E,P_x,P_y,P_z)\,, \tag{3.17}$$

the weight Eq.(3.15) can be expressed as:

$$\mathcal{W}^{\mathcal{Q}_1^l;\mathcal{Q}_g^l}(V_1;V_g|\beta,u_\mu,\mu_j) = Z(V_1,\beta,u_\mu,\mu_j) \times \frac{\mathcal{Z}^{\mathcal{Q}_g^l-\mathcal{Q}_1^l}(V_g-V_1,\beta,u_\mu,\mu_j)}{\mathcal{Z}^{\mathcal{Q}_g^l}(V_g,\beta,u_\mu,\mu_j)} \,. \quad (3.18)$$

The general expression for the partition function $\mathcal{Z}^{\mathcal{Q}^l}(V,\beta,u_\mu,\mu_j)$ in the large volume limit is given by Eq.(2.29):

$$\mathcal{Z}^{\mathcal{Q}^l}(V,\beta,u_\mu,\mu_j) \;\simeq\; \frac{Z(V,\beta,u_\mu,\mu_j)}{(2\pi V)^{L/2}\det|\sigma|} \;\exp\left[-\frac{1}{2}\,\frac{1}{V}\,\xi^l\xi_l\right] \,, \quad (3.19)$$

where, unlike in Eq.(2.26), the volume is split off:

$$\xi^l \;=\; \left(\mathcal{Q}^k - V\kappa_1^k\right)\;\left(\sigma^{-1}\right)_k^l \,, \quad (3.20)$$

while the definition of the sigma tensor, Eq.(2.23), remains:

$$\sigma_k^l \;=\; \left(\kappa_2^{1/2}\right)_k^l \,. \quad (3.21)$$

Here κ_1 and κ_2 are the GCE vector of mean values and the GCE covariance matrix respectively. The values of β, μ_j and u_μ are chosen such (Eq.(2.39)) that:

$$\left.\frac{\partial\mathcal{Z}^{\mathcal{Q}^l}}{\partial\mathcal{Q}^l}\right|_{\mathcal{Q}^l=\mathcal{Q}_{eq}^l} \;=\; 0_l. \quad (3.22)$$

The approximation (3.19) gives then a reliable description of $\mathcal{Z}^{\mathcal{Q}_g^l}$ around the equilibrium value $\mathcal{Q}_g^l = V_g\kappa_1^l$, provided V_g is sufficiently large. The charge vector, Eq.(2.26), is then equal to the null-vector $\xi_l = 0_l$ ($\mathcal{Q}_g^l = V_g\kappa_1^l$). For the denominator in Eq.(3.18) one then finds:

$$\left.\mathcal{Z}^{\mathcal{Q}_g^l}(V_g,\beta,u_\mu,\mu_j)\right|_{\mathcal{Q}_g^l=\mathcal{Q}_{g,eq}^l} \;\simeq\; \frac{Z(V_g,\beta,u_\mu,\mu_j)}{(2\pi V_g)^{L/2}\det|\sigma|} \;\exp\left[\,0\,\right] \,, \quad (3.23)$$

while for the numerator one obtains:

$$\left.\mathcal{Z}^{\mathcal{Q}_g^l-\mathcal{Q}_1^l}(V_g-V_1,\beta,u_\mu,\mu_j)\right|_{\mathcal{Q}_g^l=\mathcal{Q}_{g,eq}^l} \simeq \frac{Z(V_g-V_1,\beta,u_\mu,\mu_j)}{(2\pi\,(V_g-V_1))^{L/2}\det|\sigma|} \times\exp\left[-\frac{1}{2}\,\frac{1}{(V_g-V_1)}\,\xi^l\xi_l\right] \,, \quad (3.24)$$

where the charge vector ξ^l, Eq.(3.20), in Eq.(3.24) is:

$$\xi^l = (\Delta\mathcal{Q}_2)^k \left(\sigma^{-1}\right)^l_k \ . \tag{3.25}$$

Then, using the condition $\mathcal{Q}^k_g = \mathcal{Q}^k_{g,eq} = V_g\kappa^k_1$ yields:

$$(\Delta\mathcal{Q}_2)^k = (\mathcal{Q}_g - \mathcal{Q}_1)^k - (V_g - V_1)\,\kappa^k_1 \ = \ -\,(\mathcal{Q}_1 - V_1\kappa_1)^k \ . \tag{3.26}$$

Substituting Eq.(3.23) and Eq.(3.24) into Eq.(3.18) results in:

$$\begin{aligned}\mathcal{W}^{\mathcal{Q}^l_1;\mathcal{Q}^l_g}(V_1;V_g|\beta,u_\mu,\mu_j)\Big|_{\mathcal{Q}^l_g=\mathcal{Q}^l_{g,eq}} \ \simeq \ & \frac{Z(V_1,\beta,u_\mu,\mu_j)\ Z(V_g-V_1,\beta,u_\mu,\mu_j)}{Z(V_g,\beta,u_\mu,\mu_j)} \\ & \times \ \frac{(2\pi V_g)^{L/2}\det|\sigma|}{(2\pi\,(V_g-V_1))^{L/2}\det|\sigma|} \\ & \times \ \exp\left[-\frac{1}{2}\ \frac{1}{(V_g-V_1)}\ \xi^l\xi_l\right] . \end{aligned} \tag{3.27}$$

The GCE partition functions are multiplicative in the sense that their product is $Z(V_1,\beta,u_\mu,\mu_j)\ Z(V_g-V_1,\beta,u_\mu,\mu_j) = Z(V_g,\beta,u_\mu,\mu_j)$, and thus the first term in Eq.(3.27) is equal to unity. Now using Eq.(3.9), $\lambda = V_1/V_g$, one can re-write Eq.(3.27) as:

$$\begin{aligned}\mathcal{W}^{\mathcal{Q}^l_1;\mathcal{Q}^l_g}(V_1;V_g|\beta,u_\mu,\mu_j)\Big|_{\mathcal{Q}^l_g=\mathcal{Q}^l_{g,eq}} \ \simeq \ & \frac{1}{(1-\lambda)^{L/2}} \\ & \times \ \exp\left[-\frac{1}{2}\left(\frac{\lambda}{1-\lambda}\right)\frac{1}{V_1}\ \xi^l\xi_l\right] . \end{aligned} \tag{3.28}$$

Model parameters are hence the intensive variables inverse temperature β, four-velocity u^μ and chemical potentials μ^j, which regulate energy and charge densities, and collective motion. Provided V_1 is sufficiently large, a family of thermodynamically equivalent ensembles is defined, which can now be studied in their dependence of fluctuation and correlation observables on the size of the bath $V_2 = V_g - V_1$. Hence, one can test the sensitivity of such observables, for example, to globally applied conservation laws. The expectation values are then identical to GCE expectation values, while higher moments will depend crucially on the choice of λ.

3.1.3 The Limits of $\mathcal{W}$

The largest weight is given to states for which $\xi^l\xi_l = 0$, i.e. with extensive quantities $\mathcal{Q}_1^l = \mathcal{Q}_{1,eq.}^l$. Hence, the maximal weight a micro state (or event) at a given value of $\lambda = V_1/V_g$ can assume is $\mathcal{W}_{max}^{\mathcal{Q}_1^l;\mathcal{Q}_g^l}(V_1; V_g|\beta, u_\mu, \mu_j) = (1-\lambda)^{-L/2}$. Taking the limits of Eq.(3.28), it is easy to see that:

$$\lim_{\lambda\to 0} \mathcal{W}^{\mathcal{Q}_1^l;\mathcal{Q}_g^l}(V_1; V_g|\beta, u_\mu, \mu_j) \;=\; 1 \;. \tag{3.29}$$

I.e. for $\lambda = 0$ the GCE is sampled, and all events have a weight equal to unity. Hence, one also finds $\langle \mathcal{W}^2 \rangle = 1$ and therefore $\langle (\Delta\mathcal{W})^2 \rangle = 0$, implying a low statistical error. For $\lambda \to 1$, effectively the sample-reject limit [113, 114, 115] is approached. Accordingly:

$$\lim_{\lambda\to 1} \mathcal{W}^{\mathcal{Q}_1^l;\mathcal{Q}_g^l}(V_1; V_g|\beta, u_\mu, \mu_j) \;\propto\; \delta(\mathcal{Q}_1^l - V_1\kappa_1^l) \;. \tag{3.30}$$

However, as now not all events have equal weight, $\langle (\Delta\mathcal{W})^2 \rangle$ grows and so too the statistical error of finite samples. Also, the larger the number L of extensive quantities considered for re-weighting, the larger will be the statistical uncertainty.

3.2 The GCE Sampling Procedure

The Monte Carlo sampling procedure for a GCE system in the Boltzmann approximation is now explained. The system to be sampled is assumed to be in an equilibrium state enclosed in a volume V_1 with temperature $T = \beta^{-1}$ and chemical potentials $\mu_j = (\mu_B, \mu_S, \mu_Q)$. Additionally, the system is assumed to be at rest. The four-velocity is then $u^\mu = (1, 0, 0, 0)$ and the four-temperature is $\beta^\mu = (\beta, 0, 0, 0)$. In this case, multiplicity distributions are Poissonian, while momentum spectra are of Boltzmann type. The GCE sampling process is composed of four steps, each discussed below.

Multiplicity Generation

In the first step, multiplicities N_1^i are randomly sampled of all particle species i considered in the model. The expectation value of the multiplicity of thermal

Boltzmann particles in the GCE is given by:

$$\langle N_1^i \rangle \;=\; \frac{g_i V_1}{2\pi^2}\; m_i^2\; \beta^{-1}\; K_2\left(m_i\beta\right)\; e^{\mu_i \beta}\;. \tag{3.31}$$

Multiplicities $\{N_1^i\}_n$ are randomly generated for each event n according to Poissonians with mean values $\langle N_1^i \rangle$:

$$P(N_1^i) \;=\; \frac{\langle N_1^i \rangle^{N_1^i}}{N_1^i!}\; e^{-\langle N_1^i \rangle}\;. \tag{3.32}$$

In the above, m_i and g_i are the mass and spin-degeneracy factor of a particle of species i respectively. The chemical potential $\mu_i = \mu_j q_i^j = \mu_B b_i + \mu_S s_i + \mu_Q q_i$, where $q_i^j = (b_i, s_i, q_i)$ represents the quantum number content of a particle of species i.

Momentum Spectra

In the second step, momenta are generated for each particle according to a Boltzmann spectrum. For a static thermal source spherical coordinates are convenient:

$$\frac{dN_i}{d|p|} \;=\; \frac{g_i V_1}{2\pi^2}\; \beta^{-3}\; |p|^2\; e^{-\varepsilon\beta}\;. \tag{3.33}$$

These momenta are then isotropically distributed in momentum space. Hence:

$$p_x \;=\; |p|\;\sin\theta\;\cos\phi\;, \tag{3.34}$$

$$p_y \;=\; |p|\;\sin\theta\;\sin\phi\;, \tag{3.35}$$

$$p_z \;=\; |p|\;\cos\theta\;, \tag{3.36}$$

$$\varepsilon \;=\; \sqrt{|p|^2 + m_i^2}\;, \tag{3.37}$$

where p_x, p_y, and p_z are the components of the three-momentum, ε is the energy, and $|p| = \sqrt{p_x^2 + p_y^2 + p_z^2}$ is the total momentum. The polar and azimuthal angles are sampled according to:

$$\theta \;=\; \cos^{-1}\left[2\left(x - 0.5\right)\right]\;, \tag{3.38}$$

$$\phi \;=\; 2\,\pi\left(x - 0.5\right)\;, \tag{3.39}$$

where x is uniformly distributed between 0 and 1. Additionally, the transverse momentum p_T and rapidity y are calculated for each particle:

$$p_T = \sqrt{p_x^2 + p_y^2}\,, \tag{3.40}$$

$$y = \frac{1}{2}\ln\left(\frac{\varepsilon + p_z}{\varepsilon - p_z}\right)\,. \tag{3.41}$$

Finally, particles are distributed homogeneously in a sphere of radius r_1 and decay times are calculated based on the Breit-Wigner width of the resonances.

Resonance Decay

The third step (if applicable) is resonance decay. Following the prescription used by the authors of the THERMINATOR package [130], only 2 and 3 body decays are performed, while unstable daughter particles are allowed to decay in a successive manner. Only strong and electromagnetic decays are considered, while weak decays are omitted. Particle decay is first calculated in the parent's rest frame, with daughter momenta then boosted into the lab frame. Finally, decay positions are generated based on the parent's production point, momentum and life time.

Throughout this thesis, always only the lightest states of the following baryons:

$$\mathrm{p} \quad \mathrm{n} \quad \Lambda \quad \Sigma^+ \quad \Sigma^- \quad \Xi^- \quad \Xi^0 \quad \Omega^- \tag{3.42}$$

and their respective anti-baryons, as well as following mesons:

$$\pi^+ \quad \pi^- \quad \pi^0 \quad K^+ \quad K^- \quad K^0 \quad \overline{K}^0 \tag{3.43}$$

are considered as stable. The system could now be given collective velocity u^μ.

Re-weighting

In the fourth step, the values of extensive quantities are calculated for the events generated by iteration over the particle list of each event. For the values of extensive quantities $\mathcal{Q}^l_{1,n} = (B_{1,n}, S_{1,n}, Q_{1,n}, E_{1,n}, P_{x,1,n}, P_{y,1,n}, P_{z,1,n})$ in

subsystem V_1 of event n one may write:

$$\mathcal{Q}^l_{1,n} \;=\; \sum_{\text{particles } i_n} \mathfrak{q}^l_{i_n} \;, \tag{3.44}$$

where $\mathfrak{q}^l_{i_n} = (b_{i_n}, s_{i_n}, q_{i_n}, \varepsilon_{i_n}, p_{x,i_n}, p_{y,i_n}, p_{z,i_n})$ is the 'charge vector' of particle i in event n. Based on $\mathcal{Q}^l_{1,n}$ the weight w_n is calculated for the event:

$$w_n = \mathcal{W}^{\mathcal{Q}^l_{1,n};\mathcal{Q}^l_g}(V_1; V_g|\beta, u_\mu, \mu_j) \;, \tag{3.45}$$

according to Eq.(3.28). All micro states (or events) with the same set of extensive quantities $\mathcal{Q}^l_{1,n}$ are still counted equally.

Monte Carlo Distributions

The Monte Carlo output is essentially a distribution $P_{MC}(X_1, X_2, X_3, ...)$ of a set of observables X_1, X_2, X_3, etc. For all practical purposes this distribution is obtained by histograming all events n according to their values of $X_{1,n}$, $X_{2,n}$, $X_{3,n}$, etc. and their weight w_n. One can then define moments of two observables X_i and X_j through:

$$\langle X^n_i X^m_j \rangle \;\equiv\; \sum_{X_i, X_j} X^n_i \; X^m_j \; P_{MC}(X_i, X_j) \;. \tag{3.46}$$

Additionally, the variance $\langle (\Delta X_i)^2 \rangle$ and the covariance $\langle \Delta X_i \Delta X_j \rangle$ respectively are, defined as:

$$\langle (\Delta X_i)^2 \rangle \;\equiv\; \langle X^2_i \rangle \;-\; \langle X_i \rangle^2 \;, \qquad \text{and} \tag{3.47}$$

$$\langle \Delta X_i \Delta X_j \rangle \;\equiv\; \langle X_i X_j \rangle \;-\; \langle X_i \rangle \langle X_j \rangle \;. \tag{3.48}$$

In the following, the correlation coefficient ρ_{ij}, defined as:

$$\rho_{ij} \;\equiv\; \frac{\langle \Delta X_i \Delta X_j \rangle}{\sqrt{\langle (\Delta X_i)^2 \rangle \langle (\Delta X_j)^2 \rangle}} \;, \tag{3.49}$$

and later on the scaled variance ω_i, given by:

$$\omega_i \equiv \frac{\langle(\Delta X_i)^2\rangle}{\langle X_i\rangle} , \tag{3.50}$$

are used for quantification of fluctuations and correlations. The scaled variance ω_i, is often also called the 'Fano Factor' [107], and is a useful measure for the width of a distribution, provided $X_i > 0$, such as in the case of particle multiplicity.

3.3 Discussion

In this chapter distributions of extensive quantities in equilibrium systems with finite thermodynamic bath have been discussed. A recipe for a thermal model Monte Carlo event generator has been presented. The event generator is capable of extrapolating fluctuation and correlation observables for Boltzmann systems of large volume from their GCE values to the MCE limit. This approach has a strong advantage compared to analytical approaches or standard micro canonical sample-and-reject Monte Carlo techniques, in that resonance decays as well as (very) large system sizes can handled at the same time.

To introduce the scheme, a micro canonical system has been conceptually divided into two subsystems. These subsystems are assumed to be in equilibrium with each other, and subject to the constraints of joint energy-momentum and charge conservation. Particles are only measured in one subsystem, while the second subsystem provides a thermodynamic bath. By keeping the size of the first subsystem fixed, while varying the size of the second, one can thus study the dependence of statistical properties of an ensemble on the fraction of the system observed (i.e. assess their sensitivity to globally applied conservation laws). The ensembles generated are thermodynamically equivalent in the sense that mean values in the observed subsystem remain unchanged when the size of the bath is varied, provided the combined system is sufficiently large.

The Monte Carlo process can be divided into four steps. In the first two steps primordial particle multiplicities for each species, and momenta for each particle, are generated for each event by sampling the grand canonical partition function. In the third step resonance decay of unstable particles is performed. Lastly, the values of extensive quantities are calculated for each event and a corresponding

weight factor is assigned. All events with the same set of extensive quantities hence still have 'a priori equal probabilities'. In the limit of an infinite bath, all events have a weight equal to unity. In the opposite limit of a vanishing bath, only events with an exactly specified set of extensive quantities have non-vanishing weight. In between, extrapolation is done in a controlled manner. The method is particularly efficient for systems of large volume, inaccessible to sample-and-reject procedures, and agrees well, where available, with analytic asymptotic micro canonical solutions.

Given the success of the hadron resonance gas model in describing experimentally measured average hadron yields, and its ability to reproduce low temperature lattice susceptibilities, the question arises as to whether fluctuation and correlation observables also follow its main line. The first and, in particular, second moments of joint distributions of extensive quantities will be studied in the following. The focus will be mainly on particle multiplicity distributions and distributions of 'conserved' charges. In particular, the effects of resonance decay, conservation laws, and limited acceptance in momentum space are discussed. Due to the Monte Carlo nature, data can be analyzed in close relation to experimental analysis techniques. The hadron resonance gas is an ideal testbed for this type of study, in that it is simple and intuitive.

Chapter 4

Grand Canonical Ensemble

The grand canonical ensemble of the hadron resonance gas model will be the starting point of the discussion of statistical properties of equilibrium systems. The GCE is considered to be the most accessible amongst the standard ensembles. Its discussion will provide the basis for the study of canonical and micro canonical ensembles in the following chapters. The GCE is the correct ensemble to choose, if the observed subsystem is embedded into a much larger heat and charge bath. Primordial momenta of particles within a small subvolume are then uncorrelated with each other in the Boltzmann approximation.

Extensive quantities are fluctuating, while corresponding intensive variables are constant. Hence, in a subvolume one finds the energy content (extensive) to fluctuate, while temperature (intensive) is constant. Chemical potentials are constants, but the corresponding net-charge content is fluctuating. And naturally in a relativistic gas, the systems total particle number and integrated transverse momentum (no Lagrange multiplier associated with them) also fluctuate. However, extensive quantities do not merely fluctuate, but are also correlated with each other.

On the other hand, correlations observables do not depend on where they are measured in coordinate space, due to the infinite bath assumption. Observable correlation and fluctuation signals are, however, sensitive on the location and size of the available acceptance window in momentum space within which particles can be measured.

In Section 4.1 joint distributions of fully phase space integrated extensive quantities are considered. In Section 4.2 momentum spectra of primordial and

final state hadrons are analyzed. Correlations between extensive quantities are studied in their dependence on the acceptance window in momentum space in Sections 4.3 and 4.4.

4.1 Joint Distributions of Extensive Quantities

A neutral and static GCE hadron resonance gas with local temperature $T = 0.160$ GeV and volume $V = 2000$ fm^3 has been sampled according to the procedure described in Section 3.2. The values of net-charges and energy and momentum $\mathcal{Q}^l_{1,n}$ are calculated by iteration for the particle list of each event, according to Eq.(3.44). In the GCE all events have weight $w_n = 1$, Eq.(3.45). In Figs.(4.1-4.3) the event output is summarized. GCE joint distributions of extensive quantities are shown for samples of $5 \cdot 10^5$ events.

Charge fluctuations directly probe the degrees of freedom of a system, i.e. they are sensitive to its particle mass spectrum (and its quantum number configurations). The correlation coefficient and variances carry information about orientation and elongation of the probability distributions in Figs.(4.1-4.3). Firstly, charge correlations and the contributions of different particle species to the covariance $\langle \Delta X_i \Delta X_j \rangle$, Eq.(3.48), and therefore to the correlation coefficient ρ_{ij}, Eq.(3.49), are considered.

All baryons have baryon number $b = +1$. Baryons can only carry strange (valence) quarks, i.e. their strangeness is always $s \leq 0$. Anti-baryons have $b = -1$, and $s \geq 0$. I.e., both groups contribute negatively to the baryon-strangeness covariance, and so $\langle \Delta B \Delta S \rangle < 0$, and therefore $\rho_{BS} < 0$, as seen in Fig.(4.1) (*left*) and indicated by the solid lines in Fig.(4.5).

Positively charged baryons and their anti-particles contribute positively to the baryon-electric charge covariance $\langle \Delta B \Delta Q \rangle$, while negatively charged baryons (and their anti-particles) contribute negatively. Two observations can be made on the hadron resonance gas mass spectrum: there are more positively charged baryons than negatively charged ones, and their average mass is lower. I.e., in a neutral gas ($\mu_B = \mu_Q = \mu_S = 0$) the contribution of positively charged baryons (and negatively charged anti-baryons) dominates and therefore $\langle \Delta B \Delta Q \rangle > 0$ and $\rho_{BQ} > 0$, as seen in Fig.(4.1) (*right*) and indicated by the solid lines in Fig.(4.6).

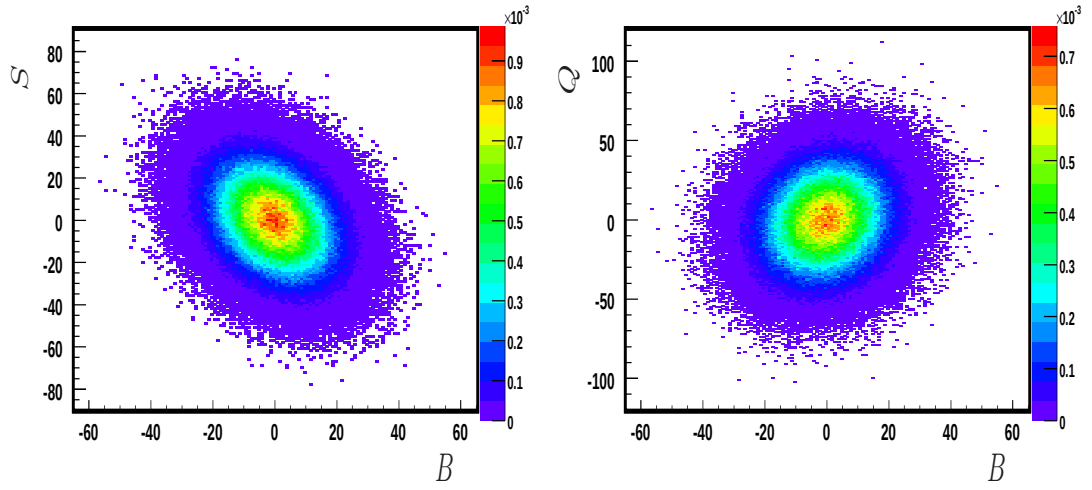

Figure 4.1: Grand canonical joint distribution of baryon number B and strangeness S (*left*), and grand canonical joint distribution of baryon number B and electric charge Q (*right*), for a neutral hadron resonance gas at $T = 0.160$ GeV and $V = 2000$ fm^3. Here $5 \cdot 10^5$ events have been sampled.

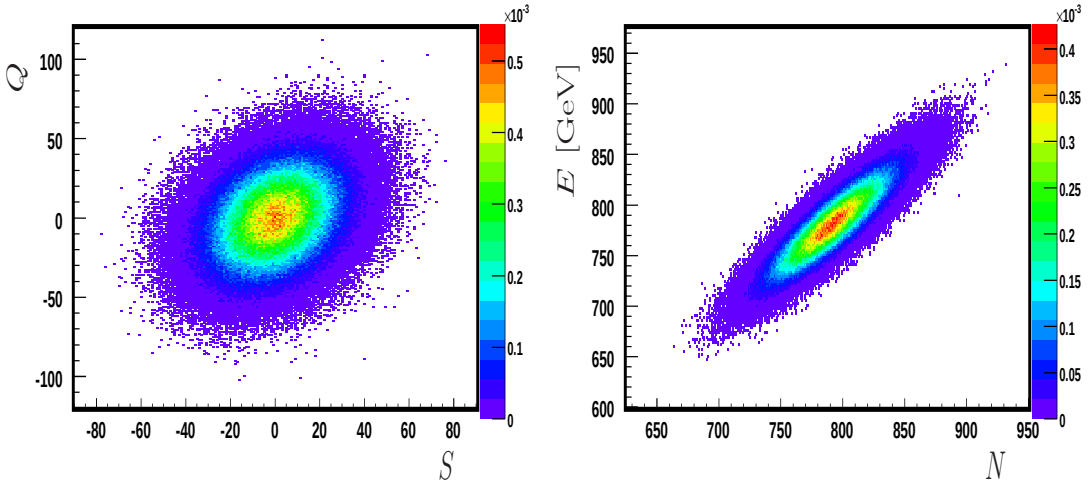

Figure 4.2: Grand canonical joint distribution of strangeness S and electric charge Q (*left*), and grand canonical joint distribution of energy E and total particle number N (*right*). The rest as in Fig.(4.1).

Mesons and their anti-particles always contribute positively to the strangeness-electric charge correlation coefficient ρ_{SQ}. Electrically charged strange mesons are either composed of an u-quark and a $\bar{s}$-quark, or of an $\bar{u}$-quark and a s-quark (and superpositions thereof). Their contribution to $\langle \Delta S \Delta Q \rangle$ is in either case positive. On the baryonic side, only the Σ^+ (as well as its degenerate states and

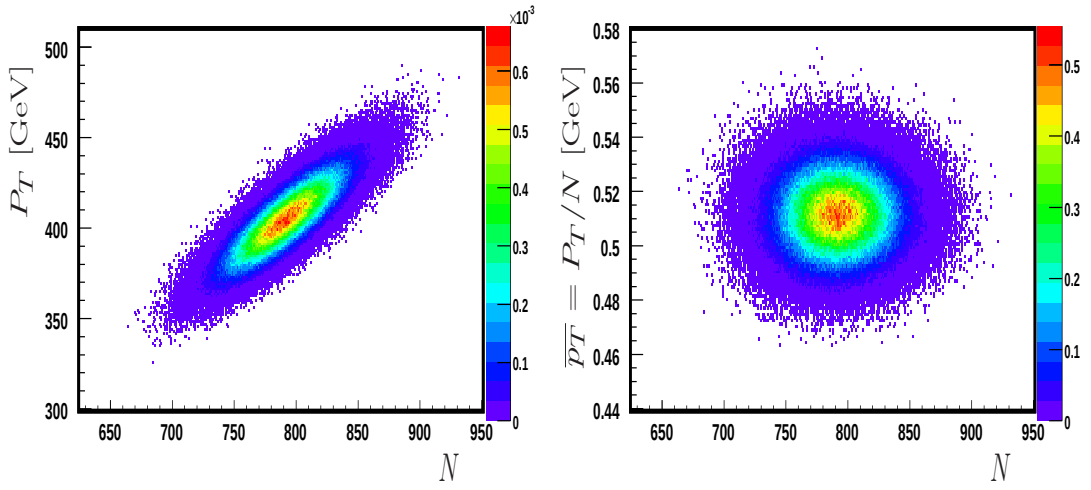

Figure 4.3: Grand canonical joint distribution $P(N, P_T)$ of total particle number N and total transverse momentum P_T (*left*), and grand canonical joint distribution $P(N, \overline{p_T})$ of total particle number N and mean transverse momentum $\overline{p_T} = P_T/N$ (*right*). The rest as in Fig.(4.1).

their respective anti-particles) has a negative contribution to $\langle \Delta S \Delta Q \rangle$, while all other strangeness carrying baryons have either electric charge $q = -1$, or $q = 0$. Therefore, one finds $\rho_{SQ} > 0$, as seen in Fig.(4.2) (*left*) and indicated by the solid lines in Fig.(4.7).

Since there are more particles (at $\mu_B = 0$, and $T = 0.160$ GeV) which carry electric charge than particles which carry strangeness, one finds the electric charge variance to be larger than the strangeness variance $\langle (\Delta Q)^2 \rangle > \langle (\Delta S)^2 \rangle$. Similarly, as there are more strangeness or anti-strangeness carrying particles than thermal baryon and anti-baryons, strangeness fluctuations are found to be stronger than baryon number fluctuation, $\langle (\Delta S)^2 \rangle > \langle (\Delta B)^2 \rangle$.

The correlation between particle number N and energy E in Fig.(4.2) (*right*) is more obvious. The more particles are in a subvolume, the more energy it will contain at a certain temperature β^{-1}. The total transverse momentum P_T can be seen as a measure for the kinetic energy in the system, Fig.(4.3) (*left*). And naturally, the more particles are inside the subvolume, the more kinetic energy is stored in them. These extensive quantities are strongly correlated in the GCE. Due to the independent sampling of primordial particle momenta in the GCE, however, the mean energy per particle $\overline{\varepsilon} = E/N$ and the mean transverse momentum $\overline{p_T} = P_T/N$, are event-by-event un-correlated with the particle number N of

the events. Here, the mean transverse momentum versus particle number distribution is shown in Fig.(4.3) (*right*).

4.2 Momentum Spectra

To prepare a more detailed analysis of charge fluctuations and correlations, inclusive momentum spectra are analyzed. In Fig.(4.4) transverse momentum and rapidity spectra of positively charged hadrons, both primordial and final state, are shown for a static thermal system.

Based on these momentum spectra acceptance bins $\Delta p_{T,i}$ and Δy_i are constructed following [98, 106, 127] and [59, 131]. Momentum bins are chosen such that each of the five bins contains on average one fifth of the total yield of positively charged particles. The values defining the bounds of the momentum space bins $\Delta p_{T,i}$ and Δy_i are summarized in Table 4.1.

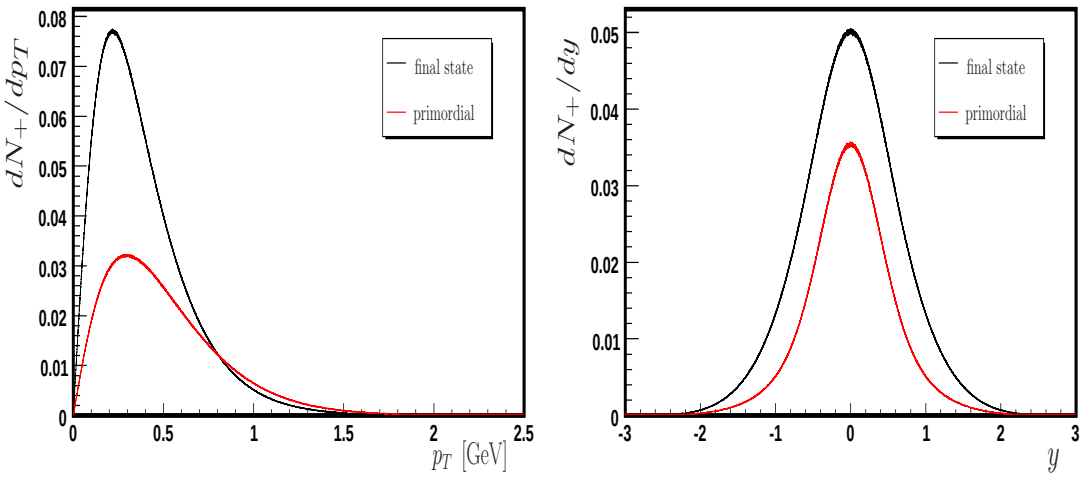

Figure 4.4: (*Left:*) Transverse momentum spectrum of positively charged hadrons, both primordial and final state. (*Right:*) Rapidity spectrum of positively charged hadrons, both primordial and final state. Here $2 \cdot 10^6$ events have been sampled for a static neutral hadron resonance gas in Boltzmann approximation with temperature $T = 0.160$ GeV.

Resonance decay shifts the transverse momentum distribution to lower average transverse momentum $\langle p_T \rangle$ and widens the rapidity distribution of thermal 'fireballs' [132, 133]. Transverse momentum bins of final state spectra are hence slightly 'contracted', while rapidity bins get slightly 'wider', when compared to

their respective primordial counterparts.

	$p_{T,1}$ [GeV]	$p_{T,2}$ [GeV]	$p_{T,3}$ [GeV]	$p_{T,4}$ [GeV]	$p_{T,5}$ [GeV]	$p_{T,6}$ [GeV]
Primordial	0.0	0.22795	0.36475	0.51825	0.73995	5.0
Final state	0.0	0.17105	0.27215	0.38785	0.56245	5.0
	y_1	y_2	y_3	y_4	y_5	y_6
Primordial	-5.0	-0.4275	-0.1241	0.1241	0.4273	5.0
Final state	-5.0	-0.5289	-0.1553	0.1551	0.5289	5.0

Table 4.1: Transverse momentum and rapidity bins $\Delta p_{T,i} = [p_{T,i}, p_{T,i+1}]$ and $\Delta y_i = [y_i, y_{i+1}]$, both primordial and final state, for a static neutral hadron resonance gas in Boltzmann approximation with temperature $T = 0.160$ GeV.

Resonance decay combined with transverse as well as longitudinal flow provides a rather good description of experimentally observed momentum spectra in relativistic heavy ion collisions at SPS and RHIC energies [130, 134, 135]. The momentum spectra discussed here, on the other hand, contain no flow, and results, thus, cannot be directly compared to experimental data or transport simulations. However, qualitatively one might observe the effects discussed in the following sections.

4.3 Correlations between Charges

An interesting example of quantities - for which the measured value depends on the observed part of the momentum spectrum - are the correlation coefficients between the charges baryon number B, strangeness S and electric charge Q. Also variances and covariances of the baryon number, strangeness, and electric charge distribution are strongly sensitive to the acceptance cuts applied. Their values are additionally rather sensitive to the effects of globally enforced conservation laws. If the size of the 'bath' is reduced, a change in one interval of phase space will have to be balanced (preferably) by a change in another interval, and not by the (finite) 'bath'.

The correlation coefficients ρ_{BS}, ρ_{BQ}, and ρ_{SQ} in limited acceptance bins $\Delta p_{T,i}$ and Δy_i, as defined in Table 4.1, are considered in the grand canonical ensemble. Primordial particles in one momentum bin are then sampled independently from particles in any other momentum space segment, due to the 'infinite bath'

assumption. Nevertheless, the way in which quantum numbers are correlated is different in different momentum bins[1], as different particle species have, due to their different masses, different momentum spectra. Resulting correlation functions are hence spectra, rather than simply values.

Figs.(4.5-4.7) show the correlation coefficients between baryon number and strangeness, ρ_{BS}, between baryon number and electric charge, ρ_{BQ}, and between strangeness and electric charge, ρ_{SQ}, as measured in the acceptance bins $\Delta p_{T,i}$ and Δy_i defined in Table 4.1, both primordial and final state. The average baryon number, strangeness, and electric charge in each bin is equal to zero, since the system was assumed to be neutral. The primordial values (15 bins) shown in Figs.(4.5-4.7) are calculated using analytical solutions. The error bars on many data points are smaller than the symbol used.

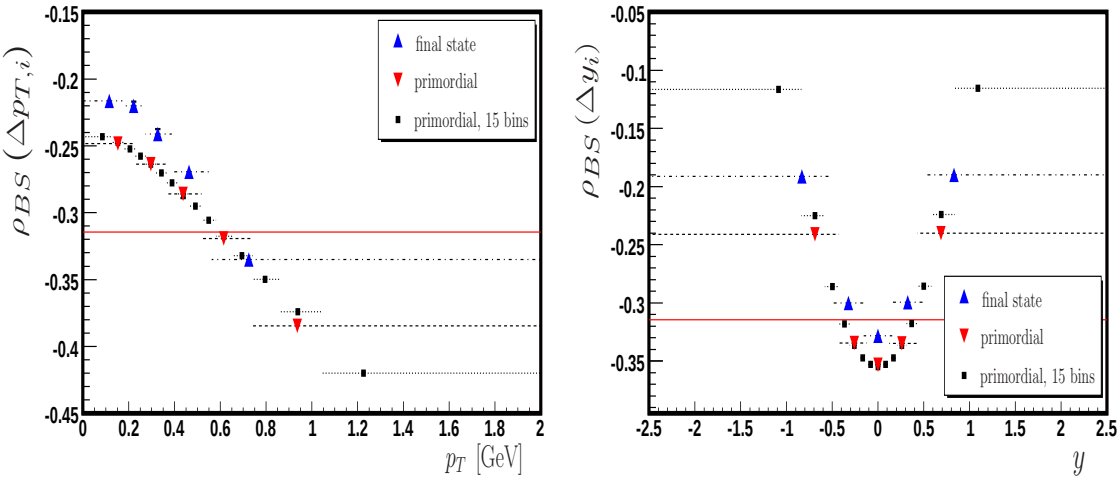

Figure 4.5: Baryon-strangeness correlation coefficient ρ_{BS} in the GCE in limited acceptance windows, both primordial and final state in transverse momentum bins $\Delta p_{T,i}$ (*left*), and in rapidity bins Δy_i (*right*). Horizontal error bars indicate the width and position of the momentum bins (And not an uncertainty!). Vertical error bars indicate the statistical uncertainty of 20 Monte Carlo runs of 10^5 events each. The marker indicates the center of gravity of the corresponding bin. The solid lines show the fully phase space integrated GCE result.

Tables 4.2 to 4.4 summarize the transverse momentum and rapidity dependence of the correlation coefficients ρ_{BS}, ρ_{BQ}, and ρ_{SQ}. The statistical error quoted corresponds to 20 Monte Carlo runs of 10^5 events each. The analytical

[1]For the extensive quantities energy E and longitudinal momentum P_z the correlation in limited acceptance bins $\Delta p_{T,i}$ and Δy_i is more apparent than for quantum numbers.

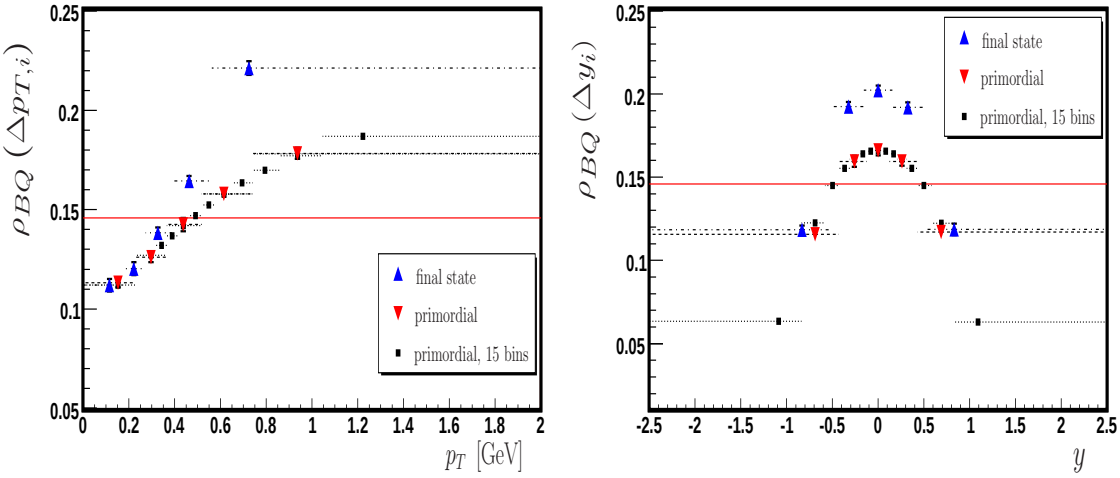

Figure 4.6: Baryon-electric charge correlation coefficient ρ_{BQ} in the GCE in limited acceptance windows, both primordial and final state in transverse momentum bins $\Delta p_{T,i}$ (*left*), and in rapidity bins Δy_i (*right*). The rest as in Fig.(4.5).

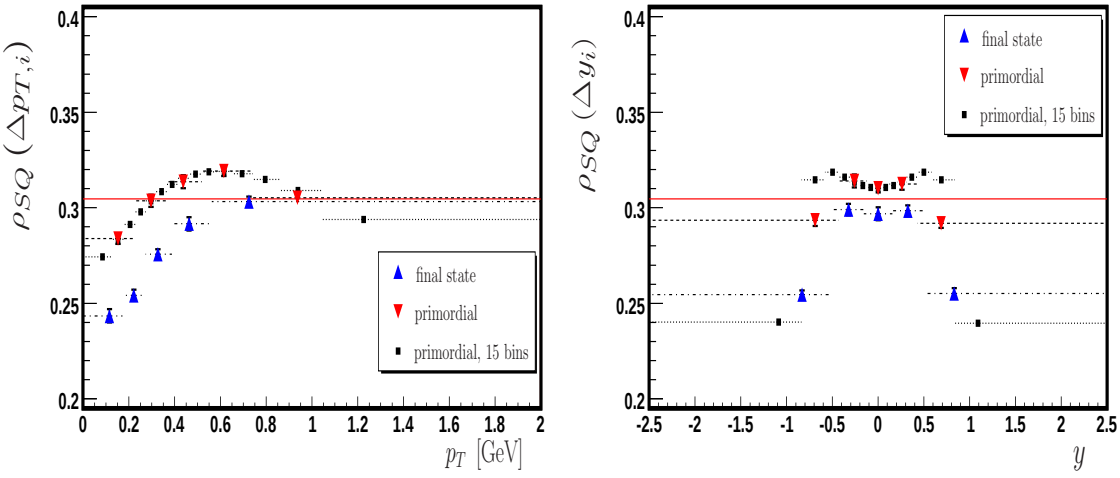

Figure 4.7: Strangeness-electric charge correlation coefficient ρ_{SQ} in the GCE in limited acceptance windows, both primordial and final state in transverse momentum bins $\Delta p_{T,i}$ (*left*), and in rapidity bins Δy_i (*right*). The rest as in Fig.(4.5).

values (5 bins) listed in the tables are calculated using the momentum bins defined in Table 4.1. Mild differences between Monte Carlo and analytical results are unavoidable. The calculated values are also not exactly symmetric in Δy_i, as the exact size of the acceptance bins constructed is sensitive to the number of bins used for the calculation of the momentum spectra. Correlation coefficients ρ are also rather sensitive to exact bin size, and the fourth digit becomes somewhat

ρ_{BS}	$\Delta p_{T,1}$	$\Delta p_{T,2}$	$\Delta p_{T,3}$	$\Delta p_{T,4}$	$\Delta p_{T,5}$
ρ_{prim}^{calc}	-0.2479	-0.2641	-0.2864	-0.3188	-0.3839
ρ_{prim}	-0.248 ± 0.003	-0.264 ± 0.003	-0.286 ± 0.003	-0.319 ± 0.002	-0.385 ± 0.002
ρ_{final}	-0.216 ± 0.002	-0.220 ± 0.003	-0.241 ± 0.004	-0.269 ± 0.003	-0.335 ± 0.003
ρ_{BS}	Δy_1	Δy_2	Δy_3	Δy_4	Δy_5
ρ_{prim}^{calc}	-0.2407	-0.3345	-0.3536	-0.3345	-0.2408
ρ_{prim}	-0.241 ± 0.003	-0.334 ± 0.003	-0.353 ± 0.003	-0.335 ± 0.003	-0.240 ± 0.003
ρ_{final}	-0.191 ± 0.002	-0.300 ± 0.002	-0.328 ± 0.002	-0.299 ± 0.002	-0.190 ± 0.002

Table 4.2: Baryon-strangeness correlation coefficient ρ_{BS} in the GCE in transverse momentum bins $\Delta p_{T,i}$ and rapidity bins Δy_i, both primordial and final state. For comparison, analytical values ρ_{prim}^{calc} for primordial correlations are included. The statistical uncertainty corresponds to 20 Monte Carlo runs of 10^5 events each.

ρ_{BQ}	$\Delta p_{T,1}$	$\Delta p_{T,2}$	$\Delta p_{T,3}$	$\Delta p_{T,4}$	$\Delta p_{T,5}$
ρ_{prim}^{calc}	0.1120	0.1271	0.1420	0.1579	0.1781
ρ_{prim}	0.113 ± 0.002	0.126 ± 0.002	0.143 ± 0.003	0.158 ± 0.002	0.178 ± 0.003
ρ_{final}	0.112 ± 0.003	0.120 ± 0.003	0.138 ± 0.003	0.164 ± 0.003	0.221 ± 0.003
ρ_{BQ}	Δy_1	Δy_2	Δy_3	Δy_4	Δy_5
ρ_{prim}^{calc}	0.1160	0.1601	0.1658	0.1601	0.1160
ρ_{prim}	0.116 ± 0.002	0.160 ± 0.003	0.166 ± 0.003	0.159 ± 0.003	0.117 ± 0.002
ρ_{final}	0.118 ± 0.003	0.192 ± 0.003	0.202 ± 0.003	0.192 ± 0.003	0.119 ± 0.003

Table 4.3: Baryon-electric charge correlation coefficient ρ_{BQ} in the GCE in transverse momentum bins $\Delta p_{T,i}$ and rapidity bins Δy_i, both primordial and final state.

ρ_{SQ}	$\Delta p_{T,1}$	$\Delta p_{T,2}$	$\Delta p_{T,3}$	$\Delta p_{T,4}$	$\Delta p_{T,5}$
ρ_{prim}^{calc}	0.2831	0.3033	0.3150	0.3185	0.3055
ρ_{prim}	0.284 ± 0.003	0.304 ± 0.003	0.314 ± 0.003	0.319 ± 0.002	0.305 ± 0.002
ρ_{final}	0.243 ± 0.003	0.254 ± 0.003	0.276 ± 0.003	0.292 ± 0.003	0.303 ± 0.002
ρ_{SQ}	Δy_1	Δy_2	Δy_3	Δy_4	Δy_5
ρ_{prim}^{calc}	0.2934	0.3137	0.3104	0.3137	0.2934
ρ_{prim}	0.294 ± 0.003	0.314 ± 0.003	0.310 ± 0.002	0.312 ± 0.003	0.292 ± 0.002
ρ_{final}	0.255 ± 0.002	0.299 ± 0.003	0.297 ± 0.003	0.298 ± 0.003	0.255 ± 0.003

Table 4.4: Strangeness-electric charge correlation coefficient ρ_{SQ} in the GCE in transverse momentum bins $\Delta p_{T,i}$ and rapidity bins Δy_i, both primordial and final state.

unreliable.

The rapidity dependence of ρ_{BS}, ρ_{BQ}, and ρ_{SQ} is now considered. Strange baryons are, on average, heavier than non-strange baryons, so their thermal rapidity distributions are narrower. The kaon rapidity distribution is then, compared to baryons, again wider. A change in baryon number (strangeness) at high $|y|$ is less likely to be accompanied by a change in strangeness (baryon number) than at low $|y|$. The value of ρ_{BS}, therefore, drops toward higher rapidity, as shown in Fig.(4.5) (*right*).

By the same argument, one finds a weakening of the baryon-electric charge correlation ρ_{BQ} at higher rapidity, Fig.(4.6) (*right*)), as the rapidity distribution of electrically charged particles is wider than the one of baryons. The strangeness-electric charge correlation coefficient ρ_{SQ} first rises mildly and then drops somewhat stronger towards higher rapidity. As one shifts ones acceptance window to higher values of $|y|$, first the contribution of baryons (in particular Σ^+) decreases and, as the meson contribution grows, ρ_{SQ} rises slightly. Towards the highest $|y|$, pions again dominate and de-correlate the quantum numbers.

The transverse momentum dependence can be understood as follows: heavier particles have higher average transverse momentum $\langle p_T \rangle$ and, hence, their influence increases towards higher p_T. Heavy particles, in particular baryonic resonances, often carry several quantum numbers, causing the correlation coefficients to grow.

The contribution of strange baryons compared to non-strange baryons grows for higher transverse momentum, since strange baryons have on average larger mass than non-strange baryons. The correlation coefficient ρ_{BS}, thus, becomes strongly negative at high p_T. As the contribution of baryons compared to mesons grows stronger towards larger p_T, a change in baryon number (electric charge) is now more likely to be accompanied by a change in electric charge (baryon number) than at low p_T, and ρ_{BQ} increases with p_T (the Δ resonances[2] ensure it keeps rising). For the $\Delta p_{T,i}$ dependence of ρ_{SQ} one notes that one of the strongest contributors at higher p_T is the Ω^-, with a relatively low mass of $m_{\Omega^-} = 1.672$ GeV. So after a rise, ρ_{SQ} drops again towards highest p_T, due to an increasing Σ^+ contribution[3].

Since resonance decay has the habit of dropping the lighter particles (mesons)

[2]Included in the THERMUS particle table up to the $\Delta(2420)$.
[3]Included in the THERMUS particle table up to the $\Sigma(2030)$.

at low p_T and higher $|y|$, while keeping heavier particles (baryons) at higher p_T and at mid-rapidity, none of the above arguments about the transverse momentum and rapidity dependence are essentially changed by resonance decay. The correlation coefficient ρ_{BS} becomes more negative towards higher p_T, while becoming weaker towards higher $|y|$. Similarly, ρ_{BQ} grows larger at high p_T and drops with increasing y. The larger contributions of baryons to the high p_T tail of the transverse momentum spectrum, and their decreased contribution to the tails of the rapidity distribution, compared to mesons, are to blame. The bump in the p_T dependence of ρ_{SQ}, caused by the Σ^+, has vanished, as the Σ^+ is only considered as stable in its lightest version with mass $m_{\Sigma^+} = 1.189$ GeV. The small bump in the y dependence of ρ_{SQ}, however, stays. The correlation is first increased by a growing kaon contribution and then again decreased by a growing pion contribution at larger rapidities.

4.4 Correlation Functions

Above results are now applied to measures of correlations used in heavy ion phenomenology. The measurement of charge correlations appears to be a good discriminating tool between different physics scenarios, such as the ones provided by lattice QCD [136], effective field theories [137], or non-equilibrium transport models [138]. Acceptance effects are studied in this section. A discussion of the dependence of fully phase space integrated quantities on temperature and chemical potential can be found in Chapters 8 and 9. In this context variances of marginal distributions are studied.

Following the definitions of Ref. [139] one can relate the correlation coefficients ρ_{BS} and ρ_{SQ} to the baryon number strangeness correlation measure C_{BS}:

$$C_{BS} \equiv -3 \frac{\langle \Delta B \Delta S \rangle}{\langle (\Delta S)^2 \rangle} = -3 \rho_{BS} \sqrt{\frac{\langle (\Delta B)^2 \rangle}{\langle (\Delta S)^2 \rangle}} , \tag{4.1}$$

and the electric charge strangeness correlation measure C_{QS}:

$$C_{QS} \equiv 3 \frac{\langle \Delta Q \Delta S \rangle}{\langle (\Delta S)^2 \rangle} = 3 \rho_{SQ} \sqrt{\frac{\langle (\Delta Q)^2 \rangle}{\langle (\Delta S)^2 \rangle}} . \tag{4.2}$$

In the ideally weakly coupled QGP the fully phase space integrated values are for

the baryon number strangeness correlation measure $C_{BS}^{QGP} = 1$, and for the electric charge strangeness correlation measure $C_{QS}^{QGP} = 1$ [139, 140]. On the other hand, if correlations were determined by hadronic degrees of freedom, the fully phase space integrated correlation measures would be $C_{BS}^{HRG} \simeq 0.66$, and $C_{QS}^{HRG} \simeq 1.2$ respectively, for a hadron resonance gas at $T = 0.170$ GeV and $\mu_B = 0.0$ GeV [139]. The 'quark Molecular Dynamics' (qMD) model [138] is in agreement with hadron resonance gas results below the critical temperature T_c, while following lattice QCD calculations above T_c. Additionally, the baryon number electric charge correlation measure C_{BQ} is defined to be:

$$C_{BQ} \;=\; 3\,\frac{\langle \Delta B \Delta Q \rangle}{\langle (\Delta Q)^2 \rangle} \;=\; 3\,\rho_{BQ}\,\sqrt{\frac{\langle (\Delta B)^2 \rangle}{\langle (\Delta Q)^2 \rangle}} \tag{4.3}$$

Since the motivation in [139] for having the baryon number variance $\langle (\Delta B)^2 \rangle$ not in the denominator, was that the electrically neutral neutron is hard to measure, the covariance in Eq.(4.3) is divided by the electric charge variance $\langle (\Delta Q)^2 \rangle$, which is experimentally more accessible. The fully phase space integrated hadron resonance gas estimate, Fig.(4.9), is $C_{BQ}^{HRG} \simeq 0.23$. A QGP estimate is not reported.

In Figs.(4.8-4.10) the correlation measures C_{BS} (baryon number - strangeness), C_{BQ} (baryon number - electric charge), and C_{SQ} (strangeness - electric charge), are shown as measured in the acceptance bins $\Delta p_{T,i}$ and Δy_i defined in Table 4.1, both primordial and final state. The average baryon number, strangeness, and electric charge in each bin is equal to zero, since the system the assumed to be neutral. The analytical primordial values (15 bins) shown in Figs.(4.8-4.10) are calculated using analytical methods. It is mentioned that, again, the error bars on many data points are smaller than the symbol used. Fully phase space integrated values, indicated by solid lines, are compatible of hadron resonance gas results of Ref. [139]. Nevertheless the results here show a strong dependence on the acceptance cuts applied. The fully phase space integrated values give a good estimate of the average. The data in limited acceptance are consistently above the weakly coupled QGP estimates [139, 140] in the case of C_{BS}, or below as for C_{QS}. The momentum space dependence of charge correlations in the QGP has not yet been calculated. In the hadron resonance gas the momentum space dependence is caused by different momentum spectra due to different hadron masses.

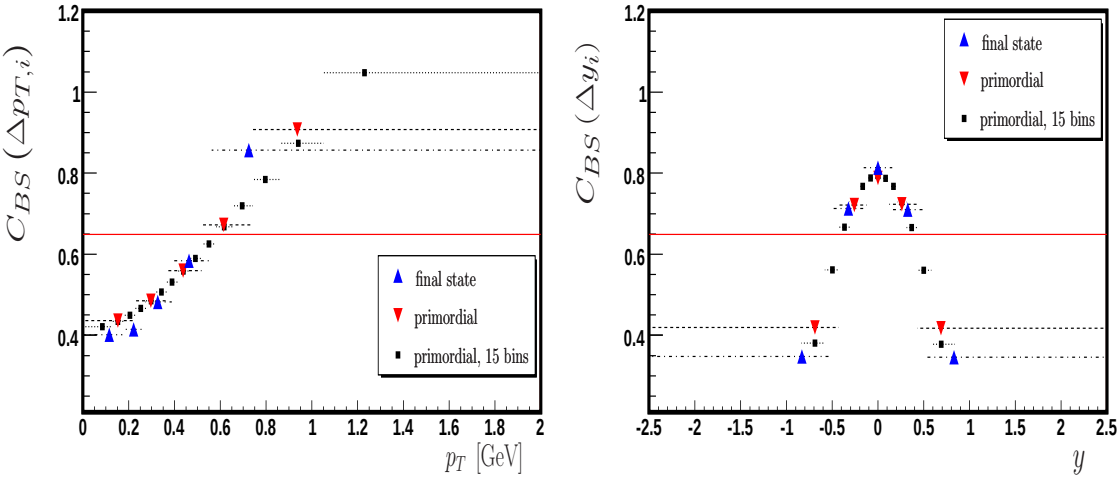

Figure 4.8: Baryon-strangeness correlation measure C_{BS} in the GCE in limited acceptance windows, both primordial and final state, in transverse momentum bins $\Delta p_{T,i}$ (*left*), and in rapidity bins Δy_i (*right*). Horizontal error bars indicate the width and position of the momentum bins (And not an uncertainty!). Vertical error bars indicate the statistical uncertainty of 20 Monte Carlo runs of 10^5 events each. The marker indicates the center of gravity of the corresponding bin. The solid lines show the fully phase space integrated GCE result.

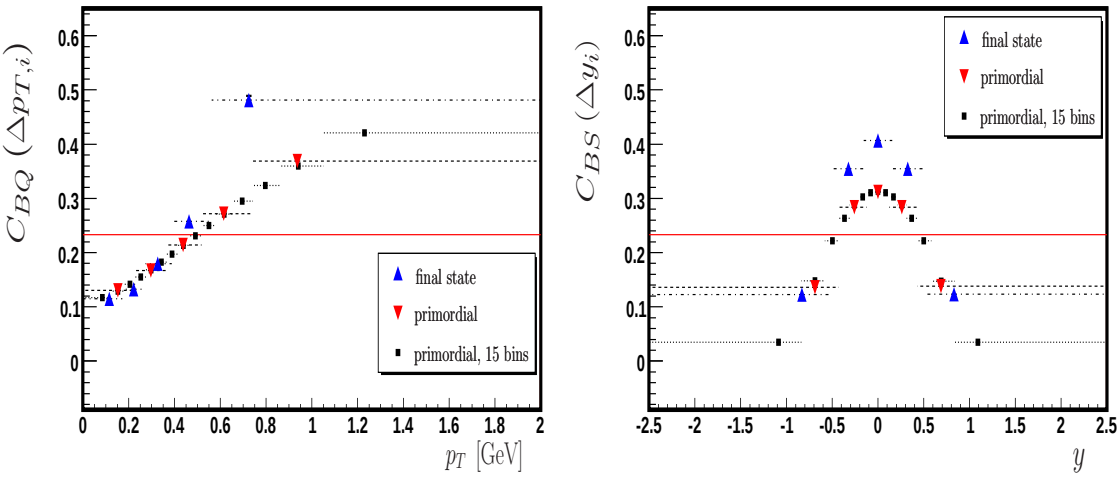

Figure 4.9: Baryon-electric charge correlation measure C_{BQ} in the GCE in limited acceptance windows, both primordial and final state, in transverse momentum bins $\Delta p_{T,i}$ (*left*), and in rapidity bins Δy_i (*right*). The rest as in Fig.(4.8).

One notes a qualitatively similar behavior of the correlation coefficients ρ shown in Figs.(4.5-4.7) to the correlation measure C. To illustrate their differences, joint distributions are considered in limited acceptance. The correla-

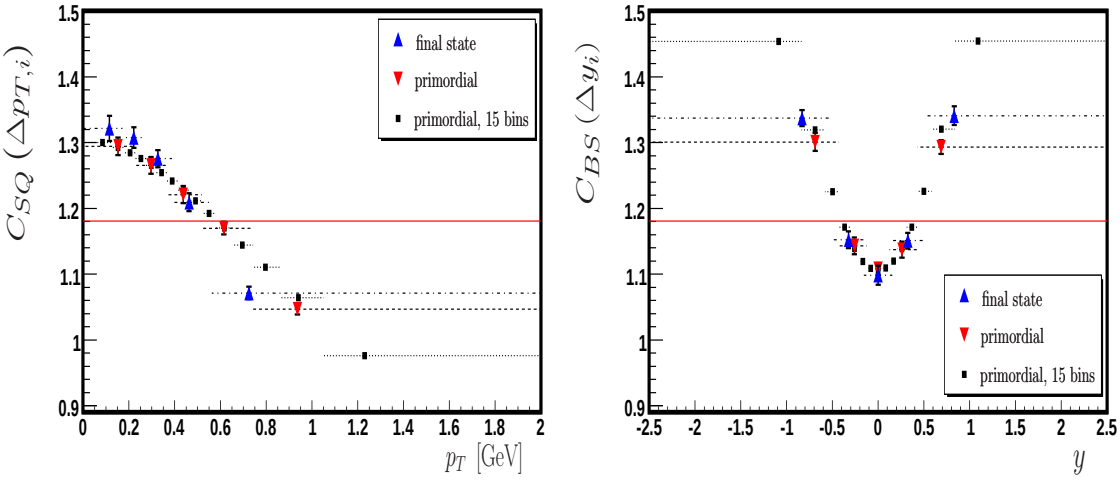

Figure 4.10: Strangeness-electric charge correlation measure C_{SQ} in the GCE in limited acceptance windows, both primordial and final state, in transverse momentum bins $\Delta p_{T,i}$ (*left*), and in rapidity bins Δy_i (*right*). The rest as in Fig.(4.8).

tion measures ρ and C are similar in their $\Delta p_{T,i}$ and Δy_i dependence, and are essentially explained by arguments above. Additionally, the momentum space dependence of variances in Eqs.(4.1-4.2) needs to be taken into account.

Fig.(4.11) shows the GCE joint baryon number strangeness distribution as calculated in the acceptance windows $\Delta p_{T,i}$ (*top*) and Δy_i (*bottom*), while Fig.(4.12) summarizes the primordial baryon number variance $\langle(\Delta B)^2\rangle$, strangeness variance $\langle(\Delta S)^2\rangle$, and the baryon number strangeness covariance $\langle\Delta B\Delta S\rangle$ in the GCE in transverse momentum bins $\Delta p_{T,i}$ (*left*) and rapidity bins Δy_i (*right*).

The marginal variances $\langle(\Delta B)^2\rangle$ and $\langle(\Delta S)^2\rangle$ get wider in the transverse momentum direction $\Delta p_{T,i}$, Fig.(4.11) (*top*), while the correlation ρ_{BS} gets stronger. The contribution of baryons (compared to all hadrons) increases towards higher transverse momentum, which causes the baryon distribution to widen. Strangeness carrying particles are heavier than non-strange particles, so their variance increases, too. Together they drive up their covariance $\langle\Delta B\Delta S\rangle$. In rapidity Δy_i direction, Fig.(4.11) (*bottom*), the arguments are somewhat reversed. Particles carrying baryon number and strangeness are predominantly produced (thermally) around mid-rapidity. At larger rapidity, the pions take over, and the baryon number and strangeness variances decrease. And as the kaon rapidity distribution is wider than the one of the Λ, one finds the correlation ρ_{BS} to decrease

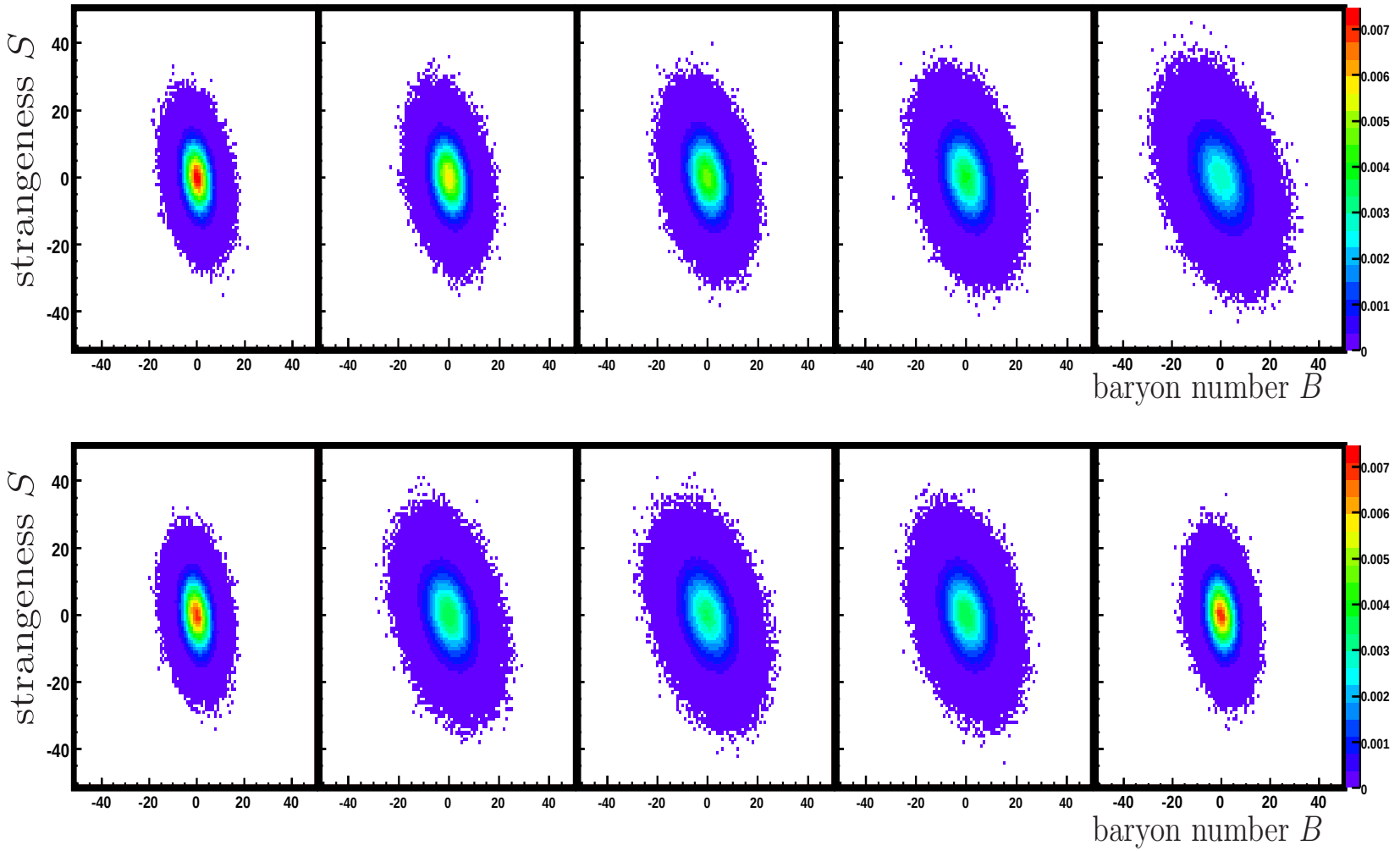

Figure 4.11: (*Top:*) Joint baryon number strangeness distribution in transverse momentum bins, from left to right $\Delta p_{T,1}$ to $\Delta p_{T,5}$. (*Bottom:*) Joint baryon number strangeness distribution in rapidity bins, from left to right Δy_1 to Δy_5.

towards higher $|y|$.

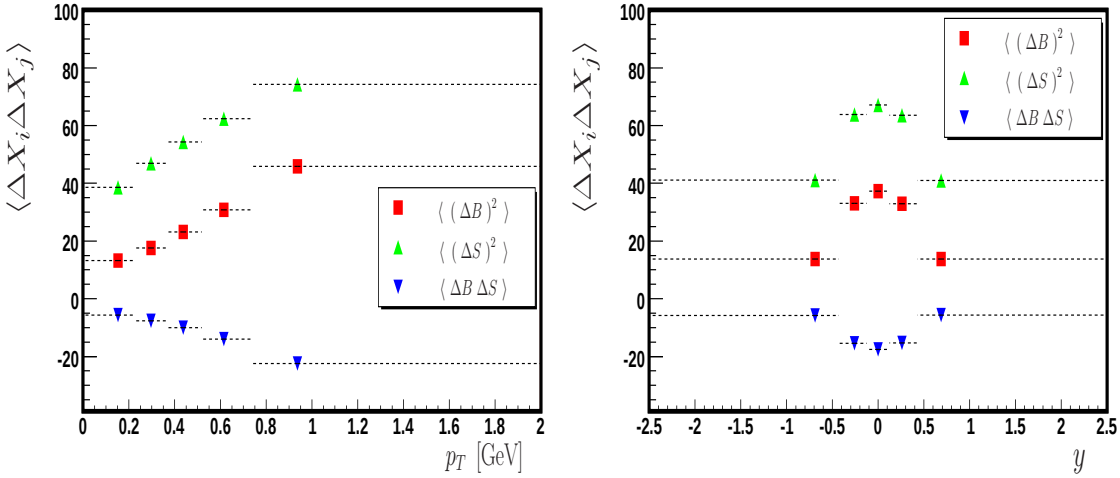

Figure 4.12: Primordial baryon number variance $\langle(\Delta B)^2\rangle$, strangeness variance $\langle(\Delta B)^2\rangle$, and the baryon number strangeness covariance $\langle\Delta B\Delta S\rangle$ in the GCE in limited acceptance windows: (*Left:*) transverse momentum bins $\Delta p_{T,i}$. (*Right:*) rapidity bins Δy_i. Horizontal error bars indicate the width and position of the momentum bins (And not an uncertainty!). Vertical error bars are smaller than the statistical uncertainty of 20 Monte Carlo runs of 10^5 events each. The marker indicates the center of gravity of the corresponding bin.

Similarly, in full acceptance one finds for the variances of the marginal charge distributions in limited acceptance $\langle(\Delta B)^2\rangle < \langle(\Delta S)^2\rangle < \langle(\Delta Q)^2\rangle$. Yet, the dependence of their ratios on transverse momentum and rapidity cuts is stronger for some and weaker for others. Baryons dominate at high p_T; strangeness carrying particles are heavier; accordingly both variances increase at large p_T compared to the electric charge variance (not shown). Heavier particles live around mid-rapidity. The ratios $\langle(\Delta B)^2\rangle/\langle(\Delta Q)^2\rangle$ and $\langle(\Delta B)^2\rangle/\langle(\Delta S)^2\rangle$ get larger at larger p_T and $|y|$, while the ratio $\langle(\Delta Q)^2\rangle/\langle(\Delta S)^2\rangle$ gets smaller at larger momentum. Therefore, the momentum dependence is stronger for C_{BS} and C_{BQ} than for ρ_{BS} and ρ_{BQ}, while being weaker for C_{QS} than for ρ_{SQ}.

4.5 Discussion

In this chapter samples of grand canonical Monte Carlo events have been analyzed. Joint distributions of extensive quantities have been considered with full

acceptance, or with limited acceptance, in momentum space assumed. Attention was given to the effects of resonance decay.

The correlations and fluctuations of extensive quantities of a statistical system are determined by the degrees of freedom, i.e. particles and their masses and quantum numbers, available to the system. So is, for instance, the correlation between energy and particle multiplicity dependent on the type of particle species measured and the experimental acceptance window assumed.

Due to the assumption of an infinite thermodynamic bath, occupation numbers of individual momentum levels are un-correlated with each other. Likewise, particle multiplicities of two distinct groups of particles appear un-correlated. Together with occupation number fluctuations unconstrained by global constraints, all extensive quantities, bar the volume, fluctuate on an event-by-event or micro state-by-micro state basis. Therefore, the energy content and particle multiplicity are strongly correlated, while the average energy per particle is un-correlated with multiplicity. The net-charge content of baryon number and strangeness in the system are correlated because some hadron species carry both charges. Different hadron species have different quantum numbers and different spectra. The correlation of baryon number and strangeness depends, like the one of energy and momentum, or energy and particle multiplicity, on which part of the spectrum is accessible for measurement.

The correlation coefficients between quantum numbers increase towards higher p_T, since heavier particles have higher average transverse momentum $\langle p_T \rangle$. Heavy particles, in particular baryonic resonances, often carry several quantum numbers, causing the correlation coefficients to grow. For a thermal fireball this effect is strongest in a mid-rapidity window.

The values of ρ or C after resonance decay are directly sensitive to how the data is analyzed. In the above study only final state particles (stable against strong decays) are analyzed. One could, however, also reconstruct decay positions and momenta of parent resonances and could then count them as belonging to the acceptance bin the parent momentum would fall into. In the situation above, however, this would again yield the primordial scenario. If reconstruction of resonances is not done, one is sensitive to charge correlations carried by final state particles. As in the primordial case, a larger acceptance bin effectively averages over smaller bins. However, the smaller the acceptance bin, the more information is lost due to resonance decay. In full acceptance, final state and

primordial correlation coefficients ought to be the same, since quantum numbers (and energy-momentum) are conserved in the decays of resonances (weak decays omitted).

Chapter 5

Extrapolating to the MCE

In the previous chapter the grand canonical ensemble and limited acceptance effects have been studied. In this chapter, fully phase space integrated extensive quantities are considered and studied in their dependence on the size of the thermodynamic bath for a neutral and static system. Firstly, mean values, covariances, and correlations coefficients of joint distributions of extensive quantities are analyzed in Section 5.1. Then, in Section 5.2, the joint distributions themselves, and, in Section 5.3, the weight factor are considered more closely. This discussion will prepare the analysis of multiplicity fluctuations and correlations, Chapter 6, and the effect of conservation laws on them.

5.1 Fully Phase Space Integrated Quantities

Fully phase space integrated grand canonical results are extrapolated to the micro canonical limit. For this purpose hadron resonance gas events for various values of $\lambda = V_1/V_g$ are iteratively generated, re-weighted, and analyzed. By construction of the weight factor $\mathcal{W}$, Eq.(3.28), the extrapolation proceeds in a systematic fashion such that, for instance, particle momentum spectra as well as mean values of extensive quantities remain unchanged. On the other hand, all variances and covariances of extensive quantities subject to re-weighting converge linearly to their micro canonical values.

This can be seen from the form of the analytical large volume approximation to the grand canonical distribution of (fully phase space integrated) extensive

quantities $P_{gce}(\mathcal{Q}_1^l)$ (from Eq.(2.30)):

$$P_{gce}(\mathcal{Q}_1^l) \simeq \frac{1}{(2\pi V_1)^{L/2}\det|\sigma|} \exp\left[-\frac{1}{2}\frac{1}{V_1}\xi^l\xi_l\right] , \tag{5.1}$$

where the variable ξ^l is given by Eq.(3.20). Now taking the weight factor $\mathcal{W}_\lambda$, Eq.(3.28), (σ and ξ_l are the same in both equations) one obtains for the distribution $P_\lambda(\mathcal{Q}_1^l)$ of extensive quantities $\mathcal{Q}_1^l$ in subsystem 1:

$$\begin{aligned} P_\lambda(\mathcal{Q}_1^l) &\simeq \mathcal{W}_\lambda^{\mathcal{Q}_1^l;\mathcal{Q}_g^l} P_{gce}(\mathcal{Q}_1^l) \\ &\simeq \frac{1}{(2\pi(1-\lambda)V_1)^{L/2}\det|\sigma|} \exp\left[-\frac{1}{2}\frac{1}{(1-\lambda)\ V_1}\xi^l\xi_l\right] . \end{aligned} \tag{5.2}$$

This is essentially the same multivariate normal distribution as the grand canonical version $P_{gce}(\mathcal{Q}_1^l)$, however linearly contracted. Monte Carlo results will then be compared to Eq.(5.2).

Again a static and neutral hadron resonance gas with collective four-velocity $u_\mu = (1,0,0,0)$, chemical potential vector $\mu_j = (0,0,0)$, local temperature $T = \beta^{-1} = 0.160$ GeV, and volume $V_1 = 2000$ fm^3 is considered. This is a system large enough[1] for using the large volume approximation worked out in Section 2.2.

In Figs.(5.1) and (5.2) the results of Monte Carlo runs of $2.5 \cdot 10^4$ events each are shown. Each value of λ has been sampled 20 times to allow for calculation of a statistical uncertainty estimate. 19 different values of λ have been studied. In this case study, the extensive quantities baryon number B, strangeness S, electric charge Q, energy E, and longitudinal momentum P_z are considered for re-weighting. Conservation of transverse momenta P_x and P_y can be shown not to affect the $\Delta p_{T,i}$ and Δy_i dependence of multiplicity fluctuations and correlations studied in Chapter 6. Their Δy_i dependence is, however, rather sensitive to P_z conservation. Angular correlations, considered in Chapter 7, on the other hand, are strongly sensitive to joint P_x and P_y conservation [106, 127].

Fig.(5.1) (*left*) summarizes the results for mean values of baryon number $\langle B\rangle$, strangeness $\langle S\rangle$, electric charge $\langle Q\rangle$, energy $\langle E\rangle$, and the momenta $\langle P_x\rangle$ and $\langle P_z\rangle$.

[1] Generally it is not easy to define when a system is 'large enough' for the large volume approximation to be valid. Here, good agreement is found with asymptotic analytic solutions. Charged systems, or Bose-Einstein/Fermi-Dirac systems, usually converge more slowly to their asymptotic solution.

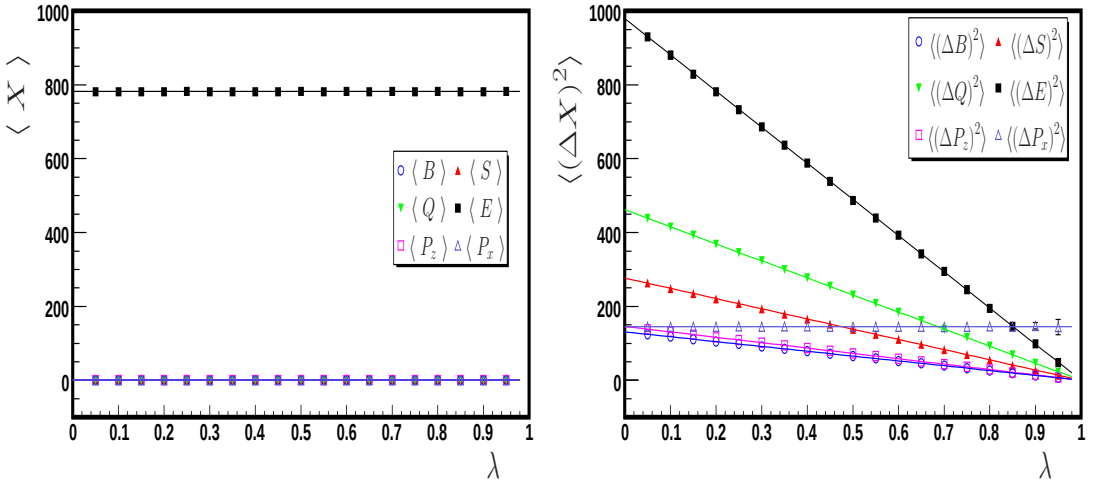

Figure 5.1: Mean values (*left*) and variances (*right*) of various extensive quantities, as listed in the legends, as a function of λ. Each marker and its error bar represents the result of 20 Monte Carlo runs of $2.5 \cdot 10^4$ events each. 19 different equally spaced values of λ have been investigated. Solid lines indicate GCE values (*left*), or linear extrapolations from the GCE value to the MCE limit (*right*).

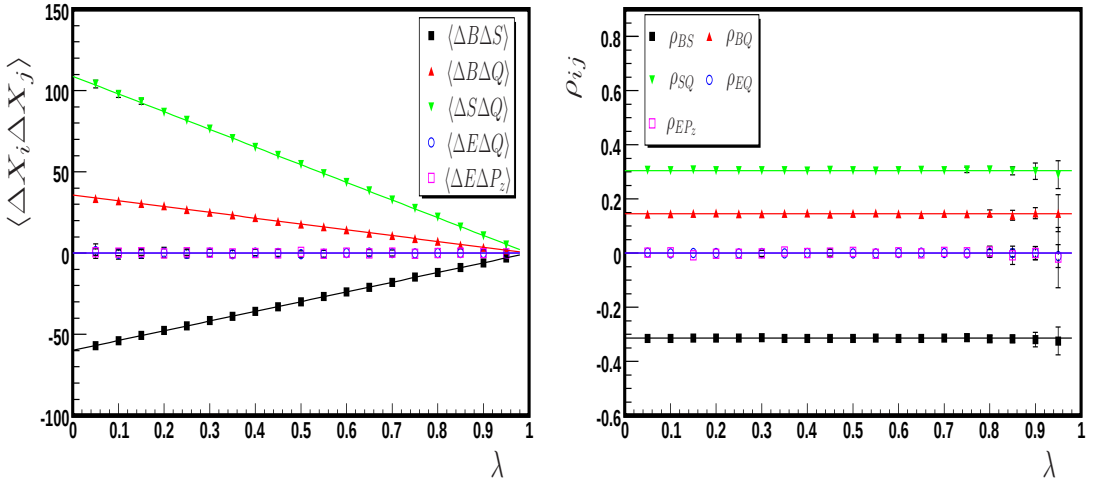

Figure 5.2: Covariances (*left*) and correlation coefficients (*right*) between various extensive quantities, as listed in the legends, as a function of λ. Solid lines indicate linear extrapolations from the GCE value to the MCE limit (*left*), or GCE values (*right*). The rest as in Fig.(5.1).

The solid lines represent GCE values. Only the expectation value of energy is not equal to 0, since the system sampled is assumed to be static and neutral with $T \neq 0$. The evolution of the respective variances is shown in Fig.(5.1) (*right*). Variances of extensive quantities subject to re-weighting converge linearly to 0

as λ goes to 1. One notes that $\langle(\Delta P_x)^2\rangle$ remains constant (within error bars), as this quantity is not re-weighted in this case study. Error bars on many data points are smaller than the symbol used.

In Fig.(5.2) (*left*) the evolution of covariances $\langle\Delta B\Delta S\rangle$, $\langle\Delta B\Delta Q\rangle$, $\langle\Delta S\Delta Q\rangle$, and $\langle\Delta E\Delta Q\rangle$ is shown as a function of the 'size of the bath'. As seen, the covariances between quantities considered for re-weighting converge linearly to 0. In a neutral system, covariances between energy and charges are equal to 0. As an example, $\langle\Delta E\Delta Q\rangle$ is shown. In a static system, also the covariances between momenta and any other extensive quantity are equal to 0. As an example here $\langle\Delta E\Delta P_z\rangle$ is shown. The correlation coefficients, Eq.(3.49), on the other hand, remain constant as a function of λ, as shown in Fig.(5.2) (*right*). The values of fully phase space integrated correlation coefficients ρ_{BS}, ρ_{BQ}, and ρ_{SQ} can be compared to the GCE results denoted by the solid lines shown in Figs.(4.5-4.7) in Section 4.3.

5.2 Probability Distributions

It is also interesting to study probability distributions as a function of the size of the bath λ. Firstly joint distributions of charges, $P_\lambda(B,S)$, $P_\lambda(B,Q)$, and $P_\lambda(S,Q)$ from (*left*) to (*right*), are attended to in Fig.(5.3). Mean values of net-charges stay constant throughout the extrapolation, see also Fig.(5.1) (*left*). Their variances and covariances, compare Fig.(5.1) (*right*) and Fig.(5.2) (*left*), converge to 0 as the size of the bath is reduced. All three quantities, B, S, and Q are re-weighted, and thus correlation coefficients amongst them, Fig.(5.2) (*right*), stay constant. Hence events in a small region around $\langle B_1\rangle$, $\langle S_1\rangle$, and $\langle Q_1\rangle$, are highlighted, while correlations between them are left unchanged[2].

In Fig.(5.4) (*left*) the joint energy and particle number distribution $P_\lambda(E,N)$ is shown. Here only one of the two quantities was re-weighted. In the GCE one finds particle number to be strongly correlated with energy. The more particles are in a box of volume V_1, the more energy is contained inside this box. This distribution does obviously not converge to a δ-function, as the size of the bath is

[2]Sometimes it may not be clear which ensemble one should choose to apply to a given statistical system. The three standard ensembles remain particular idealizations. Also the scenario discussed here is a particular limit. The system under investigation could have a bath which might impose its own correlations. Or in practical terms, have a more general form of the weight $\mathcal{W}^{Q_1^l}$ then the one discussed here.

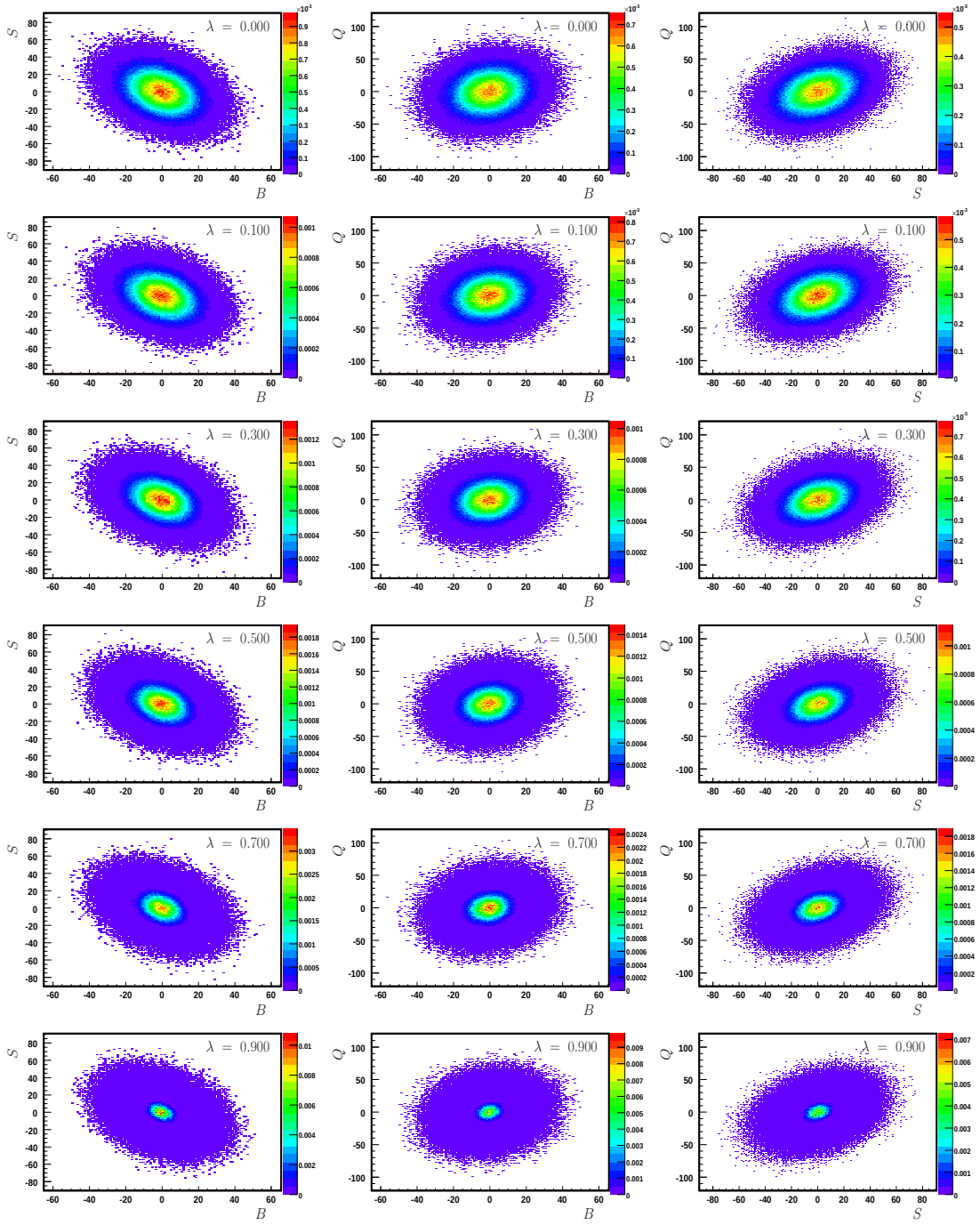

Figure 5.3: Evolution of the joint distribution of baryon number and strangeness, $P_\lambda(B,S)$ (*left*), baryon number and electric charge, $P_\lambda(B,Q)$ (*center*), and strangeness and electric charge, $P_\lambda(S,Q)$ (*right*), with the size of the bath $\lambda = V_1/V_g$. Here $5 \cdot 10^5$ events have been sampled for each value of λ.

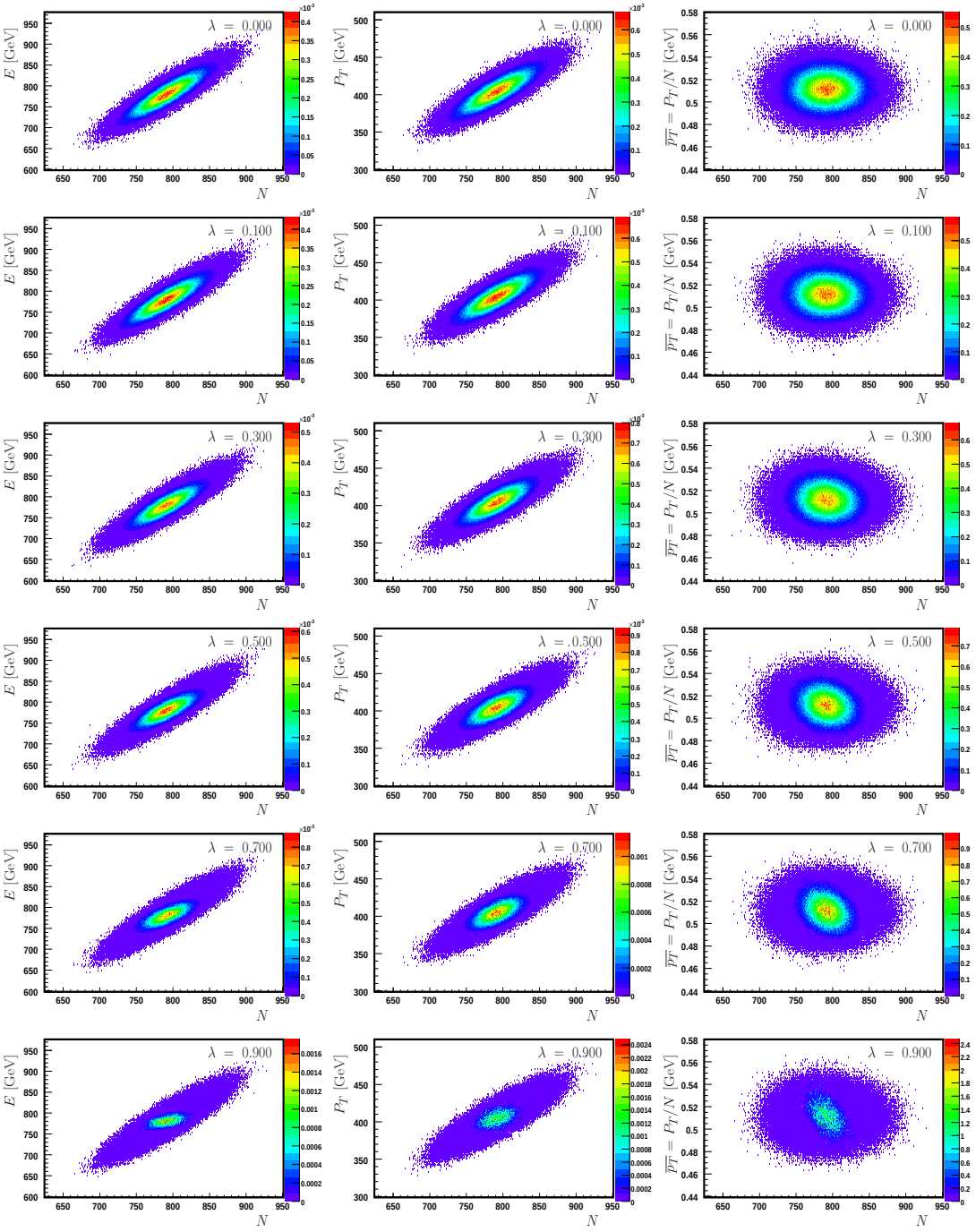

Figure 5.4: Evolution of the joint distributions of energy and particle number, $P_\lambda(E, N)$ (*left*), particle number and transverse momentum, $P_\lambda(N, P_T)$ (*center*), and particle number and mean transverse momentum, $P_\lambda(N, \overline{p_T})$ (*right*), with the size of the bath $\lambda = V_1/V_g$. Here $5 \cdot 10^5$ events have been sampled for each value of λ.

reduced. In direction of energy the distribution gets successively narrower, while retaining some width along the particle number direction. Along the way, the correlation coefficient for finite size of the bath changes. Therefore, the correlation coefficient $\rho_{EN} \to 0$ as $\lambda \to 1$.

Finally, distributions with neither quantity being re-weighted are considered. The distributions of particle number and total transverse momentum $P_\lambda(N, P_T)$, Fig.(5.4) (*center*), and of particle number versus mean transverse momentum $P_\lambda(N, \overline{p_T} = P_T/N)$, Fig.(5.4) (*right*), will serve as examples. Although the total transverse momentum P_T is strongly correlated with particle number N in the GCE, the mean transverse momentum $\overline{p_T} = P_T/N$ is not. The more particles are inside a box, the more kinetic energy is contained within its boundaries. Due to the infinite heat bath assumption, individual particle momenta are however un-correlated with each other. Measuring a particle with a certain momentum vector, does not constrain the remaining system in any way or shape. As the size of the bath is now reduced, this does not hold true anymore. The total transverse momentum is still positively correlated with particle number, yet weaker as $\lambda \to 1$. The mean transverse momentum distribution makes this rather plain. At fixed energy, the larger the particle multiplicity, the more the energy goes into mass, and the less energy into thermal motion, or vice versa. The correlation coefficient is hence negative $\rho_{N\overline{p_T}} < 0$, and the more particles are measured in an event, the less kinetic energy the individual particle will carry on average. Please note, that although the distribution $P_\lambda(N, \overline{p_T})$ changes, neither of the mean values does; $\langle N \rangle$ and $\langle \overline{p_T} \rangle$ stay constant. The expectation value of mean transverse momentum at fixed particle number $\langle \overline{p_T} \rangle_N$, obtained from the conditional distribution $P(\overline{p_T}|N)$, however, decreases as N increases.

5.3 Monte Carlo Weight Factor

The Monte Carlo sample was therefore successively transformed. With decreasing size of the bath, $\lambda \to 1$, larger and larger weight is given to events in the immediate vicinity of the equilibrium expectation value, and smaller and smaller weight to events away from it. The distribution of extensive quantities considered for re-weighting (a multivariate normal distribution in the GCE in the large volume limit) hence gets contracted to a δ-function with vanishing variances and

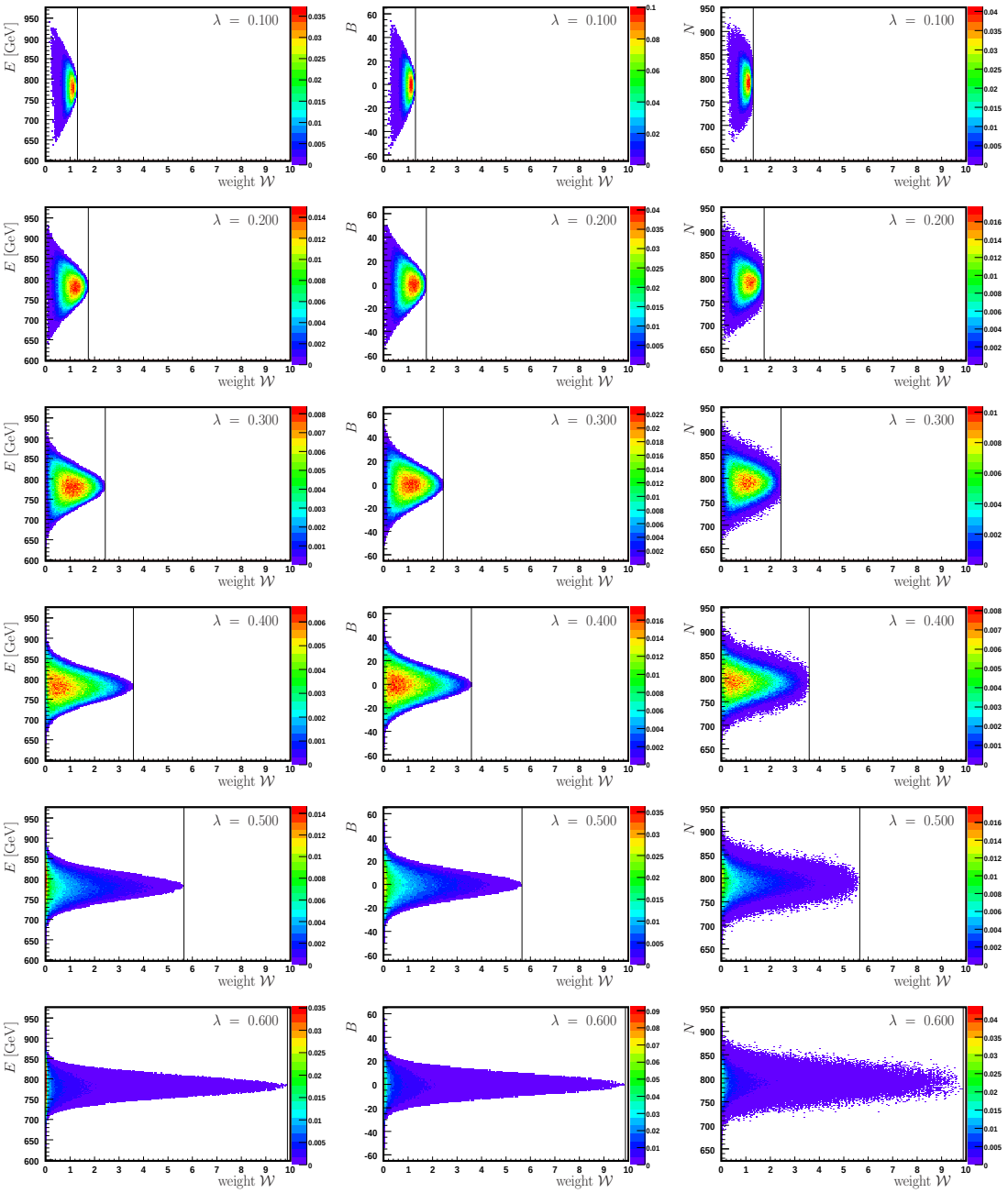

Figure 5.5: Evolution of the weight factor distribution with the size of the bath $\lambda = V_1/V_g$. The occurrence of certain weight factors is shown with the value of the extensive quantities energy E (*left*), baryon number B (*center*), and particle number N (*right*). The extensive quantities B, S, Q, E, P_z are considered for re-weighting. Here $5 \cdot 10^5$ events have been sampled for each value of λ. The solid vertical lines indicate the maximal weight $w_n^{max} = (1-\lambda)^{-L/2}$.

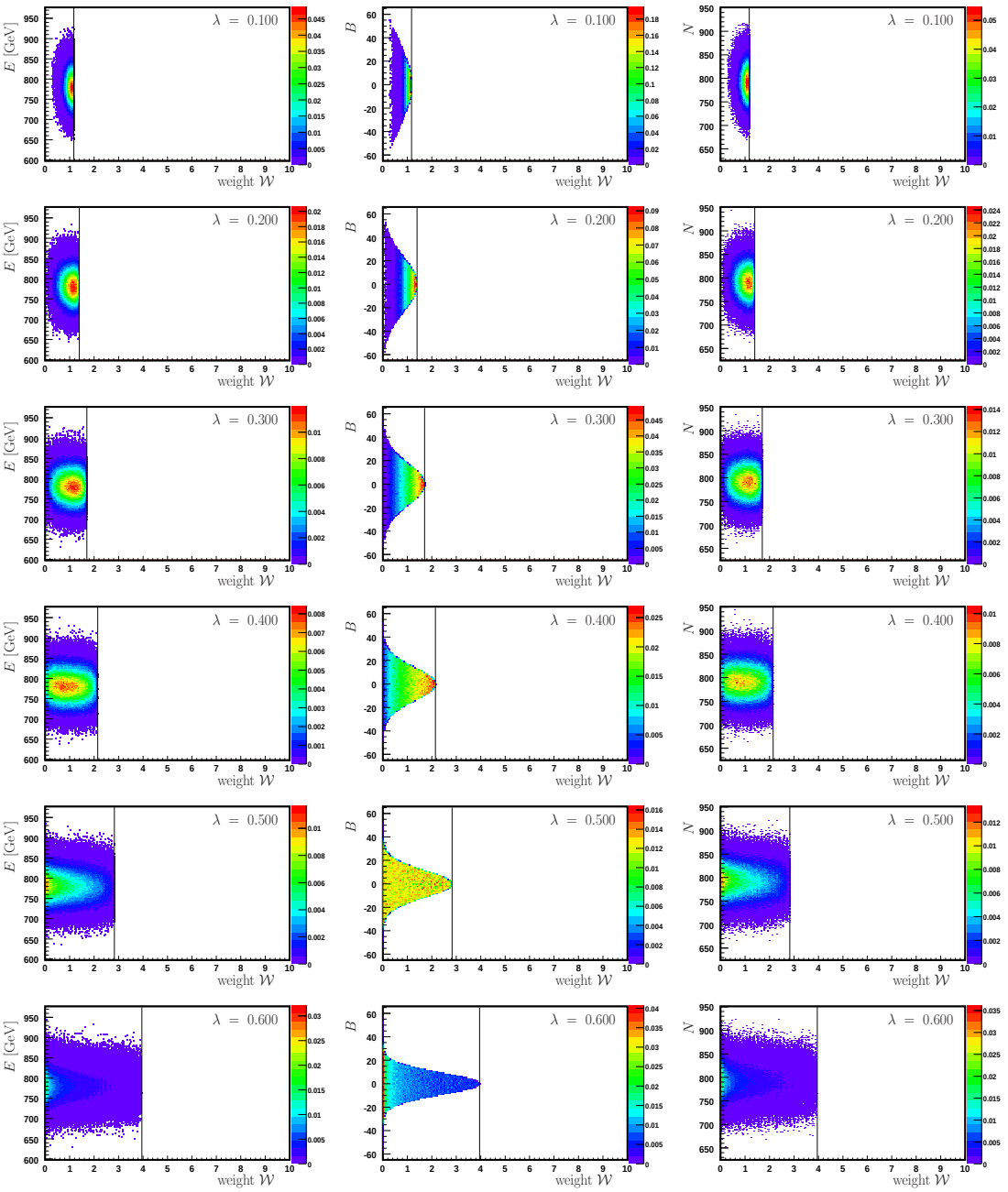

Figure 5.6: Evolution of the weight factor distribution with the size of the bath $\lambda = V_1/V_g$. The occurrence of certain weight factors is shown with the value of the extensive quantities energy E (*left*), baryon number B (*center*), and particle number N (*right*). Only the extensive quantities B, S, Q are considered for re-weighting. Here $5 \cdot 10^5$ events have been sampled for each value of λ. The solid vertical lines indicate the maximal weight $w_n^{max} = (1-\lambda)^{-L/2}$.

covariances. I.e., successively the properties of events which have very similar values of extensive quantities are highlighted. This will have a bearing on charge correlations and, in particular, multiplicity fluctuations and correlations which will be discussed in the following sections.

Considering the evolution of the weight factor distribution with the size of the bath $\lambda = V_1/V_g$, Fig.(5.5) shows the occurrence of certain weight factors w_n, Eq.(3.45), with the value of the extensive quantities energy $E_{1,n}$ (*left*), baryon number $B_{1,n}$ (*center*), and particle number $N_{1,n}$ (*right*).

In the GCE, $\lambda = 0$ all events have weight equal to unity as discussed in Chapter 3. In the limit $\lambda \to 1$, i.e. approaching the MCE, one finds for quantities which are re-weighted, that basically all events have weight equal to 0, except for those in the immediate vicinity of the equilibrium value. Not all events with the same value of energy $E_{1,n}$ receive the same weight $\mathcal{W}_n^{Q_1^l;Q_g^l}$. The energy value might be close to the peak. If the baryon number (and strangeness, longitudinal momentum, etc.) value are now also close to their equilibrium values, the events obtain a higher weight, if the baryon value is far away, a lower weight. The largest weight an event can assume is, Eq.(3.28), $w_n^{max} = (1-\lambda)^{-L/2}$. For intermediate λ a small hill, where most events are located, emerges. As λ is increased most events receive smaller and smaller weight and this small hill gets pushed to the left. The evolution of the baryon number distribution, Fig.(5.5) (*center*) is similar.

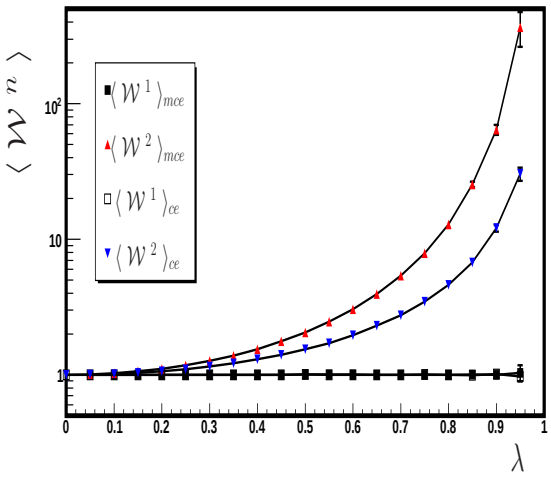

Figure 5.7: First and second moment of the weight factor Eq.(3.28) as a function of λ. The rest as in Fig.(5.1).

The extensive quantity particle number is not re-weighted. Hence its distribution does not converge to a δ-function. The connection between the extensive quantity N and other (re-weighted) quantities manifests itself indirectly. Events have certain energy, baryon number or strangeness. These quantities are correlated with particle number. Events with unusually large or small multiplicities

now receive mostly small weight factors, because chance has it, that they also have values of energy, net-baryon number or net-strangeness which are far from the equilibrium expectation value. But even in the limit $\lambda \to 1$ a certain width remains, and no sharp tip forms, as particle number continues to fluctuate in the MCE. In Fig.(5.7) the second moment of the weight factor, Eq.(3.28) is shown as a function of λ for both the extrapolation to the MCE and to the CE. A large second moment $\langle \mathcal{W}^2 \rangle$ implies a large statistical uncertainty and, hence, usually requires a larger sample.

For comparison, the evolution of weight factors for an extrapolation to the CE limit is presented in Fig.(5.6). Events are re-weighted only according to the values of their extensive quantities baryon number $B_{1,n}$, strangeness $S_{1,n}$, and electric charge $Q_{1,n}$. As in Fig.(5.5), the distributions for the extensive quantities energy E, baryon number B, and particle multiplicity N are shown for different values of λ. The energy distribution, Fig.(5.6) (*left*), is much wider than the one in Fig.(5.5) (*left*). The systems energy content continues to fluctuate, $\langle (\Delta E) \rangle \neq 0$, in the CE. The baryon number distribution Fig.(5.6) (*center*) on the other hand converges, as in the MCE, to a δ-function. The particle number distribution Fig.(5.6) (*right*) is then also wider than for an extrapolation to the MCE, Fig.(5.5) (*right*). The last observation is that, indeed, the maximal weight w_n^{max} an event can receive (at some fixed value of λ) is smaller for the extrapolation to the CE, Fig.(5.6), than for an extrapolation to the MCE, Fig.(5.5).

5.4 Discussion

In this chapter fully phase space integrated grand canonical results have been extrapolated to the micro canonical limit. For this purpose samples of events for various values of $\lambda = V_1/V_g$ have been iteratively generated, re-weighted, and analyzed. By construction of the weight factor $\mathcal{W}$ the extrapolation proceeds in a systematic fashion such that, for instance, particle momentum spectra, as well as mean values of extensive quantities, remain unchanged.

The GCE distribution of extensive quantities considered for re-weighting converges to a δ-function. Mean values as well as correlation coefficients stay constant, while variances and covariances converge to 0. Events in the vicinity of the equilibrium expectation value are projected out, the rest is suppressed.

Although the extensive quantities particle multiplicity N and total transverse momentum P_T are not re-weighted, their fluctuations and correlations are nevertheless strongly affected. The effects of decreasing size of the heat bath emerge because N and P_T are correlated with E, Q, etc., which are re-weighted.

As the system under investigation gets larger, a smaller fraction of events will have values of $E_{1,n}$,$B_{1,n}$, $Q_{1,n}$, etc. in the vicinity of a desired equilibrium value, and the straight sample and reject method becomes ever more inefficient. This method can handle large system sizes, due to additional information obtained from the extrapolation. However, as λ grows, so too does the statistical uncertainty. In the limit $\lambda \rightarrow 1$, one approaches a sample-reject type of formalism. One cannot, therefore, directly obtain the micro canonical limit for the large system size studied here, as this is prohibited by available computing power. However, extrapolation to this limit is possible. It is pointed out in this context that the intermediate ensembles, between the limits of GCE and MCE, may be of phenomenological interest, too.

Chapter 6

Multiplicity Fluctuations and Correlations

In this chapter joint multiplicity distributions of charged hadrons are analyzed in different ensembles with limited acceptance in momentum space assumed. Multiplicity fluctuations and correlations are qualitatively affected by the choice of ensemble and are directly sensitive to the fraction of the system observed. For vanishing size of ones acceptance window, one would lose all information on how the multiplicities of any two distinct groups N_i and N_j of particles are correlated, and measure $\rho_{ij} = 0$. This information, on the other hand, is to some extent preserved in ρ_{BS}, ρ_{BQ}, and ρ_{SQ}, i.e. the way in which quantum numbers are correlated, if at least occasionally a particle is detected during an experiment.

The Monte Carlo scheme is employed further. In Section 6.1, the joint distributions of positively and negatively charged particles in momentum bins $\Delta p_{T,i}$ and Δy_i are constructed. Then, in turn, primordial and final state GCE results on the scaled variance ω, Eq.(3.50), and the correlation coefficient ρ, Eq.(3.49), are extrapolated to the MCE limit in Section 6.2. To complement the above study of micro canonical effects, canonical (charge conservation) effects on final state multiplicity fluctuations are studied in Section 6.3. Further discussion of MCE effects is presented in Chapter 7.

6.1 Grand Canonical Ensemble

In Fig.(6.1) the $\Delta p_{T,i}$ (*left*) and Δy_i (*right*) dependence of the GCE scaled variance ω_+ of positively charged hadrons are shown, both primordial and final state. In the primordial Boltzmann case one finds no dependence of multiplicity fluctuations on the position and size of the acceptance window. The observed multiplicity distribution is, within error bars, a Poissonian with scaled variance $\omega_+ = 1$. In fact, in the primordial GCE Boltzmann case any selection of particles has $\omega = 1$, as particle multiplicity, as well as momenta, are sampled independently.

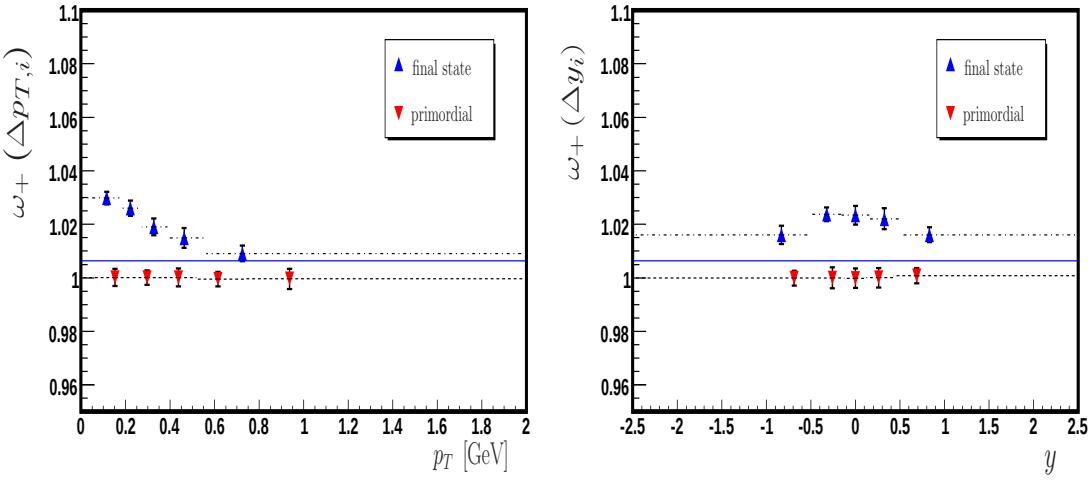

Figure 6.1: GCE scaled variance ω_+ of multiplicity fluctuations of positively charged hadrons, both primordial and final state, in transverse momentum bins $\Delta p_{T,i}$ (*left*) and rapidity bins Δy_i (*right*). Horizontal error bars indicate the width and position of the momentum bins (And not an uncertainty!). Vertical error bars indicate the statistical uncertainty of 20 Monte Carlo runs of $2 \cdot 10^5$ events each. The markers indicate the center of gravity of the corresponding bin. The solid line indicates the final state acceptance scaling estimate.

Fig.(6.2) shows the $\Delta p_{T,i}$ (*left*) and Δy_i (*right*) dependence of the GCE correlation coefficient ρ_{+-} between positively and negatively charged hadrons, both primordial and final state. In the primordial Boltzmann case one finds also no dependence of multiplicity correlations on the position and size of the acceptance window. The observed joint multiplicity distribution is a product of two Poissonians with correlation coefficient $\rho_{+-} = 0$.

Fig.(6.3) presents the $\Delta p_{T,i}$ (*left*) and Δy_i (*right*) dependence of the GCE

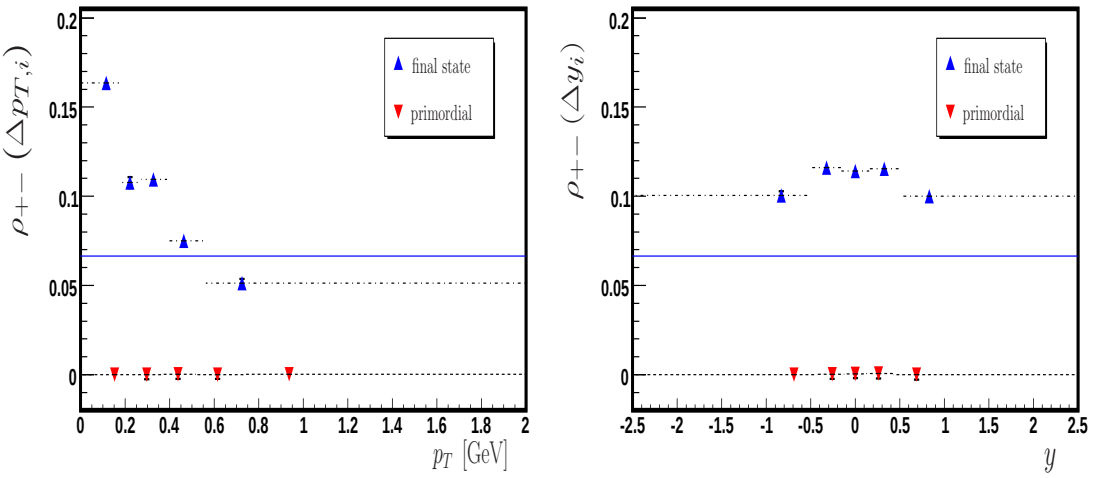

Figure 6.2: GCE multiplicity correlations ρ_{+-} between positively and negatively charged hadrons, both primordial and final state, in transverse momentum bins $\Delta p_{T,i}$ (*left*) and rapidity bins Δy_i (*right*). The rest as in Fig.(6.1).

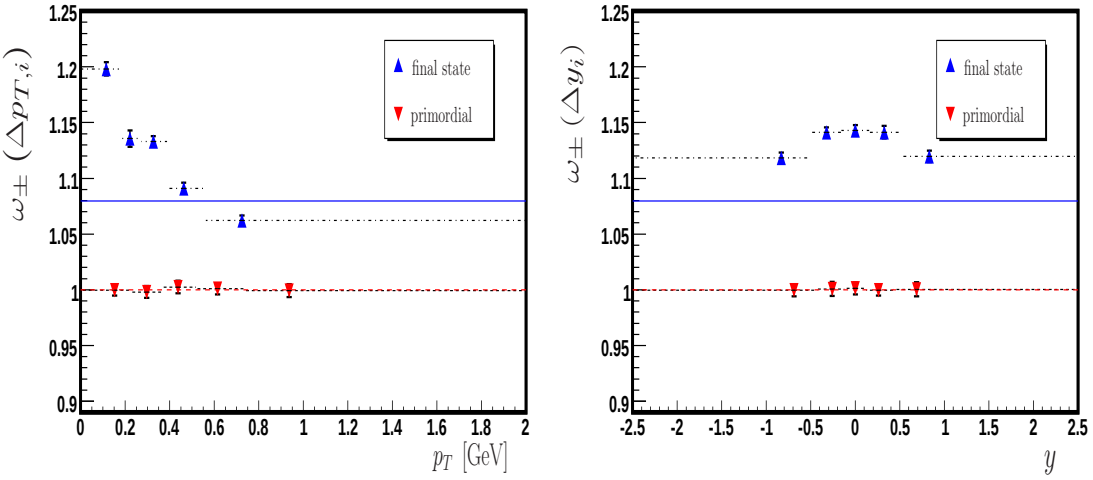

Figure 6.3: GCE scaled variance $\omega_{\pm}$ of multiplicity fluctuations of all charged hadrons, both primordial and final state, in transverse momentum bins $\Delta p_{T,i}$ (*left*) and rapidity bins Δy_i (*right*). The rest as in Fig.(6.1).

scaled variance $\omega_{\pm}$ of all charged hadrons, both primordial and final state. As the correlation coefficient between positively and negatively charged hadrons is $\rho_{+-} = 0$ in the primordial GCE one also finds $\omega_{\pm} = \omega_{+} = 1$.

Resonance decay is the only source of correlation in an ideal GCE Boltzmann gas. Neutral hadrons decaying into two hadrons of opposite electric charge are the strongest contributors to the correlation coefficient ρ_{+-}. The chance that

both (oppositely charged) decay products are dropped into the same momentum space bin is obviously highest at low transverse momentum (i.e. the correlation coefficient is strongest in $\Delta p_{T,1}$). The rapidity dependence is somewhat milder again, because heavier particles (parents) are dominantly produced around mid-rapidity and spread their daughter particles over a range in rapidity. One notes that the scaled variances and correlation coefficients in the respective acceptance bins in Figs.(6.1,6.2) are generally larger than the acceptance scaling procedure[1] suggests, with the notable exception of $\rho_{+-}(\Delta p_{T,5})$.

There is a simple relation connecting the scaled variance of the fluctuations of all charged hadrons $\omega_{\pm}$ to the fluctuations of only positively charged particles ω_{+} via the correlation coefficient ρ_{+-} between positively and negatively charged hadrons in a neutral system:

$$\omega_{\pm} \; = \; \omega_{+} \; (1 \; + \; \rho_{+-}) \, . \tag{6.1}$$

The contribution of neutral parent particles to $\omega_{\pm}$ is stronger than to ω_{+}, as both oppositely charged decay products go into the analysis rather than just one of them. Therefore, the effects of resonance decay on the $\Delta p_{T,i}$ dependence of $\omega_{\pm}$ are considerably enhanced compared to the one of ω_{+}, and generally $\omega_{\pm} > \omega_{+}$, as the correlation coefficient ρ_{+-} remains positive in the final state GCE, in Fig.(6.3). Compared to this, the final state values of $\omega_{\pm}$, ω_{+} and ρ_{+-} remain rather flat with Δy_i in the GCE.

If one would construct now a larger and larger number of momentum space bins of equal average particle multiplicities, one would successively lose more and more information about how multiplicities of distinct groups of particles are correlated, and approach the Poissonian limit also for final state particles.

6.2 Micro Canonical Ensemble

In the very same way in which fully phase space integrated extensive quantities were extrapolated to the MCE limit in Chapter 5, now multiplicity fluctuations ω_{+} and correlations ρ_{+-} in transverse momentum bins $\Delta p_{T,i}$ and rapidity bins Δy_i for a hadron resonance gas are extrapolated from the GCE ($\lambda = 0$) to the MCE

[1] For the acceptance scaling approximation it is assumed that particles are randomly detected with a certain probability $q = 0.2$, independent of their momentum.

($\lambda \to 1$). Analytical primordial MCE results are obtained in the infinite volume approximation [106, 127], providing some guidance as to asses the accuracy of the extrapolation scheme. For final state fluctuations and correlations in limited acceptance, on the other hand, no analytical results are available.

Mean values of particle numbers of positively charged hadrons $\langle N_+ \rangle$ and negatively charged hadrons $\langle N_- \rangle$ in the respective acceptance bins, defined in Table 4.1, remain constant as λ goes from 0 to 1, while the variances $\langle (\Delta N_+)^2 \rangle$ and $\langle (\Delta N_-)^2 \rangle$, and covariance $\langle \Delta N_+ \Delta N_- \rangle$ converge linearly to their respective MCE limits. The correlation coefficient ρ_{+-} between positively and negatively charged hadrons, on the other hand, will not approach its MCE value linearly, as discussed in Chapter 5.

Primordial

In Fig.(6.4) the primordial scaled variance ω_+ of positively charged hadrons in transverse momentum bins $\Delta p_{T,i}$ (*left*) and rapidity bins Δy_i (*right*) is shown as a function of the size of the bath $\lambda = V_1/V_g$, while in Fig.(6.5) the dependence of the primordial correlation coefficient ρ_{+-} between positively and negatively charged hadrons in transverse momentum bins $\Delta p_{T,i}$ (*left*) and rapidity bins Δy_i (*right*) is presented as a function of λ.

The results of $8 \cdot 20$ Monte Carlo runs of $2 \cdot 10^5$ events each are summarized in Table 6.1. The system sampled was assumed to be neutral $\mu_j = (0, 0, 0)$ and static $u_\mu = (1, 0, 0, 0)$ with local temperature $\beta^{-1} = 0.160$ GeV and a system volume of $V_1 = 2000$ fm^3. 8 different values of λ have been studied. The last marker ($\lambda = 1$) denotes the result of the extrapolation. Only primordial hadrons are analyzed. Values for both $\Delta p_{T,i}$ and Δy_i bins are listed. Analytical numbers are calculated according to the method developed in [106, 127], using the acceptance bins defined in Table 4.1, and are shown for comparison. The effects of energy-momentum and charge conservation on primordial multiplicity fluctuations and correlations in finite acceptance will also be discussed in Chapter 7.

Firstly fully phase space integrated results, also later discussed in Chapters 8 and 9, are attended to. The scaled variance of multiplicity fluctuations is lowest in the MCE due to the requirement of exact energy and charge conservation, somewhat larger in the CE (see also Section 6.2), and largest in the GCE, as now all constraints on the micro states of the system have been dropped [101, 103, 105].

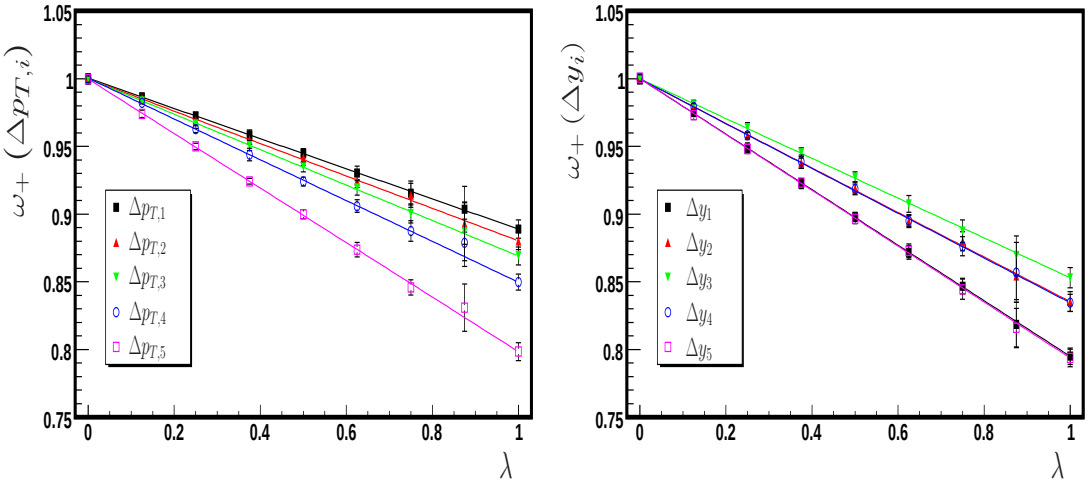

Figure 6.4: Evolution of the primordial scaled variance ω_+ of positively charged hadrons with the Monte Carlo parameter $\lambda = V_1/V_g$ for transverse momentum bins $\Delta p_{T,i}$ (*left*) and for rapidity bins Δy_i (*right*). The solid lines show an analytic extrapolation from GCE results ($\lambda = 0$) to the MCE limit ($\lambda \to 1$). Each marker and its error bar, except the last, represents the result of 20 Monte Carlo runs of $2 \cdot 10^5$ events. 8 different equally spaced values of λ have been investigated. The last marker denotes the result of the extrapolation.

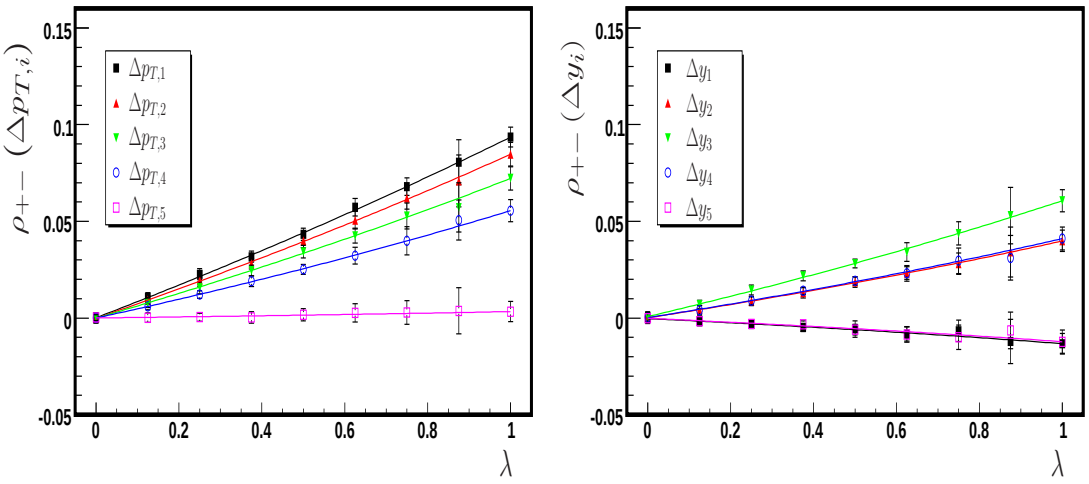

Figure 6.5: Evolution of the primordial correlation coefficient ρ_{+-} between positively and negatively charged hadrons with the Monte Carlo parameter $\lambda = V_1/V_g$ for transverse momentum bins $\Delta p_{T,i}$ (*left*) and for rapidity bins Δy_i (*right*). The rest as in Fig.(6.4).

The fully phase space integrated MCE and CE correlation coefficients between oppositely charged particles are rather close to 1. Doubly charged particles allow

for mild deviation, as also the Δ^{++} resonance is counted as only one particle.

Primordial	$\Delta p_{T,1}$	$\Delta p_{T,2}$	$\Delta p_{T,3}$	$\Delta p_{T,4}$	$\Delta p_{T,5}$
ω_+^{gce}	1.000 ± 0.002	1.000 ± 0.002	1.000 ± 0.002	1.000 ± 0.002	1.000 ± 0.002
ω_+^{mce}	0.889 ± 0.007	0.880 ± 0.007	0.869 ± 0.007	0.850 ± 0.006	0.798 ± 0.007
$\omega_+^{mce,c}$	0.8886	0.8802	0.8682	0.8489	0.7980
ρ_{+-}^{gce}	0.000 ± 0.002	-0.000 ± 0.002	-0.000 ± 0.002	0.000 ± 0.002	0.000 ± 0.001
ρ_{+-}^{mce}	0.094 ± 0.005	0.085 ± 0.006	0.072 ± 0.006	0.056 ± 0.006	0.003 ± 0.005
$\rho_{+-}^{mce,c}$	0.0935	0.0844	0.0730	0.0554	0.0040
Primordial	Δy_1	Δy_2	Δy_3	Δy_4	Δy_5
ω_+^{gce}	1.000 ± 0.002	1.000 ± 0.002	1.000 ± 0.003	1.000 ± 0.002	1.000 ± 0.002
ω_+^{mce}	0.795 ± 0.006	0.835 ± 0.007	0.853 ± 0.008	0.834 ± 0.006	0.794 ± 0.007
$\omega_+^{mce,c}$	0.7950	0.8350	0.8521	0.8351	0.7949
ρ_{+-}^{gce}	-0.000 ± 0.001	0.000 ± 0.002	0.001 ± 0.002	0.000 ± 0.002	-0.000 ± 0.002
ρ_{+-}^{mce}	-0.013 ± 0.005	0.040 ± 0.006	0.061 ± 0.006	0.041 ± 0.006	-0.012 ± 0.006
$\rho_{+-}^{mce,c}$	-0.0135	0.0406	0.0616	0.0406	-0.0135

Table 6.1: Summary of the primordial scaled variance ω_+ of positively charged hadrons and the correlation coefficient ρ_{+-} between positively and negatively charged hadrons in transverse momentum bins $\Delta p_{T,i}$ and rapidity bins Δy_i. Both the GCE result ($\lambda = 0$) and the extrapolation to MCE ($\lambda = 1$) are shown. The uncertainty quoted corresponds to 20 Monte Carlo runs of $2 \cdot 10^5$ events (GCE) or is the result of the extrapolation (MCE). Analytic MCE results $\omega_+^{mce,c}$ and $\rho_{+-}^{mce,c}$ are listed too.

The transverse momentum dependence can be understood as follows: a change in particle number at high transverse momentum involves a large amount of energy, i.e., in order to balance the energy record, one needs to create (or annihilate) either a lighter particle with more kinetic energy, or two particles at lower p_T. This leads to suppressed multiplicity fluctuations in high $\Delta p_{T,i}$ bins compared to low $\Delta p_{T,i}$ bins. By the same argument, it seems favorable, due to the constraint of energy and charge conservation, to balance electric charge, by creating (or annihilating) pairs of oppositely charged particles, predominantly in lower $\Delta p_{T,i}$ bins, while allowing for a more un-correlated multiplicity distribution, i.e. also larger net-charge ($\delta Q = N_+ - N_-$) fluctuations, in higher $\Delta p_{T,i}$ bins.

For the rapidity dependence similar arguments hold. Here, however, the strongest role is played by longitudinal momentum conservation. A change in particle number at high y involves now, in addition to a large amount of energy, a large momentum p_z to be balanced. The constraints of global P_z conservation

are, hence, felt least severely around $|y| \sim 0$, and it becomes favorable to balance charge predominantly at mid-rapidity (ρ_{+-} larger) and to allow for stronger multiplicity fluctuations (ω_+ larger) compared to forward and backward rapidity bins.

In a somewhat casual way one could say: events of a neutral hadron resonance gas with values of extensive quantities B, S, Q, E and P_z in the vicinity of $\langle \mathcal{Q}_1^l \rangle$ have a tendency to have similar numbers of positively and negatively charged particles at low transverse momentum p_T and rapidity y and less strongly so at high p_T and $|y|$.

Final State

Now the extrapolation of final state multiplicity fluctuations and correlations to the MCE limit is attended to. An independent Monte Carlo run for the same physical system was done, but now with only stable final state particles 'detected'.

In Fig.(6.6) the final state scaled variance ω_+ of positively charged hadrons in transverse momentum bins $\Delta p_{T,i}$ (*left*) and rapidity bins Δy_i (*right*) is shown as a function of λ, while in Fig.(6.7) the dependence of the final state correlation coefficient ρ_{+-} between positively and negatively charged hadrons in transverse momentum bins $\Delta p_{T,i}$ (*left*) and rapidity bins Δy_i (*right*) on the size of the bath $\lambda = V_1/V_g$ is shown.

The $\Delta p_{T,i}$ and Δy_i dependence on λ of the final state MCE scaled variance ω_+ is qualitatively similar to that of the primordial versions, Fig.(6.4), and is essentially also explained by the arguments of the previous section. The effects of charge and energy-momentum conservation work very much the same way as before, and it still seems favorable to have events with wider multiplicity distributions at low p_T and low y, and more narrow distributions at larger p_T and larger $|y|$. The dependence of the final state correlation coefficients ρ_{+-} on λ, Fig.(6.7), is a slightly different to the primordial case, Fig.(6.5). However, in the MCE limit, events still tend to have more similar numbers of oppositely charged particles at low p_T and low y, than at large p_T and large $|y|$.

The effects of resonance decay are qualitatively different in the MCE, CE, and GCE (see also Section 6.3). Again, firstly attending to fully phase space integrated multiplicity fluctuations discussed in [103, 101] and Chapter 9. The final state scaled variance increases in the GCE and CE compared to the primordial

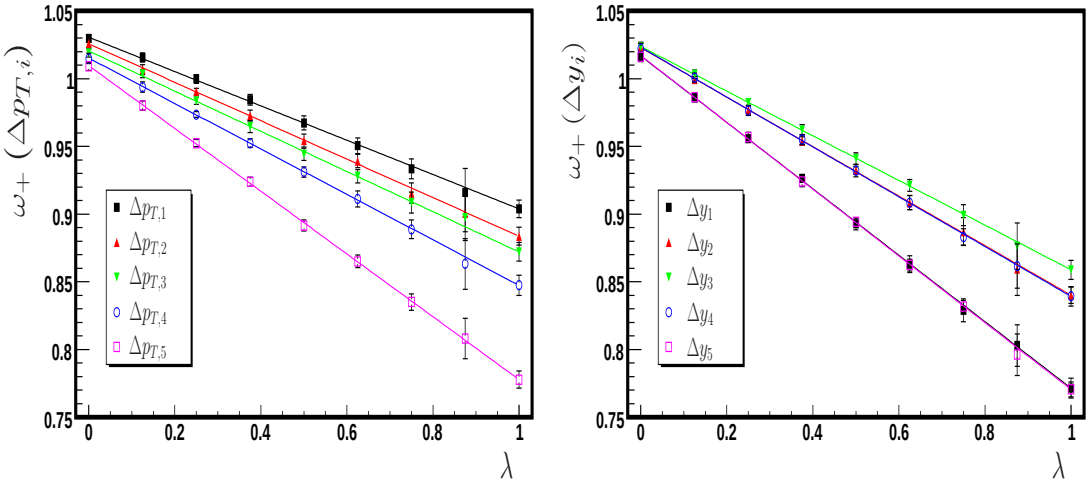

Figure 6.6: Evolution of the final state scaled variance ω_+ of positively charged hadrons with the Monte Carlo parameter $\lambda = V_1/V_g$ for transverse momentum bins $\Delta p_{T,i}$ (*left*) and for rapidity bins Δy_i (*right*). The solid lines show an analytic extrapolation from GCE results ($\lambda = 0$) to the MCE limit ($\lambda \to 1$). Each marker, except the last, represents the result of 20 Monte Carlo runs of $2 \cdot 10^5$ events. 8 different equally spaced values of λ have been investigated. The last marker denotes the result of the extrapolation.

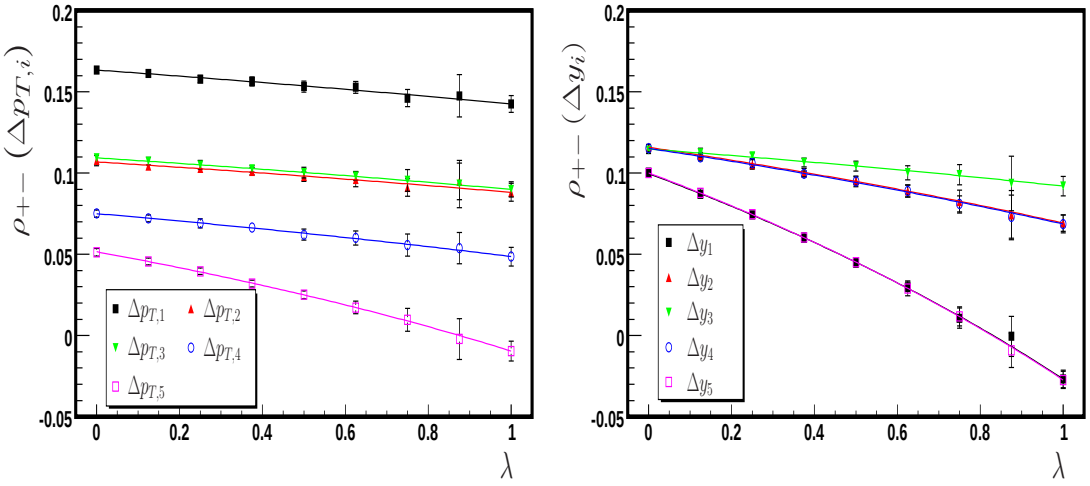

Figure 6.7: Evolution of the final state correlation coefficient ρ_{+-} between positively and negatively charged hadrons with the Monte Carlo parameter $\lambda = V_1/V_g$ for transverse momentum bins $\Delta p_{T,i}$ (*left*) and for rapidity bins Δy_i (*right*). The rest as in Fig.(6.6).

scaled variance. Multiplicity fluctuations of neutral mesons remain unconstrained by (charge) conservation laws. However, they often decay into oppositely charged

particles, which increases multiplicity fluctuations of pions, for instance. In the MCE, due to the constraint of energy conservation, the event-by-event fluctuations of primordial pions are correlated to the event-by-event fluctuations of, in general, primordial parent particles, and $\omega^{final} < \omega^{prim}$ is possible in the MCE.

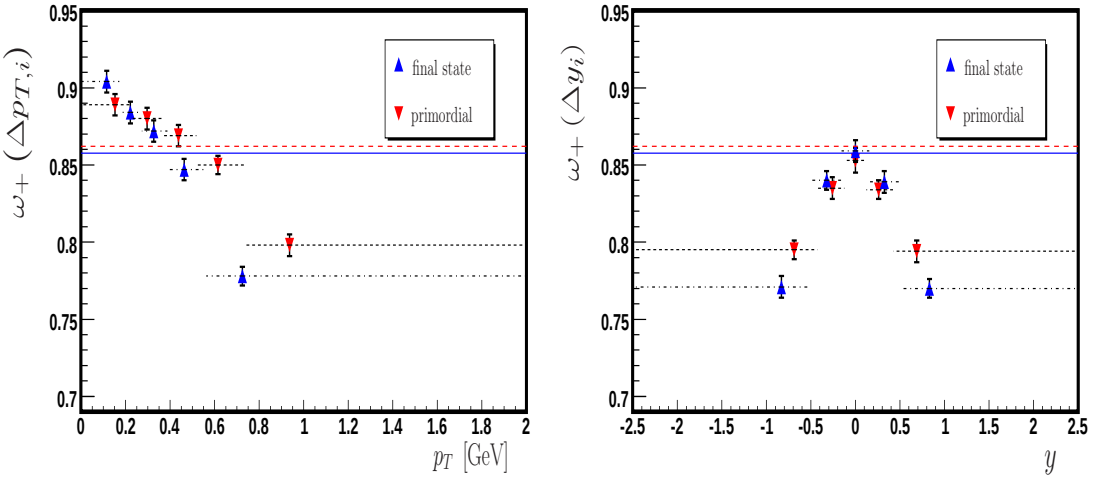

Figure 6.8: MCE scaled variance ω_+ of multiplicity fluctuations of positively charged hadrons, both primordial and final state, in transverse momentum bins $\Delta p_{T,i}$ (*left*) and rapidity bins Δy_i (*right*). Horizontal error bars indicate the width and position of the momentum bins (And not an uncertainty!). Vertical error bars indicate the statistical uncertainty quoted in Table 6.2. The markers indicate the center of gravity of the corresponding bin. The solid and the dashed lines show final state and primordial acceptance scaling estimates respectively.

Figs.(6.8-6.10) compare the final state $\Delta p_{T,i}$ (*left*) and Δy_i (*right*) dependence of the MCE scaled variance of positively charged hadrons ω_+, the MCE correlation coefficient between positively and negatively charged hadrons ρ_{+-}, and the MCE scaled variance of all charged hadrons $\omega_\pm$, respectively to their primordial counterparts. The results of $8 \cdot 20$ Monte Carlo runs of $2 \cdot 10^5$ events each for a static and neutral hadron resonance gas with $T = 0.160$ GeV are summarized in Table 6.2.

A few words to summarize Figs.(6.8-6.10): resonance decay and (energy) conservation laws work in the same direction, as far as the transverse momentum dependence of the scaled variances ω_+, $\omega_\pm$ and the correlation coefficient ρ_{+-} is concerned. Both effects lead to increased multiplicity fluctuations and an increased correlation between the multiplicities of oppositely charged particles in the low p_T region, compared to the high p_T domain. Compared to this, the

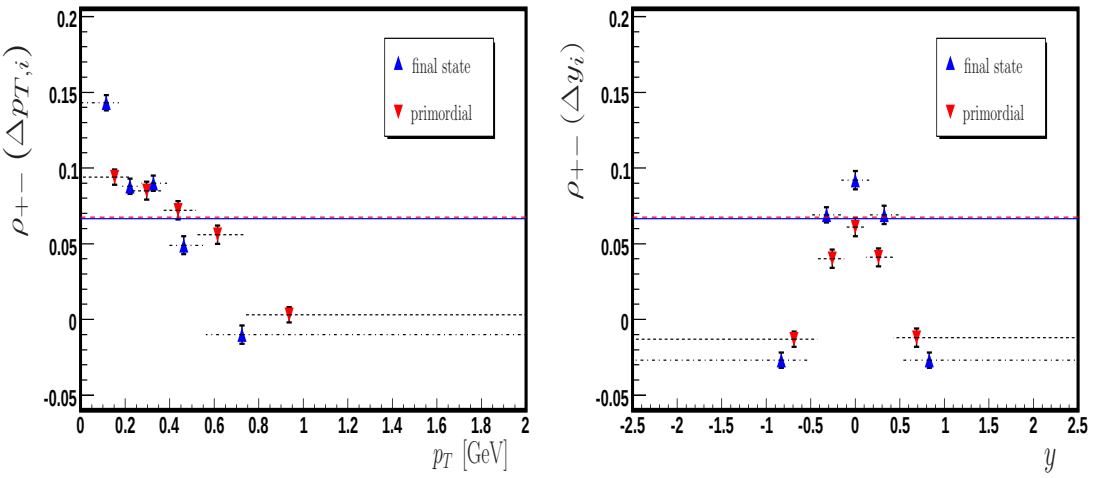

Figure 6.9: MCE multiplicity correlation coefficient ρ_{+-} between positively and negatively charged hadrons, both primordial and final state, in transverse momentum bins $\Delta p_{T,i}$ (*left*) and rapidity bins Δy_i (*right*). The rest as in Fig.(6.8).

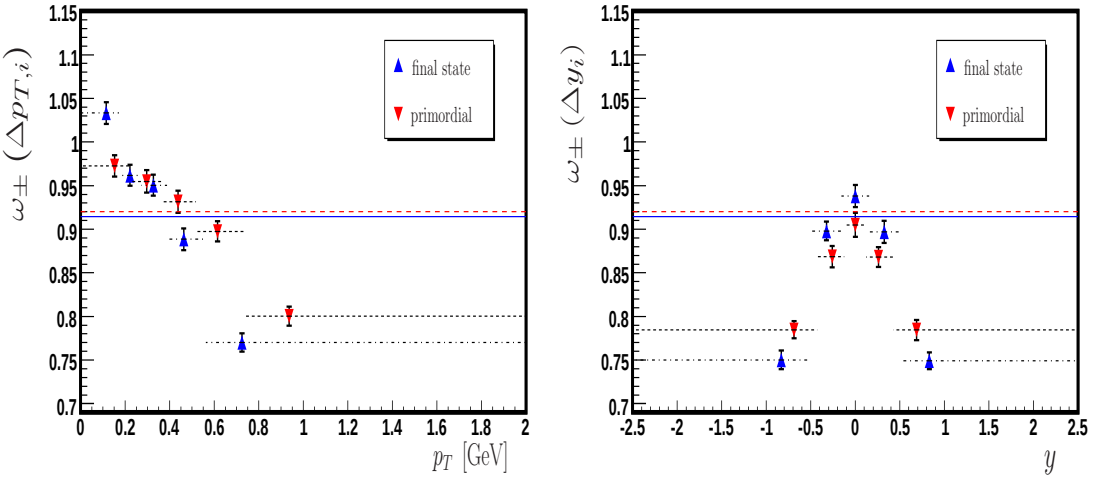

Figure 6.10: MCE scaled variance $\omega_{\pm}$ of multiplicity fluctuations of all charged hadrons, both primordial and final state, in transverse momentum bins $\Delta p_{T,i}$ (*left*) and rapidity bins Δy_i (*right*). The rest as in Fig.(6.8).

MCE Δy_i dependence of ω_+, ρ_{+-}, and $\omega_{\pm}$ is mainly dominated by global conservation of P_z. Resonance decay effects, see also the GCE versions, Figs.(6.1-6.3), act more equal across rapidity, than in transverse momentum.

Again, the scaled variance of all charged particles is found to be larger than the scaled variance of only positively charged hadrons $\omega_{\pm} > \omega_+$, except for when $\rho_{+-} < 0$, i.e when the multiplicities of oppositely charged particles are

Final state	$\Delta p_{T,1}$	$\Delta p_{T,2}$	$\Delta p_{T,3}$	$\Delta p_{T,4}$	$\Delta p_{T,5}$
ω_+^{gce}	1.031 ± 0.002	1.026 ± 0.002	1.020 ± 0.002	1.015 ± 0.002	1.010 ± 0.002
ω_+^{mce}	0.904 ± 0.007	0.884 ± 0.007	0.872 ± 0.007	0.847 ± 0.007	0.778 ± 0.006
ρ_{+-}^{gce}	0.163 ± 0.001	0.107 ± 0.001	0.109 ± 0.001	0.075 ± 0.002	0.052 ± 0.002
ρ_{+-}^{mce}	0.143 ± 0.005	0.088 ± 0.005	0.090 ± 0.005	0.049 ± 0.006	-0.010 ± 0.006
Final state	Δy_1	Δy_2	Δy_3	Δy_4	Δy_5
ω_+^{gce}	1.017 ± 0.002	1.023 ± 0.002	1.024 ± 0.002	1.023 ± 0.003	1.017 ± 0.002
ω_+^{mce}	0.771 ± 0.007	0.840 ± 0.006	0.859 ± 0.007	0.839 ± 0.007	0.770 ± 0.006
ρ_{+-}^{gce}	0.100 ± 0.001	0.116 ± 0.001	0.115 ± 0.002	0.115 ± 0.002	0.100 ± 0.001
ρ_{+-}^{mce}	-0.027 ± 0.005	0.069 ± 0.005	0.092 ± 0.006	0.069 ± 0.006	-0.027 ± 0.005

Table 6.2: Summary of the final state scaled variance ω_+ of positively charged hadrons and the correlation coefficient ρ_{+-} between positively and negatively charged hadrons in transverse momentum bins $\Delta p_{T,i}$ and rapidity bins Δy_i. Both the GCE result ($\lambda = 0$) and the extrapolation to the MCE ($\lambda = 1$) are shown. The uncertainty quoted corresponds to 20 Monte Carlo runs of $2 \cdot 10^5$ events (GCE) or is the result of the extrapolation (MCE).

anti-correlated, as for instance in $\Delta p_{T,5}$, Δy_1, and Δy_5. In contrast to that, however narrowly, $\omega_\pm > 1$ in the lowest transverse momentum bin $\Delta p_{T,1}$. Acceptance scaling provides a good estimate of the average in transverse momentum. In rapidity, however the approximation somewhat overshoots the limited acceptance results, pointing to correlations amongst momentum bins, Chapter 7.

6.3 Canonical Ensemble

To complement the discussion of multiplicity fluctuations and correlations for a hadron resonance gas in transverse momentum and rapidity segments, the canonical ensemble limit is studied next. Events will be re-weighted according to their extensive quantities baryon number B, strangeness S, and electric charge Q. Conservation laws for energy E and longitudinal momentum P_z (as well as for transverse momenta P_x and P_y) are hence not applied. Again some guidance for assessing the quality of the extrapolation is provided by analytical methods. Two independent (final state and primordial) Monte Carlo runs of $8 \cdot 20 \cdot 2 \cdot 10^5$ events each have been generated. The same system as before is considered and the same acceptance cuts are applied.

Resonance decay is a process respecting the conservation laws for charge, en-

ergy and momentum. So despite the fact that charge conservation laws do not correlate primordial particle momenta, these additional correlations are introduced into the final state momentum space dependence, as in the GCE.

In Figs.(6.11-6.13) the final state scaled variance ω_+ of positively charged hadrons, the final state correlation coefficient ρ_{+-} between positively and negatively charged hadrons, and the final state scaled variance $\omega_\pm$ of all charged hadrons, in transverse momentum bins $\Delta p_{T,i}$ (*left*) and rapidity bins Δy_i (*right*) are shown as a function of λ. Primordial results are not included.

Figs.(6.14-6.16) compare the final state $\Delta p_{T,i}$ (*left*) and Δy_i (*right*) dependence of the CE scaled variances ω_+, and $\omega_\pm$, and the CE correlation coefficient ρ_{+-} respectively to their primordial counterparts. The results of $8 \cdot 20$ Monte Carlo runs of $2 \cdot 10^5$ events each for a static and neutral hadron resonance gas with temperature $T = 0.160$ GeV are summarized in Table 6.3.

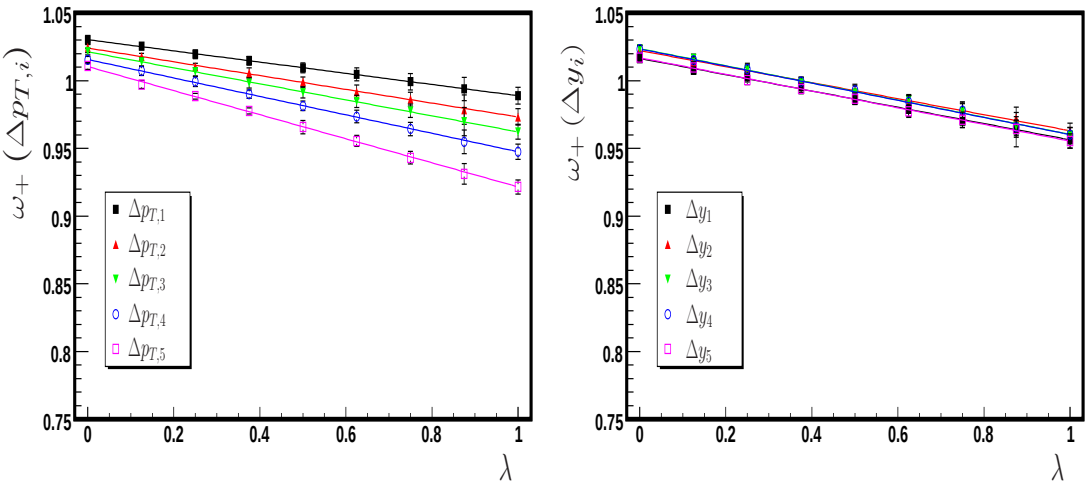

Figure 6.11: Evolution of the final state scaled variance ω_+ of positively charged hadrons with the Monte Carlo parameter $\lambda = V_1/V_g$ for transverse momentum bins $\Delta p_{T,i}$ (*left*) and for rapidity bins Δy_i (*right*). The solid lines show an analytic extrapolation from GCE results ($\lambda = 0$) to the CE limit ($\lambda \to 1$). Each marker, except the last, represents the result of 20 Monte Carlo runs of $2 \cdot 10^5$ events. 8 different equally spaced values of λ have been investigated. The last marker denotes the result of the extrapolation.

Firstly the primordial scenario is considered. Charge conservation does not introduce any correlations in momentum space. Primordial results are thus independent of where in momentum space the acceptance window is located. Only the fraction of the system observed matters. One therefore finds the scaled vari-

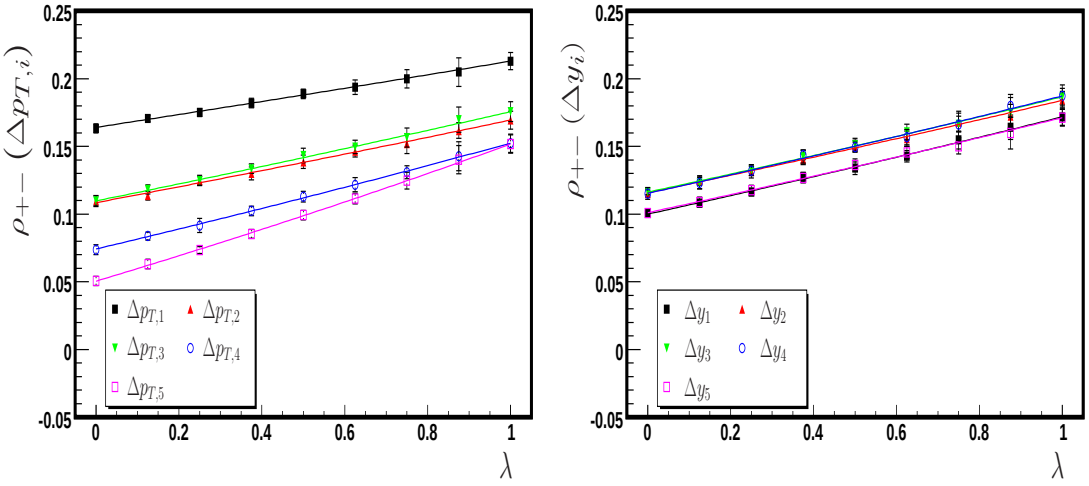

Figure 6.12: Evolution of the final state correlation coefficient ρ_{+-} between positively and negatively charged hadrons with the Monte Carlo parameter $\lambda = V_1/V_g$ for transverse momentum bins $\Delta p_{T,i}$ (*left*) and for rapidity bins Δy_i (*right*). The rest as in Fig.(6.11).

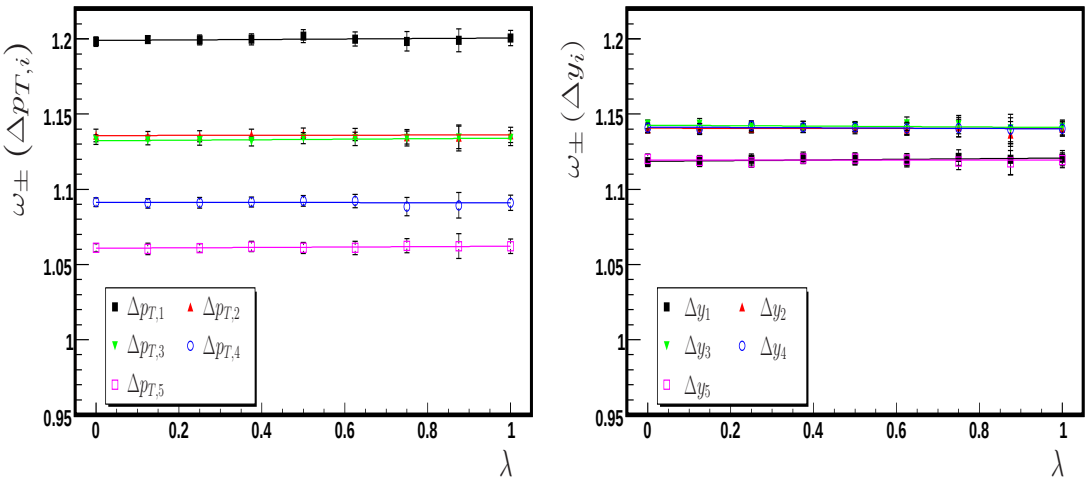

Figure 6.13: Evolution of the final state scaled variance $\omega_{\pm}$ between all charged hadrons with the Monte Carlo parameter $\lambda = V_1/V_g$ for transverse momentum bins $\Delta p_{T,i}$ (*left*) and for rapidity bins Δy_i (*right*). The rest as in Fig.(6.11).

ance and the correlation coefficient the same in all $\Delta p_{T,i}$ and Δy_i bins. All values converge to the one suggested by the CE acceptance scaling approximation with acceptance probability $q = 0.2$ (i.e. 5 bins of equal average particle number content). Fully phase space integrated values ω and ρ can be found in [101, 103, 141, 142] and later on in Chapters 8 and 9.

The primordial scaled variance ω_+ of positively charged hadrons drops linearly to its CE limit as the size of the charge bath is reduced. Here one also finds $\omega_+^{mce} < \omega_+^{ce}$, however almost equal in $\Delta p_{T,1}$, in limited acceptance. Combined energy and charge conservation leads to more constrained multiplicity fluctuations. The primordial correlation coefficient ρ_{+-} between positively and negatively charged particles, on the other hand, rises as the size of the bath decreases, $\lambda \to 1$. The correlation coefficient is indeed positive, as one would expect from charge conservation. In full phase space ρ_{+-}^{ce} and ρ_{+-}^{mce} are rather close to unity, as discussed earlier. However the correlation coefficient in limited acceptance appears weaker in the MCE than in the CE, $\rho_{+-}^{mce} < \rho_{+-}^{ce}$. Energy conservation de-correlates the joint multiplicity distribution. In a primordial neutral CE system one finds the width of the distribution of all charged hadrons, Eq.(6.1), $\omega_\pm \simeq 1$, i.e. essentially a Poissonian, in any momentum bin [93, 101]. Fluctuations of the number of all charged particles appear to be unconstrained by charge conservation and, thus, to yield the same result as in the GCE [94]. But also, like for ω, the observed value is independent of the position and shape of the acceptance window. This is in contrast to primordial MCE calculations where the ω and ρ show a distinctive dependence on the bins $\Delta p_{T,i}$ and Δy_i. See Figs.(6.4-6.5).

No additional correlations are introduced into the momentum space dependence of the final state multiplicity distribution, apart from the well-known correlations due to resonance decay. The CE final state scaled variance ω_+ in transverse momentum bins in Fig.(6.14) (*left*) shows qualitatively a similar behavior as in the GCE, Fig.(6.1) (*left*), and in the MCE, Fig.(6.8) (*left*). The scaled variance decreases as charge conservation is turned on, however not as strongly as in the MCE. Neutral hadrons lead to enhancement mostly at low p_T, hence ω_+^{ce} is larger in $\Delta p_{T,1}$ than in $\Delta p_{T,5}$. As resonance decay works more evenly across rapidity, one finds the Δy_i dependence mostly flat in Fig.(6.14) (*right*).

The CE final state correlation coefficient ρ_{+-} in transverse momentum bins in Fig.(6.15) (*left*) qualitatively shows an equally similar behavior as in the GCE, Fig.(6.2) (*left*), and in the MCE, Fig.(6.9) (*left*). However with a notably stronger correlation at larger p_T bins in Fig.(6.15) (*left*) than in GCE and MCE. The extrapolations in Figs.(6.7) (*left*) to the final state MCE and in Fig.(6.12) (*left*) to the final state CE correlation coefficient, show hence different behavior. Starting from the final state GCE values the correlation coefficient grows as the charge

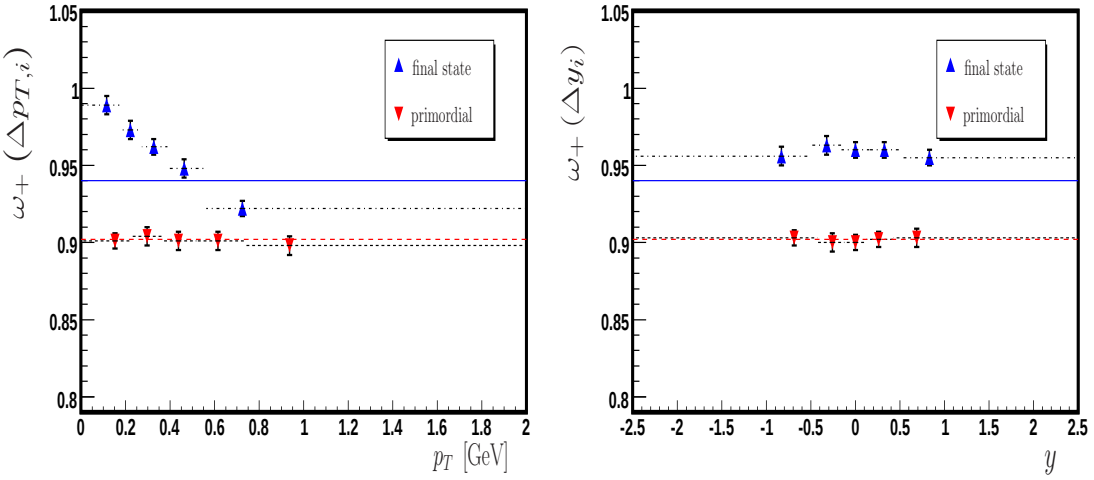

Figure 6.14: CE scaled variance ω_+ of multiplicity fluctuations of positively charged hadrons, both primordial and final state, in transverse momentum bins $\Delta p_{T,i}$ (*left*) and rapidity bins Δy_i (*right*). Horizontal error bars indicate the width and position of the momentum bins (And not an uncertainty!). Vertical error bars indicate the statistical uncertainty quoted in Table 6.3. The markers indicate the center of gravity of the corresponding bin. The solid and the dashed lines show final state and primordial acceptance scaling estimates respectively.

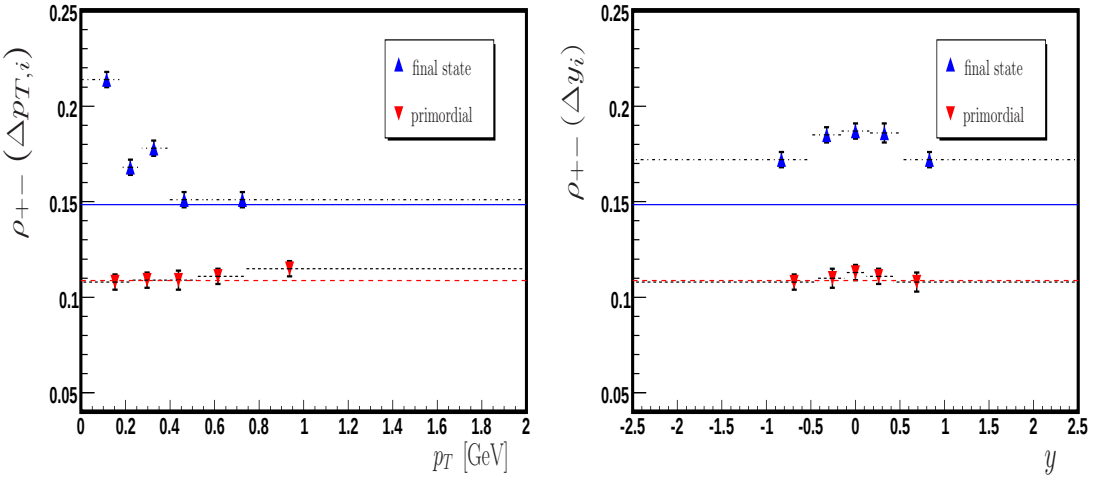

Figure 6.15: CE multiplicity correlation coefficient ρ_{+-} between positively and negatively charged hadrons, both primordial and final state, in transverse momentum bins $\Delta p_{T,i}$ (*left*) and rapidity bins Δy_i (*right*). The rest as in Fig.(6.14).

bath is removed, but drops when both, charge and heat bath, are removed. Resonance decay introduces a positive correlation. Charge conservation makes this trend stronger. In the MCE energy conservation works in the opposite direction.

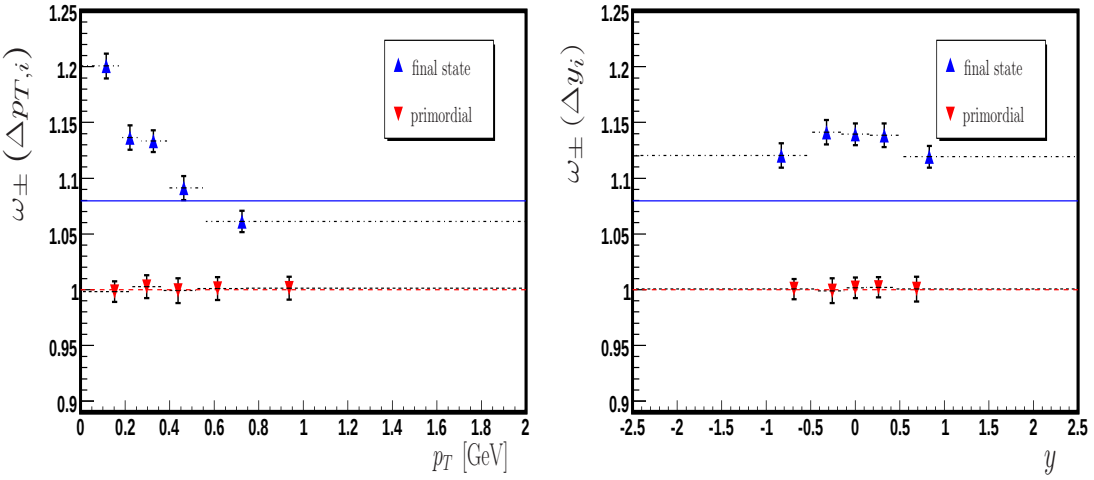

Figure 6.16: CE scaled variance $\omega_\pm$ of multiplicity fluctuations of all charged hadrons, both primordial and final state, in transverse momentum bins $\Delta p_{T,i}$ (*left*) and rapidity bins Δy_i (*right*). The rest as in Fig.(6.14).

Primordial	$\Delta p_{T,1}$	$\Delta p_{T,2}$	$\Delta p_{T,3}$	$\Delta p_{T,4}$	$\Delta p_{T,5}$
ω_+^{ce}	0.901 ± 0.005	0.904 ± 0.006	0.901 ± 0.006	0.901 ± 0.006	0.898 ± 0.006
ρ_{+-}^{ce}	0.108 ± 0.004	0.109 ± 0.004	0.109 ± 0.005	0.111 ± 0.004	0.115 ± 0.004
Primordial	Δy_1	Δy_2	Δy_3	Δy_4	Δy_5
ω_+^{ce}	0.903 ± 0.005	0.900 ± 0.006	0.900 ± 0.005	0.902 ± 0.005	0.903 ± 0.006
ρ_{+-}^{ce}	0.108 ± 0.004	0.110 ± 0.005	0.113 ± 0.004	0.111 ± 0.004	0.108 ± 0.005
Final state	$\Delta p_{T,1}$	$\Delta p_{T,2}$	$\Delta p_{T,3}$	$\Delta p_{T,4}$	$\Delta p_{T,5}$
ω_+^{ce}	0.989 ± 0.006	0.973 ± 0.006	0.962 ± 0.005	0.948 ± 0.006	0.922 ± 0.005
ρ_{+-}^{ce}	0.214 ± 0.004	0.168 ± 0.004	0.178 ± 0.004	0.151 ± 0.004	0.151 ± 0.004
Final state	Δy_1	Δy_2	Δy_3	Δy_4	Δy_5
ω_+^{ce}	0.956 ± 0.006	0.963 ± 0.006	0.960 ± 0.005	0.960 ± 0.005	0.955 ± 0.005
ρ_{+-}^{ce}	0.172 ± 0.004	0.185 ± 0.004	0.187 ± 0.004	0.186 ± 0.005	0.172 ± 0.004

Table 6.3: Summary of the final state and primordial scaled variance ω_+ of positively charged hadrons and the correlation coefficient ρ_{+-} between positively and negatively charged hadrons in transverse momentum bins $\Delta p_{T,i}$ and rapidity bins Δy_i. Both the GCE result ($\lambda = 0$) and the extrapolation to CE ($\lambda = 1$) are shown. Analytical primordial CE values are $\omega_+^{ce} = 0.9019$ and $\rho_{+-}^{ce} = 0.1088$, while final state acceptance scaling values are $\omega_+^{ce} = 0.9401$ and $\rho_{+-}^{ce} = 0.1485$. The uncertainty quoted corresponds to 20 Monte Carlo runs of $2 \cdot 10^5$ events (GCE) or is the result of the extrapolation (CE).

The Δy_i dependence is again mild in the CE, Fig.(6.9) (*right*).

The final state CE values of $\omega_\pm$ in Fig.(6.16) can be compared to their GCE counterparts in Fig.(6.3). As charge conservation does not introduce any correlations in momentum space, and as the effect of charge conservation is not seen in $\omega_\pm$, also final state values are equal (within error bars) to the GCE results. GCE and CE values for $\omega_\pm$ are the same in full phase space for a neutral system (both primordial and final state). As charge conservation ensures (in the absence of energy conservation) a positive correlation coefficient ρ_{+-}, one finds $\omega_+ < \omega_\pm$ in the CE in any momentum bin. The acceptance scaling estimate gives a good average in transverse momentum bins $\Delta p_{T,i}$, while under-predicting correlations and fluctuations in rapidity bins Δy_i, due to correlations introduced by resonance decay.

6.4 Discussion

GCE joint distributions of particle multiplicity were extrapolated to the MCE and CE limits. A few remarks attempt to summarize. The final state transverse momentum dependence $\Delta p_{T,i}$ of multiplicity fluctuations and correlations are qualitatively similar in MCE, CE, and GCE. On the other hand, their (final state) rapidity dependence Δy_i exhibits only a very mild dependence in GCE and CE, which is in contrast to the MCE (with momentum conservation), where effects are strong. In the primordial case there is no momentum space dependence of multiplicity fluctuations and correlations in ensembles without energy conservation. Resonance decay trends are enhanced in the MCE. Charge conservation effects cease in a neutral system, and thus final state values of $\omega_\pm$ are the same in GCE and CE, even after resonance decay in limited acceptance, which provides a valuable cross check with analytical solutions.

The extrapolation scheme works rather accurate and efficient. The statistical error on the ‘data‘ points grows as $\lambda \to 1$. The extrapolation helps greatly to keep the statistical uncertainty on the MCE (or CE) limit low, which can be seen from a comparison of the right most markers on the extrapolation lines. The last point and its error bar denote the result of a linear extrapolation of variances and covariances, while the second to last data point and its error bar are the result of 20 Monte Carlo runs with $\lambda = 0.875$. The analytical MCE (or

CE) values are well within error bars of extrapolated Monte Carlo results, and agree surprisingly well, given the large number of 'conserved' quantities (5 and 3, respectively) and a relatively small sample size of $8 \cdot 20 \cdot 2 \cdot 10^5 = 3.2 \cdot 10^7$ events. In a sample-reject type of approach this sample size would yield a substantially larger statistical error, as only events with exact values of extensive quantities are kept for the analysis. As the system size is increased, a sample-reject formalism, hence, becomes increasingly inefficient, while the extrapolation method still yields good results. Error bars are mildly smaller for an CE extrapolation than for an extrapolation to the MCE, due to a smaller number of conserved quantities. For further discussion see Appendices F and G.

The qualitative picture presented in Fig.(6.8) could be compared to similar analysis of UrQMD transport simulation data [131], or recently published NA49 data on multiplicity fluctuations in limited momentum bins [59]. Both (data and transport simulation) appear qualitatively similar to the MCE scenario, which could hint at a potentially strong role of conservation laws on fluctuation and correlation observables. The arguments used are general enough to believe they might hold as '*rules of thumb*' in non-equilibrium situations too. If, in one event, one has a larger (smaller) number of particles in a momentum bin with larger and positive p_z, than also a larger (smaller) number should go in the negative p_z direction. This effect should be considerable as long as the momentum bins contain a not too small fraction of the particles of the whole event, say 20% as here. Or even smaller (11%) as in Chapter 7. Or yet smaller ($< 10\%$) as in the UrQMD transport simulation [131].

It should be hard to assess the importance of conservations laws in simulations, let alone in data. This model is simple as one can follow things step by step and turn on and off certain effects. This is much harder in considerabely more complicated transport simulations, where individual sources of correlations can not that easily be pinned down.

The systems to be studied are in general not neutral, so mean values of positively and negatively charged hadrons are not the same, hence the spectra will also vary. A simultanious measurement of the momentum space dependence of ω_-, ω_+, and $\rho_\pm$, and their mean values $\langle N_- \rangle$, and $\langle N_+ \rangle$ should help to disentangle effects. For instance $\omega_+ > \omega_\pm$ in a high momentum bin, while $\omega_+ < \omega_\pm$ in a low momentum bins is hard to do, except with energy conservation.

Chapter 7

Micro Canonical Ensemble

In this chapter the MCE is studied more closely, as it appears to be the most interesting amongst the standard ensembles. A simplified physical system is chosen to allow for smoother discussion. Owing to available analytical solutions [127] Fermi-Dirac (FD) and Bose-Einstein (BE) effects are included into the analysis. The Monte Carlo scheme only facilitated Maxwell-Boltzmann (MB) statistics. For the examples a gas with three degenerate massive particles (with positive, negative and zero charge) with mass $m = 0.140$ GeV in three different statistics (MB, FD, BE) has been chosen. Thus examples, in particular the FD case, are a little academic in the sense that there is no fermion of this mass. In a hadron resonance gas, discussed in the previous chapters, the lightest fermion is the nucleon for which quantum effects are probably negligible.

In Section 7.1 multiplicity fluctuations and correlations in transverse momentum bins $\Delta p_{T,i}$ and rapidity bins Δy_i are discussed. Section 7.2 will turn to multiplicity correlations between bins disconnected in momentum space (y_A and y_B, or $p_{T,A}$ and $p_{T,B}$), and correlations between bins separated by some distance ϕ_{gap} or y_{gap} in azimuth and rapidity.

7.1 Fluctuations and Correlations within one Momentum Bin

The properties of a static thermal system will be discussed first. Joint distributions of multiplicities N_+ and N_- are measured in limited bins of transverse momentum $\Delta p_{T,i}$ and of rapidity Δy_i. Results will, in particular, be compared to

the acceptance scaling approximation employed in [94, 101, 103], which assumes random observation of particles with a certain probability q, regardless of particle momentum (see also Appendix E). Corresponding results for scaled variance in MB statistics can also be found in [106].

Static System

The momentum spectra are assumed to be ideal GCE spectra due to the large volume approximation. In Fig.(7.1) transverse momentum and rapidity spectra are shown for MB statistics. BE and FD statistics yield similar spectra, unless chemical potentials are large. Momentum bins $\Delta p_{T,i}$ and Δy_i are indicated by drop-lines.

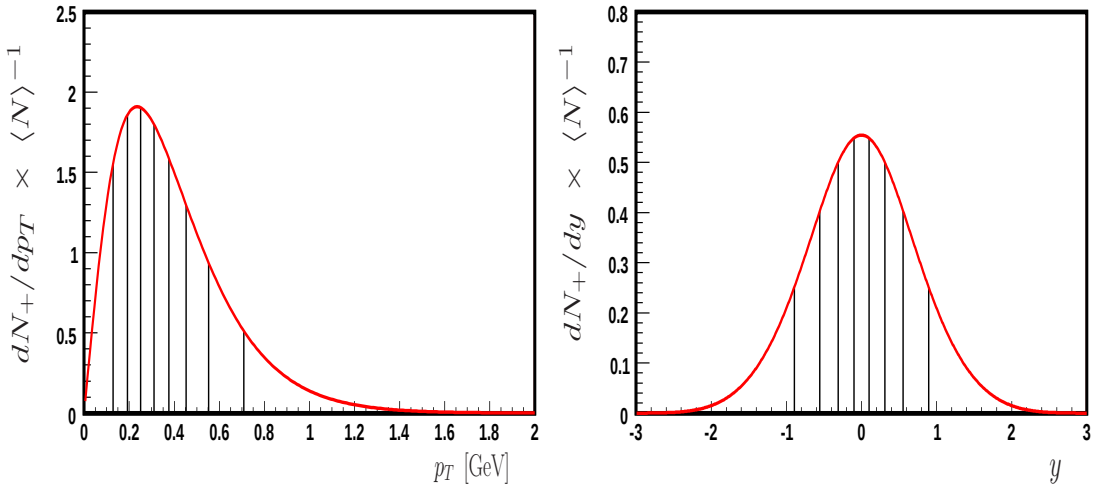

Figure 7.1: Differential particle spectra for a 'pion gas' at $T = 0.160$ GeV. Transverse momentum spectrum (*left*) and rapidity spectrum (*right*). Both curves are normalized to unity. The bins are constructed such that each bin contains 1/9 of the total yield.

In Fig.(7.2) the scaled variance of positively charged particles ω_+ is presented within different transverse momentum bins $\Delta p_{T,i}$ (*left*) and rapidity bins Δy_i (*right*). The scaled variance in limited bins of momentum space is more sensitive to the choice of particle statistics than the spectra would suggest. BE and FD effects are particularly strong in momentum space bins in which occupation numbers are large. Hence, at the low momentum tail one finds suppression of fluctuations for FD and enhancement for BE, while at the high momentum tail, one finds $\omega_{BE} \simeq \omega_{MB} \simeq \omega_{FD}$, Fig.(7.2) (*left*).

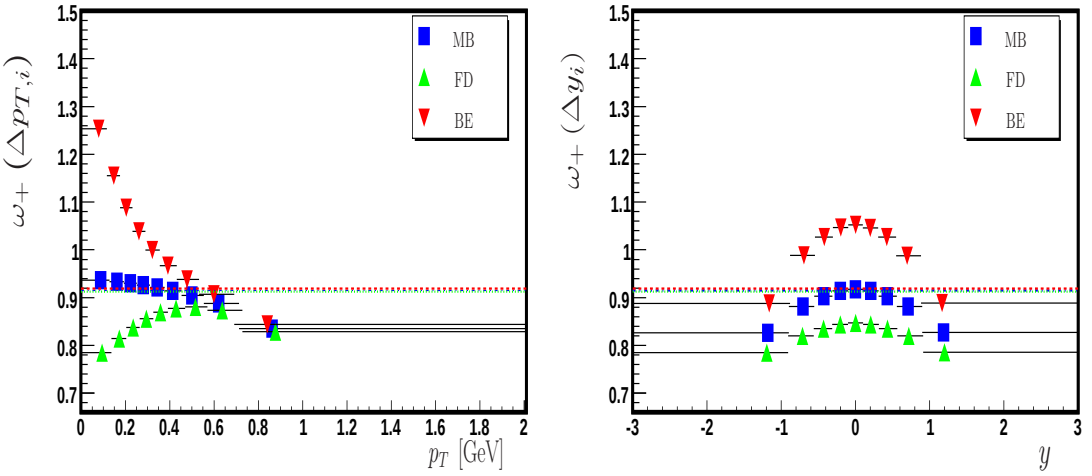

Figure 7.2: Transverse momentum (*left*) and rapidity dependence (*right*) of the MCE scaled variance of positively charged particles at $T = 0.160$ GeV, for a MB (blue), FD (green), BE (red) 'pion gas' at zero charge density. Momentum bins are constructed such that each bin contains the same fraction q of the average π^+ yield. The horizontal bars indicate the width of the $\Delta p_{T,i}$ or Δy_i bins, while the marker indicates the position of the center of gravity of the corresponding bin. Dashed lines indicate acceptance scaling results.

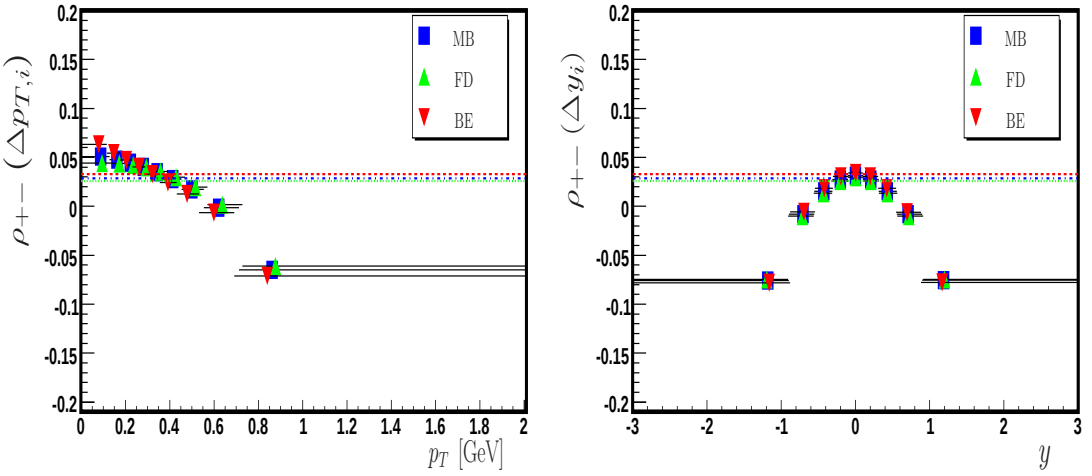

Figure 7.3: Same as Fig.(7.2), but for the MCE correlation coefficient between positively and negatively charged particles. Dashed lines indicate acceptance scaling results.

The rapidity dependence, Fig.(7.2) (*right*), has a different behavior. The reason is, that in any Δy_i bin there is some contribution from a low p_T tail of the differential momentum spectrum $dN/dy/dp_T$ where quantum statistics ef-

fects are pronounced. This leads to a clear separation of the curves and one finds $\omega_{BE} > \omega_{MB} > \omega_{FD}$. In contrast to this, the fully phase space integrated (all particles observed) scaled variance is rather insensitive to the choice of statistics [100] (unless chemical potentials are large). There are in fact three different 'acceptance scaling' lines in Fig.(7.2), which extrapolate the fully phase space integrated scaled variance to limited acceptance. The differences are however very small and all three lines lie practically on top of each other.

Fig.(7.3) presents the correlation coefficient ρ_{+-} between positively and negatively charged particles in transverse momentum bins $\Delta p_{T,i}$ (*left*) and rapidity bins Δy_i (*right*). The fully phase space integrated correlation coefficient between positively and negatively charged particles would be $\rho_{+-} = 1$ in the CE and MCE. In the GCE it would be 0. In the MB CE it would not show any momentum space dependence and would always be $\rho_{+-} > 0$. In the MCE the situation is qualitatively different: in low momentum bins particles are positively correlated, while in high momentum bins they can even be anti-correlated. Horizontal lines again indicate acceptance scaling. Quantum effects for the correlation coefficient remain small as there is no explicit local (quantum) correlations between particles of different charge.

It should be stressed that the $\Delta p_{T,i}$ dependence in Figs.(7.2,7.3) is a direct consequence of energy conservation. The Δy_i dependence of ω_+ and ρ_{+-}, however, is due to joint energy and longitudinal momentum (P_z) conservation. Disregarding P_z conservation leads to a substantially milder Δy_i dependence, see Fig.(7.4).

This behavior can be intuitively explained: in a low momentum bin it is comparatively easy to balance charge, as each individual particle carries little energy and momentum. In contrast to this, in a high momentum bin with, say an excess of positively charged particles, it is unfavorable to balance charge, as one would also have to have more than on average negatively charged particles, and each particle carries large energy and momentum. This leads to suppressed fluctuations and correlations in high momentum bins when compared to low momentum bins.

In a small mid-rapidity window, with $|y| < 0.3$, the effects of globally applied motional conservation laws cease to be important (see Fig.(7.5)). Local correlations due to BE and FD statistics begin to dominate, and MCE deviations from the GCE results, Eq.(7.1), are relevant only for the highest momentum bins. In

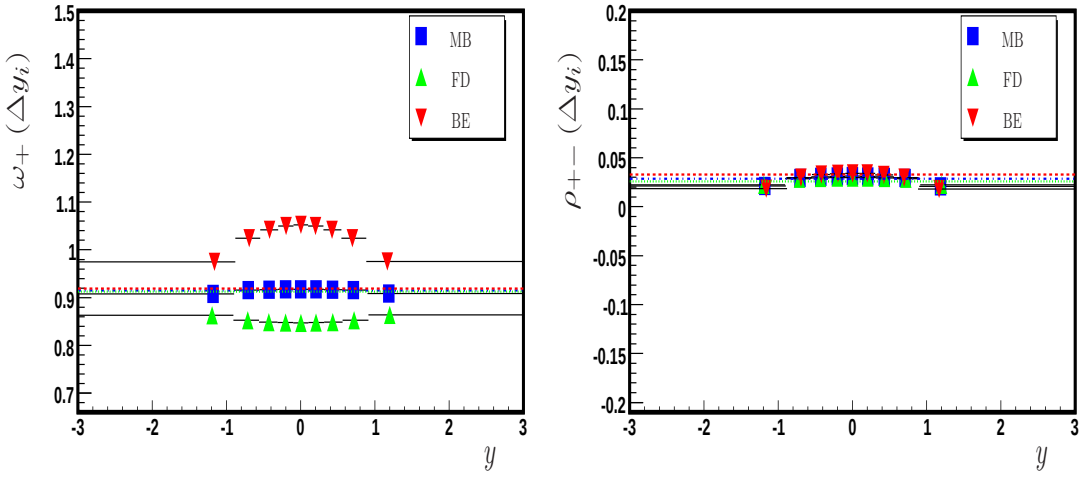

Figure 7.4: Rapidity dependence of the scaled variance of positively charged particles (*left*) and of the correlation coefficient between positively and negatively charged particles (*right*). Calculations are done for the same system as in Figs.(7.2,7.3), however disregarding momentum conservation.

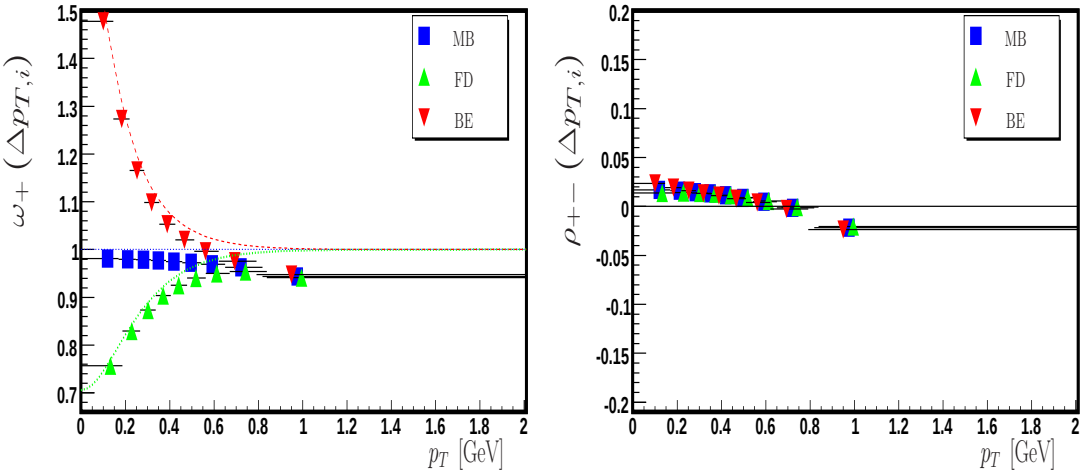

Figure 7.5: Transverse momentum dependence of MCE scaled variance of negatively charged particles (*left*) and the MCE correlation coefficient between positively and negatively charged particles (*right*). Only particles in a mid-rapidity window $|y| < 0.3$ are measured. Dashed lines denote the GCE result, Eq.(7.1).

BE or FD statistics one finds for vanishing bin size ($\delta y,\ \delta p_T$):

$$\omega_\delta^{GCE} \;=\; \frac{\kappa_2^{N_\delta,N_\delta}}{\kappa_1^{N_\delta}} \;\simeq\; \frac{1}{1 \pm e^{-\beta m_T \cosh y + \beta\mu}} \;. \tag{7.1}$$

BE and FD effects are strongest around mid-rapidity $y = 0$, especially at

low p_T, where occupation numbers are large. MCE calculations in Fig.(7.5) are close to the GCE estimate Eq.(7.1). In MB statistics one finds only a weak Δp_T dependence in a small mid-rapidity window. Please note that the acceptance scaling procedure predicts a Poisson distribution with $\omega_+ \to 1$ and $\rho_{+-} \to 0$ for all three statistics in the limit of very small acceptance.

Collectively Moving System

As established a long time ago, in order to properly define the thermodynamics of a system with collective motion, the partition function needs to be Lorentz invariant [125, 126]. The expectation values of observables need hence to transform according to the Lorentz transformation properties of these observables. In particular, the inverse temperature $\beta = T^{-1}$ is promoted to a four-vector β^μ (combining local temperature with collective velocity). The entropy, as well as particle multiplicities, remain Lorentz-scalars.

These requirements are in general not satisfied unless momentum conservation is put on an equal status with energy conservation. If the system is described by a MCE, then momentum should be conserved as well as energy [125, 126]. If the system is exchanging energy with a bath, it needs to exchange momentum as well.

For ensemble averages, neglecting these rules and treating momentum differently from energy is safe as long as the system is close to the thermodynamic limit, since there ensembles become equivalent. The same is not true for fluctuation and correlation observables, which remain ensemble-specific [94]. For a system at rest, these requirements are not apparent since the net-momentum is zero. Statistical mechanics observables in a collectively moving system, however, lose their Lorentz invariance, if this is not maintained in the definition of the partition function.

To illustrate this point, the properties of a system moving along the z-axis with a collective boost y_0 are considered. The total energy of the fireball is then $E = M\cosh(y_0)$, while its total momentum is given by $P_z = M\sinh(y_0)$. The mass of the fireball in its rest frame is $M = P^\mu u_\mu$. The system four-temperature is $\beta^\mu = \beta u^\mu$. Local temperature and chemical potentials remain unchanged. The second rank tensor (or co-variance matrix) κ_2, Eq.(2.18), will be discussed in this section.

The second order cumulant κ_2, Eq.(2.18), is given by the second derivatives of the cumulant generating function with respect to the fugacities. Essentially this is the Hessian matrix of the function Eq.(2.8), encoding the structure of its minima. The diagonal elements $\kappa_2^{X,X}$ are the variances of the GCE distributions of extensive quantities X. For example, $\kappa_2^{N_A,N_A}$ measures the GCE variance of the distribution of particle multiplicity of species A, while $\kappa_2^{Q,Q}$ denotes the GCE electric charge fluctuations, etc. The off-diagonal $\kappa_2^{X,Y}$ elements give GCE co-variances of two extensive quantities X and Y.

For a boost along the z-axis the general co-variance matrix for a relativistic gas with one conserved charge reads:

$$\kappa_2 = \begin{pmatrix} \kappa_2^{N_A,N_A} & \kappa_2^{N_A,N_B} & \kappa_2^{N_A,Q} & \kappa_2^{N_A,E} & \kappa_2^{N_A,P_x} & \kappa_2^{N_A,P_y} & \kappa_2^{N_A,P_z} \\ \kappa_2^{N_B,N_A} & \kappa_2^{N_B,N_B} & \kappa_2^{N_B,Q} & \kappa_2^{N_B,E} & \kappa_2^{N_B,P_x} & \kappa_2^{N_B,P_y} & \kappa_2^{N_B,P_z} \\ \kappa_2^{Q,N_A} & \kappa_2^{Q,N_B} & \kappa_2^{Q,Q} & \kappa_2^{Q,E} & 0 & 0 & 0 \\ \kappa_2^{E,N_A} & \kappa_2^{E,N_B} & \kappa_2^{E,Q} & \kappa_2^{E,E} & 0 & 0 & \kappa_2^{E,P_z} \\ \kappa_2^{P_x,N_A} & \kappa_2^{P_x,N_B} & 0 & 0 & \kappa_2^{P_x,P_x} & 0 & 0 \\ \kappa_2^{P_y,N_A} & \kappa_2^{P_y,N_B} & 0 & 0 & 0 & \kappa_2^{P_y,P_y} & 0 \\ \kappa_2^{P_z,N_A} & \kappa_2^{P_z,N_B} & 0 & \kappa_2^{P_z,E} & 0 & 0 & \kappa_2^{P_z,P_z} \end{pmatrix} . \quad (7.2)$$

Off-diagonal elements correlating a globally conserved charge with one of the momenta, i.e. κ_2^{Q,P_x}, as well as elements denoting correlations between different momenta, i.e. $\kappa_2^{P_x,P_y}$, are equal to zero due to antisymmetric momentum integrals. The values of elements correlating particle multiplicity and momenta, i.e. $\kappa_2^{N_A,P_x}$, depend strongly on the acceptance cuts applied. For fully phase space integrated multiplicity fluctuations and correlations these elements are equal to 0, again due to antisymmetric momentum integrals.

It is instructive to review the transformation properties of κ under the Lorentz group: $\kappa_2^{X,Y}$ contains the correlations between four-momenta P^μ and, in general, (scalar) conserved quantities and particle multiplicities Q^j. Hence, the elements $\kappa_2^{P^\mu,P^\nu}$, i.e. $\langle \Delta P^\mu \Delta P^\nu \rangle$, will transform as a tensor of rank 2 under Lorentz transformations; $\kappa_2^{P^\mu,Q^j}$, i.e. $\langle \Delta P^\mu \Delta Q^j \rangle$, will transform as a vector (the rapidity distribution will simply shift); and the remaining $\kappa_2^{Q^j,Q^k}$ will be scalars.

For a static system the one finds for the co-variances of energy and momenta $\kappa_2^{E,P_x} = \kappa_2^{E,P_y} = \kappa_2^{E,P_z} = 0$. Under these two conditions, a static system and full particle acceptance, i.e. $\kappa_2^{N_A,P_x} = \kappa_2^{N_B,P_x} = \kappa_2^{N_A,P_y} = \cdots = 0$, some

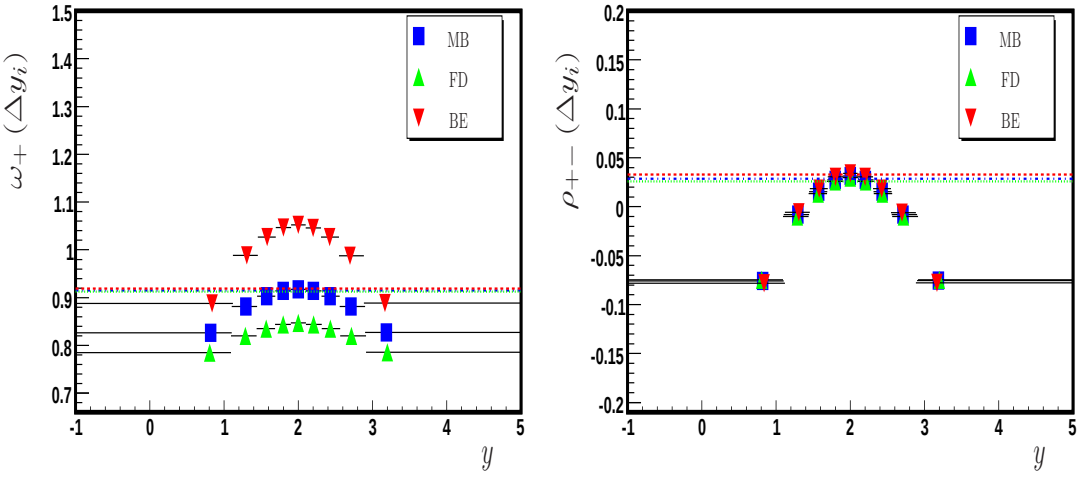

Figure 7.6: Same as Fig.(7.2) (*right*) and Fig.(7.3) (*right*), but for a system moving with $y_0 = 2$.

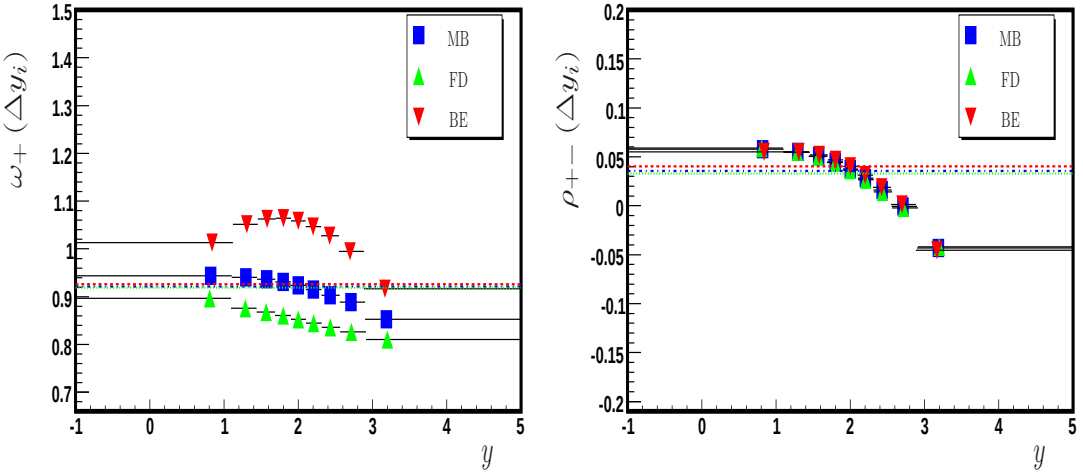

Figure 7.7: Same as Fig.(7.6), but without P_z exact conservation.

eigenvalues of the matrix Eq.(7.2) factorize, and momentum conservation can be shown to drop out of the calculation [106]. For a boost along the z-axis (and arbitrary particle acceptance) non-vanishing elements $\kappa_2^{P_z,E} = \kappa_2^{E,P_z} \neq 0$ appear, and ensure that the determinant of the matrix κ_2, Eq.(7.2), remains invariant against such a boost. Note that still $\kappa_2^{P_x,E} = \kappa_2^{P_y,E} = 0$. Transverse momenta P_x and P_y remain un-correlated with energy E.

In Fig.(7.6) multiplicity fluctuations (*left*) and correlations (*right*) are shown for a system with boost $y_0 = 2$. The rapidity spectrum of Fig.(7.1) (*right*) is

simply shifted to the right by two units. The construction of the acceptance bins is done as before. Multiplicity fluctuations and correlations within a rapidity bin Δy_i transform as a vector (i.e., its z component shifts in rapidity) as inferred from their Lorentz-transformation properties, provided both energy and momentum along the boost direction are conserved.

This last point deserves attention because usually, starting from [1], micro canonical calculations only conserve energy and not momentum. Imposing exact conservation for energy, and only average conservation of momentum will make the system non-Lorentz invariant, since in a different frame from the co-moving one energy and momentum will mix, resulting in micro state by micro state fluctuations in both momentum and energy. This result is not obvious, because energy-momentum is a vector of separately conserved currents. It is therefore natural to assume that these currents can be treated within different ensembles; they are, after all, conserved separately. It must be kept in mind, however, that it is not energy or momentum, but particles that are exchanged between the system and any canonical or grand canonical bath. The amount of energy and momentum carried by each particle are correlated by the dispersion relation [126].

In the situation examined here (unlike in a Cooper-Frye formalism [143], where the system is frozen out on a hyper surface, a space-time four-vector correlated with four-momentum) all time dependence within the system under consideration is absent due to the equilibrium assumption. Furthermore, the system is entirely thermal: the correlation between particle numbers when the system is sampled at different times is a $\delta-$function, that stays a $\delta-$function under all Lorentz-transformations. Hence, unlike what happens in a Cooper-Frye freeze-out, energy-momentum and space-time do not mix in the partition function. Together with the constraint from the particle dispersion relations, this means that different components of the four-momentum need to be treated by the same ensemble.

This situation is explicitly shown in Fig.(7.7). Here, multiplicity fluctuations and correlations are calculated for the same system as in Fig.(7.6), but with exact conservation of only energy (and charge), but not momentum. In the co-moving frame of the system, the fluctuations and correlations are identical to Fig.(7.4). When the system is boosted the distribution changes (not only by a shift in rapidity, as required by Lorentz-invariance), and loses its symmetry around the system's average boost.

This last effect can be understood from the fact that momentum does not have to be conserved event-by-event, but energy does. It is easier, therefore, to create a particle with less longitudinal momentum (energy) than the average, than with larger longitudinal momentum (energy), and still conserve energy overall. This leads to suppressed multiplicity fluctuations and a negative correlation coefficient for rapidity bins in the forward direction in comparison to rapidity bins in the backward direction. In Fig.(7.6), where the system also needs to conserve momentum exactly, this enhancement is balanced by the fact that it will be more difficult to conserve momentum globally when particles having less momentum than the boost are created.

7.2 Correlations between disconnected Momentum Bins

Next, correlations between particles in different momentum bins are studied. 'Long range correlations' between bins well disconnected in momentum have been suggested to arise from dynamical processes. Examples include color glass condensate [50, 51], droplet formation driven hadronization [144], and phase transitions within a percolation-type mechanism [50, 145]. The elliptic flow measurements, widely believed to signify the production of a liquid at RHIC [10, 146, 147, 148], are also, ultimately, correlations between particles disconnected in phase space (here, the azimuthal angle).

As will be shown, conservation laws will also introduce such correlations between any two (connected or not) distinct regions of momentum space. No dynamical effects are taken into consideration (only an isotropic thermal system).

Considering correlations between the multiplicities of particles A and B, within two bins, each centered around the rapidities y_A and y_B, with (constant) widths $\Delta y_A = \Delta y_B = 0.2$, in Fig.(7.8) (*left*) the correlation coefficient ρ_{+-} between positively and negatively charged particles are shown as a function of y_A and y_B. Fig.(7.8) (*right*) presents the correlation coefficients between like-charge ρ_{++}, unlike-charge ρ_{+-}, and all charged particles $\rho_{\pm\pm}$, as a function of the separation of the two bin centers $y_{gap} = y_A - y_B$. In Fig.(7.9) the correlation coefficients ρ_{++} (*left*) and $\rho_{\pm\pm}$ (*right*) are shown as a function of y_A and y_B. The main diagonal contains multiplicities in the same momentum bin. In the

case of ρ_{++} and $\rho_{\pm\pm}$ this leads to a double counting of each particle and hence to $\rho = 1$.

Energy conservation always leads to anti-correlation between different momentum space bins. Charge conservation leads to a positive correlation of unlike charged particles and anti-correlation of like-sign particles. Longitudinal momentum conservation, however, is responsible for the structure visible in Fig.(7.8)(*left*). Having a small (large) number of particles of one charge in a bin with positive average longitudinal momentum, leads to a larger (smaller) number of particles of opposite charge in a bin with different but also positive P_z, (blue dips). This makes also a state with smaller (larger) particle number with opposite average longitudinal momentum $-P_z$ more likely (red hills). At large values of y_A the correlation coefficient $\rho \simeq 0$ for any y_B, because the yield $\langle N_A \rangle$ in Δy_A is asymptotically vanishing.

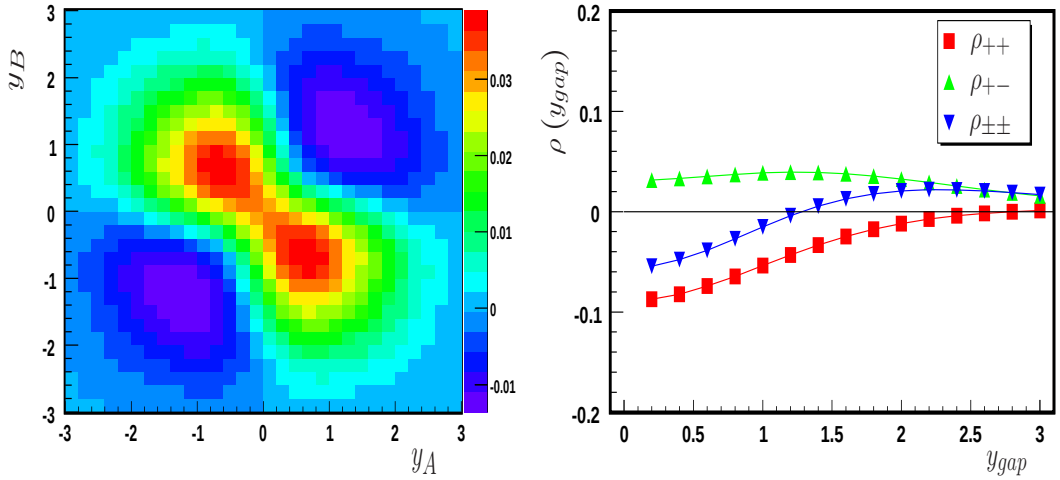

Figure 7.8: (*Left*): The correlation coefficient ρ_{+-} between the multiplicity of positively charged particles in a bin located at y_A with negatively charged particles in a bin located at y_B, both with a 0.2 width in rapidity. (*Right*): The correlation coefficients ρ_{+-}, ρ_{++}, and $\rho_{\pm\pm}$ between multiplicities in two bins separated by y_{gap} of like, unlike, and all charged particles. Both plots show MCE MB results.

The correlation coefficients ρ_{++}, Fig.(7.9)(*left*), and $\rho_{\pm\pm}$, Fig.(7.9)(*right*), show strong anti-correlations around center-rapidity, as to be expected from charge, energy and momentum conservation. In the case of ρ_{++} the correlation stays negative. For $\rho_{\pm\pm}$ one observes a positive correlation between the numbers of all charged particles going in opposite directions, while seeing an anti-correlation for particle multiplicities measured in the same direction. This

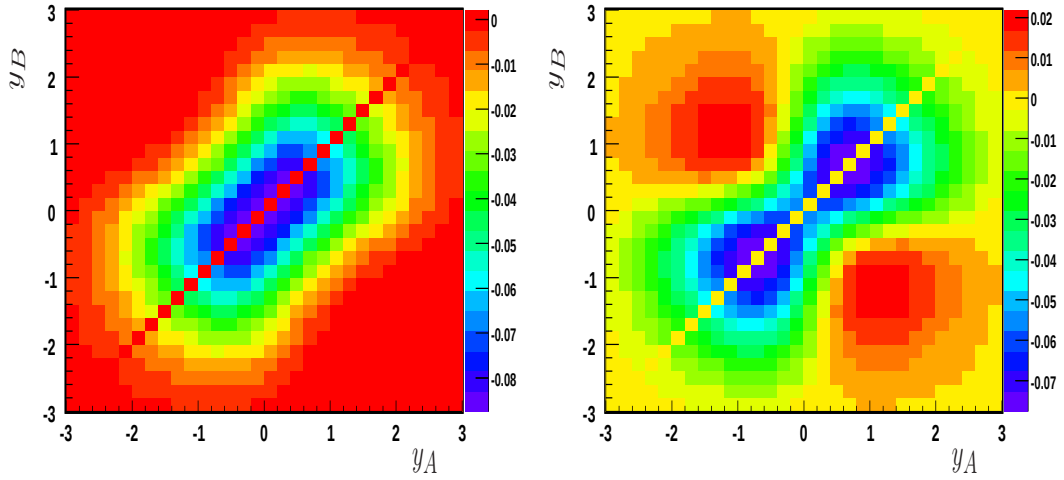

Figure 7.9: The correlation coefficient ρ_{++} between the multiplicity of positively charged particles in a bin located at y_A with positively charged particles in a bin located at y_B (*left*), and the correlation coefficient $\rho_{\pm\pm}$ between the multiplicity of all charged particles in a bin located at y_A with all charged particles in a bin located at y_B (*right*). Both plots show MCE MB results.

behavior is similar to that in Fig.(7.8)(*left*). For ρ_{+-} energy, momentum, and charge conservation favor pairs of oppositely charge particles in opposite directions over particles in the same direction. For like sign particles the correlation stays negative, however milder for bins located in opposite direction. For not charge separated multiplicities the effect of charge conservation cancels out and energy and momentum conservation determine the correlation function.

In Fig.(7.8) (*right*) the correlation coefficient is presented along the diagonal from top left to bottom right as a function of separation $y_{gap} = y_A - y_B$. Unlike-sign particles are positively correlated. Like-sign and all charged particles are negatively correlated at small separation y_{gap}. For large separation the correlation becomes asymptotically zero, because the yield is zero. However, please note that in particular $\rho_{\pm\pm} > \rho_{+-}$ at large y_{gap}. Here P_z conservation is indeed dominant.

Fig.(7.10) shows the correlation coefficient ρ_{+-} between positive and negative particles as a function of y_A and y_B, this time disregarding momentum conservation, for a static source (*left*) and a source with a collective boost of $y_0 = 2$ (*right*). Disregarding P_z conservation destroys the particular structure in Fig.(7.8) (*left*) and leads to a single peak at the origin. The correlation is then insensitive to the momentum direction, and only sensitive to the energy content of a bin Δy. The

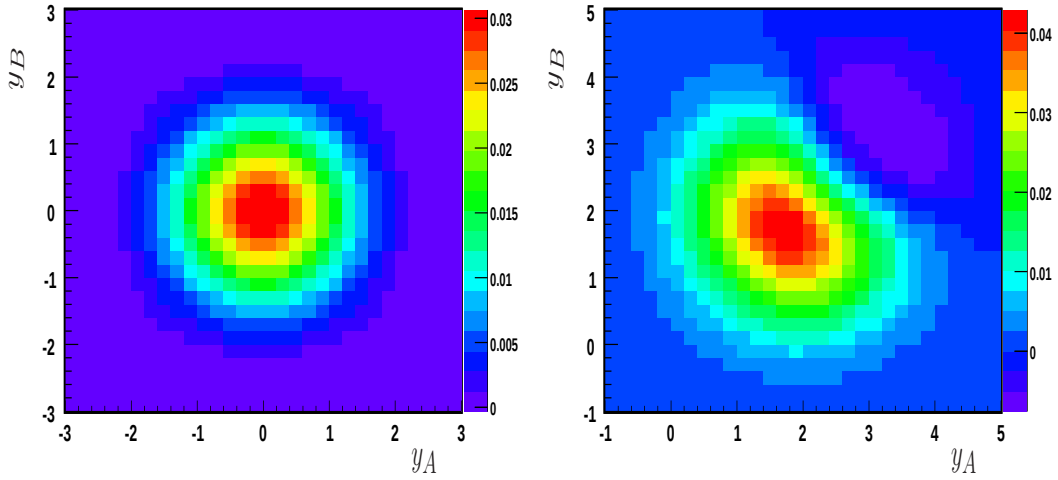

Figure 7.10: The correlation coefficient ρ_{+-} between the multiplicity of positively charged particles in a bin located at y_A with negatively charged particles in a bin located at y_B, without conservation of longitudinal momentum P_z, for a static source (*left*) and a source with a collective boost of $y_0 = 2$ (*right*).

observables in Figs.(7.8,7.9) do not, Fig.(7.10) (*right*), transform under boosts ($y_{A,B} \to y_{A,B} - y_0$), unless momentum along the boost axis is exactly conserved.

To complement the discussion of correlations across rapidity intervals, correlations between two distinct transverse momentum bins are studied. Here the discussion can be reduced to energy and charge conservation. Fig.(7.11) shows the correlation coefficient ρ_{+-} between the multiplicities of positively charged particles in transverse momentum bins of equal size ($\Delta p_T = 0.2$ GeV) centered around $p_{T,A}$ with the one of negatively charged particles in transverse momentum bins located at $p_{T,B}$ (*left*), and the correlation coefficient ρ_{++} between the multiplicities of positively charged particles in transverse momentum bins located at $p_{T,A}$ with positively charged particles in bins located at $p_{T,B}$ (*right*).

From charge conservation alone it follows that particles with electric charge of unlike sign are positively correlated, while the multiplicities of particles of the same charge are negatively correlated. The main diagonal in Fig.(7.11) (*right*) is excluded, as there $\rho_{++} = 1$ by construction. In Fig.(7.11) (*left*) there is an island of weak anti-correlation. The correlation function has its maximum close to the peak of the transverse momentum spectrum, i.e. where the average particle yield is largest. In these bins, and charge, and in particular, energy conservation have strong effects.

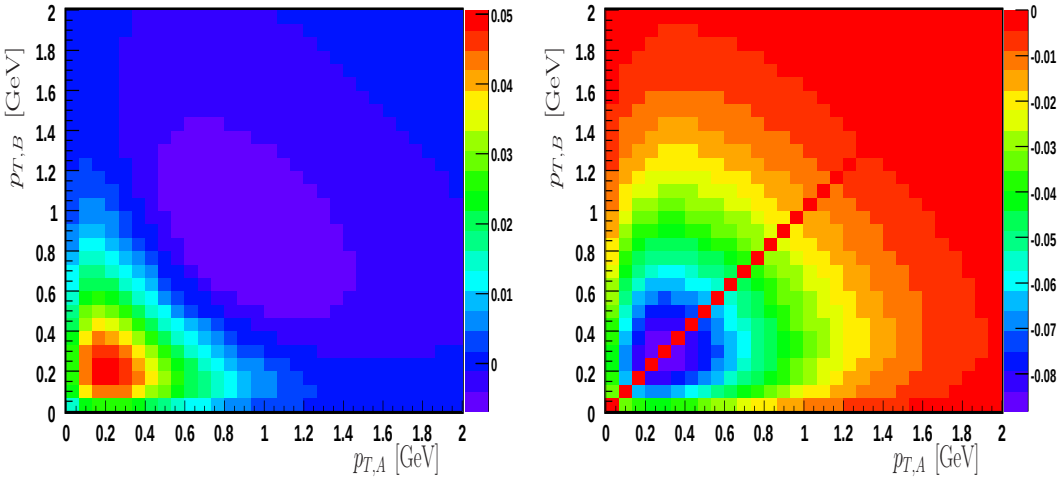

Figure 7.11: (*Left:*) The correlation coefficient ρ_{+-} between the multiplicity of positively charged particles in a bin located at $p_{T,A}$ with negatively charged particles in a bin located at $p_{T,B}$. (*Right:*) The correlation coefficient ρ_{++} between the multiplicity of positively charged particles in a bin located at $p_{T,A}$ with positively charged particles in a bin located at $p_{T,B}$.

Angular correlations, lastly, could arise due to conservation of transverse momenta P_x and P_y. In Fig.(7.12) the correlation coefficient between particles in different $\Delta\phi$ bins are shown. The flat[1] angular spectrum $dN/d\phi$ has been divided into 10 equal size bins and the correlation coefficient is presented as a function of separation of the centers of the corresponding bins.

Considering Fig.(7.12) one firstly notes that when disregarding exact conservation of P_x and P_y the correlation coefficients are insensitive to the distance ϕ_{gap} of any two bins. Only the correlations due to energy and charge conservation affect the result. Charge conservation leads to correlation of unlike-sign particles and to anti-correlation of like-sign particles. Energy conservation always anti-correlates multiplicities in two bins. For $\rho_{\pm\pm}$ the effect of charge conservation cancels for a neutral system, however, effects of energy-momentum conservation are stronger, as a larger number of particles (hence a larger part of the total system) is observed.

Conservation of transverse momenta P_x and P_y is now responsible for the ϕ_{gap} dependence of ρ. The line of arguments is similar to the ones before: Observing a larger (smaller) number of particles in some bin at ϕ_0 implies that, in order

[1]Only globally equilibrated systems are considered, and elliptic flow is disregarded here.

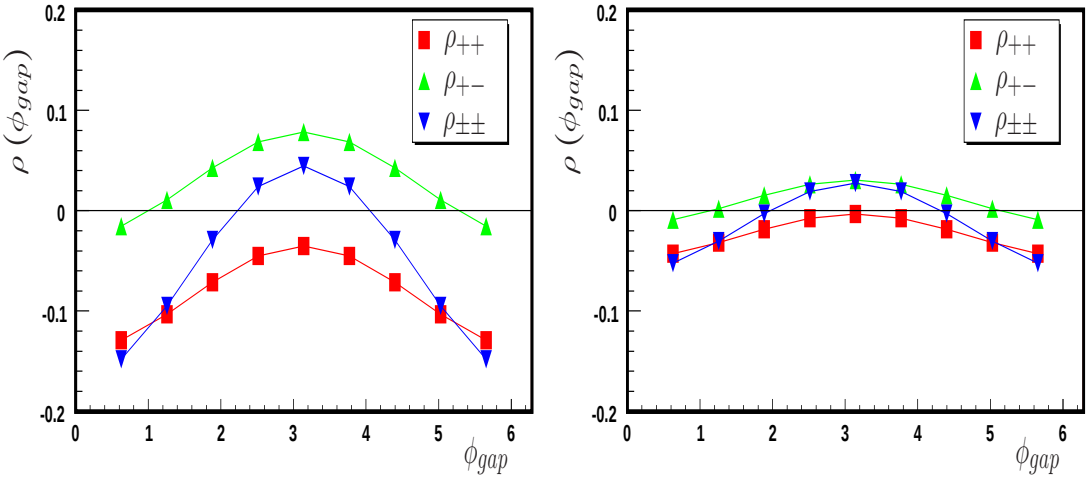

Figure 7.12: The correlation coefficients of particles in distinct $\Delta\phi$ bins as a function of separation ϕ_{gap} in azimuth. (*Left:*) integrated over all phase space. (*Right:*) only particles with $|y| < 0.3$ are observed. Both plots show MCE MB results. No elliptic flow is considered.

to balance momenta $P_x = P_y = 0$, one should also observe a larger (smaller) number of particles in the opposite direction $\pi - \phi_0$. A larger (smaller) number of particles in a bin with $\phi_{gap} = \pi/2$ would do little to help to balance momentum, but conflict with energy conservation.

The observable effects of energy-momentum conservation are weaker, if the experimental acceptance only covers a mid-rapidity region of $|y| < 0.3$, as in Fig.(7.12) (*right*), rather than the whole rapidity distribution, Fig.(7.12) (*left*).

7.3 Discussion

In this chapter multiplicity fluctuations and correlations in limited momentum bins for ideal relativistic gases have been discussed in the MCE in the thermodynamic limit. For the discussion a gas with three degenerate massive particles (positive, negative, neutral) in three different statistics (Maxwell-Boltzmann, Fermi-Dirac, Bose-Einstein) was chosen.

For the width of multiplicity distributions in limited bins of momentum space a simple and intuitive picture emerges. In the Maxwell-Boltzmann approximation one finds a wider distribution for momentum bins with low average momentum when compared to bins with higher average momentum but same average

particle number. This qualitative behavior is a direct consequence of energy and momentum conservation. The results in Fermi-Dirac and Bose-Einstein statistics, furthermore, show pronounced effects at the low momentum tail of the spectrum.

The correlation coefficient additionally shows a similar qualitative behavior. In bins with low average momentum the correlation coefficient between positively and negatively charged particles is indeed positive, as one would expect from charge conservation. However, in bins with large average momentum the effects of joint energy and momentum conservation can lead to anti-correlated distributions of unlike-charged particles.

The role of exactly imposed motional conservation laws is particularly important for systems with collective velocity. Fluctuations and correlations transform under boosts, provided momentum conservation along the boost direction is taken into account. This ensures, in particular, that they become boost-invariant if the underlying system is boost-invariant.

Lastly, it was found that even in the thermodynamic limit long range correlations between disconnected regions in momentum space prevail. Multiplicities in different bins in rapidity, transverse momentum, or in azimuth, can have a non-zero correlation coefficient.

Chapter 8

The Phase Diagram

In this chapter the statistical properties of a hadron resonance gas are studied in their dependence on 'freeze-out' parameters, and choice of ensemble. Fully phase space integrated extensive quantities are investigated, omitting limited acceptance effects, but still considering resonance decay.

Preceding chapters were mostly concerned with neutral and static gases. Attention was given, in particular, to the consequences of limited acceptance in momentum space. Here, fully phase space integrated fluctuations and correlations observables for a hadron resonance gas will be studied in their dependence on energy and net-baryon density. For simplicity, remaining chemical potentials are chosen to be zero. Thus, mesons and anti-mesons contribute equally to the partition function. But as, for instance, the proton carries electric charge, and the Λ carries strangeness, the system is only for $\mu_B = 0$, i.e. equal baryon and anti-baryon contribution, also electric charge and strangeness neutral. For positive μ_B, while $\mu_Q = \mu_S = 0$, the system has positive electric charge density and negative strangeness density. For this discussion the phase space occupancy factors [116, 117, 118] are taken to be $\gamma_s = \gamma_q = 1$. Nevertheless, the constant average energy per average particle multiplicity $\langle E\rangle/\langle N\rangle \simeq 1$ GeV freeze-out line [20] is shown for orientation.

Above this freeze-out line the following discussion should be taken with a caveat mentioned: First and foremost, a phase transition is expected to occur. Degrees of freedom should hence be deconfined quarks and gluons, not hadrons. Furthermore, even on the hadronic side, inclusion of Hagedorn states might become important close to the phase transition line [149, 150]. The exponentially

rising Hagedorn mass spectrum [83] then would lead to a diverging partition function, above a certain limiting temperature, and the phase is not even defined. This discontinuity could in principle be fixed [151, 152], by allowing for a transition to a bag model phase. Quantum number configurations or decay channels of these Hagedorn states or bags[1] are however unknown, and would have to be assumed. The chemical freeze-out line could be seen as an estimate of where in the phase diagram these effects would become important.

It is stressed, again, that no hadronic phase should exist above the freeze-out line. It should also be mentioned that, in principle, the intensive variables T and μ_B are an unconventional choice to present MCE (or CE) correlation functions. Nevertheless, this choice of presentation was made, to allow for a comparison of statistical properties of different ensemble formulations at different energy and net-baryon densities. To highlight certain aspects, phase diagrams are extended to negative values of μ_B.

In the CE or MCE charge correlation and fluctuations would be vanishing in full acceptance, since charges (or additionally energy and momentum) are exactly conserved in these ensembles. As discussed in Chapter 5, charge fluctuations are determined by the thermodynamic bath available, and remain, full acceptance assumed, unaffected by resonance decay. Charge, energy and momentum conservation is respected by each decay process (weak decays omitted). In contrast to this, multiplicity correlation coefficients in the primordial GCE are equal to zero, while multiplicity fluctuations are Poissonian in the Boltzmann approximation. Correlations in the GCE appear due to resonance decay, and are strongly modified, along with a suppression of multiplicity fluctuations, by conservation laws in the CE or MCE, see Chapters 6 and 7.

Acceptance effects are neglected here. The correlation coefficients and variances studied here, with full acceptance assumed, would also exhibit the qualitative behavior presented in Chapters 4 for charge correlations, and Chapters 6 and 7 for multiplicity fluctuations and correlations.

The T-μ_B phase diagram will be explored for GCE charge correlations and fluctuations in Section 8.1, while in Sections 8.2 and 8.3 multiplicity correlations and fluctuations will be discussed in different ensembles.

[1]The terms Hagedorn state, string, cluster, bag, or resonance are used equivalently in this chapter. The only property they are required to have is that they decay into hadrons.

8.1 Charge Correlations and Fluctuations

In Fig.(8.1) grand canonical correlation coefficients between charges are shown in their dependence on the freeze-out parameters T and μ_B. The correlation coefficients ρ_{BS}, ρ_{BQ}, and ρ_{SQ}, as well as related variances and covariances are symmetric around $\mu_B = 0$ in the T-μ_B phase diagram. The sum of baryon and anti-baryon yield is equal in systems with baryon chemical potentials of opposite sign, since here additionally remaining chemical potentials are chosen to be $\mu_S = \mu_Q = 0$. Further, one finds $\langle \Delta B \Delta S \rangle$, $\langle \Delta B \Delta Q \rangle$, $\langle (\Delta Q)^2 \rangle$, etc. to be the same for μ_B and $-\mu_B$, due to equal contributions of particles and their anti-particles. The meson contribution then only depends on the temperature. The discussion will proceed by considering the four corners of the phase diagrams depicted in Fig.(8.1), starting from the bottom left.

At low T and μ_B the systems is mostly composed of pions. Accordingly one finds the correlation coefficients $\rho_{BS} \simeq \rho_{BQ} \simeq \rho_{SQ} \simeq 0$ in the bottom left corners of phase diagrams shown in Fig.(8.1). The system is too cold to populate states with hadrons which could mediate the correlation. Pions carry only electric charge, and thus cannot correlate to the strangeness and baryon number content of the system.

As T is increased, but still at small μ_B, the system starts to equally excite baryon and anti-baryon states. The correlation between baryon number and strangeness content of the system, ρ_{BS}, therefore grows negative due to emerging Λ and $\overline{\Lambda}$ states. Compared to ρ_{BS}, the baryon number electric charge correlation coefficient ρ_{BQ} grows more mildly. Protons and anti-protons are being equally produced, yet abundant pions de-correlate the quantum numbers B and Q more strongly than heavier kaons can de-correlate the quantum numbers B and S. Lastly, in the top left corner of Fig.(8.1) (*right*), the strangeness electric charge correlation coefficient ρ_{SQ} has a peak. All mesons and baryons (except the Σ^+) contribute positively to the covariance $\langle \Delta S \Delta Q \rangle$. The combined contribution of particles and anti-particles at a given temperature is strongest in charge neutral matter. Only at rather large temperature heavy Σ^+ resonances (and their anti-particles) start to again decrease ρ_{SQ}.

The bottom right corners in Fig.(8.1) represent a hadronic phase of low temperature and large net-baryon density. The correlation coefficient of baryon number and strangeness ρ_{BS} grows in this direction due to Λ production. The system

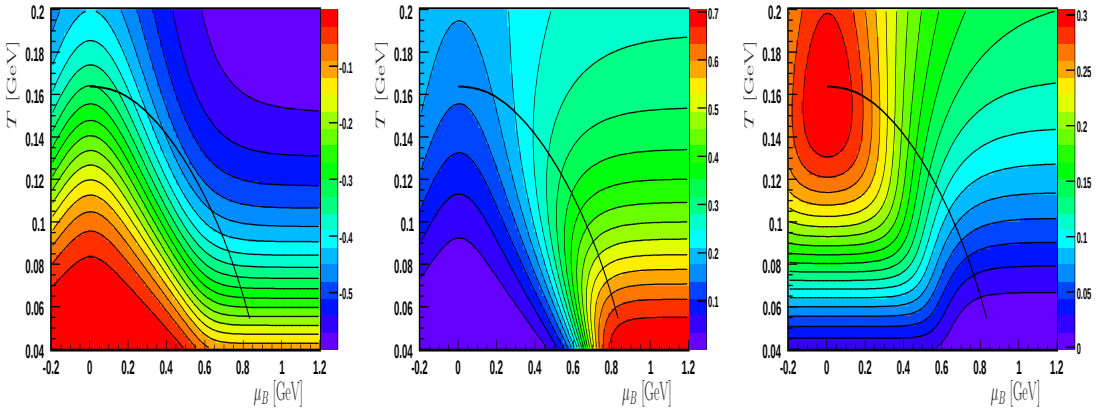

Figure 8.1: Phase diagram showing grand canonical charge correlation coefficients of baryon number and strangeness ρ_{BS} (*left*), baryon number and electric charge ρ_{BQ} (*center*), and strangeness and electric charge ρ_{SQ} (*right*). The solid line indicates the $\langle E\rangle/\langle N\rangle = 1$ GeV chemical freeze-out line [20].

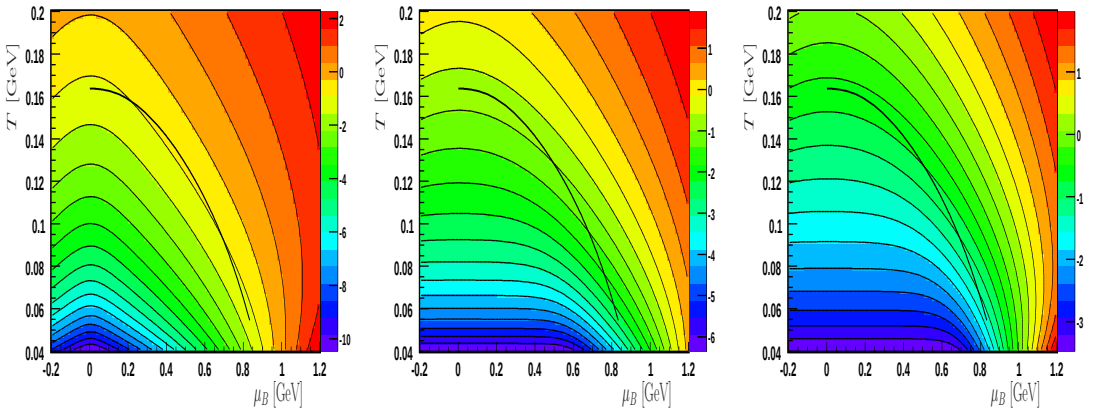

Figure 8.2: Phase diagram showing normalized grand canonical charge fluctuations of baryon number $\langle(\Delta B)^2\rangle$ (*left*), strangeness $\langle(\Delta S)^2\rangle$ (*center*), and electric charge $\langle(\Delta Q)^2\rangle$ (*right*). The color scale is logarithmic.

is on the other hand is too cold to produce kaons, which could de-correlate the quantum numbers B and S, in sufficient numbers. As protons (and neutrons or light Δs) are the dominant particles in this phase, the correlation between baryon number and electric charge ρ_{BQ} is particularly strong. And, as kaons are not sufficiently produced at low temperature (and the Λ is electrically neutral), ρ_{SQ}, the strangeness electric charge correlation coefficient, remains small at small T. The increase of ρ_{SQ} for large μ_B is due to the onset of Σ production.

Finally, moving into the top right corners in Fig.(8.1), with the above mentioned caveat in mind. The correlation ρ_{BS} becomes strongly negative in hot net-baryon rich matter, as strangeness carrying baryons are produced abundantly. The correlation ρ_{BQ} stays modest as heavy negatively charged baryons emerge too, and like pions, de-correlate the systems electric net-charge from its net-baryon number content. Much for the same reasons ρ_{SQ} stays modest, too. Here heavy Σ^+ resonances decrease the correlation.

In Fig.(8.2) grand canonical charge fluctuations are shown in their dependence on the freeze-out parameters T and μ_B on a logarithmic color scale. The variance is, unlike the correlation coefficient, an extensive quantity. The variances are therefore shown normalized to an unit volume. In a neutral system, with symmetric particle and anti-particle contribution to the partition function, charge fluctuations are largest. With increasing temperature, not only average occupation numbers, but also fluctuations in occupation numbers on individual momentum levels grow. Accordingly, net-charge fluctuations become stronger. For increasing μ_B, i.e. average baryon occupation numbers are enhanced, while occupation numbers of anti-baryons are suppressed by Boltzmann factors $e^{\pm\mu_B\beta}$, charge fluctuations decrease. At low temperature, few particles are produced, and the net-charge content of the system cannot fluctuate much. As μ_B is increased at low T, baryon states are populated due to charge density. The net-charge content of the system can then fluctuate, by virtue of μ_B induced particle density.

The baryon number variance $\langle(\Delta B)^2\rangle$ in Fig.(8.2) (*left*) increases rapidly with baryon density and temperature. At low T and μ_B essentially no baryon states are occupied, and hence their number cannot fluctuate strongly. The strangeness variance $\langle(\Delta S)^2\rangle$ in Fig.(8.2) (*center*) and electric charge variance $\langle(\Delta Q)^2\rangle$ in Fig.(8.2) (*right*) are similar. Strangeness and electric charge density are introduced indirectly via the baryons p and Λ. Although the strangeness and electric charge variances are initially larger, they grow more slowly than the baryon number variance. The mass difference between the lightest baryons and mesons becomes less important at very large temperature, and $\langle(\Delta B)^2\rangle$ eventually overtakes $\langle(\Delta S)^2\rangle$ and $\langle(\Delta Q)^2\rangle$.

In direction from bottom left to top right in Figs.(8.1,8.2), i.e. increasing both T and μ_B, a transition from a mesonic to baryonic matter [153] occurs. The variance $\langle(\Delta B)^2\rangle$ and the correlation coefficient ρ_{BS} grow as the entropy of the

system is increasingly carried by baryons. If one would instead follow the $\langle E\rangle/\langle N\rangle$ freeze-out line one would observe a monotonous decrease in ρ_{BQ} as colliding beam energy is increased, due to emerging pion production de-correlating the charges B and Q. The correlation between S and Q, ρ_{SQ}, on the other hand, increases, because kaons, and not Λ, now carry the bulk of the system strangeness at large center of mass energy. Along the freeze-out line ρ_{BS} has a strong minimum around $T \sim 0.13$ GeV and $\mu_B \sim 0.5$ GeV. The strangeness and electric charge variances $\langle(\Delta S)^2\rangle$ and $\langle(\Delta Q)^2\rangle$ increase along this line, while $\langle(\Delta B)^2\rangle$ stays more or less flat.

8.2 Multiplicity Correlations

In this section the correlation coefficients $\rho_{\mathrm{p}\pi^+}$ and $\rho_{\mathrm{p}\pi^-}$ between the event-by-event multiplicities of protons, N_{p}, and either of the charged pions, N_{π^+} and N_{π^-} are studied for different ensembles. The discussion is then extended to multiplicity fluctuations of positively and negatively charged hadrons ω_+ and ω_-. The hadrons p and $\pi^\pm$ are the most abundant charged particles, and their relative yield determines structure of the T-μ_B phase diagram to a large extent. In turn, GCE, CE, and MCE correlation functions will be compared. Resulting (primordial) correlations are not due to local interaction amongst constituents, but due to globally implemented conservation laws for energy and charge.

Grand Canonical Ensemble

The multiplicities of any two distinct groups of primordial particles are uncorrelated in the grand canonical ensemble, $\rho = 0$, due to the infinite thermodynamic bath assumption. Their joint distribution factorizes into a product of two Poissonians with scaled variance $\omega = 1$. In the final state grand canonical ensemble the proton and charged pion multiplicities are correlated by the decay of parent baryons N. The following decay channels, containing protons and charged pions,

are considered:

$$N^- \longleftrightarrow \mathrm{p} + \pi^- + \pi^- \tag{8.1}$$
$$N^0 \longleftrightarrow \mathrm{p} + \pi^- \tag{8.2}$$
$$N^+ \longleftrightarrow \mathrm{p} + \pi^+ + \pi^- \tag{8.3}$$
$$N^{++} \longleftrightarrow \mathrm{p} + \pi^+ \tag{8.4}$$

Baryonic resonances can decay into protons and charged pions taking channels of kind (8.1) to (8.4). Negatively charged baryons N^-, could only decay into negatively charged pions and a proton via (8.1). The Δ^- resonances, however, mostly decay via $\Delta^- \rightarrow \mathrm{n} + \pi^-$. Strangeness carrying N^- also cannot strongly populate the channel (8.1), as either daughter particle, baryon or meson, has to pick up the strange quark. The channel (8.2) for decay of neutral baryons N^0 is also not too efficient. Two thirds of neutral baryons decay via $N^0 \rightarrow \mathrm{n} + \pi^0$ due to "Clebsch-Gordan" coefficients. Although most low lying Δ^+ decay via the channel (8.3), $\Delta^+ \rightarrow \mathrm{p} + \pi^0$, and do hence not contribute much to either correlation coefficient, heavier Δ^+ resonances, often produce several pions, and positively correlate p with both, π^+ and π^-. Finally, channels (8.4) are abundant due to a strong contribution of the $\Delta^{++}(1232)$ resonance and its degenerate states.

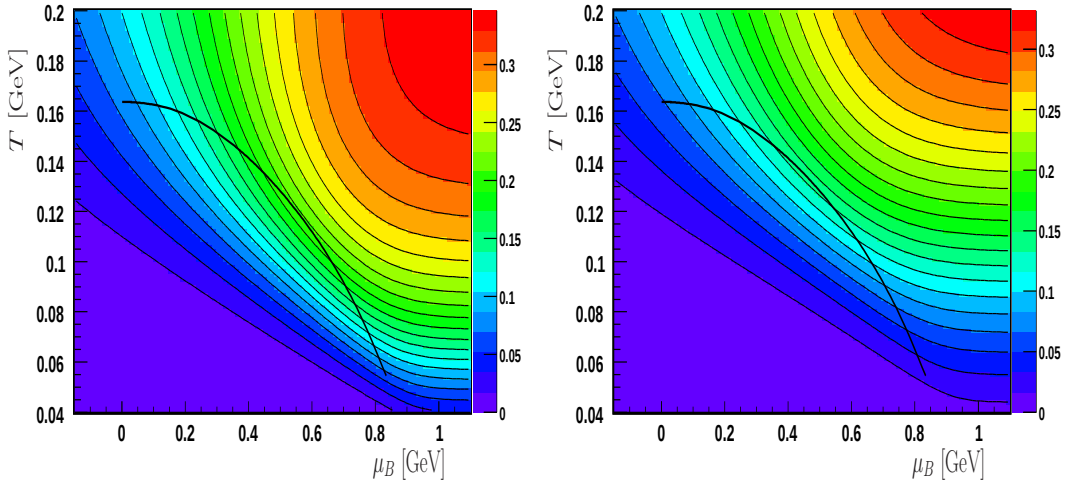

Figure 8.3: Final state GCE correlation coefficient between the multiplicities of protons and positively charged pions $\rho_{\mathrm{p}\pi^+}$ (*left*), and between the multiplicities of protons and negatively charged pions $\rho_{\mathrm{p}\pi^-}$ (*right*).

The reverse arrows indicate back-reactions. The strong interaction between the ground state hadrons proton, neutron, and pion is conceptually taken into account in the hadron resonance gas model by inclusion of resonance states which mediate the interaction [154, 155]. In thermal and chemical equilibrium reaction rates are the same in both directions. The system is said to have attained "detailed balance". Only the existence of resonances states is relevant, and not how many particles are involved in each microscopic reaction. The ability of a non-equilibrium state to evolve into a chemical equilibrium state, on the other hand, is strongly increased by multi-hadronic (or Hagedorn) channels [150].

Hence, in the final state GCE, Fig.(8.3), both, π^+ and π^- are positively correlated with p. Phase diagrams showing multiplicity correlations are generally not symmetric around $\mu_B = 0$. The correlation is particularly strong in hot baryonic matter. For negative μ_B either correlation coefficient $\rho_{\mathrm{p}\pi^+} \simeq \rho_{\mathrm{p}\pi^-} \simeq 0$, as protons are then suppressed compared to anti-protons. Charged pions would now be strongly correlated with the more abundant anti-protons.

The fact that π^+ are more strongly correlated via resonance decay with p, than the π^-, i.e. $\rho_{\mathrm{p}\pi^-} < \rho_{\mathrm{p}\pi^+}$, can be understood considering reaction channels (8.1) to (8.4). Essentially one may add additional pions ($\pi^+ + \pi^-$) to each channel. Channels (8.1) and (8.2) are not very effective at correlating p and π^-, since they are not very abundant. Channel (8.3) contributes equally to the p-π^- correlation and the p-π^+ correlation, while channel (8.4) strongly correlates p and π^+, yet hardly p and π^-. The influence of the $\Delta^{++}(1232)$ can clearly be seen in a comparison of the bottom right corners of Fig.(8.3) (*left*) to (*right*).

Canonical Ensemble

The event-by-event multiplicities of p and π^+ are anti-correlated in the primordial CE, Fig.(8.4) (*left*), while the multiplicities of p and π^- are positively correlated, Fig.(8.5) (*left*), due to electric charge conservation. Additionally, multiplicity fluctuations of either species are suppressed in the CE (see also Chapter 9).

The multiplicities of the hadrons p and π^+ are most strongly anti-correlated at low T and large μ_B. The multiplicity of baryons cannot fluctuate strongly in cold net-baryon rich matter, due to suppressed anti-baryon states, compare Fig.(8.2) (*left*). Charge conservation now requires that once one removes (adds)

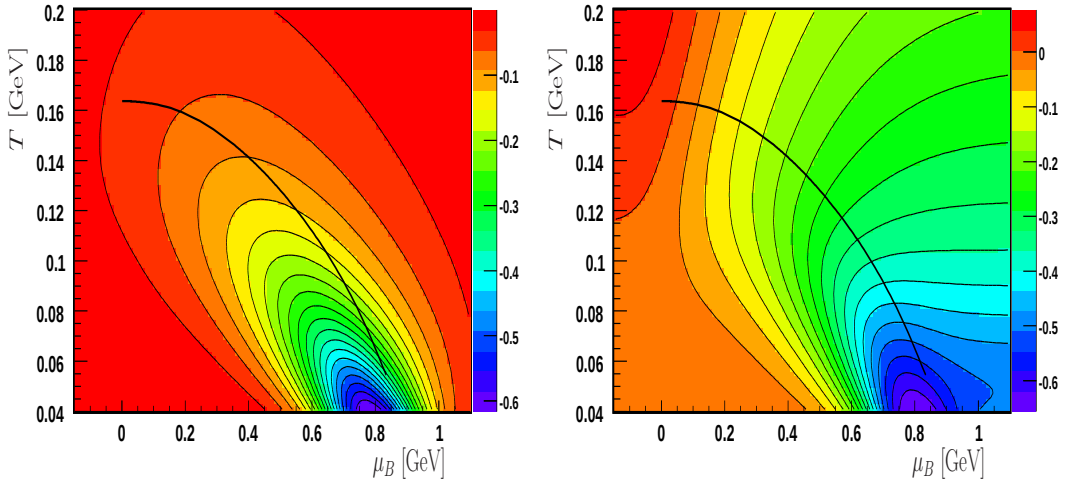

Figure 8.4: CE correlation coefficient between the multiplicities of protons and positively charged pions $\rho_{\mathrm{p}\pi^+}$. Both, primordial (*left*), and final state (*right*).

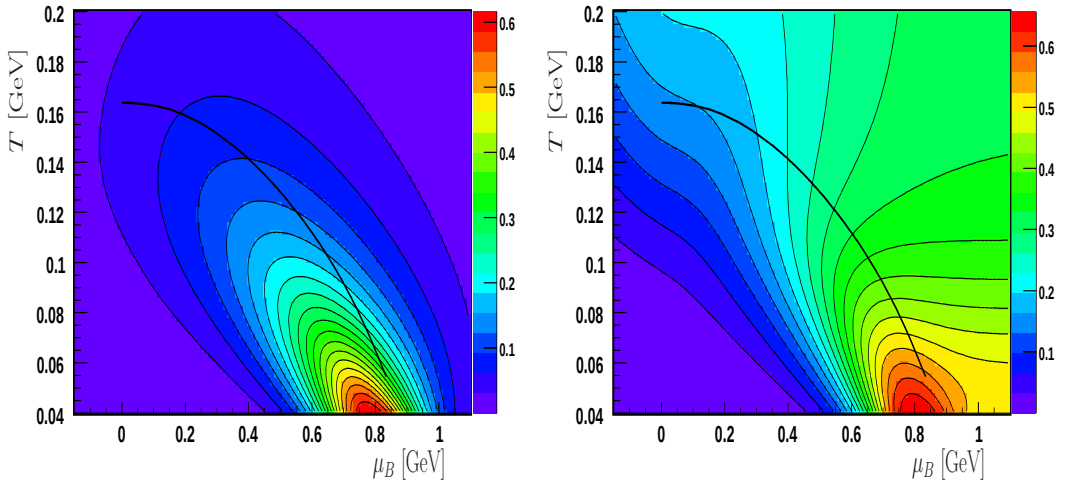

Figure 8.5: CE correlation coefficient between the multiplicities of protons and negatively charged pions $\rho_{\mathrm{p}\pi^-}$. Both, primordial (*left*), and final state (*right*).

a proton from (to) the system, to add (remove) a neutron and a positively charged pion, $\mathrm{p} \leftrightarrow \mathrm{n} + \pi^+$. The system is too cold to allow for strong baryon multiplicity fluctuations[2]. In a neutral, but hot, hadron resonance gas the anti-correlation is weaker, since channels involving anti-baryons are open. In a hot and baryon rich phase, the appearance of heavy Δ resonances makes the p-π channel less

[2]Energy fluctuations in the CE are also suppressed in comparison to the GCE [93].

influential, and accordingly $\rho_{\mathrm{p}\pi^+} \simeq 0$ there.

For the final state CE correlation coefficient $\rho_{\mathrm{p}\pi^+}$, in Fig.(8.4) (*right*), the anti-correlation between p and π^+ extents to high μ_B and T. Primordial parent particles, in particular positively charged Δ resonances, are anti-correlated, due to baryon number and electric charge conservation, with primordial p and π^+. These Δ decay into both, p and π^+, and partially re-correlate their multiplicities, yet an residual anti-correlation remains. At low T and low μ_B the correlation is then weaker, since the system is too cold to produce sufficient baryonic resonances which could correlate p and π^+ via their decay, i.e. the primordial and the final state scenario $\rho_{\mathrm{p}\pi^+}$ are similar in this region of the phase diagram. At high T, but $\mu_B \simeq 0$, the final state correlation coefficient is positive, $\rho_{\mathrm{p}\pi^+} > 0$, unlike one would expect from electric charge conservation. In a neutral and hot hadron resonance gas, baryon and anti-baryon number fluctuations are sufficient, to de-correlate primordial p and π^+. The positive resonance decay contribution causes then an overall positive correlation. In final state GCE one always finds $\rho_{\mathrm{p}\pi^+} > 0$.

In the primordial CE, one finds the correlation coefficient between the multiplicities of p and π^- to be positive, $\rho_{\mathrm{p}\pi^-} > 0$, Fig.(8.5) (*left*), due to electric charge conservation. Their correlation is particularly strong for low T and large μ_B, since there baryon multiplicity fluctuations are strongly suppressed, making the channel $\mathrm{n} \leftrightarrow \mathrm{p} + \pi^-$ dominant. The correlation is weaker elsewhere in the T-μ_B phase diagram. The final state $\rho_{\mathrm{p}\pi^-}$, Fig.(8.5) (*right*), is similar to the primordial scenario for low temperature. For larger T and μ_B, resonance decay then again correlates the event-by-event multiplicities of p and π^-, when compared to the primordial scenario.

Micro Canonical Ensemble

The primordial MCE correlation coefficient $\rho_{\mathrm{p}\pi^+}$, Fig.(8.6) (*left*), is generally weaker than its CE counterpart $|\rho^{mce}_{\mathrm{p}\pi^+}| < |\rho^{ce}_{\mathrm{p}\pi^+}|$, with the exception of a deeper pocket in the bottom right corner of the phase diagram, denoting cold baryonic matter, where $|\rho^{mce}_{\mathrm{p}\pi^+}| > |\rho^{ce}_{\mathrm{p}\pi^+}|$. The anti-correlation $\mathrm{p} \leftrightarrow \mathrm{n} + \pi^+$ is made stronger at low temperature in the MCE by combined energy and charge conservation. The sum of the multiplicities of p and n cannot vary much due to strongly suppressed $\overline{\mathrm{p}}$ and $\overline{\mathrm{n}}$ yields. The anti-correlation between the multiplicities of p and π^+ is strongly mediated by the n multiplicity. At larger temperature other channels,

like $\Delta^+ \leftrightarrow \mathrm{n} + \pi^+$, seem preferable for energy conservation. Charge conservation does not distinguish between these two channels, leading to $|\rho^{ce}_{\mathrm{p}\pi^+}| > |\rho^{mce}_{\mathrm{p}\pi^+}|$ elsewhere in the phase diagram, except in the pocket.

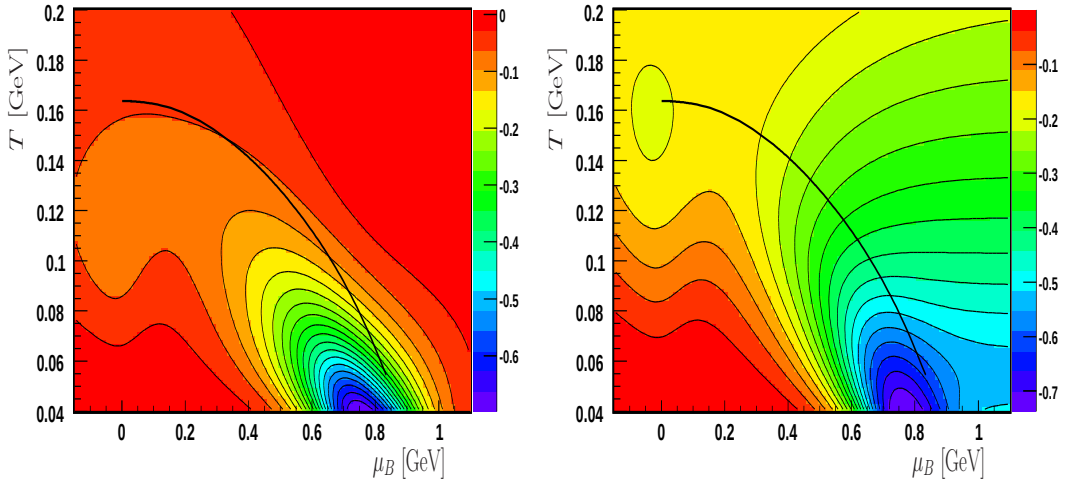

Figure 8.6: MCE correlation coefficient between the multiplicities of protons and positively charged pions $\rho_{\mathrm{p}\pi^+}$. Both, primordial (*left*), and final state (*right*).

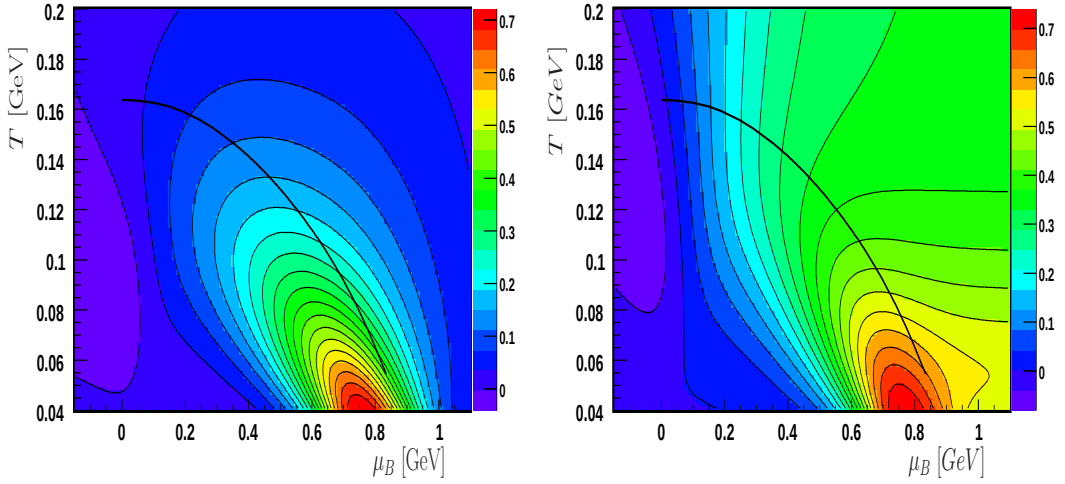

Figure 8.7: MCE correlation coefficient between the multiplicities of protons and negatively charged pions $\rho_{\mathrm{p}\pi^-}$. Both, primordial (*left*), and final state (*right*).

The final state MCE correlation coefficient $\rho_{\mathrm{p}\pi^+}$, Fig.(8.6) (*right*), is negative, $\rho_{\mathrm{p}\pi^+} < 0$, and notably stronger than in the final state CE. Energy conservation,

and hence anti-correlation between primordial parent particles and primordial p and π^+, is responsible.

The primordial MCE correlation coefficient $\rho_{\mathrm{p}\pi^-}$, Fig.(8.7) (*left*), is again positive, $\rho_{\mathrm{p}\pi^-} > 0$, like in the CE. The channel $\mathrm{n} \leftrightarrow \mathrm{p} + \pi^-$ is not much affected by additional energy conservation, with the notable exception of a stronger positive correlation $\rho^{mce}_{\mathrm{p}\pi^-} > \rho^{ce}_{\mathrm{p}\pi^-}$ in cold baryonic matter.

From a comparison to the final state MCE correlation coefficient $\rho_{\mathrm{p}\pi^-}$, Fig.(8.7) (*right*), again a positive resonance decay contribution is visible. One notes that the CE enhancement in net-baryon free and hot matter has vanished in the MCE. Energy fluctuations in the CE at a given temperature are strongest if the system is charge neutral. In the MCE the energy content is fixed, and anti-correlation amongst primordial parent resonance and primordial p and π^+ balances the enhancement due to resonance decay.

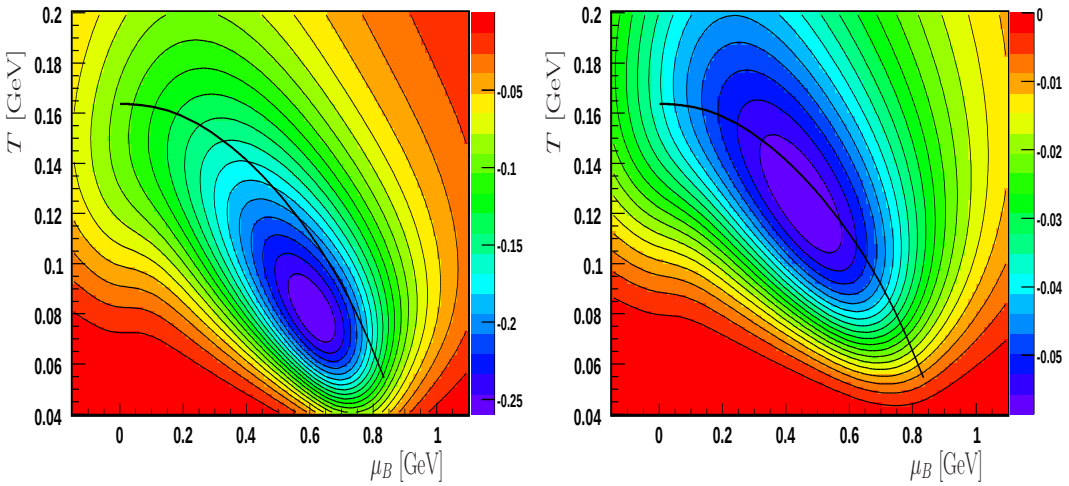

Figure 8.8: Primordial MCE correlation coefficient between the multiplicities of the doublely charged $\Delta^{++}(1232)$ and positively charged pions $\rho_{\Delta^{++}(1232)\pi^+}$ (*left*), and between the multiplicities of the doublely charged $\Delta^{++}(1600)$ and positively charged pions $\rho_{\Delta^{++}(1600)\pi^+}$ (*right*).

To conclude the discussion of multiplicity correlations primordial MCE correlation coefficient between the multiplicities of the doublely charged $\Delta^{++}(1232)$ and positively charged pions $\rho_{\Delta^{++}(1232)\pi^+}$, and between the multiplicities of the doublely charged $\Delta^{++}(1600)$ and positively charged pions $\rho_{\Delta^{++}(1600)\pi^+}$, are shown in Fig.(8.8) (*left*) and (*right*) respectively.

The Δ resonances have larger rest-mass than the ground state nucleons n and p. Hence, they start to contribute to the system partition function only at larger T, and preferably at large μ_B. The correlation between the event-by-event multiplicities of Δ resonances and π mesons is the stronger the larger a fraction of the total energy density they make up. The maxima in Fig.(8.8) (*left*) and (*right*) are hence in different positions. The heavier particle shows a weaker correlation. The correlation coefficients $\rho_{\Delta^{++}(1232)\pi^+}$ and $\rho_{\Delta^{++}(1600)\pi^+}$ should be compared to the primordial MCE $\rho_{\mathrm{p}\pi^+}$ in Fig.(8.6) (*left*). The CE yields a similar structure. In the GCE no primordial correlations appear in the ideal gas approximation.

Meson Baryon Correlations

Lastly, the correlation coefficients $\rho_{\mathcal{MB}}$ between the event-by-event multiplicities of mesons plus anti-mesons, $N_{\mathcal{M}} = N_{\mathrm{M}} + N_{\overline{\mathrm{M}}}$, and the event-by-event multiplicities of baryon plus anti-baryons, $N_{\mathcal{B}} = N_{\mathrm{B}} + N_{\overline{\mathrm{B}}}$, are considered in different ensembles. In Fig.(8.9) the temperature - baryon chemical potential phase diagram is shown for the final state correlation coefficient $\rho_{\mathcal{MB}}$ in the GCE (*left*) and CE (*right*). In Fig.(8.10) the MCE correlation coefficient $\rho_{\mathcal{MB}}$ is shown, both primordial (*left*) and final state (*right*).

No primordial correlation amongst distinct groups of hadrons exists in the GCE. Resonance decay is then again the only source of correlation, Fig.(8.9) (*left*), between mesons and baryons. Yet, resonances essentially do not decay into baryon anti-baryon pairs, $\mathrm{B} + \overline{\mathrm{B}}$. At low temperature, where few resonances are formed, the correlation coefficient is then $\rho_{\mathcal{MB}} \sim 0$. On the other hand, when the net-baryon density is large (positive or negative), either baryon or anti-baryons are strongly suppressed, and the multiplicities $N_{\mathcal{M}} = N_{\mathrm{M}} + N_{\overline{\mathrm{M}}}$, are essentially correlated with N_{B} ($\mu_B > 0$) or $N_{\overline{\mathrm{B}}}$ ($\mu_B < 0$).

Also in the CE primordial correlations are absent, due to the particular choice made for strangeness and electric charge chemical potentials $\mu_Q = \mu_S = 0$. Resonance decay enhancement, Fig.(8.9) (*right*), is again visible at large T and μ_B. At large T, but small μ_B, however the correlation coefficient is somewhat stronger (than in the GCE). The expectation value of the sum of baryons plus anti-baryons $N_{\mathcal{B}} = N_{\mathrm{B}} + N_{\overline{\mathrm{B}}}$ is largest (at a given temperature) for charge neutral matter. However, the strangeness and electric charge content of the baryonic sector is still fluctuating, leading to a weak and positive correlation to the mesonic

sector.

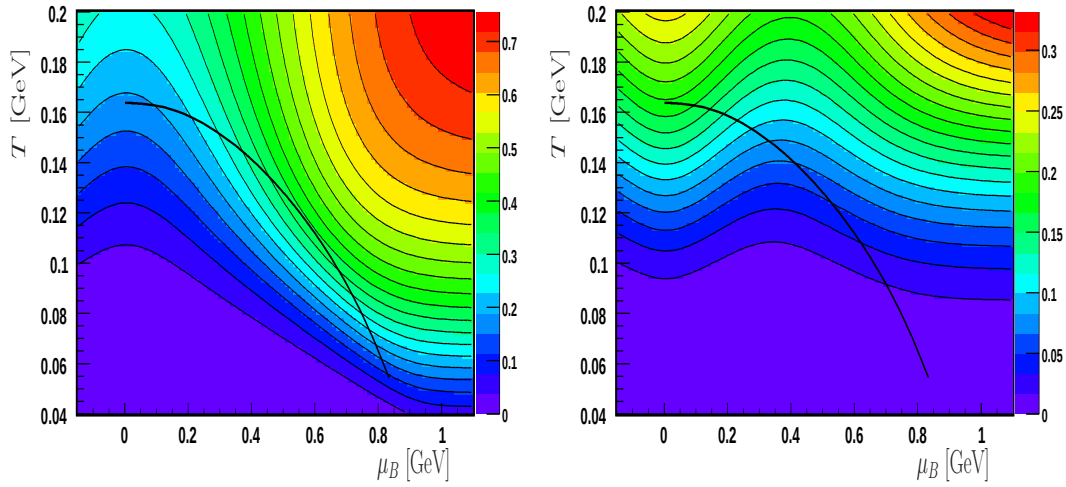

Figure 8.9: Final state correlation coefficient $\rho_{\mathcal{MB}}$ between the event-by-event multiplicities of mesons plus anti-mesons and baryon plus anti-baryons in the GCE (*left*) and CE (*right*).

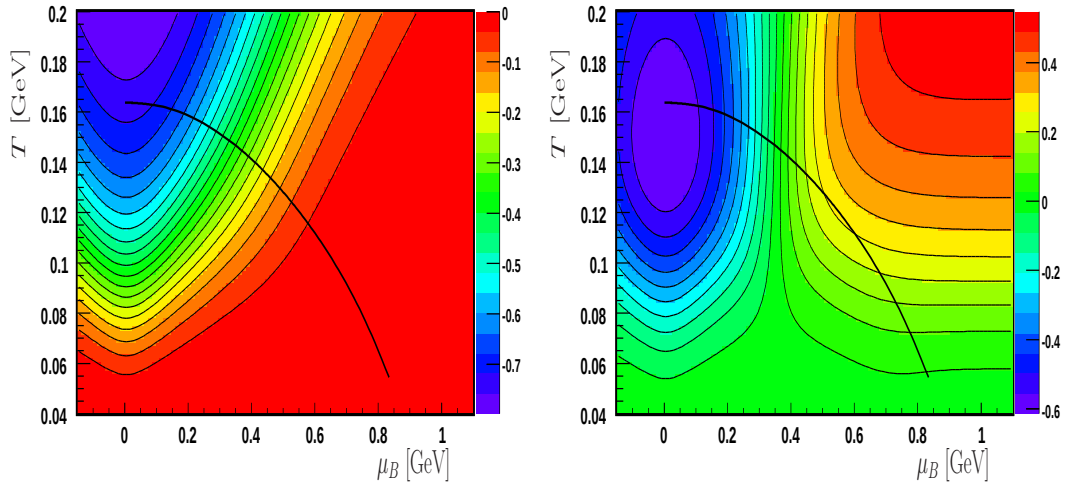

Figure 8.10: MCE correlation coefficient $\rho_{\mathcal{MB}}$ between the event-by-event multiplicities of mesons plus anti-mesons and baryon plus anti-baryons in the MCE, both, primordial (*left*) and final state (*right*).

In the primordial MCE, Fig.(8.10) (*left*) one observes a strong correlation between the event-by-event multiplicities of mesons plus anti-mesons and baryon plus anti-baryons. Unlike in the GCE and CE, the primordial MCE correlation

coefficient is non-vanishing and negative, $\rho_{\mathcal{MB}} < 0$. The difference between the multiplicities of baryons and of anti-baryons, i.e. the system baryon number is conserved, $B = N_{\rm B} - N_{\overline{\rm B}}$. Yet, fluctuations of their sum, $N_{\mathcal{B}} = N_{\rm B} + N_{\overline{\rm B}}$, however release or bind a large amount of energy. But as energy is conserved in the MCE, the multiplicity $N_{\mathcal{M}} = N_{\rm M} + N_{\overline{\rm M}}$ needs to adjust. Energy is spent either on the production of a baryon anti-baryon pair, or on the production of a few (> 2) mesons and anti-mesons. This effect is particularly strong in hot and neutral matter. Resonance decay in the MCE, Fig.(8.10) (*right*), leads again to a positive correlation large T and μ_B amongst final state hadrons, yet, a strong anti-correlation at large T and $\mu_B \sim 0$ remains.

Following the $\langle E\rangle/\langle N\rangle \simeq 1$ GeV freeze-out line of Fig.(8.10) (*right*), one would observe a weak positive correlation at small $\sqrt{s_{NN}}$, and a strong anti-correlation at large $\sqrt{s_{NN}}$. In the SPS energy range a maximum might emerge. In particular, for the region of the phase diagram accessible to RHIC experiments, the MCE formulation implies that some events will be mostly composed of mesons and anti-mesons, while other events should be mostly composed of baryons and anti-baryons. The bulk of the events should be quite normal, but some events could be either predominantly mesonic (bosonic) or predominately baryonic (fermionic).

8.3 Multiplicity Fluctuations

In this section the phase diagrams for primordial and final state multiplicity fluctuations of positively and negatively charged hadrons ω_+ and ω_- are compared in CE and MCE in Figs.(8.11-8.14). GCE calculations will, in addition, be presented in Section 9.1.

Some general comments attempt to summarize. At positive μ_B, also the electric charge density is positive. The electric net-charge content of the system $Q = N_+ - N_-$ is conserved. As now the average multiplicity of positively charged hadrons is larger than the one of negatively charged hadrons, $\langle N_+\rangle > \langle N_-\rangle$ (but as the variances ought to be equal, $\langle(\Delta N_+)^2\rangle = \langle(\Delta N_-)^2\rangle$) one finds the multiplicity distribution of positively charged hadrons to be more narrow than the one of negatively charged hadrons, $\omega_+ < \omega_-$. At negative baryon chemical potential μ_B, i.e. for negative electric charge density, the situation is reversed, and $\omega^+ > \omega^-$. Their fluctuations are equal for $\mu_B \simeq 0$.

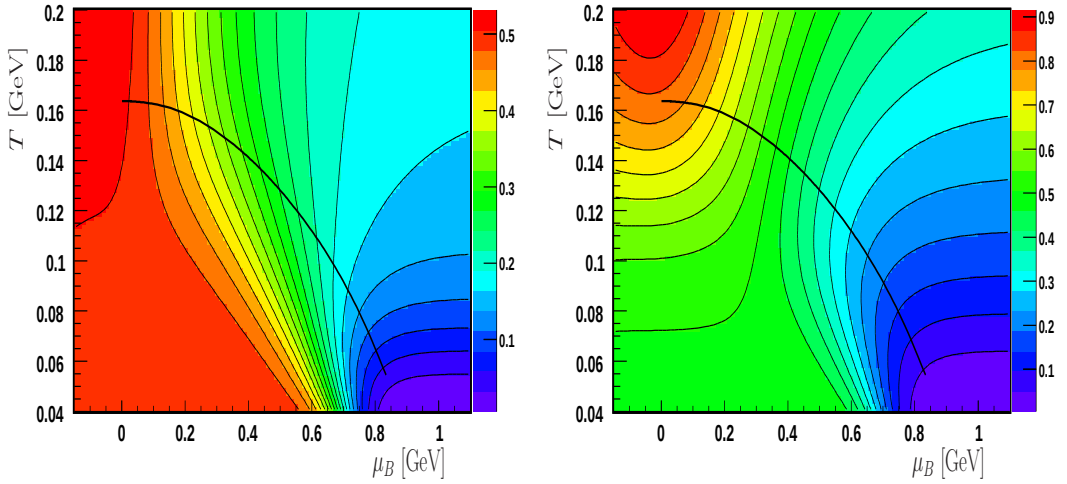

Figure 8.11: CE fluctuations of the multiplicities of positively charged hadrons ω_+. Both, primordial (*left*), and final state (*right*).

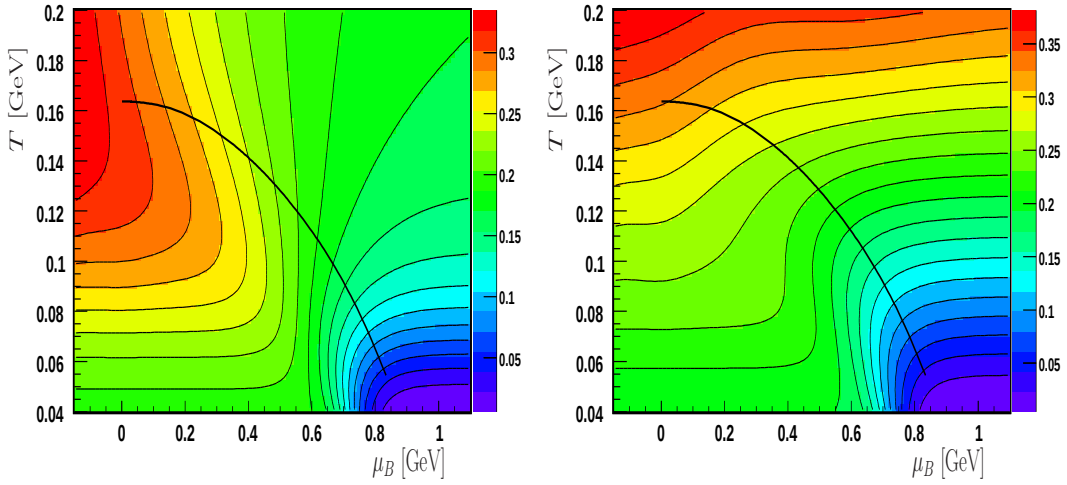

Figure 8.12: MCE fluctuations of the multiplicities of positively charged hadrons ω_+. Both, primordial (*left*), and final state (*right*).

With increasing temperature the system becomes more and more relativistic, and particle number increasingly fluctuates in the MCE. In the CE this is already less apparent. A very mild temperature dependence of the scaled variance of multiplicity fluctuations arises only due to heavy hadrons carrying multiple charges. In a CE with only one species of particles in Boltzmann approximation, the scaled variance in neutral matter is $\omega^+ = \omega^- = 0.5$ [94] independent of temperature. In

the primordial Boltzmann GCE fluctuations are Poissonian independent of either thermal parameter. Note the different color scales in Figs.(8.11-8.14).

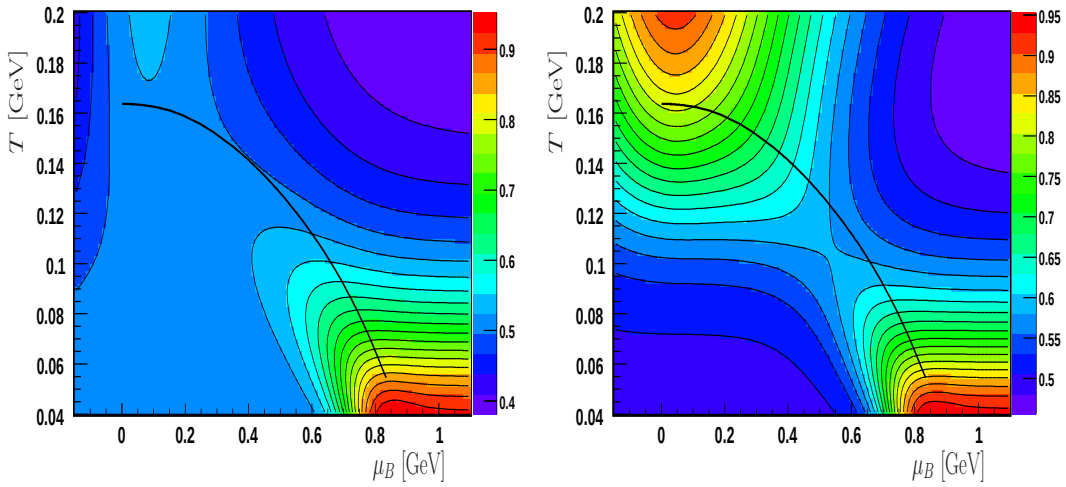

Figure 8.13: CE fluctuations of the multiplicities of negatively charged hadrons ω^-. Both, primordial (*left*), and final state (*right*).

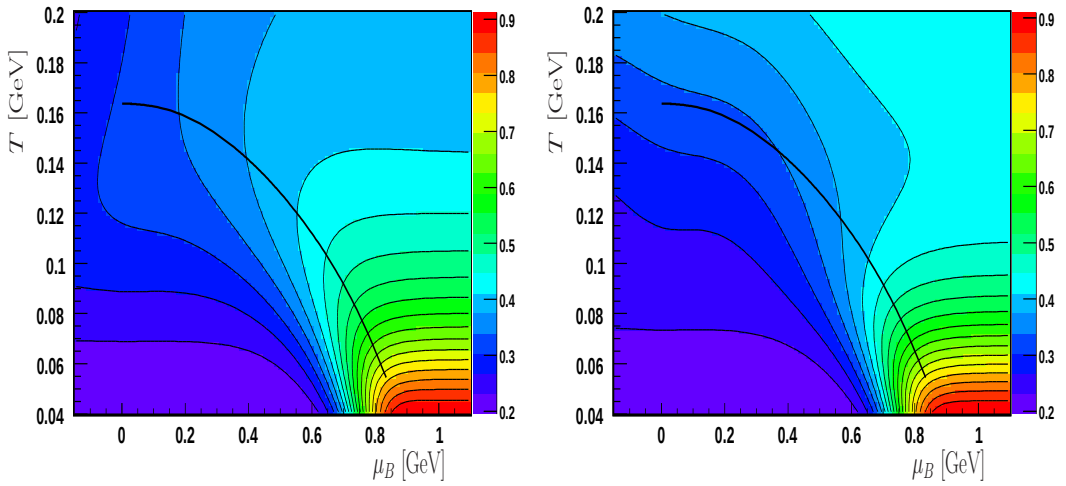

Figure 8.14: MCE fluctuations of the multiplicities of negatively charged hadrons ω^-. Both, primordial (*left*), and final state (*right*).

Comparing primordial CE Fig.(8.11) (*left*) primordial MCE Fig.(8.12) (*left*), one finds at low temperature $\omega_+^{mce} < \omega_+^{ce}$. In a cold gas particle multiplicity of positively charged hadrons cannot fluctuate much due to combined energy

and charge conservation. At large T and μ_B, however very mildly, $\omega_+^{mce} > \omega_+^{ce}$. Baryon multiplicity fluctuations induce meson fluctuations in hot baryonic matter, see Fig.(8.10). The net-baryon number is conserved, $B = N_B - N_{\overline{B}}$. Yet, fluctuations in the sum of baryon number and anti-baryon number, $N_B + N_{\overline{B}}$, release or bind a large fraction of the available energy of the system, with the meson multiplicity adjusting. In the CE, with only charge conservation, meson multiplicity fluctuations are less affected.

A weak, yet generally useful, rule of thumb is: Resonance decay in the CE Fig.(8.11) (*right*) increases ω, while in the MCE Fig.(8.12) (*right*) decreases ω, when compared to their respective primordial scenarios (*left*). With the notable exception of very large T. There it seems more economical to produce particles via decay of resonances, rather than thermally with large kinetic energy due to temperature. The correlation between primordial parents and stable daughters is then weaker. And $\omega_+^{final} > \omega_+^{prim}$ in the MCE is possible. In final state one always finds $\omega_+^{mce} < \omega_+^{ce}$. It is mentioned in this context, that even in the ultra-relativistic limit $\omega^{mce} < \omega^{ce}$ [95].

Having stated this rule of thumb, its caveat shall be discussed. Its validity depends strongly on possible cluster formation and their decay modes[3]. Yet energy can only be spent once. Either on primordial particle production, or the formation of a cluster, bag, string, or Hagedorn state. If particle production via cluster is more economical, i.e. more energy spent "on mass" and less "on motion", then final state fluctuations can be larger than primordial fluctuations in the MCE.

Now, turning to the fluctuations of negatively charged hadrons in the positive μ_B half of the T-μ_B phase diagram, the diagrams depicted in Figs.(8.11,8.12) could be connected to the reflected Figs.(8.13,8.14). The scaled variances of positively and negatively charged hadrons are equal at $\mu_B = 0$. For a change in sign of μ_B, the roles of ω_+ and ω_- are interchanged, i.e. the phase diagrams are not symmetric around $\mu_B = 0$.

The scaled variance ω_- is maximal where the ratio $\langle N_- \rangle / \langle N_+ \rangle$ is minimal, i.e. when the electric charge density is strongly positive. For the primordial case, comparing CE, Fig.(8.13) (*left*) to MCE, Fig.(8.14) (*left*), one finds generally $\omega_-^{mce} < \omega_-^{ce}$. The final state enhancement at low μ_B and large T in

[3]In this context the terms cluster, string, Hagedorn state, or bag are used equivalently.

the CE, Fig.(8.13) (*right*) is due to resonance decay. For the final state MCE, Fig.(8.14) (*right*) this enhancement is weaker, due to correlation of primordial parent resonances with stable particles via energy conservation. Similar to ω_+, at very large T and μ_B one finds $\omega_-^{mce} > \omega_-^{ce}$ in final state. Again, baryon multiplicity fluctuations induce meson multiplicity fluctuations.

8.4 Discussion

The T-μ_B phase diagram of the hadron resonance gas model has been explored in this chapter for fluctuation and correlation observables in their dependence on the chemical freeze-out parameters temperature and baryon chemical potential, omitting limited acceptance effects, but still considering resonance decay.

Grand canonical baryon number, strangeness and electric charge fluctuations and correlations are strongly sensitive to the degrees of freedom, i.e. different particle species, available to the system. The contributions of different hadron species is rather different in different corners of the T-μ_B phase diagram. Mesons dominate at low temperatures. With increasing temperature and net-baryon density however baryonic degrees of freedom take a larger fraction of the system entropy. Two charges are strongly (anti-)correlated if particles which carry both quantum numbers are abundant. The same argument was essentially used to explain the momentum space dependence of charge fluctuations and correlations in Chapter 4.

Multiplicity correlations in the canonical and micro canonical ensembles follow suit. So is for instance the correlation between protons and charged pions strongly mediated by the neutron in cold baryonic matter. These correlations appear solely due to implementation of global conservation laws for charges and energy, and not due to a local interaction amongst constituent particles. With increasing temperature more channels, i.e. resonance formation and decay, become available to the statistical system, and subtle differences between canonical and micro canonical ensembles emerge.

Multiplicity fluctuations highlight then the connection between energy spent on resonance formation and energy spent on primordial particle production. The event-by-event multiplicities of stable particles and unstable parent resonances are anti-correlated in the micro canonical ensemble, while being almost unaffected in

the canonical ensemble, and independent of each other in the grand canonical ensemble.

Above the freeze-out line, no hadronic phase should exist. Even in the presence of critical phenomena close to the phase transition, baseline contributions of the kind discussed here, and in previous chapters, should remain.

Chapter 9

The Chemical Freeze-out Line

In this chapter the results of the hadron resonance gas for the scaled variances and correlation coefficients are presented for freeze-out parameters following the constant average energy per average particle multiplicity $\langle E\rangle/\langle N\rangle \simeq 1$ GeV chemical freeze-out line [20]. Different ensemble predictions will be confronted with recent NA49 measurements of charged hadron multiplicity fluctuations.

Mean hadron multiplicities in central heavy ion collisions at high energies are usually fitted within the GCE formulation of the hadron resonance gas model. The fit parameters then are: volume V, temperature T, baryon chemical potential μ_B, and saturation parameters γ_s [116] and γ_q [117, 118]. The former allows for non-equilibrium strange hadron yields, while the latter describes non-equilibrium light quark numbers. For reviews of the model see Refs. [3, 4, 5, 6, 7, 8, 9, 10].

Recent discussion of system size and energy dependence of freeze-out parameters and comparison of different (chemical) freeze-out criteria can be found in Refs. [18, 19, 20, 21, 22]. The set of model parameters, V, T, μ_B, and γ_s, chosen in the following should correspond to chemical freeze-out conditions in heavy ion collisions[1]. The evolution of model parameters with collision energy is taken from previous analysis of mean hadron multiplicity data. Hadron resonance gas model fits should then be able to provide a link between experimental control parameters, center of mass energy, and size of colliding ions, and the region probed in the phase diagram of strongly interacting matter.

[1]The Bose-Einstein condensation model is not considered, as the analytic expansion used for the calculation here is inappropriate. However, one notes that energy conservation essentially prohibits diverging susceptibilities, if degrees of freedom have finite mass.

The dependence of the baryon chemical potential μ_B on the collision energy is parametrized as [18]: $\mu_B\left(\sqrt{s_{NN}}\right) = 1.308\ \text{GeV} \cdot (1 + 0.273\ \sqrt{s_{NN}})^{-1}$, where the center of mass energy per nucleon pair, $\sqrt{s_{NN}}$, is taken in units of GeV. The system is assumed to be net-strangeness free, $S = 0$, and to have the electric charge to baryon density ratio of the initial colliding nuclei, $Q/B = 0.4$. These two conditions define the system's strangeness, μ_S, and electric charge, μ_Q, chemical potentials. The average energy per average particle yield [20] $\langle E\rangle/\langle N\rangle = 1$ GeV was chosen to fix the temperature T. Finally, the strangeness saturation factor is parametrized [21], $\gamma_s = 1 - 0.396\ \exp\left(-\ 1.23\ T/\mu_B\right)$. The asymptotic (or large volume) solutions for the scaled variance and correlation coefficients are assumed. This determines all parameters of the model.

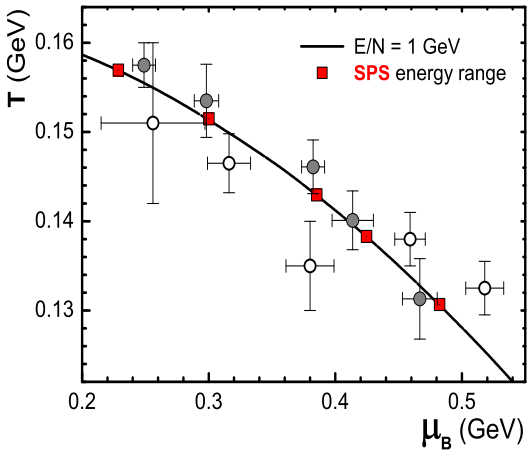

Figure 9.1: Chemical freeze-out points in the T-μ_B plane for central Pb+Pb collisions. The solid line indicates the $\langle E\rangle/\langle N\rangle = 1$ GeV freeze-out line. Square markers denote SPS beam energies from 20A GeV (right) to 158A GeV (left). Full and open circles are the best fit parameters from Refs. [21] and [22], respectively. The Figure is taken from [103].

Here, some further details should be mentioned. Quantum statistics effects are considered, while the non-zero (Breit-Wigner) width of resonances is disregarded. The standard THERMUS particle table includes all known particles and resonances up to a mass of about 2.5 GeV and their respective decay channels. Heavy resonances do not always have well established decay channels. Branching ratios given in THERMUS are re-scaled to unity, where it was necessary to ensure global charge conservation. To make correspondence with NA49 data, both strong and electromagnetic decays should be taken into account, while weak decays should be omitted.

In Section 9.1 multiplicity fluctuations and correlations are considered for different ensembles along the chemical freeze-out line. In Section 9.2 a comparison to recent NA49 data on charged hadron multiplicity fluctuations is attempted.

9.1 Fluctuations and Correlations

In Fig.(9.2) the scaled variances of negatively charged hadrons, ω^- (*left*), and the scaled variances of positively charged hadrons, ω^+ (*right*), are shown, both primordial and final state, along the chemical freeze-out line for most central Pb+Pb (Au+Au) collisions. In Fig.(9.3) (*left*) the scaled variances of all charged particles, ω^{ch}, is shown[2]. The three standard ensembles are considered in turn, and some qualitative features are discussed.

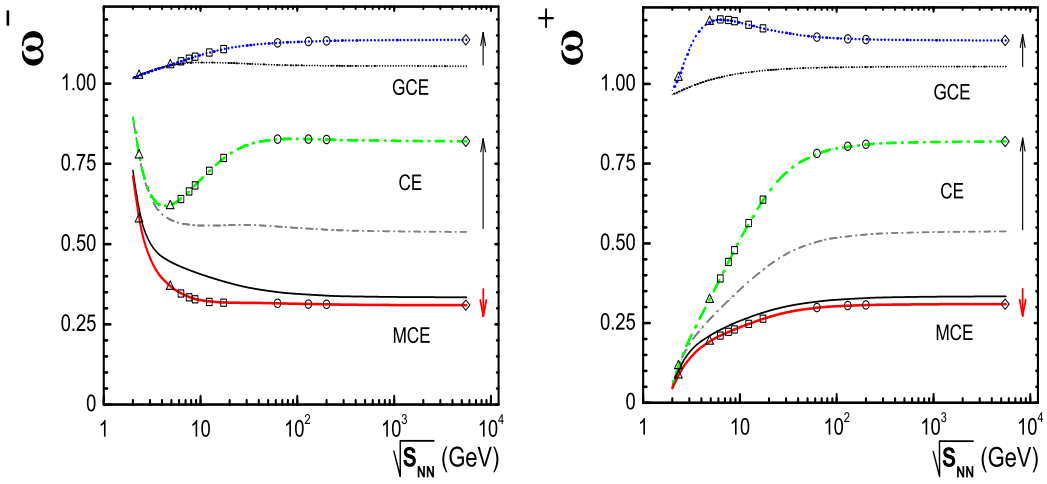

Figure 9.2: The scaled variances of negatively charged particles, ω^- (*left*), and the scaled variances of positively charged particles, ω^+ (*right*), both primordial and final state, along the chemical freeze-out line for central Pb+Pb (Au+Au) collisions. Different lines present GCE, CE, and MCE results. Symbols on the lines for final state fluctuations correspond to specific collision energies, ranging from SIS and AGS (triangles), SPS (squares), RHIC (circles), to LHC (diamonds). Arrows indicate the effect of resonance decay. Figures are taken from [103].

The effects of Bose-Einstein and Fermi-Dirac statistics are seen best in the primordial GCE. At low temperatures most positively charged hadrons are protons, and Fermi-Dirac statistics dominate, leading to sub-Poissonian multiplicity fluctuations, ω^+_{gce}, $\omega^{ch}_{gce} < 1$. On the other hand, in the limit of high temperature most charged hadrons are pions and the effects of Bose-Einstein statistics dominate. The multiplicity distribution is then wider than a Poissonian refer-

[2]Figures are taken form [103]. In previous chapters the scaled variances of positively, negatively, and all charged hadrons were denoted as ω_+, ω_-, and $\omega_\pm$. In this chapter these quantities are refered to as ω^+, ω^-, and ω^{ch}.

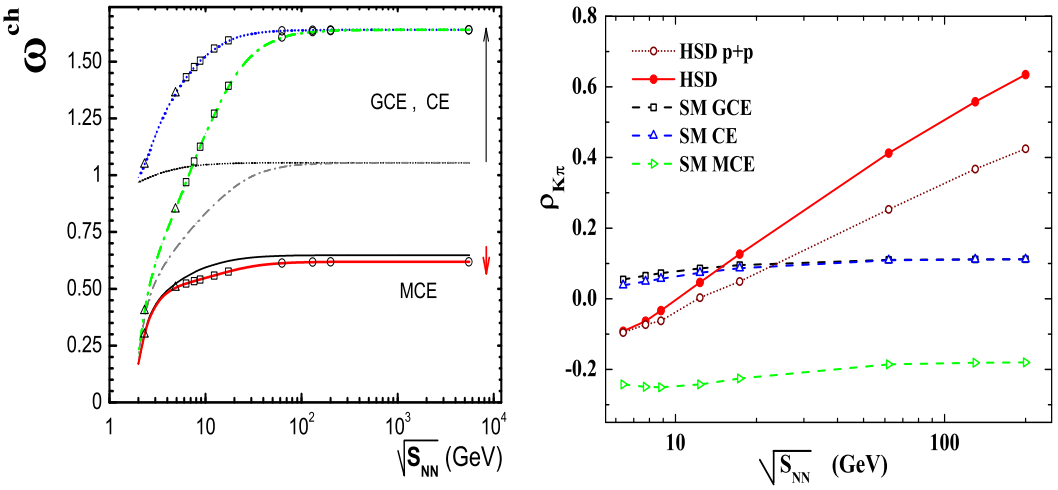

Figure 9.3: The scaled variances of all charged particles, ω^{ch}, both primordial and final state (*left*), and the final state correlation coefficient $\rho_{K\pi}$ (*right*) along the chemical freeze-out line. HSD transport model results for $\rho_{K\pi}$ in p+p and Au+Au collisions are shown for comparison. Figures are taken from [103] (*left*) and [141] (*right*).

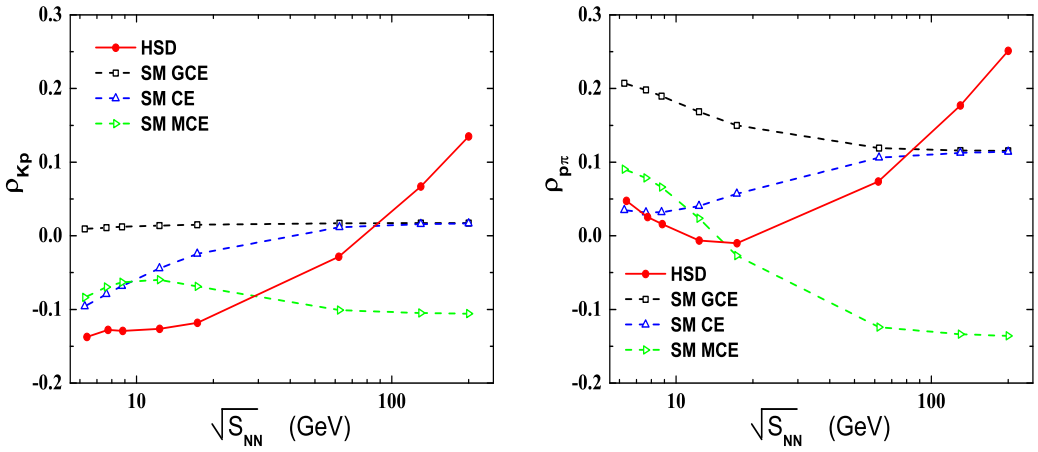

Figure 9.4: The final state correlation coefficient ρ_{Kp} (*left*), and the final state correlation coefficient $\rho_{\mathrm{p}\pi}$ (*right*) along the chemical freeze-out line. HSD transport model results for Au+Au collisions are shown for comparison. Figures are taken from [142].

ence, $\omega^{\pm}_{gce}$, $\omega^{ch}_{gce} > 1$. Along the chemical freeze-out line, ω^{-}_{gce} is always slightly larger than one, as π^- mesons are the most abundant negatively charged hadrons

at, both, low and high temperatures, Fig.(9.2) (*left*).

The bump in ω^+_{gce} for final state particles seen in Fig.(9.2) (*right*) at small collision energies is due to correlated production of protons and π^+ mesons from Δ^{++} decay. This single resonance contribution dominates for ω^+_{gce} at small collision energies (small temperatures), but becomes relatively unimportant at high collision energies. Along the freeze-out line the final state GCE correlation coefficient $\rho_{\mathrm{p}\pi^+}$, Fig.(8.3), has a maximum in the same region. For the final state ω^-_{gce} no bump is seen due to a weaker resonance decay contribution at low $\sqrt{s_{NN}}$. For comparison, the GCE resonance decay enhancement of multiplicity fluctuations is strongest for all charged hadrons, Fig.(9.3) (*left*).

A minimum in ω^-_{ce} for final particles is seen in Fig. (9.2) (*left*). This is due to two effects. As the number of negatively charged particles is relatively small, $\langle N_- \rangle \ll \langle N_+ \rangle$, at low collision energies, both CE suppression and the effect of resonance decay are small. With increasing $\sqrt{s_{NN}}$, the CE effect alone leads to a decrease of ω^-_{ce}, but resonance decay leads to an increase of ω^-_{ce}. The combination of these two effects, CE suppression and resonance decay enhancement, leads to a minimum of ω^-_{ce}. The primordial ω^-_{ce} decreases monotonously with $\sqrt{s_{NN}}$, compare also Fig.(8.13). At large $\sqrt{s_{NN}}$ the system is essentially charge neutral, CE suppression of ω^+_{ce} and enhancement of ω^-_{ce} therefore cease, and one finds $\omega^-_{ce} = \omega^+_{ce}$ accordingly. Both, primordial and final state, ω^+_{ce} in Fig. (9.2) (*right*) hence increase with $\sqrt{s_{NN}}$, compare Fig.(8.11). For a charge neutral system the CE effects cancel exactly for the multiplicity fluctuations of all charged hadrons, both in final state and primordial, $\omega^{ch}_{ce} = \omega^{ch}_{gce}$, Fig. (9.3) (*left*). Compare also Fig.(6.13).

As to be expected, $\omega_{mce} < \omega_{ce}$, along the chemical freeze-out line. Energy conservation further suppresses particle multiplicity fluctuations. A particular feature of the MCE is the additional suppression of multiplicity fluctuations after resonance decay, compare Figs.(8.12,8.14). Energy conservation does not allow for strong multiplicity fluctuations at low temperature. With increasing $\sqrt{s_{NN}}$ one finds ω^{ch}_{mce} and ω^+_{mce} to grow. On the other hand, ω^-_{mce} drops. Negatively charged particles are outnumbered by positively charged particles at small collision energies. Therefore, as the variances of the distributions of positively and negatively charged hadrons are the same, one finds ω^-_{mce} to grow towards smaller $\sqrt{s_{NN}}$, essentially due to a dropping mean value $\langle N^- \rangle$. One also notes, that the resonance decay enhancement of ω^-_{ce} around $\sqrt{s_{NN}} = 10$ GeV is not seen for ω^-_{mce}, due

to a strong correlation of primordial parent resonances with primordial hadrons resulting from global energy conservation. This effect is even stronger for ω^{ch}_{mce}.

The correlation coefficient $\rho_{K\pi}$ between the event-by-event multiplicities of charged kaons, $N_{K^+} + N_{K^-}$, and charged pions, $N_{\pi^+} + N_{\pi^-}$, is shown in Fig.(9.3) (*right*) as a function of center of mass energy $\sqrt{s_{NN}}$ for final state hadrons only. Fig.(9.4) additionally shows the correlation coefficient $\rho_{K\mathrm{p}}$ (*left*) between the event-by-event multiplicities of charged kaons and protons plus anti-protons, $N_{\mathrm{p}} + N_{\overline{\mathrm{p}}}$ (*left*), and the correlation coefficient $\rho_{\mathrm{p}\pi}$ (*right*) between the event-by-event multiplicities of protons plus anti-protons and both charged pions[3]. The three correlation functions are discussed in turn.

In the final state GCE the correlation coefficient $\rho_{K\pi}$ remains weak. A very mild increase at large $\sqrt{s_{NN}}$ is due to rare resonances decay feeding this channel. In the final state CE $\rho_{K\pi}$ is somewhat weaker than in the GCE. Charge conservation effects remain small for the particle selections of both charged kaons, $N_{K^+} + N_{K^-}$, and both charged pions, $N_{\pi^+} + N_{\pi^-}$. At large $\sqrt{s_{NN}}$, i.e. for a neutral system, $\rho^{gce}_{K\pi} \simeq \rho^{ce}_{K\pi}$, CE suppression ceases entirely. As to be expected, the event-by-event multiplicities of charged kaons and charged pions, are anti-correlated by energy conservation in the MCE. Due to a missing strong decay contribution, the correlation coefficient $\rho^{mce}_{K\pi}$ stays negative at all $\sqrt{s_{NN}}$.

The final state GCE correlation coefficient $\rho_{K\mathrm{p}}$ is also rather weak due to a weak resonance decay contribution. In the CE the event-by-event multiplicities of protons plus anti-protons and charged kaons are anti-correlated at low $\sqrt{s_{NN}}$. Their anti-correlation, $\rho_{K\mathrm{p}} < 0$, is mediated by correlation with primordial strangeness carrying baryons, in particular the Λ, at large baryon chemical potential μ_B. With increasing $\sqrt{s_{NN}}$ the temperature rises and μ_B drops. Charge conservation effects cease again for a neutral system, $\rho^{gce}_{K\mathrm{p}} \simeq \rho^{ce}_{K\mathrm{p}}$, for the particle selections of both charged kaons, $N_{K^+}+N_{K^-}$, and both charged pions, $N_{\pi^+}+N_{\pi^-}$. At small $\sqrt{s_{NN}}$ the results of CE and MCE are similar. At larger $\sqrt{s_{NN}}$, however, the correlation $\rho^{mce}_{K\mathrm{p}}$ remains negative, again due to energy conservation.

Lastly, the final state correlation coefficient $\rho_{\mathrm{p}\pi}$ is considered along the chemical freeze-out line in different ensembles. In Section 8.2 the correlation coef-

[3]Figures are taken form [141, 142]. In previous chapters the correlation coefficients denoted only the correlation between proton and either charged pion. In this chapter always both, proton and anti-proton, or both charged kaons, or both charged pions are correlated.

ficient $\rho_{\mathrm{p}\pi^+}$ and $\rho_{\mathrm{p}\pi^-}$ were discussed. Here, both proton and anti-proton and both charged pions are counted, while in Section 8.2 only the proton was correlated with either of the charged pions. In the final state GCE the correlation amongst not charge separated multiplicities is stronger than for charge separated multiplicities, $\rho^{gce}_{\mathrm{p}\pi} > \rho^{gce}_{\mathrm{p}\pi^+}, \rho^{gce}_{\mathrm{p}\pi^-}$.

The anti-proton multiplicity is strongly suppressed at low $\sqrt{s_{NN}}$, and hence their contribution to $\rho_{\mathrm{p}\pi}$ is weak. On the other hand, compare Fig.(8.3), one finds a strong resonance decay contribution at low $\sqrt{s_{NN}}$. Approaching a neutral system, one finds all three final state GCE correlation coefficients to drop. Charge conservation, i.e. CE, effects again cease in a neutral system for the fluctuations of multiplicities $N_{\mathrm{p}} + N_{\overline{\mathrm{p}}}$ and $N_{\pi^+} + N_{\pi^-}$. At low $\sqrt{s_{NN}}$ a weak, but positive, final state correlation remains, compare Figs.(8.4,8.5). In the MCE, one finds a baryon density induced positive correlation. Anti-protons are essentially absent. The correlation coefficient $\rho_{\mathrm{p}\pi^+}$ is negative, while the correlation coefficient $\rho_{\mathrm{p}\pi^-}$ is positive. The correlation coefficient $\rho_{\mathrm{p}\pi}$ is then weakly positive due to abundant neutrons and Δ resonances, allwoing for $\mathrm{n} \leftrightarrow \mathrm{p} + \pi^-$ and $\Delta \leftrightarrow \mathrm{p} + \pi$. At large $\sqrt{s_{NN}}$, hence for a neutral system, the anti-correlation between primordial parent particles and primordial protons, anti-protons and charge pions takes over. For the charge separated counterpart, one finds on the other hand $\rho_{\mathrm{p}\pi^-} \sim \rho_{\mathrm{p}\pi^+} \sim 0$, compare Figs.(8.6,8.7), for large T and $\mu_B \simeq 0$.

The results of the relativistic transport model HSD on correlations coefficients between particle multiplicities of charged kaons, charged pions, and protons plus anti-protons are summarized in Refs. [141, 142].

9.2 Comparison with NA49 Data

The fluctuations in nucleus-nucleus collisions are studied on an event-by-event basis: a given quantity is measured for each collision and a distribution of this quantity is constructed for a selected sample of these collisions. In the following a few aspects are discussed. Details of the experimental setup and analysis can be found in [58, 59].

Centrality Selection

The fluctuations in the number of nucleon participants provide a dominant contribution to hadron multiplicity fluctuations. In the language of statistical models, fluctuations of the number of nucleon participants correspond to volume fluctuations caused by the variations in the collision geometry. Mean hadron multiplicities are proportional (in the large volume limit) to the volume, hence, volume fluctuations translate directly to the multiplicity fluctuations. Thus, a comparison between data and predictions of statistical models should be performed for results which correspond to collisions with a fixed number of nucleon participants.

Due to experimental limitations it is only possible to measure the number of participants of the projectile nucleus, N_P^{proj}, in fixed target experiments (e.g. NA49 at the CERN SPS). This is done by measuring the energy deposited in a downstream Veto calorimeter. A large fraction of this energy is due to projectile spectators N_S^{proj}. Using baryon number conservation for the projectile nucleus ($A = N_P^{proj} + N_S^{proj}$) the number of projectile participants can be estimated. However, also a fraction of non-spectator particles, mostly protons and neutrons, contribute to the Veto energy [58, 59]. Furthermore, the total number of nucleons participating in the collision can fluctuate considerably even for collisions with a fixed number of projectile participants, especially for peripheral collisions (see Ref. [156, 157]). This is due to fluctuations of the number of target participants. The consequences of the asymmetry in the event selection depend on the dynamics of nucleus-nucleus collisions (see Ref. [158] for details). Still, for the most central Pb+Pb collisions selected by the number of projectile participants an increase of the scaled variance can be estimated to be smaller than a few % [158] due to the target participant fluctuations. In the following hadron resonance gas results will be compared with the data of the NA49 collaboration on the 1% most central Pb+Pb collisions at 20A-158A GeV [58, 59].

Modeling of Acceptance

In the experimental study of nuclear collisions at high energies only a fraction of all produced particles is registered. Thus, the multiplicity distribution of the measured particles is expected to be different from the distribution of all produced particles. In general, in statistical models, the correlations in momentum space

are caused by resonance decays, quantum statistics and the energy-momentum conservation law. In this section these correlations are neglected and the procedure of Appendix E is applied for different ensembles. This may be reasonably valid for ω^+ and ω^-, as most decay channels only contain one positively (or negatively) charged particle, but is certainly much worse for ω^{ch}, for instance due to decays of neutral resonances into two charged particles. In order to limit correlations caused by resonance decays, the analysis is restricted to negatively and positively charged hadrons.

The NA49 acceptance used for the fluctuation measurements is located in the forward hemisphere ($1 < y(\pi) < y_{beam}$, where $y(\pi)$ is the hadron rapidity calculated assuming pion mass, and shifted to the collision center of mass system [58, 59]). The acceptance probabilities for positively and negatively charged hadrons are approximately equal, $q^+ \approx q^-$, and the numerical values at different SPS energies are: $q^{\pm} = 0.038,\ 0.063,\ 0.085,\ 0.131,\ 0.163$ at $\sqrt{s_{NN}} = 6.27,\ 7.62,\ 8.77,\ 12.3,\ 17.3$ GeV, respectively.

Comparison with NA49 Data

Fig.(9.5) presents the scaled variances ω^- and ω^+, obtained from applying the acceptance procedure of Appendix E to hadron resonance gas calculations in the GCE, CE, and MCE shown in Fig. (9.2).

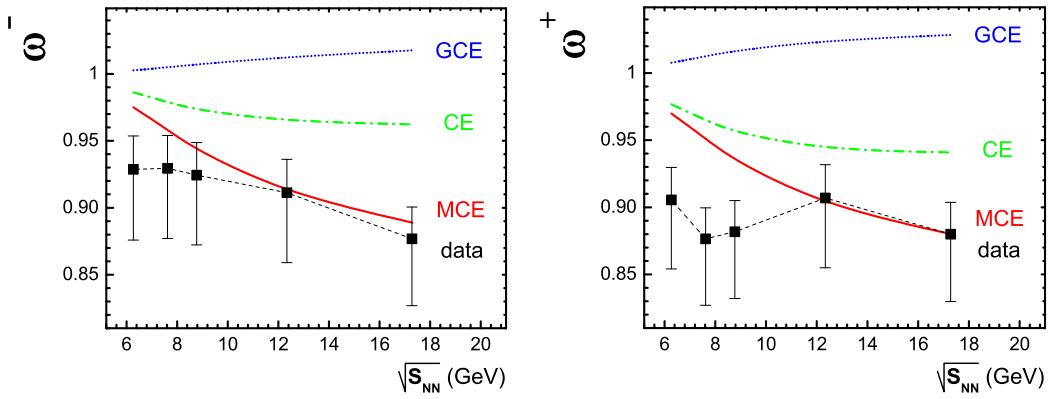

Figure 9.5: The scaled variances for negatively charged (*left*) and positively charged hadrons (*right*) along the chemical freeze-out line for central Pb+Pb collisions at SPS energies. Full squares show the data of NA49 [58, 59]. Total (statistical+systematic) errors are indicated. Lines show the GCE, CE, and MCE acceptance scaling estimates. Figures are taken from [103].

From Fig.(9.5) it follows that the NA49 data for ω^- and ω^+ extracted from 1% of the most central Pb+Pb collisions at all SPS energies are best described by the results of the hadron resonance gas model calculated within the MCE. The data reveal even stronger suppression of the particle number fluctuations. Given that the NA49 acceptance is located in the forward rapidity hemisphere, one would expect further suppression of multiplicity fluctuations compared to the acceptance scaling estimate employed here. See also Chapters 6 and 7.

As discussed, the multiplicity distribution in statistical models in the full phase space and in the large volume limit approaches a normal distribution. Particle detection is modeled by the simple procedure, Appendix E, which is applicable to any form of full acceptance distribution $P_{4\pi}(N)$. In the following multiplicity distributions in limited acceptance are discussed, and the statistical model results in different ensembles are compared with data on negatively and positively charged hadrons. The multiplicity distribution is, after the acceptance scaling procedure was applied, not Gaussian anymore. It is enough to mention that a Gaussian is symmetric around its mean value, while the new distribution, in the limit of very small acceptance, converges to a Poissonian.

In the following for each beam energy the volume is adjusted to fit the mean values for negatively (V^-) and positively (V^+) charged yields, separately. Note that values for the volume are about $10-20\%$ larger than the ones in [21, 22], which were obtained using a much less stringent centrality selection (here only the 1% most central data is analyzed). One finds that the volume parameters V^- and V^+ deviate from each other by less than 10%. Deviations of a similar magnitude are observed between the data on hadron yield systematics and hadron resonance gas model fits.

In order to allow for a detailed comparison of the distributions the ratios of data and model distributions to a Poissonian reference are presented in Fig.(9.6). The results for negatively and positively charged hadrons at 20A GeV, 30A GeV, 40A GeV, 80A GeV, and 158A GeV are shown separately. The convex shape of the data reflects the fact that the measured distribution is significantly narrower than a Poissonian. This suppression of fluctuations is observed for both charges, at all five SPS energies, and it is consistent with the results for the scaled variance shown and discussed previously. The GCE hadron resonance gas results are broader than the corresponding Poisson distribution. The ratio has a concave

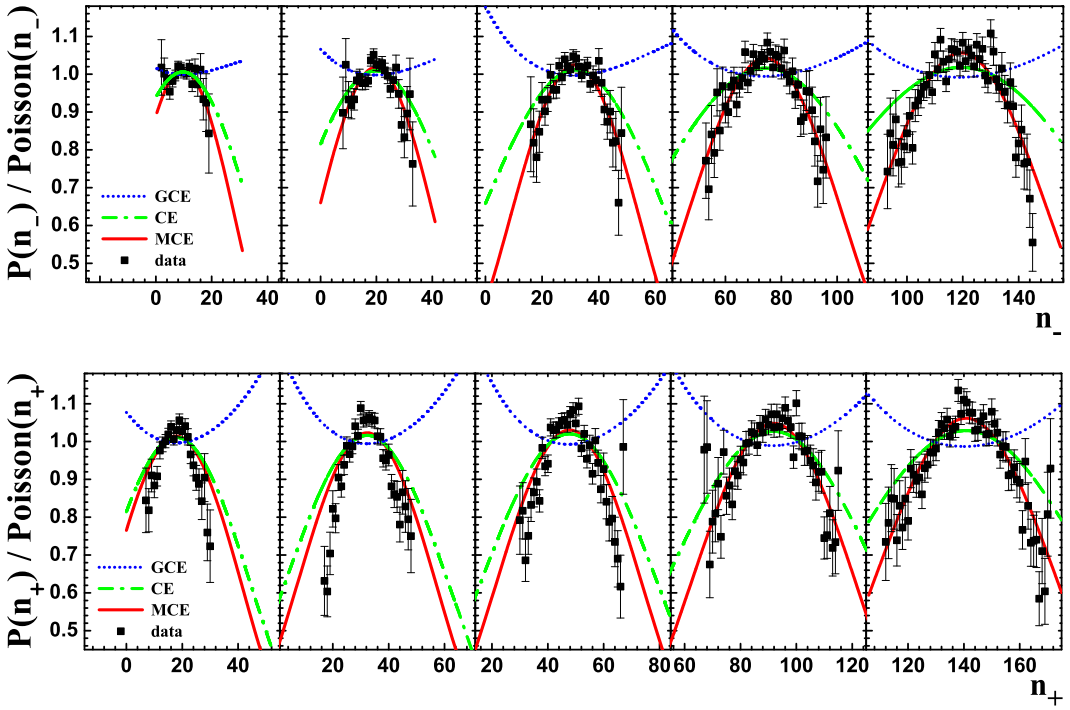

Figure 9.6: The ratio of the multiplicity distributions to Poisson ones for negatively charged (*top*) and positively charged hadrons (*bottom*) produced in central (1%) Pb+Pb collisions at 20A GeV, 30A GeV, 40A GeV, 80A GeV, and 158A GeV (*left*) to (*right*) in the NA49 acceptance. The experimental data (solid points) of NA49 [58, 59] are compared with the acceptance scaling estimates of the hadron resonance gas model obtained within different statistical ensembles, the GCE (dotted lines), the CE (dashed-dotted lines), and the MCE (solid lines). Figures are taken from [103].

shape. Introduction of quantum number conservation laws leads to the convex shape and significantly improves agreement with the data. Further improvement is obtained by additional introduction of energy conservation.

9.3 Discussion

In this chapter multiplicity fluctuations and correlations have been analyzed for thermal parameter sets following the chemical freeze-out line for most central heavy ion collisions. The evolution of model parameters was taken from previous hadron resonance gas model comparison to experimental on average hadron production yields. These fits provide a connection between experimental con-

trol parameters center of mass energy and ion size, and the region of the phase diagram probed by the experiment.

Taking the model in its present form, a naive comparison the NA49 data on charged hadron multiplicity fluctuations has been attempted. High resolution of the NA49 experimental data could in principle allow to distinguish between multiplicity fluctuations expected in hadron resonance gas model for different statistical ensembles. The measured spectra clearly favor predictions of the micro canonical ensemble. Worse description is obtained for the canonical ensemble and disagreement is seen considering the grand canonical one.

All calculations were performed in the thermodynamical limit which is a proper approximation for the considered reactions. Thus, these results could be treated as an observation of the recently predicted [93, 94, 95, 99, 100, 115, 159, 160, 161] suppression of multiplicity fluctuations due to conservation laws in relativistic gases in the large volume limit. Similar observations have been made in detector physics [107], and in low temperature Bose-Einstein condensation [109].

The experimental resolution of the NA49/61 detector for the measurement of enhanced fluctuations due to the onset of deconfinement can be increased by increasing acceptance. This will give a chance to observe, for example, the dynamical fluctuations discussed in Ref. [41, 42]. The observation of the MCE suppression effects of the multiplicity fluctuations by NA49 was possible only because a selection of a sample of collisions without projectile spectators. This selection seems to be possible only in the fixed target experiments.

In collider experiments nuclear fragments which follow the beam direction cannot be measured, and another measure has to be used to determine which centrality class a given event (or collision) would fall into. Often, a charged hadron multiplicity reference distribution is employed. This measure (like any other) provides, however, only indirect access to the initial collision geometry.

Likewise, the energy deposited in the interaction region, and hence the amount of energy available for particle production cannot be considered as fixed across a whole sample of heavy ion collisions. Yet, for each individual collision the energy content available for particle production and (collective) motion is fixed. Thus, even if a centrality class of collision events cannot be seen as a representative a micro canonical sample with the same values of global observables, the final state of each collision will in general fulfill energy-momentum and charge conservation. One could then hope that the transverse momentum and rapidity dependence

will not be washed out by a less stringent centrality selection, but merely shifted up or down.

More differential data on multiplicity fluctuations and correlations are required for further tests of the validity of the statistical models and observation of possible signals of the phase transitions. Simultaneous differential measurement of mean values $\langle N_+ \rangle$, and $\langle N_- \rangle$, variances $\langle (\Delta N_+)^2 \rangle$, and $\langle (\Delta N_-)^2 \rangle$, and of the covariance $\langle \Delta N_+ \Delta N_- \rangle$ should lead to an improved understanding.

The momentum space dependence for scaled variances demanded by the micro canonical ensemble is qualitatively also seen in (non-equilibrium) transport simulations [131] and recent data of the NA49 collaboration [59]. The experimental and theoretical study of multiplicity fluctuations should be complemented with a study of multiplicity correlation coefficients. This study could in principle be extended by a transverse momentum measurement. This would the be either a three by three covariance matrix, or if P_T is charge separated, a four by four covariance matrix. The $\sqrt{s_{NN}}$ and ion size program [71] should be complemented by an acceptance effect study. Critical and quantum phenomena might more strongly feature at low transverse momentum.

Chapter 10

Summary

In this thesis the statistical properties of ideal relativistic hadronic equilibrium ensembles have been studied. Apart from the three standard canonical ensembles being discussed, a class of ensembles with finite thermodynamic bath has been introduced. The influence of global conservation laws, resonance decay, quantum statistics, finite acceptance in momentum space, and thermal freeze-out parameters on fluctuation and correlation observables of a sample of hadron resonance gas events have been considered. It was argued that the emerging picture would at least qualitatively apply to heavy ion physics.

In Chapter 2 grand canonical joint distributions of extensive quantities were obtained by Fourier integration of the grand canonical partition function. An analytical expansion method for calculation of distributions at finite volume for the canonical as well as the micro canonical ensembles of the ideal relativistic hadron resonance gas was presented. The introduction of temperature into the micro canonical partition function and chemical potentials into the canonical partition function have lead to the identification of the grand canonical partition function with the characteristic function of associated joint probability distributions. Micro canonical and canonical multiplicity distributions could then be defined through conditional distributions, i.e. the probability of finding a certain multiplicity, while other parameters (global charge or energy) were taken to be fixed.

In Chapter 3 joint distributions of extensive quantities were then considered for statistical systems with finite rather than infinite thermodynamic bath. To introduce the scheme, a micro canonical system was conceptually divided into two

subsystems. These subsystems were assumed to be in equilibrium with each other, and subject to the constraints of joint energy-momentum and charge conservation. Particles are only measured in one subsystem, while the second subsystem provides a thermodynamic bath. By keeping the size of the first subsystem fixed, while varying the size of the second, one can thus study the dependence of statistical properties of an ensemble on the fraction of the system observed, i.e. assess their sensitivity to globally applied conservation laws. The ensembles generated are thermodynamically equivalent in the sense that mean values in the observed subsystem remain unchanged when the size of the bath is varied, provided the combined system is sufficiently large. As the three standard canonical ensembles remain particular idealizations of physical systems, these intermediate ensembles might be of phenomenological interest, too. These two chapters form the mathematical basis for analytical calculations and Monte Carlo simulations performed in this thesis.

The analysis of hadron resonance gas events started with the study of the grand canonical ensemble in Chapter 4. The grand canonical ensemble is considered to be the most accessible amongst the standard canonical ensembles. Due to the assumption of an infinite thermodynamic bath, occupation numbers of individual momentum levels are un-correlated with each other. Likewise, particle multiplicities of any two distinct groups of particles appear un-correlated. Together with occupation number fluctuations unconstrained, by global constraints, all extensive quantities, except for the volume, fluctuate on an event-by-event (or micro state-by-micro state) basis. Therefore, one finds the energy content and particle multiplicity to be strongly correlated, while the average energy per particle is un-correlated with multiplicity. The net-charge content of baryon number and strangeness in the system are correlated because some hadron species carry both charges. Different hadron species have different quantum numbers and follow different momentum spectra. The correlation between baryon number and strangeness then depends, like the one of energy and momentum, or energy and particle multiplicity, on which part of the momentum spectrum is accessible to measurement.

In Chapter 5 joint distributions of extensive quantities were extrapolated to their micro canonical limit. For this iteratively samples of events were generated and analyzed for decreasing size of the thermodynamic bath. By construction, the distribution of extensive quantities considered for re-weighting converges to a

δ-function, while the positions of the mean values stayed constant. Whereas mean transverse momentum per particle and particle multiplicity were un-correlated in the grand canonical ensemble, this is not true anymore for systems with finite heat bath. Through successive focusing on events in the vicinity of a chosen equilibrium value the effects of global conservation laws became apparent. This proceeded in a systematic manner, allowing for extrapolation of observables from their grand canonical to their micro canonical limit. A caveat is that the statistical uncertainty, associated with finite samples, grows as the sample-reject limit is approached.

In Chapter 6 multiplicity fluctuations and correlations were studied for a neutral hadron resonance gas in limited acceptance in momentum space. The effects of resonance decay were considered, and the extrapolation scheme was applied to obtain the canonical and micro canonical ensemble limits. Comparison to analytical asymptotic solutions, available for primordial distributions in limited acceptance, suggests good agreement. The larger the number of conserved quantities, the larger the statistical uncertainty associated with finite samples of events. Yet, micro canonical effects are accurately reproduced by the Monte Carlo approach. As conservation laws are turned on, multiplicity fluctuations and correlations are modified. Momentum space effects on primordial multiplicity fluctuations and correlations arise due to conservation laws. For an ideal primordial grand canonical ensemble in the Boltzmann approximation (the original sample), multiplicity distributions are just uncorrelated Poissonians, regardless of the acceptance cuts applied, as particles are assumed to be produced independently. The requirement of energy-momentum and charge conservation leads to suppressed fluctuations and enhanced correlations between the multiplicities of two distinct groups of particles at the 'high momentum' end of the momentum spectrum compared to the 'low momentum' end of the momentum spectrum, provided some fraction of an isolated system is observed. Resonance decay does not change these trends.

Chapter 7 was dedicated to the micro canonical ensemble. A simplified physical system was chosen to allow for smoother discussion. Owing to available analytical solutions, Fermi-Dirac and Bose-Einstein effects have been included into the analysis. Bose-Einstein enhancement and Fermi-Dirac suppression of multiplicity fluctuations are strong in momentum space segments where occupation numbers are large. This effect has been found to be much stronger than previous calculations of fully phase space integrated multiplicity fluctuations of

Fermi-Dirac and Bose-Einstein systems suggested. For systems in collective motion is was found that the role of exactly imposed kinematic conservation laws is particularly important. Fluctuation and correlation observables transform under boosts, provided momentum conservation along the boost direction is taken into account. Lastly, it has been found that even in the thermodynamic limit long range correlations between disconnected regions in momentum space prevail. Multiplicities in different bins of rapidity, transverse momentum, or of azimuth, can have a non-vanishing correlation coefficient.

In Chapter 8 the temperature - baryon chemical potential phase diagram of the hadron resonance gas model has been explored. Grand canonical charge correlations and fluctuations are different in different corners of the phase diagram. Like in the acceptance analysis, the correlation between two charges is strong when particles carrying both charges are abundant. At low temperature and baryon chemical potential mesons dominate, at high temperature and baryon chemical potential baryons take over. Fluctuations and correlations of charges systematically evolve accordingly. Multiplicity fluctuations and correlations in canonical and micro canonical ensembles follow suit. The influence of a particular conservation law on multiplicity fluctuations is strong if the analyzed species is abundant. A comparison between ensembles with and without energy, charge, or momentum conservation reveals subtle differences, such as for instance resonance decay in canonical and micro canonical ensembles. Resulting (primordial) multiplicity correlations are not due to local interactions amongst constituents, but due to globally implemented conservation laws for energy and charge.

In Chapter 9 multiplicity fluctuations and correlations were analyzed for thermal parameter sets following the chemical freeze-out line. Model parameters were taken from previous hadron resonance gas model comparisons to experimental on average hadron production yields. These fits provide a connection between experimental control parameters center of mass energy and ion size and the region of the phase diagram probed by an experiment. A first comparison to available experimental data suggests good agreement with hadrons resonance gas calculations. In particular the micro canonical formulation of the model seems to accurately reproduce qualitative features.

The calculations presented here provide qualitative effects affecting multiplicity fluctuations and correlations. These effects arise solely from statistical mechanics and conservation laws. It will be interesting to see whether these qual-

itative effects are visible in further experimental measurements of the momentum dependence of fluctuations and correlations. If so, these effects might well be of similar magnitude to the signals for new physics. Disentangling them from dynamical correlations will then be an important, and likely non-trivial task. Equilibrium correlations are residual correlations which remain after the system has ‘forgotten‘ its history. If the system breaks up before equilibrium is attained, then correlations due to the initial configuration will remain. Yet, even if the system stays far from any equilibrium point throughout its lifetime, correlations due to global conservation laws remain.

Appendix A

Partition Function

This section serves to provide a connection between Eqs.(2.3-2.5) and Eq.(2.13); namely to prove the following relation:

$$\mathcal{Z}^{P^\mu,Q^j}(V,\beta,u_\mu,\mu_j) = e^{-P^\mu u_\mu \beta}\; e^{Q^j \mu_j \beta}\; Z(V,P^\mu,Q^j)\;, \tag{A.1}$$

where $Z(V,P^\mu,Q^j)$ is the standard MCE partition function for a system of volume V, collective four-momentum P^μ and a set of conserved Abelian charges Q^j, as worked out in [113, 114]. The MCE partition function $Z(V,P^\mu,Q^j)$ counts the number of micro states consistent with this set of fixed extensive quantities. Likewise, one could interpret the partition function $\mathcal{Z}^{P^\mu,Q^j}(V,\beta,u_\mu,\mu_j)$ as the number of micro states with the same set of extensive quantities for a GCE with local inverse temperature β, four-velocity u_μ, and chemical potentials μ_j.

The starting point for this calculation is Eq.(2.13):

$$\begin{aligned}\mathcal{Z}^{P^\mu,Q^j}(V,\beta,u_\mu,\mu_j) \;&=\; \int_{-\pi}^{\pi} \frac{d^J\phi}{(2\pi)^J}\; e^{-iQ^j\phi_j} \int_{-\infty}^{\infty} \frac{d^4\alpha}{(2\pi)^4}\; e^{-iP^\mu\alpha_\mu} \\ &\quad\times\; \exp\left[V\Psi\left(\beta,u_\mu,\mu_j;\alpha_\mu,\phi_j\right)\right]\;. \end{aligned}\tag{A.2}$$

Taking a closer look at the exponential of Eq.(A.2), one can spell out the single partition functions, Eq.(2.9), of the cumulant generating function, Eq.(2.8), after

having used the substitutions Eqs.(2.11) and (2.12):

$$\exp\left[\sum_i \frac{V g_i}{(2\pi)^3}\int d^3p \ln\left(1 \pm e^{-p_i^\mu(\beta u_\mu - i\alpha_\mu)} e^{q_i^j(\beta\mu_j + i\phi_j)}\right)^{\pm 1}\right] . \tag{A.3}$$

Expanding the logarithm yields:

$$\exp\left[\sum_i \frac{V g_i}{(2\pi)^3}\int d^3p \sum_{n_i=1}^{\infty} \frac{(\mp 1)^{n_i}}{n_i} e^{-n_i\, p_i^\mu(\beta u_\mu - i\alpha_\mu)} e^{n_i\, q_i^j(\beta\mu_j + i\phi_j)}\right] . \tag{A.4}$$

Replacing now the momentum integration in Eq.(A.4) by the usual summation over individual momentum levels $\frac{V}{(2\pi)^3}\int d^3p \to \sum_{k_{n_i}}$ gives:

$$\exp\left[\sum_i \sum_{n_i=1}^{\infty} \sum_{k_{n_i}} \frac{g_i\,(\mp 1)^{n_i}}{n_i} e^{-n_i\, p^\mu_{k_{n_i}}(\beta u_\mu - i\alpha_\mu)} e^{n_i\, q_i^j(\beta\mu_j + i\phi_j)}\right] . \tag{A.5}$$

Finally, expanding the exponential results in:

$$\mathcal{Z}^{P^\mu, Q^j}(V,\beta,u_\mu,\mu_j) = \int_{-\pi}^{\pi} \frac{d^J\phi}{(2\pi)^J}\, e^{-iQ^j\phi_j} \int_{-\infty}^{\infty} \frac{d^4\alpha}{(2\pi)^4}\, e^{-iP^\mu\alpha_\mu} \prod_i \prod_{n_i=1}^{\infty} \prod_{k_{n_i}} \sum_{c_{k_{n_i}}=0}^{\infty}$$
$$\times \frac{1}{c_{k_{n_i}}!}\left(\frac{g_i\,(\mp 1)^{n_i}}{n_i}\right)^{c_{k_{n_i}}} e^{-c_{k_{n_i}} n_i\, p^\mu_{k_{n_i}}(\beta u_\mu - i\alpha_\mu)} e^{c_{k_{n_i}} n_i\, q_i^j(\beta\mu_j + i\phi_j)} . \tag{A.6}$$

Only sets of numbers $\{c_{k_{n_i}}\}$ which meet the requirements:

$$\sum_i \sum_{n_i=1}^{\infty} \sum_{k_{n_i}} c_{k_{n_i}} n_i\, p^\mu_{k_{n_i}} = P^\mu , \qquad \text{and} \qquad \sum_i \sum_{n_i=1}^{\infty} \sum_{k_{n_i}} c_{k_{n_i}} n_i\, q_i^j = Q^j , \tag{A.7}$$

have a non-vanishing contribution to the integrals. Therefore one can pull these factors in front of the integral:

$$\mathcal{Z}^{P^\mu, Q^j}(V,\beta,u_\mu,\mu_j) = e^{-P^\mu u_\mu \beta}\, e^{Q^j\mu_j\beta} \int_{-\pi}^{\pi} \frac{d^J\phi}{(2\pi)^J}\, e^{-iQ^j\phi_j} \int_{-\infty}^{\infty} \frac{d^4\alpha}{(2\pi)^4}\, e^{-iP^\mu\alpha_\mu}$$
$$\times \prod_i \prod_{n_i=1}^{\infty} \prod_{k_{n_i}} \sum_{c_{k_{n_i}}=0}^{\infty} \frac{1}{c_{k_{n_i}}!}\left(\frac{g_i\,(\mp 1)^{n_i}}{n_i}\right)^{c_{k_{n_i}}} e^{ic_{k_{n_i}} n_i\, p^\mu_{k_{n_i}}\alpha_\mu}\, e^{ic_{k_{n_i}} n_i\, q_i^j\phi_j} . \tag{A.8}$$

Reverting the above expansions one returns to the definition of $Z(V, P^\mu, Q^j)$ from Refs. [113, 114] times the Boltzmann factors:

$$\mathcal{Z}^{P^\mu,Q^j}(V,\beta,u_\mu,\mu_j) \;=\; e^{-P^\mu u_\mu \beta}\; e^{Q^j \mu_j \beta} \int\limits_{-\pi}^{\pi} \frac{d^J\phi}{(2\pi)^J}\; e^{-iQ^j\phi_j} \int\limits_{-\infty}^{\infty} \frac{d^4\alpha}{(2\pi)^4}\; e^{-iP^\mu \alpha_\mu}$$
$$\times\; \exp\left[\sum_i \frac{V g_i}{(2\pi)^3} \int d^3p \ln\left(1 \pm e^{ip_i^\mu\;\alpha_\mu}\; e^{iq_i^j\phi_j}\right)^{\pm 1}\right] \;, \tag{A.9}$$

which proves Eq.(A.1). Therefore, writing for the GCE distribution of extensive quantities:

$$P_{gce}(P^\mu, Q^j) \;=\; \frac{e^{-P^\mu u_\mu \beta}\; e^{Q^j \mu_j \beta}\; Z(V, P^\mu, Q^j)}{Z(V,\beta,u_\mu,\mu_j)} \;=\; \frac{\mathcal{Z}^{P^\mu,Q^j}(V,\beta,u_\mu,\mu_j)}{Z(V,\beta,u_\mu,\mu_j)} \;, \tag{A.10}$$

provides the promised connection between Eqs.(2.3-2.5) and Eq.(2.13).

Appendix B

Second Derivative Test

Considering the integrand of Eq.(2.13), after change of notation Eq.(2.16), one may use short hand notation:

$$I(\theta) \equiv e^{-i\mathcal{Q}^l\theta_l} \exp\left[V\ \Psi(\theta)\right]. \tag{B.1}$$

Taking the first derivative, i.e. the gradient, yields:

$$\frac{\partial I(\theta)}{\partial\theta_l} = I(\theta) \times \left[\ V\ \frac{\partial\Psi(\theta)}{\partial\theta_l} - iQ^l\ \right]. \tag{B.2}$$

At the origin, using the definition of the cumulant tensor, Eq.(2.18), one finds:

$$\left.\frac{\partial I(\theta)}{\partial\theta_l}\right|_{\theta_l=0_l} = Z_{GCE} \times i\left[\ V\ \kappa_1^l - Q^l\ \right]. \tag{B.3}$$

The GCE partition function $Z_{GCE} = \exp\left[V\Psi(0)\right]$ is the 0^{th} cumulant. Therefore, the real part of Eq.(B.3) is identical to zero. In the large volume limit the imaginary part is also zero, for $Q^l = V\kappa_1^l$. Hence, Eq.(B.1) has a stationary point at $\theta_l = 0_l$. A second derivative test [119, 124] should be done in order to distinguish relative minimum, relative maximum or saddle point. Now, taking the second derivative, i.e. calculating the Hessian at the origin yields:

$$\left.\frac{\partial I(\theta)}{\partial\theta_l\ \partial\theta_m}\right|_{\substack{\theta_l\ =\ 0_l \\ \theta_m=\ 0_m}} = -Z_{GCE} \times \left[\left[V\kappa_1^l\ -\ Q^l\ \right]\left[V\kappa_1^m\ -\ Q^m\ \right] +\ V\kappa_2^{m,l}\right]. \tag{B.4}$$

Here the imaginary part of Eq.(B.4) is equal to zero, while in the large volume limit (choosing intensive variables such that $Q^l = V\kappa_1^l$) the real part converges to:

$$\left.\frac{\partial I(\theta)}{\partial\theta_l\,\partial\theta_m}\right|_{\substack{\theta_l\,=\,0_l\\ \theta_m=\,0_m}} = -\,Z_{GCE}\;\times\;V\kappa_2^{m,l} \tag{B.5}$$

In order to have a maximum for the integrand $I(\theta)$ at the origin, the Hessian, Eq.(B.5), has to be negative definite. Therefore, $\kappa_2^{m,l}$ has to be positive definite. For a symmetric matrix it is enough to demand that all eigenvalues are positive. This is the case for all situations considered in this thesis. The derivatives are proportional to the GCE partition function Z_{GCE}. In conclusion, the integrand of Eq.(2.13) is strongly peaked at $\theta_l = 0_l$ in the thermodynamic limit.

Appendix C

The Cumulant Tensor

In this section the κ-tensor Eq.(2.18) is examined. Only a static source in full acceptance is considered here. Resonance decay effects are included. For calculation of asymptotic multiplicity fluctuations and correlations, integrated over full momentum space, it is not necessary to take momentum conservation into account. The choice of ensemble naturally defines the cumulants needed for calculations. Limited acceptance and moving sources, requiring momentum conservation, are considered in Refs.[106, 127].

The analogs of the matrix κ_2 and the vector κ_1, however in different notation, were used in both previously published methods for calculation of scaled variance under the thermodynamic limit; the micro-correlator approach, see [93, 95, 99, 100, 101, 102], and saddle point expansion method [115].

Cumulant structure

Cumulants of order one give GCE expectation values, hence average baryon, strangeness, electric charge, and particle density. The second cumulant contains information about GCE fluctuations of some quantity (diagonal elements), as well as correlations between different quantities (off-diagonal elements). The first two cumulants are:

$$\kappa_1^{l_1} = \left(-i\frac{\partial}{\partial\theta_{l_1}}\right)\Psi\Big|_{\theta_l\,=\,0_l}, \tag{C.1}$$

and

$$\kappa_2^{l_1,l_2} = \left(-i\frac{\partial}{\partial\theta_{l_1}}\right)\left(-i\frac{\partial}{\partial\theta_{l_2}}\right)\Psi\Big|_{\theta_l\,=\,0_l}. \tag{C.2}$$

The index l denotes one of L conserved quantities which form the vector $\mathcal{Q}^l$. For the asymptotic solution to the distributions $P(\mathcal{Q}^l)$ the first and second cumulants are sufficient. The set of conserved quantities could be B, S, Q, E, with additionally particle multiplicities N_A and N_B included, hence:

$$\kappa_1^{l_1} = \left(\kappa_1^{N_A},\ \ \kappa_1^{N_B},\ \ \kappa_1^{B},\ \ \kappa_1^{S},\ \ \kappa_1^{Q},\ \ \kappa_1^{E}\right)\ , \tag{C.3}$$

and

$$\kappa_2^{l_1,l_2} = \begin{pmatrix} \kappa_2^{N_A,N_A} & \kappa_2^{N_A,N_B} & \kappa_2^{N_A,B} & \kappa_2^{N_A,S} & \kappa_2^{N_A,Q} & \kappa_2^{N_A,E} \\ \kappa_2^{N_B,N_A} & \kappa_2^{N_B,N_B} & \kappa_2^{N_B,B} & \kappa_2^{N_B,S} & \kappa_2^{N_B,Q} & \kappa_2^{N_B,E} \\ \kappa_2^{B,N_A} & \kappa_2^{B,N_B} & \kappa_2^{B,B} & \kappa_2^{B,S} & \kappa_2^{B,Q} & \kappa_2^{B,E} \\ \kappa_2^{S,N_A} & \kappa_2^{S,N_S} & \kappa_2^{S,S} & \kappa_2^{S,S} & \kappa_2^{S,Q} & \kappa_2^{S,E} \\ \kappa_2^{Q,N_A} & \kappa_2^{Q,N_Q} & \kappa_2^{Q,Q} & \kappa_2^{Q,S} & \kappa_2^{Q,Q} & \kappa_2^{Q,E} \\ \kappa_2^{E,N_A} & \kappa_2^{E,N_E} & \kappa_2^{E,E} & \kappa_2^{E,S} & \kappa_2^{E,Q} & \kappa_2^{E,E} \end{pmatrix}\ . \tag{C.4}$$

For clarity some elements are explicitly given. A general shorthand notation for the derivatives is used:

$$\psi_i^{(a,b;c)} = (\pm 1)^{a+1}\ \frac{g_i}{(2\pi)^3}\int d^3p\ \ \varepsilon_i^c\ \frac{\left(e^{-(\varepsilon_i-\mu_i)\beta}\right)^a}{\left(1\pm e^{-(\varepsilon_i-\mu_i)\beta}\right)^b}\ . \tag{C.5}$$

The mean values of the electric charge density κ_1^Q and energy density κ_1^E are:

$$\kappa_1^Q \ = \ \left(-i\frac{\partial}{\partial\theta_Q}\right)\Psi\ \Big|_{\theta_l=0_l} \ = \ \sum_i q_i\ \psi_i^{(1,1;0)}\ , \tag{C.6}$$

$$\kappa_1^E \ = \ \left(-i\frac{\partial}{\partial\theta_E}\right)\Psi\ \Big|_{\theta_l=0_l} \ = \ \sum_i\ \psi_i^{(1,1;1)}\ . \tag{C.7}$$

For instance $\kappa_1^Q = 0$ in an electric charge neutral system, due to equal contributions of particles and anti-particles with $q_i \to -q_i$. The final state mean value $\kappa_1^{N_A}$ of particle density of species A is given by:

$$\kappa_1^{N_A} \ = \ \left(-i\frac{\partial}{\partial\theta_{N_A}}\right)\Psi\ \Big|_{\theta_l=0_l} \ = \ \sum_i\left[\sum_{n_A}\ \Gamma_i^{n_A}\ n_A\right]\ \psi_i^{(1,1;0)}\ , \tag{C.8}$$

More about resonance decay and the definition of decay channels $\Gamma_i^{n_A}$ later in this

section. In case two quantities are un-correlated, as for example primordial π^+ multiplicity and globally conserved strangeness (π^+ does not carry strangeness), then the corresponding elements $\kappa_2^{N_A,S} = \kappa_2^{S,N_A} = 0$. Energy fluctuations $\kappa_2^{E,E}$, correlations between baryonic charge and energy $\kappa_2^{B,E}$, and correlations between strangeness and baryonic charge $\kappa_2^{S,B}$, are given by:

$$\kappa_2^{E,E} = \left(-i\frac{\partial}{\partial\theta_E}\right)^2 \Psi \Big|_{\theta_l=0_l} = \sum_i \psi_i^{(1,2;2)} , \tag{C.9}$$

$$\kappa_2^{B,E} = \left(-i\frac{\partial}{\partial\theta_E}\right)\left(-i\frac{\partial}{\partial\theta_B}\right) \Psi \Big|_{\theta_l=0_l} = \sum_i b_i \; \psi_i^{(1,2;1)} , \tag{C.10}$$

$$\kappa_2^{S,B} = \left(-i\frac{\partial}{\partial\theta_S}\right)\left(-i\frac{\partial}{\partial\theta_B}\right) \Psi \Big|_{\theta_l=0_l} = \sum_i s_i \; b_i \; \psi_i^{(1,2;0)} . \tag{C.11}$$

Here for instance $\kappa_2^{B,E} = 0$ for a neutral system, yet in general $\kappa_2^{S,B} \neq 0$. The correlations between particle number N_A and baryonic charge κ_2^{B,N_A}, or energy κ_2^{E,N_A} are:

$$\begin{aligned} \kappa_2^{B,N_A} &= \left(-i\frac{\partial}{\partial\theta_B}\right)\left(-i\frac{\partial}{\partial\theta_{N_A}}\right) \Psi \Big|_{\theta_l=0_l} \\ &= \sum_i b_i \left[\sum_{n_A} \Gamma_i^{n_A} \; n_A\right] \psi_i^{(1,2;0)} , \end{aligned} \tag{C.12}$$

$$\begin{aligned} \kappa_2^{E,N_A} &= \left(-i\frac{\partial}{\partial\theta_E}\right)\left(-i\frac{\partial}{\partial\theta_{N_A}}\right) \Psi \Big|_{\theta_l=0_l} \\ &= \sum_i \left[\sum_{n_A} \Gamma_i^{n_A} \; n_A\right] \psi_i^{(1,2;1)} . \end{aligned} \tag{C.13}$$

If, for instance $N_A = N_{\rm p} + N_{\overline{\rm p}}$, then $\kappa_2^{B,N_A} = 0$ in a neutral system, as contribution of particles and anti-particles cancel each other out, and baryon number conservation does not affect multiplicity fluctuations of $N_A = N_{\rm p} + N_{\overline{\rm p}}$. Fluctuations in

the density of particle species A, $\kappa_2^{N_A,N_A}$, are:

$$\begin{aligned}\kappa_2^{N_A,N_A} &= \left(-i\frac{\partial}{\partial\theta_{N_A}}\right)^2 \Psi \Big|_{\theta_l=0_l} \\ &= \sum_i \left[\sum_{n_A} \Gamma_i^{n_A}\, n_A^2\right] \psi_i^{(1,1;0)} - \left[\sum_{n_A} \Gamma_i^{n_A}\, n_A\right]^2 \psi_i^{(2,2;0)} \,. \quad \text{(C.14)}\end{aligned}$$

Lastly, correlation between the multiplicities N_A and N_B are only due to resonance decay:

$$\begin{aligned}\kappa_2^{N_A,N_B} &= \left(-i\frac{\partial}{\partial\theta_{N_A}}\right)\left(-i\frac{\partial}{\partial\theta_{N_B}}\right) \Psi \Big|_{\theta_l=0_l} \\ &= \sum_i \left[\sum_{n_A,n_B} \Gamma_i^{n_A,n_B}\, n_A n_B\right] \psi_i^{(1,1;0)} \\ &\quad - \left[\sum_{n_A} \Gamma_i^{n_A}\, n_A\right] \left[\sum_{n_B} \Gamma_i^{n_B}\, n_B\right] \psi_i^{(2,2;0)} \,. \quad \text{(C.15)}\end{aligned}$$

Resonance Decay

In this section resonance decay is included analytically directly into the system partition function. This has proved far more efficient than the definition of a generating function [101, 103], which requires a rather cumbersome calculation of all possible primordial correlators. Particle decay is itself a random process. Nevertheless, one can assign a particular volume in phase space, given by the value of its single particle partition function ψ_i, Eq.(2.9), to one type of resonance i. Resonance decay will now populate this volume in phase space according to some weight factor, the branching ratio, for each of the possible decay modes. This weight can be assigned to the particle type(s) one is set to investigate. Based on the assumption that detected particles are drawn in the form of a random sample from all final state particles, e.g. disregarding correlation in momentum space, this procedure leads to the acceptance scaling approximation employed in Refs.[94, 101, 103]. (see also Appendix E) Conservation laws can be imposed on the primordial state (rather than the final state), since decay channels, which are experimentally measured, do not only obey charge conservation, but all relevant conservation laws (omitting weak decays).

For calculation of final state distributions, one needs to determine *final* branching ratios of a resonance type into only stable particles. As an example the decay channel $A \rightarrow B + X$ is considered with branching ratio[1] $\Gamma_{A\rightarrow B+X} = a$. Resonance B could itself be unstable and subsequently decay via the channel $B \rightarrow Y + Z$ with branching ratio $\Gamma_{B\rightarrow Y+Z} = b$. So the *final* branching ratio is defined $\Gamma_{A\rightarrow X+Y+Z} = \Gamma_{A\rightarrow B+X}\,\Gamma_{B\rightarrow Y+Z} = ab$. Decay tables in [101, 103, 141, 142] have also been generated according to this prescription.

For resonances it seems economical to define further *absolute* branching ratios $\Gamma_i^{n_A,n_B}$ as the sum over all *final* decay channels of resonance i with given numbers n_A and n_B of selected daughters. Hence $\Gamma_i^{2,0}$ is the sum over all *final* decay channels with two daughter particles A and none of species B which are of interest, i.e. two positively charged particles in case one wants to calculate ω^+. As a consequence of this definition, branching ratios $\Gamma_i^{n_a,n_B}$ will depend on which ω or ρ one is set to calculate.

For the final state one has to take all *absolute* decay channels of resonance type i into a number n_A and n_B of selected stable particles into account. For the sake of a common treatment for all particles and resonances are assigned a 'decay' channel to stable particles as well, either $\Gamma_i^{1,0} = 1$ if selected, or $\sum_{n_B} \Gamma_l^{0,n_B} = 1$ if not selected. The single particle partition function then reads:

$$\psi_i\left(\theta_E, \theta_j, \theta_{N_A}, \theta_{N_B}; \Gamma_i^{n_A,n_B}\right) = \frac{g_i}{(2\pi)^3} \int d^3p \ln \left[1 \pm e^{-(\varepsilon_i - \mu_i)\beta} e^{i\varepsilon_i \theta_E} e^{iq_i^j \theta_j} \left[\sum_{n_A,n_B} \Gamma_i^{n_A,n_B}\, e^{in_A\theta_{N_A}} e^{in_B\theta_{N_B}} \right] \right]^{\pm 1}, \quad \text{(C.16)}$$

where the form of the vector q_i^j depends on ones choice of ensemble. For instance, one could have $q_i^j = (q_i, b_i, s_i)$ for a hadron resonance gas in the CE with three conserved charges, or $q_i^j = (q_i, b_i, s_i, \varepsilon_i)$ in the MCE without momentum conservation. The sum over all decay channels of the selected types needs to be one:

$$\sum_{n_A,n_B} \Gamma_i^{n_A,n_B} = 1\ . \quad \text{(C.17)}$$

This is somewhat of a practical challenge, since decay chains of heavier resonances

[1]The the letter Γ is used instead of the more conventional Br or br to denote branching ratios.

are not always well established [162] and respective thermal models codes [88, 89, 90, 130] struggle to implement this. There are several ways to deal with this, the two extreme ones are 1) rescale all known channels according to Eq.(C.17), to unity, or 2) assign the missing fraction to the 'channel' $\Gamma_i^{0,0}$, e.g. to the channel without stable particles of interest.

Appendix D

Distributions

From the assumption that the distribution $P_{gce}(\mathcal{Q}^l, N_A, N_B)$ of a GCE with L charges $\mathcal{Q}^l$ and particle numbers of species A and B converges to a multivariate normal distribution, it also follows that the marginal distribution $P_{gce}(\mathcal{Q}^l)$, as well as the conditional distribution $P_{gce}(N_A, N_B|\mathcal{Q}^l)$, are normal distributions. Hence, $P_{mce}(N_A, N_B)$ should have a good approximation in a bivariate normal distribution $P_{BND}(N_A, N_B)$ in the large volume limit (where particle multiplicity can be appropriately treated as continuous):

$$\begin{aligned} P_{BND}(N_A, N_B) &= \frac{1}{2\pi V\sqrt{\sigma_A^2\sigma_B^2\left(1-\rho^2\right)}} \\ &\times \exp\left[-\frac{1}{2V}\left[\frac{\left(\Delta N_A\right)^2}{\sigma_A^2\left(1-\rho^2\right)} - 2\rho\frac{\left(\Delta N_A\right)\left(\Delta N_B\right)}{\sigma_A\sigma_B\left(1-\rho^2\right)} + \frac{\left(\Delta N_B\right)^2}{\sigma_B^2\left(1-\rho^2\right)}\right]\right], \end{aligned} \tag{D.1}$$

where $\Delta N_X = N_X - \langle N_X\rangle$, with $X = A, B$ and:

$$V\sigma_A^2 \equiv \langle N_A^2\rangle - \langle N_A\rangle^2 , \tag{D.2}$$

$$V\sigma_B^2 \equiv \langle N_B^2\rangle - \langle N_B\rangle^2 , \tag{D.3}$$

$$V\sigma_{AB} \equiv \langle N_A N_B\rangle - \langle N_A\rangle\langle N_B\rangle . \tag{D.4}$$

Here $V\sigma_A^2$ and $V\sigma_B^2$ are the variances of the marginal distributions of particle multiplicities N_A and N_B. The term $V\sigma_{AB}$ is called the co-variance.

The MCE joint multiplicity distribution $P_{mce}(N_A, N_B)$ is conveniently expressed by the ratio of two GCE joint distributions, i.e. is given by the conditional

probability distribution:

$$P_{mce}(N_A, N_B) = P_{gce}(N_A, N_B|\mathcal{Q}^l) \ , \tag{D.5}$$

$$= \frac{P_{gce}(N_A, N_B, \mathcal{Q}^l)}{P_{gce}(\mathcal{Q}^l)} \ . \tag{D.6}$$

In the thermodynamic limit the distributions $P_{gce}(N_A, N_B, \mathcal{Q}^l)$ and $P_{gce}(\mathcal{Q}^l)$ can be approximated by multivariate normal distributions, Eq.(2.29). The extended vector $\mathcal{Q}^j$ summarizes particle numbers N_A and N_B and extensive quantities $\mathcal{Q}^l$ to a vector of length $J = 2 + L$, hence $\mathcal{Q}^j = (N_A, N_B, \mathcal{Q}^l)$. The vector denoting the deviation of the mean values $\Delta\mathcal{Q}^j = \mathcal{Q}^j - V\kappa_1^j$ would then read:

$$\Delta\mathcal{Q}^j = \left(\Delta N_A, \ \Delta N_B, \ \Delta\mathcal{Q}^l\right) \ . \tag{D.7}$$

Evaluating the multivariate normal distribution, Eq.(2.29), around its peak for $(\mathcal{Q}^l)$ yields:

$$\Delta\mathcal{Q}^j = \left(\Delta N_A, \ \Delta N_B, \ 0^l \ \right) \ . \tag{D.8}$$

The vector Eq.(2.26) then becomes:

$$\xi^j = V^{-1/2} \begin{pmatrix} \lambda_{1,1} \ \Delta N_A + \lambda_{1,2} \ \Delta N_B \\ \lambda_{2,1} \ \Delta N_A + \lambda_{2,2} \ \Delta N_B \\ \lambda_{3,1} \ \Delta N_A + \lambda_{3,2} \ \Delta N_B \\ \lambda_{4,1} \ \Delta N_A + \lambda_{4,2} \ \Delta N_B \\ \lambda_{5,1} \ \Delta N_A + \lambda_{5,2} \ \Delta N_B \\ \cdots \end{pmatrix} \ , \tag{D.9}$$

where $\lambda_{i,j}$ are the elements of the matrix Eq.(2.23). Therefore:

$$\xi^j \, \xi_j = V^{-1} \left[(\Delta N_A)^2 \sum_{j=1}^{J} \lambda_{j,1}^2 + 2 \, (\Delta N_A) \, (\Delta N_B) \sum_{j=1}^{J} \lambda_{j,1}\lambda_{j,2} + (\Delta N_B)^2 \sum_{j=1}^{J} \lambda_{j,2}^2 \right] , \tag{D.10}$$

with $J = 2 + L = 9$, where $L = 3 + 4$ for a MCE hadron resonance gas with momentum conservation. The micro canonical joint multiplicity distribution of particle species A and B can thus be written as:

$$P_{mce}(N_A, N_B) = \frac{1}{(2\pi V)} \frac{\det|\sigma_N|}{\det|\sigma|} \exp\left[-\frac{1}{2} \, \xi^j \, \xi_j\right] \ , \tag{D.11}$$

where σ_N is the 7-dimensional inverse sigma tensor of the distribution $P_{gce}(\mathcal{Q}^l)$. Comparing this to a bivariate normal distribution, Eq.(D.1), one finds:

$$\sum_{j=1}^{J} \lambda_{j,1}^2 = \frac{1}{\sigma_A^2 (1-\rho^2)} = A \ , \tag{D.12}$$

$$\sum_{j=1}^{J} \lambda_{j,2}^2 = \frac{1}{\sigma_B^2 (1-\rho^2)} = B \ , \tag{D.13}$$

$$\sum_{j=1}^{J} \lambda_{j,1}\lambda_{j,2} = -\frac{\rho}{(1-\rho^2)\,\sigma_A\sigma_B} = -C \ . \tag{D.14}$$

After short calculation one finds for the co-variances:

$$\sigma_A^2 = \frac{B}{AB - C^2} \ , \tag{D.15}$$

$$\sigma_B^2 = \frac{A}{AB - C^2} \ , \tag{D.16}$$

$$\sigma_{A,B} = \frac{C}{AB - C^2} \ , \tag{D.17}$$

and additionally for the correlation coefficient, Eq.(3.49):

$$\rho = \frac{\sigma_{A,B}}{\sigma_A\ \sigma_B} = \frac{C}{\sqrt{AB}} \ , \tag{D.18}$$

where the terms A, B, C are given by Eqs.(D.12 - D.14). For the normalization in Eq.(D.11) (from a comparison with Eq.(D.1)) one finds:

$$\frac{\det|\sigma_N|}{\det|\sigma|} = \frac{1}{\sigma_A\sigma_B\sqrt{(1-\rho^2)}} = \sqrt{AB} \ . \tag{D.19}$$

An analytic formula for the scaled variance, without the need to invert matrices, can be found in [105].

Appendix E

Acceptance Scaling

To illustrate the 'acceptance scaling' procedure employed in [94, 101, 103] uncorrelated acceptance of particles of species A and B is assumed. Particles are measured, or observed, with probability q regardless of their momentum. The distribution of measured particles n_A, when a total number N_A is produced, is then given by a binomial distribution:

$$P_{acc}\,(n_A|N_A) \;=\; q^{n_A}\;\;(1-q)^{N_A-n_A}\,\binom{N_A}{n_A}\;. \tag{E.1}$$

The same acceptance distribution is used for particles of species B. Independent of the original multiplicity distribution $P(N_A, N_B)$, the moments of the measured particle multiplicity distribution are defined by:

$$\langle n_A^a \cdot n_B^b \rangle \;\equiv\; \sum_{n_A,n_B}\;\sum_{N_A,N_B}\; n_A^a\; n_B^b\; P_{acc}\,(n_A|N_A)\;\; P_{acc}\,(n_B|N_B)\;\; P(N_A,N_B)\;. \tag{E.2}$$

For the first moment $\langle n_A \rangle$ one finds:

$$\langle n_A \rangle \;=\; q\;\langle N_A \rangle\;. \tag{E.3}$$

The second moment $\langle n_A^2 \rangle$ and the correlator $\langle n_A \cdot n_B \rangle$ are given by:

$$\langle n_A^2 \rangle \;=\; q^2 \langle N_A^2 \rangle \;+\; q\,(1-q)\,\langle N_A \rangle\;, \tag{E.4}$$

$$\langle n_A \cdot n_B \rangle \;=\; q^2 \langle N_A \cdot N_B \rangle\;. \tag{E.5}$$

For the scaled variance ω_q^A of observed particles one now finds:

$$\omega_q^A \;=\; \frac{\langle n_A^2\rangle - \langle n_A\rangle^2}{\langle n_A\rangle} \;=\; 1 \;-\; q \;+ q\;\omega_{4\pi}^A \;, \tag{E.6}$$

where $\omega_{4\pi}^A$ is the scaled variance of the distribution if all particles of species A are observed. Lastly, the correlation coefficient ρ_q is:

$$\rho_q \;=\; \frac{\langle \Delta n_A \Delta n_B\rangle}{\sqrt{\langle (\Delta n_A)^2\rangle\;\langle (\Delta n_B)^2\rangle}} \;, \tag{E.7}$$

with $\langle \Delta n_A \Delta n_B\rangle = \langle n_A \cdot n_B\rangle - \langle n_A\rangle\langle n_B\rangle$, and $\langle (\Delta n_A)^2\rangle = \langle n_A^2\rangle - \langle n_A\rangle^2$. Substituting the above relations, one finds after a short calculation:

$$\rho_q \;=\; \rho_{4\pi}\; q\; \sqrt{\omega_{4\pi}^A \omega_{4\pi}^B}\left[q^2\omega_{4\pi}^A\omega_{4\pi}^B + q(1-q)\omega_{4\pi}^A + q(1-q)\omega_{4\pi}^B + (1-q)^2\right]^{-1/2} . \tag{E.8}$$

In case $\omega_{4\pi}^A = \omega_{4\pi}^B = \omega_{4\pi}$, Eq.(E.8) simplifies to:

$$\rho_q \;=\; \rho_{4\pi}\;\frac{q\;\omega_{4\pi}}{1\;-\;q\;+\;q\;\omega_{4\pi}} \;. \tag{E.9}$$

Both lines are independent of the mean values $\langle N_A\rangle$ and $\langle N_B\rangle$.

Appendix F

Convergence Study

Not only for the sake of completeness, the convergence of various quantities with the sample size, i.e. the number of events, N_{events}, in our Monte Carlo scheme is discussed in this section. Here only final state (stable against electromagnetic and weak decays) particles are analyzed. A closer look is taken at the data subset of $20 \cdot 2 \cdot 10^5$ events, with $\lambda = V_1/V_g = 0.875$ for the size of the bath, which already has been discussed in Chapter 6.

There is a degree of freedom at so how to estimate the statistical uncertainty on the moments of a distribution of observables of a finite sample. The approach taken here is straight forward, but could, however, certainly be improved.

In Fig.(F.1) the evolution of the mean values $\langle N_+ \rangle$ (*left*) and the variances $\langle (\Delta N_+)^2 \rangle$ (*right*) of the distributions of positively charged hadrons for the five transverse momentum bins $\Delta p_{T,i}$, defined in Table 4.1, with the sample size is shown. Mean values of particle multiplicities in respective bins are in rather good approximation equal to each other, but are, however, not identical due to finite resolution on the underlying momentum spectrum, even for $\lambda = 0.875$ (bins were constructed using GCE events from an independent run). Variances converge steadily and are different in different bins. The event output was iteratively stored in histograms, which were then evaluated after steps of $2 \cdot 10^4$ events.

In Fig.(F.2) the evolution of the scaled variance ω_+ of positively charged final state particles (*left*) and the correlation coefficient ρ_{+-} between positively and negatively charged particles (*right*) with the sample size is shown. The results for the respective transverse momentum bins can be compared to the second to last markers Figs.(6.6,6.7) (*left*), which denote the corresponding results of grouping

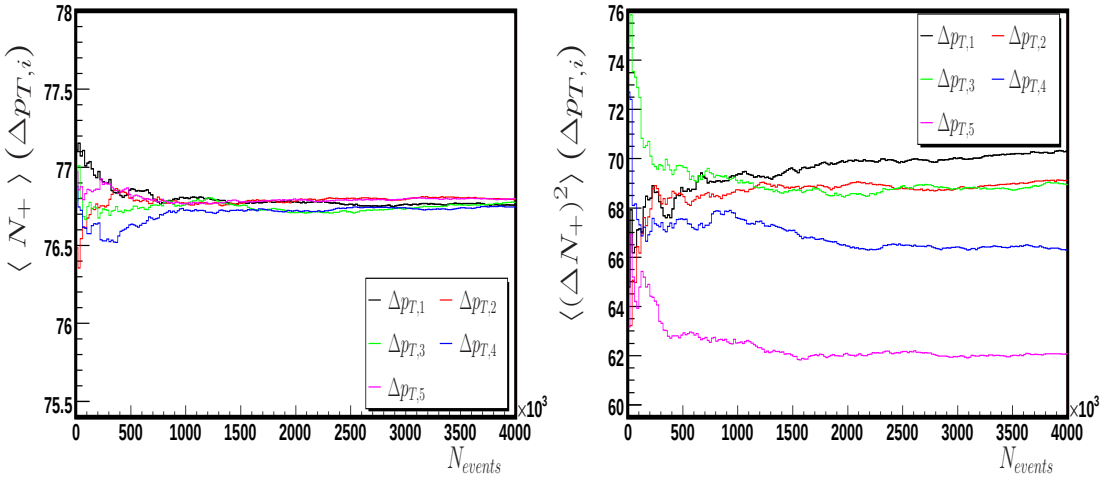

Figure F.1: Step histogram showing the convergence of the mean values $\langle N_+ \rangle$ (*left*) and variances $\langle (\Delta N_+)^2 \rangle$ (*right*) for positively charged final state hadrons in transverse momentum bins $\Delta p_{T,i}$ for a hadron resonance gas with $\lambda = V_1/V_g = 0.875$.

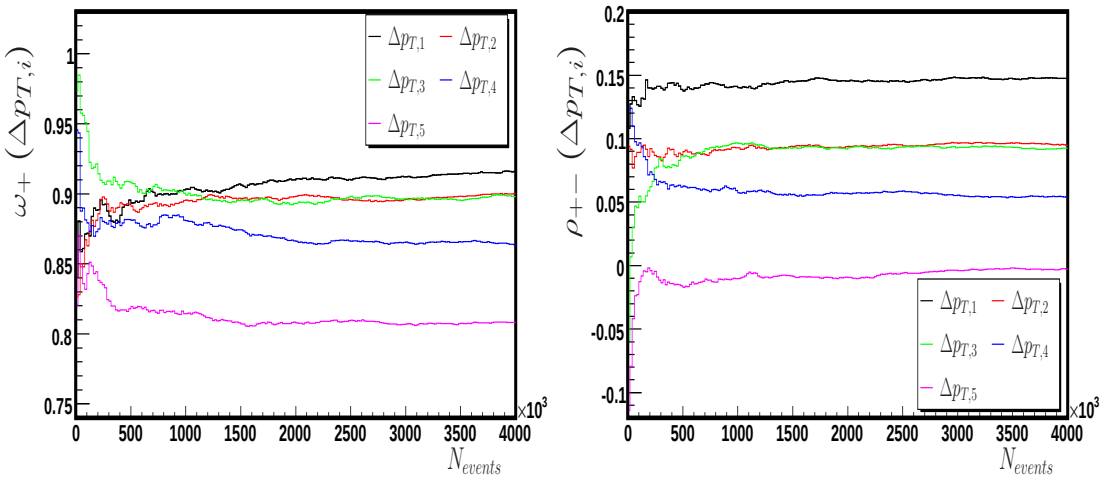

Figure F.2: Step histogram showing the convergence of the scaled variance ω_+ (*left*) of positively charged hadrons and the correlation coefficient ρ_{+-} between positively and negatively charged hadrons (*right*) in transverse momentum bins $\Delta p_{T,i}$ for a final state hadron resonance gas with $\lambda = V_1/V_g = 0.875$.

the same data into 20 Monte Carlo sets of $2 \cdot 10^5$ events each.

The distribution of scaled variances of positively charged particles ω_+ (*left*) and correlation coefficients between positively and negatively charged particles ρ_{+-} (*right*), resulting from grouping again the same data set into 200 samples of $2 \cdot 10^4$ events each are shown in Fig.(F.3). The transverse momentum bin $\Delta p_{T,5}$

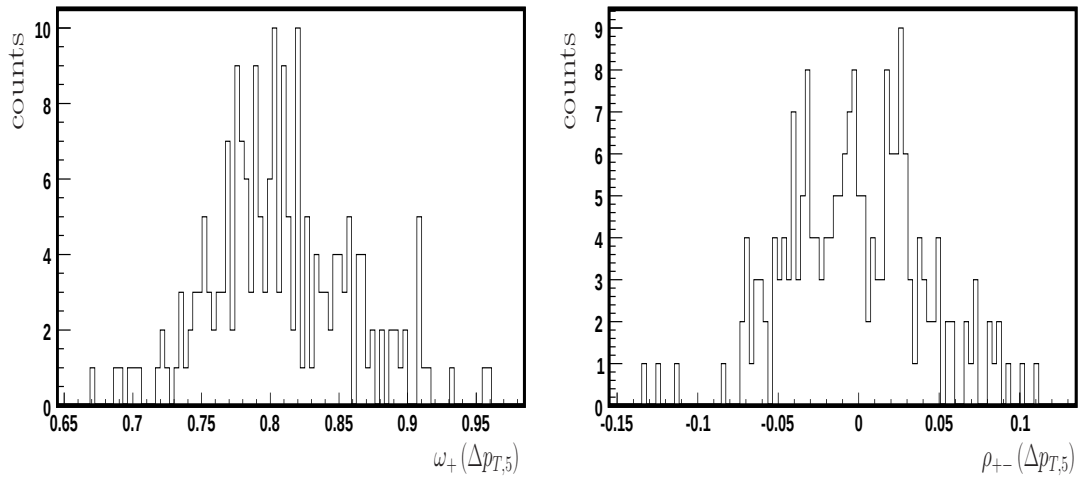

Figure F.3: Histogram showing the results for the scaled variance ω_+ (*left*) of positively charged hadrons and the correlation coefficient ρ_{+-} between positively and negatively charged hadrons (*right*) in the transverse momentum bin $\Delta p_{T,5}$ for a final state hadron resonance gas with $\lambda = V_1/V_g = 0.875$. 200 Monte Carlo runs of $2 \cdot 10^4$ events each are analyzed.

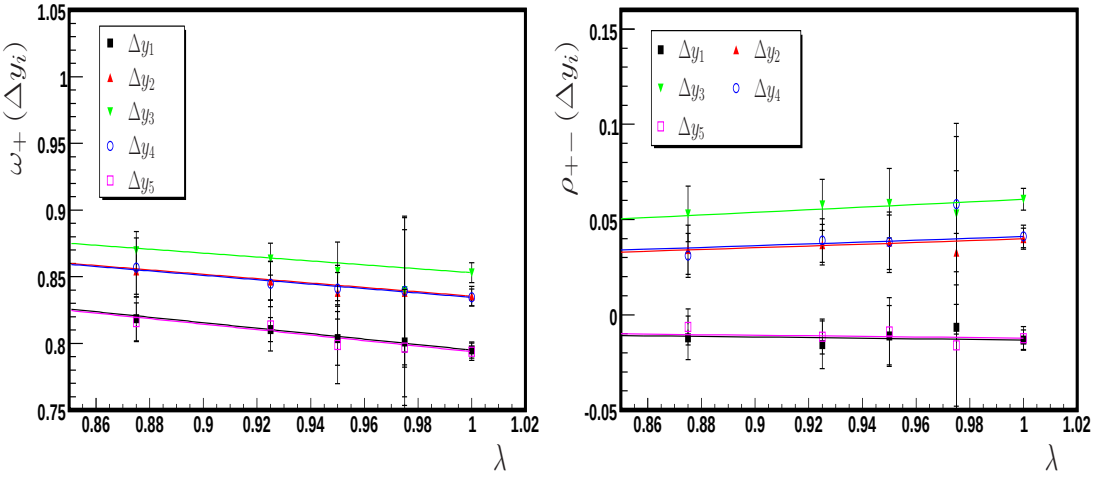

Figure F.4: Evolution of the primordial scaled variance ω_+ of positively charged hadrons (*left*) and the primordial correlation coefficient ρ_{+-} between positively and negatively charged hadrons (*right*) with the Monte Carlo parameter $\lambda = V_1/V_g$ in different rapidity bins Δy_i. The solid lines show an analytic extrapolation from GCE results ($\lambda = 0$) to the MCE limit ($\lambda \to 1$). The 5 leftmost markers and their error bars represent the results of 20 Monte Carlo runs of $2 \cdot 10^5$ events. Three additional values of λ have been investigated with 20 Monte Carlo runs of $1 \cdot 10^7$ events. The 5 rightmost markers denote the results of the extrapolation.

for a final state hadron resonance gas with $\lambda = V_1/V_g = 0.875$ was chosen.

Monte Carlo results for $\lambda = 0.875$ of the analysis shown in Fig.(F.3), are for the scaled variance $\omega_+(\Delta p_{T,5}) = 0.8069 \pm 0.0514$, and the correlation coefficient $\rho_{+-}(\Delta p_{T,5}) = -0.0026 \pm 0.0421$. They are nicely scattered around the mean values, denoted by the bottom lines in Fig.(F.2), $\omega_+(\Delta p_{T,5}) = 0.8082$, and $\rho_{+-}(\Delta p_{T,5}) = -0.0028$, respectively.

They are also compatible with the analysis shown in Figs.(6.6,6.7), of Chapter 6, $\omega_+(\Delta p_{T,5}) = 0.8081 \pm 0.0149$, and $\rho_{+-}(\Delta p_{T,5}) = -0.0022 \pm 0.0125$, at the same value of λ. The comparatively large statistical error on the analysis in Fig.(F.3) is due to the splitting up into many small sub-samples. The mean values of different analysis agree rather well.

Lastly, in Fig.(F.4) the results of additional Monte Carlo runs are shown for values of λ closer to unity. Here 20 additional runs of $1 \cdot 10^7$ primordial events for $\lambda = 0.925$, 0.950, and 0.975 were performed. As discussed above, error bars diverge, but convergence seems to be rather good. The additional data has not been used for the extrapolation, so it can serve as an un-biased cross-check.

Appendix G

The Canonical Boltzmann Gas

An analytical and instructive example is the canonical classical relativistic particle anti-particle gas discussed in [93, 94, 159, 160]. This example is used to show that, although the procedure is formally independent of ones choice of Lagrange multipliers, it is most efficient for those defined by Maxwell's relations. Starting off with Eqs.(3.1), this section will discuss, in turn, the first and second moments of the multiplicity distribution of particles, and the first four moments of the Monte Carlo weight factor.

The canonical partition function $Z_{N_1}(V_1, \beta, Q_1)$ of a system with volume V_1, temperature $T = \beta^{-1}$, charge Q_1, particle number N_1, and anti-particle number $M_1 = N_1 - Q_1$, is given by:

$$Z_{N_1}(V_1, \beta, Q_1) \;=\; \frac{(V_1\psi)^{N_1}}{N_1!}\;\frac{(V_1\psi)^{N_1-Q_1}}{(N_1-Q_1)!}\;. \tag{G.1}$$

The single particle partition function in Boltzmann approximation is given by Eq.(3.31), $\psi = \frac{g}{2\pi^2}\; m^2\; \beta^{-1}\; K_2\,(m\beta)$. The canonical partition function with arbitrary particle number, but still fixed charge Q_1, is obtained by:

$$Z(V_1, \beta, Q_1) \;=\; \sum_{N_1=Q_1}^{\infty} Z_{N_1}(V_1, \beta, Q_1) \;=\; I_{Q_1}\,(2\;V_1\;\psi)\;. \tag{G.2}$$

Here I_{Q_1} is a modified Bessel function. Temperature is the same in both subsystems; the bath and the observable part. The partition function of the bath is therefore:

$$Z(V_2, \beta, Q_2) \;=\; I_{Q_2}\,(2\;V_2\;\psi)\;. \tag{G.3}$$

Imposing the constraints $V_2 = V_g - V_1$, and $Q_2 = Q_g - Q_1$, similar to Eq.(3.4), one finds [119] for the canonical partition function, Eq.(3.5), of the combined system:

$$Z(V_g,\beta,Q_g) \;=\; \sum_{Q_1=-\infty}^{\infty} I_{Q_1}\left(2\;V_1\;\psi\right)\; I_{Q_g-Q_1}\Big(2\left(V_g-V_1\right)\psi\Big) \;=\; I_{Q_g}\left(2\;V_g\;\psi\right)\;, \tag{G.4}$$

as required. The weight factor is then:

$$W(V_1,Q_1;V_g,Q_g|\beta) \;=\; \frac{I_{Q_g-Q_1}\big(2\left(V_g-V_1\right)\psi\big)}{I_{Q_g}\left(2V_g\psi\right)}\;. \tag{G.5}$$

Analogous to Eq.(3.7) one obtains for the joint particle multiplicity and charge distribution:

$$P(Q_1,N_1) \;\;=\;\; W(V_1,Q_1;V_g,Q_g|\beta)\; Z_{N_1}(V_1,\beta,Q_1)\;. \tag{G.6}$$

Monte Carlo Weight

Next, introducing Eq.(3.12), the joint GCE distribution of charges and particle multiplicity:

$$P_{gce}(Q_1,N_1) \;=\; \frac{e^{Q_1\mu\beta}}{Z(V_1,\beta,\mu)}\; Z_{N_1}(V_1,\beta,Q_1)\;. \tag{G.7}$$

The Monte Carlo weight, Eq.(3.15), is then given by:

$$\mathcal{W}^{Q_1;Q_g}(V_1;V_g|\beta,\mu) \;\equiv\; W(V_1,Q_1;V_g,Q_g|\beta)\; Z(V_1,\beta,\mu)\; e^{-Q_1\mu\beta}\;. \tag{G.8}$$

In accordance with Eq.(3.11), the distribution Eq.(G.6) is then equivalently written as:

$$P(Q_1,N_1) \;\;=\;\; \mathcal{W}^{Q_1;Q_g}(V_1;V_g|\mu,\beta)\; P_{gce}(Q_1,N_1)\;. \tag{G.9}$$

The GCE partition function is:

$$Z(V_1,\beta,\mu) \;=\; \sum_{Q_1=-\infty}^{\infty} e^{Q_1\mu\beta}\; Z(V_1,\beta,Q_1) \;=\; \exp\left[V_1 2\cosh(\beta\mu)\right]\;. \tag{G.10}$$

Moments of Distributions

The moments of the multiplicity distributions Eq.(G.6) or Eq.(G.9) are given by:

$$\langle N_1^n \rangle \equiv \sum_{N_1=0}^{\infty} \sum_{Q_1=-\infty}^{\infty} N_1^n \; P(N_1, Q_1) \; . \tag{G.11}$$

Additionally, the moments of the weight, Eq.(G.5), are defined through:

$$\langle W^n \rangle \equiv \sum_{N_1=0}^{\infty} \sum_{Q_1=-\infty}^{\infty} \Big[W(V_1, Q_1; V_g, Q_g|\beta) \Big]^n \; Z_{N_1}(V_1, \beta, Q_1) \; , \tag{G.12}$$

and of the Monte Carlo weight, Eq.(G.8):

$$\langle \mathcal{W}^n \rangle \equiv \sum_{N_1=0}^{\infty} \sum_{Q_1=-\infty}^{\infty} \Big[\mathcal{W}^{Q_1;Q_g}(V_1; V_g|\beta, \mu) \Big]^n \; P_{gce}(Q_1, N_1) \; . \tag{G.13}$$

Next, attending to the first two moments of the multiplicity distribution, substituting Eq.(G.6), or Eq.(G.9) into Eq.(G.11) yields:

$$\langle N_1 \rangle = (V_1\psi) \; \frac{I_{Q_g-1}\,(2V_g\psi)}{I_{Q_g}\,(2V_g\psi)} \; , \qquad \text{and} \tag{G.14}$$

$$\langle N_1^2 \rangle = (V_1\psi) \; \frac{I_{Q_g-1}\,(2V_g\psi)}{I_{Q_g}\,(2V_g\psi)} + (V_1\psi)^2 \; \frac{I_{Q_g-2}\,(2V_g\psi)}{I_{Q_g}\,(2V_g\psi)} \; . \tag{G.15}$$

Canonical suppression of yields and fluctuations acts on the global volume V_g. In the GCE the first two moments are $\langle N_1 \rangle = V_1\psi e^{\mu\beta}$, and $\langle N_1^2 \rangle = \langle N_1 \rangle^2 + \langle N_1 \rangle$, respectively. The CE limit is obtained by $V_g \to V_1$, and $Q_g = \langle Q_1 \rangle$. Substituting Eq.(G.14) and Eq.(G.15) into Eq.(3.50), and using Eq.(3.9), $\lambda = V_1/V_g$, yields:

$$\omega = \lambda \; \omega_{ce} + (1 - \lambda) \; \omega_{gce} \; , \tag{G.16}$$

where the CE scaled variance ω_{ce} of the combined system is given by [93, 94]:

$$\omega_{ce} = 1 - (V_g\psi) \left[\frac{I_{Q_g-1}\,(2V_g\psi)}{I_{Q_g}\,(2V_g\psi)} - \frac{I_{Q_g-2}\,(2V_g\psi)}{I_{Q_g-1}\,(2V_g\psi)} \right] \; , \tag{G.17}$$

and $\omega_{gce} = 1$ is the GCE scaled variance, as the particle number distribution is a Poissonian.

The Monte Carlo scheme is now applied to an observable subsystem of volume $V_1 = 50$ fm^3 embedded into a system of volume $V_g = 75$ fm^3, charge $Q_g = 10$, and temperature $T = \beta^{-1} = 0.160$ GeV. Particles and anti-particles have mass $m = 0.140$ GeV and degeneracy factor $g = 1$. The average charge content in the observable subsystem is then $\langle Q_1 \rangle \simeq 6.667$. The mean particle multiplicity, Eq.(G.14), is $\langle N_1 \rangle \simeq 7.335$, and the scaled variance of particle number fluctuations, Eq.(G.16), is $\omega \simeq 0.3896$. The GCE in V_1 is sampled for various values of μ_Q. The Monte Carlo weight, Eq.(G.8), is then employed to transform these samples to have the statistical properties required by Eq.(G.6) or Eq.(G.9). For each value of μ_Q fifty samples of 2000 events each have been generated to allow for calculation of a statistical uncertainty estimate.

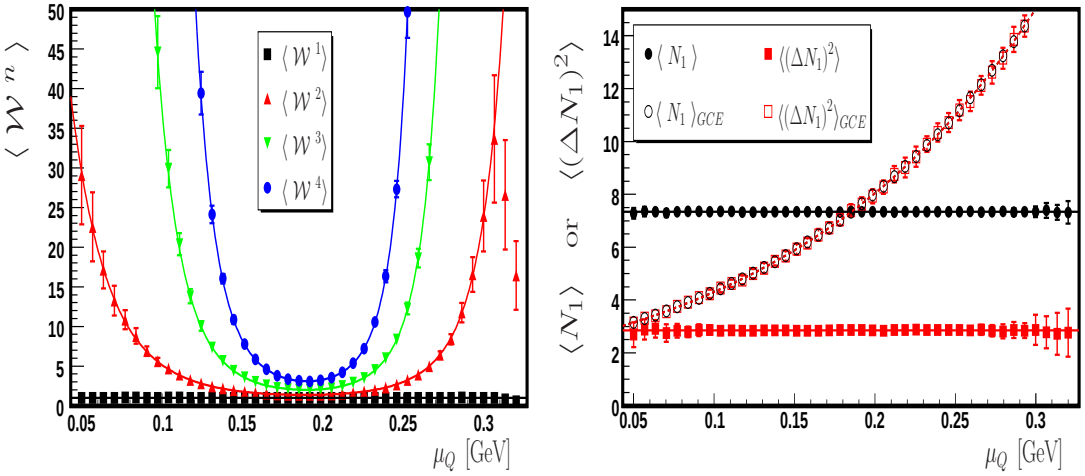

Figure G.1: The first four moments of the Monte Carlo weight, Eq.(G.8) (*left*) and the first two moments of multiplicity distributions (*right*) , as described in the text.

In Fig.(G.1) (*right*) mean value $\langle N_1 \rangle$ and variance $\langle (\Delta N_1)^2 \rangle$ of the particle multiplicity distribution of the original GCE samples for different values of chemical potential μ_Q are shown in open symbols. The closed symbols denote mean value and variance of these samples after the transformation Eq.(G.8) was applied. Independent of the original sample the result stays (within error bars) the same. However, the statistical error is lowest for a chemical potential close to:

$$\mu_Q \;=\; T \;\sinh^{-1}\left(\frac{Q_g}{2V_g\psi}\right) \;, \tag{G.18}$$

i.e. when the initial sample is already similar (at least in terms of mean values) to the desired sample. This is reflected in the moments of the Monte Carlo Weight factor, Fig.(G.1) (*left*). Higher moments have a strong minimum around $\mu_Q = 0.1896$ GeV, i.e. the weights are most homogeneously distributed amongst events, and most efficient used is made of them.

Bibliography

[1] E. Fermi. *High Energy Nuclear Events*. Progr. Theor. Phys., **5**:570–583, 1950.

[2] R. Hagedorn. *Remarks on the thermodynamical model of strong interactions*. Nucl. Phys., **B24**:93–139, 1970.

[3] J. Cleymans, D. Elliott, A. Keränen, and E. Suhonen. *Thermal model analysis of particle ratios at GSI Ni Ni experiments using exact strangeness conservation*. Phys. Rev., **C57**:3319–3323, 1998.

[4] Jean Cleymans, Helmut Oeschler, and Krzysztof Redlich. *Influence of impact parameter on thermal description of relativistic heavy ion collisions at (1-2) A-GeV*. Phys. Rev., **C59**:1663, 1999.

[5] R. Averbeck, R. Holzmann, V. Metag, and R. S. Simon. *Neutral pions and eta mesons as probes of the hadronic fireball in nucleus nucleus collisions around 1-A-GeV*. Phys. Rev., **C67**:024903, 2003.

[6] P. Braun-Munzinger, J. Stachel, J. P. Wessels, and N. Xu. *Thermal equilibration and expansion in nucleus-nucleus collisions at the AGS*. Phys. Lett., **B344**:43–48, 1995.

[7] P. Braun-Munzinger, J. Stachel, J. P. Wessels, and N. Xu. *Thermal and hadrochemical equilibration in nucleus-nucleus collisions at the SPS*. Phys. Lett., **B365**:1–6, 1996.

[8] P. Braun-Munzinger, I. Heppe, and J. Stachel. *Chemical equilibration in Pb + Pb collisions at the SPS*. Phys. Lett., **B465**:15–20, 1999.

[9] F. Becattini, M. Gaździcki, A. Keranen, J. Manninen, and R. Stock. *Study of chemical equilibrium in nucleus nucleus collisions at AGS and SPS energies.* Phys. Rev., **C69**:024905, 2004.

[10] John Adams *et al. Experimental and theoretical challenges in the search for the quark gluon plasma: The STAR collaboration's critical assessment of the evidence from RHIC collisions.* Nucl. Phys., **A757**:102–183, 2005.

[11] I. Kraus, J. Cleymans, H. Oeschler, K. Redlich, and S. Wheaton. *Statistical Model Predictions for p-p and Pb-Pb collisions at LHC.* arXiv:0707.1282 [hep-ph], 2007.

[12] A. Andronic, P. Braun-Munzinger, and J. Stachel. *Thermal model predictions of hadron ratios at LHC.* arXiv:0707.4076 [nucl-th], 2007.

[13] A. Andronic, P. Braun-Munzinger, K. Redlich, and J. Stachel. *Statistical hadronization model predictions for charmed hadrons at LHC.* arXiv:0707.4075 [nucl-th], 2007.

[14] Johann Rafelski and Jean Letessier. *Strangeness enhancement at LHC.* J. Phys., **G35**:044042, 2008.

[15] Johann Rafelski and Jean Letessier. *Soft hadron relative multiplicities at LHC.* Eur. Phys. J., **C45**:61–72, 2006.

[16] F. Becattini and J. Manninen. *Strangeness production from SPS to LHC.* J. Phys., **G35**:104013, 2008.

[17] A. Andronic, P. Braun-Munzinger, K. Redlich, and J. Stachel. *Statistical hadronization of charm: from FAIR to the LHC.* J. Phys., **G35**:104155, 2008.

[18] J. Cleymans, H. Oeschler, K. Redlich, and S. Wheaton. *Comparison of chemical freeze-out criteria in heavy-ion collisions.* Phys. Rev., **C73**:034905, 2006.

[19] J. Cleymans and K. Redlich. *Chemical and thermal freeze-out parameters from 1-A-GeV to 200-A-GeV.* Phys. Rev., **C60**:054908, 1999.

[20] J. Cleymans and K. Redlich. *Unified description of freeze-out parameters in relativistic heavy ion collisions.* Phys. Rev. Lett., **81**:5284–5286, 1998.

[21] F. Becattini, J. Manninen, and M. Gaździcki. *Energy and system size dependence of chemical freeze-out in relativistic nuclear collisions.* Phys. Rev., **C73**:044905, 2006.

[22] A. Andronic, P. Braun-Munzinger, and J. Stachel. *Hadron production in central nucleus nucleus collisions at chemical freeze-out.* Nucl. Phys., **A772**:167–199, 2006.

[23] Francesco Becattini. *A Thermodynamical approach to hadron production in e+ e- collisions.* Z. Phys., **C69**:485–492, 1996.

[24] F. Becattini and Ulrich W. Heinz. *Thermal hadron production in p p and p anti-p collisions.* Z. Phys., **C76**:269–286, 1997.

[25] F. Becattini and G. Passaleva. *Statistical hadronisation model and transverse momentum spectra of hadrons in high energy collisions.* Eur. Phys. J., **C23**:551–583, 2002.

[26] Reinhard Stock. *The parton to hadron phase transition observed in Pb + Pb collisions at 158-GeV per nucleon.* Phys. Lett., **B456**:277–282, 1999.

[27] R. Hagedorn. *The long way to the statistical bootstrap model.* Invited talk at NATO Advanced Study Workshop on Hot Hadronic Matter: Theory and Experiment, Divonne-les-Bains, France, 27 Jun - 1 Jul 1994.

[28] R. Hagedorn. *Thermodynamics of strong interactions.* CERN-71-12.

[29] Francesco Becattini. *What is the meaning of the statistical hadronization model?* J. Phys. Conf. Ser., **5**:175–188, 2005.

[30] F. Becattini and L. Ferroni. *The microcanonical ensemble of the ideal relativistic quantum gas.* Eur. Phys. J., **C51**:899–912, 2007.

[31] F. Karsch, E. Laermann, and C. Schmidt. *The chiral critical point in 3-flavor QCD.* Phys. Lett., **B520**:41–49, 2001.

[32] Z. Fodor and S. D. Katz. *Lattice determination of the critical point of QCD at finite T and μ.* JHEP, **03**:014, 2002.

[33] Kenji Fukushima. *Phase diagrams in the three-flavor Nambu–Jona-Lasinio model with the Polyakov loop.* Phys. Rev., **D77**:114028, 2008.

[34] Z. Fodor and S. D. Katz. *Critical point of QCD at finite T and mu, lattice results for physical quark masses.* JHEP, **04**:050, 2004.

[35] Yoshitaka Hatta and Takashi Ikeda. *Universality, the QCD critical / tricritical point and the quark number susceptibility.* Phys. Rev., **D67**:014028, 2003.

[36] Philippe de Forcrand and Owe Philipsen. *The QCD Phase Diagram for Three Degenerate Flavors and Small Baryon Density.* Nucl. Phys., **B673**:170–186, 2003.

[37] Bernd-Jochen Schaefer and Jochen Wambach. *Susceptibilities near the QCD (tri)critical point.* Phys. Rev., **D75**:085015, 2007.

[38] E. Scott Bowman and Joseph I. Kapusta. *Critical Points in the Linear Sigma Model with Quarks.* Phys. Rev., **C79**:015202, 2009.

[39] S. Jeon and V. Koch. *Charged particle ratio fluctuation as a signal for QGP.* Phys. Rev. Lett., **85**:2076–2079, 2000.

[40] Masayuki Asakawa, Ulrich W. Heinz, and Berndt Müller. *Fluctuation probes of quark deconfinement.* Phys. Rev. Lett., **85**:2072–2075, 2000.

[41] M. Gaździcki, Mark I. Gorenstein, and S Mrowczynski. *Fluctuations and deconfinement phase transition in nucleus nucleus collisions.* Phys. Lett., **B585**:115–121, 2004.

[42] Mark I. Gorenstein, M. Gaździcki, and O. S. Zozulya. *Fluctuations of strangeness and deconfinement phase transition in nucleus nucleus collisions.* Phys. Lett., **B585**:237–242, 2004.

[43] Sangyong Jeon and Volker Koch. *Event-by-event fluctuations.* arXiv:hep-ph/0304012, 2003.

[44] I. N. Mishustin. *Non-equilibrium phase transition in rapidly expanding QCD matter.* Phys. Rev. Lett., **82**:4779–4782, 1999.

[45] I. N. Mishustin. *Phase transitions in exploding matter.* Nucl. Phys., **A681**:064904, 2001.

[46] H. Heiselberg and A. D. Jackson. *Anomalous multiplicity fluctuations from phase transitions in heavy ion collisions.* Phys. Rev., **C63**:064904, 2001.

[47] Misha A. Stephanov, K. Rajagopal, and Edward V. Shuryak. *Signatures of the tricritical point in QCD.* Phys. Rev. Lett., **81**:4816–4819, 1998.

[48] Misha A. Stephanov, K. Rajagopal, and Edward V. Shuryak. *Event-by-event fluctuations in heavy ion collisions and the QCD critical point.* Phys. Rev., **D60**:114028, 1999.

[49] M. Stephanov. *The phase diagram of QCD and the critical point.* Acta Phys. Polon., **B35**:2939–2962, 2004.

[50] Nestor Armesto, Larry McLerran, and Carlos Pajares. *Long range forward-backward correlations and the color glass condensate.* Nucl. Phys., **A781**:201–208, 2007.

[51] T. Lappi and L. McLerran. *Some features of the glasma.* Nucl. Phys., **A772**:200–212, 2006.

[52] S. V. Afanasev *et al. Event-by-event fluctuations of the kaon to pion ratio in central Pb + Pb collisions at 158-GeV per nucleon.* Phys. Rev. Lett., **86**:1965–1969, 2001.

[53] M. M. Aggarwal *et al. Event-by-event fluctuations in particle multiplicities and transverse energy produced in 158-A-GeV Pb + Pb collisions.* Phys. Rev., **C65**:054912, 2002.

[54] John Adams *et al. Multiplicity fluctuations in Au + Au collisions at s(NN)**(1/2) = 130-GeV.* Phys. Rev., **C68**:044905, 2003.

[55] C. Roland *et al. Event-by-event fluctuations of particle ratios in central Pb + Pb collisions at 20-A-GeV to 158-A-GeV.* J. Phys., **G30**:S1381–S1384, 2004.

[56] Zheng-wei Chai *et al. Analysis of dynamic multiplicity fluctuations at PHOBOS.* J. Phys. Conf. Ser., **27**:128–133, 2005.

[57] M Rybczynski *et al. Multiplicity fluctuations in nuclear collisions at 158-A-GeV.* J. Phys. Conf. Ser., **5**:74–85, 2005.

[58] Benjamin Lungwitz *et al. Energy dependence of multiplicity fluctuations in heavy ion collisions.* PoS, **CFRNC2006**:024, 2006.

[59] C. Alt *et al. Energy Dependence of Multiplicity Fluctuations in Heavy Ion Collisions at the CERN SPS.* Phys. Rev., **C78**:034914, 2008.

[60] H. Appelshauser *et al. Event-by-event fluctuations of average transverse momentum in central Pb + Pb collisions at 158-GeV per nucleon.* Phys. Lett., **B459**:679–686, 1999.

[61] D. Adamova *et al. Event-by-event fluctuations of the mean transverse momentum in 40-A-GeV/c, 80-A-GeV/c, and 158-A-GeV/c Pb - Au collisions.* Nucl. Phys., **A727**:97–119, 2003.

[62] T. Anticic *et al. Transverse momentum fluctuations in nuclear collisions at 158-A-GeV.* Phys. Rev., **C70**:034902, 2004.

[63] Stephen Scott Adler *et al. Measurement of non-random event-by-event fluctuations of average transverse momentum in s**(1/2) = 200-GeV Au + Au and p + p collisions.* Phys. Rev. Lett., **93**:092301, 2004.

[64] John Adams *et al. Event-by-event fluctuations in Au Au collisions at s(NN)**(1/2) = 130-GeV.* Phys. Rev., **C71**:064906, 2005.

[65] Terence J. Tarnowsky. *Long-Range Multiplicity Correlations in Relativistic Heavy Ion Collisions as a Signal for Dense Partonic Matter.* arXiv:0807.1941 [nucl-ex], 2008.

[66] Stephen Scott Adler *et al. Measurement of density correlations in pseudorapidity via charged particle multiplicity fluctuations in Au+Au collisions at* $\sqrt{(s_{NN})} = 200$ *GeV.* Phys. Rev., **C76**:034903, 2007.

[67] B. B. Back *et al. Forward-backward multiplicity correlations in s(NN)**(1/2) = 200-GeV Au + Au collisions.* Phys. Rev., **C74**:011901, 2006.

[68] S. V. Afanasiev *et al. Energy dependence of pion and kaon production in central Pb + Pb collisions.* Phys. Rev., **C66**:054902, 2002.

[69] M. Gaździcki *et al. Report from NA49.* J. Phys., **G30**:S701–S708, 2004.

[70] C. Alt *et al. Pion and kaon production in central Pb+Pb collisions at 20A and 30A GeV: Evidence for the onset of deconfinement.* Phys. Rev., **C77**:024903, 2008.

[71] Marek Gaździcki *et al. A new SPS programme.* PoS, **CPOD2006**:016, 2006.

[72] G. S. F. Stephans. *critRHIC: The RHIC low energy program.* J. Phys., **G32**:S447–S454, 2006.

[73] Mikhail A. Stephanov. *QCD phase diagram and the critical point.* Prog. Theor. Phys. Suppl., **153**:139–156, 2004.

[74] Volker Koch. *Hadronic Fluctuations and Correlations.* arXiv:0810.2520 [nucl-th], 2008.

[75] Stephane Häussler, Stefan Scherer, and Marcus Bleicher. *The effect of dynamical parton recombination on event-by- event observables.* Phys. Lett., **B660**:197–201, 2008.

[76] V. P. Konchakovski, M. Hauer, G. Torrieri, M. I. Gorenstein, and E. L. Bratkovskaya. *Forward-backward correlations in nucleus-nucleus collisions: baseline contributions from geometrical fluctuations.* Phys. Rev., **C79**:034910, 2009.

[77] Adam Bzdak. *Forward-backward multiplicity correlations in the wounded nucleon model.* Phys. Rev., **C80**:024906, 2009.

[78] C. M. Ko *et al. Kinetic equation with exact charge conservation.* Phys. Rev. Lett., **86**:5438–5441, 2001.

[79] O. Fochler *et al. Canonical suppression in microscopic transport models.* Phys. Rev., **C74**:034902, 2006.

[80] Giorgio Torrieri and Johann Rafelski. *Strange hadron resonances as a signature of freeze-out dynamics.* Phys. Lett., **B509**:239–245, 2001.

[81] I. Pomeranchuk. *On multiparticle production in single interaction process (in Russian).* Proc. USSR Academy of Sciences, **43**:889, 1951.

[82] L. D. Landau. *On The Multiparticle Production In High-Energy Collisions.* Izv. Akad. Nauk Ser. Fiz., **17**:51–64, 1953.

[83] R. Hagedorn. *Statistical thermodynamics of strong interactions at high energies.* Suppl. Nuovo Cimento, **2**:147, 1965.

[84] P. Braun-Munzinger, D. Magestro, K. Redlich, and J. Stachel. *Hadron production in Au Au collisions at RHIC.* Phys. Lett., **B518**:41–46, 2001.

[85] J. Cleymans, H. Oeschler, K. Redlich, and S. Wheaton. *Status of chemical freeze-out.* J. Phys., **G32**:S165–S170, 2006.

[86] J. Letessier and J. Rafelski. *Hadrons quark - gluon plasma*, volume 18. Cambridge Monogr. Part. Phys. Nucl. Phys. Cosmol., 2002.

[87] J. Cleymans, Burkhard Kampfer, M. Kaneta, S. Wheaton, and N. Xu. *Centrality dependence of thermal parameters deduced from hadron multiplicities in Au + Au collisions at s(NN)**(1/2) = 130-GeV.* Phys. Rev., **C71**:054901, 2005.

[88] Giorgio Torrieri *et al. SHARE: Statistical hadronization with resonances.* Comput. Phys. Commun., **167**:229–251, 2005.

[89] G. Torrieri, S. Jeon, J. Letessier, and Johann Rafelski. *SHAREv2: Fluctuations and a comprehensive treatment of decay feed-down.* Comput. Phys. Commun., **175**:635–649, 2006.

[90] S. Wheaton, J. Cleymans, and M. Hauer. *THERMUS: A thermal model package for ROOT.* Comput. Phys. Commun., **180**:84–106, 2009.

[91] M. Cheng *et al. Baryon Number, Strangeness and Electric Charge Fluctuations in QCD at High Temperature.* Phys. Rev., **D79**:074505, 2009.

[92] R. K. Patriha. *Statistical Mechanics.* Butterworth Heinemann, Oxford, 1996.

[93] V. V. Begun, Mark I. Gorenstein, and O. S. Zozulya. *Fluctuations in the Canonical Ensemble.* Phys. Rev., **C72**:014902, 2005.

[94] V. V. Begun, M. Gaździcki, Mark I. Gorenstein, and O. S. Zozulya. *Particle Number Fluctuations in Canonical Ensemble.* Phys. Rev., **C70**:034901, 2004.

[95] V. V. Begun, Mark I. Gorenstein, A. P. Kostyuk, and O. S. Zozulya. *Particle Number Fluctuations in the Microcanonical Ensemble.* Phys. Rev., **C71**:054904, 2005.

[96] Mark I. Gorenstein. *Statistical Ensembles with Volume Fluctuations.* J. Phys., **G35**:125102, 2008.

[97] Murty S. S. Challa and J. H. Hetherington. *Gaussian ensemble: An alternate Monte Carlo scheme.* Phys. Rev., **A38**:6324–6337, 1988.

[98] M. I. Gorenstein and M. Hauer. *Statistical Ensembles with Fluctuating Extensive Quantities.* Phys. Rev., **C78**:041902, 2008.

[99] V. V. Begun and Mark I. Gorenstein. *Particle Number Fluctuations in Relativistic Bose and Fermi Gases.* Phys. Rev., **C73**:054904, 2006.

[100] V. V. Begun, Mark I. Gorenstein, A. P. Kostyuk, and O. S. Zozulya. *Quantum Gases in the Microcanonical Ensemble near the Thermodynamic Limit.* J. Phys., **G32**:935–948, 2006.

[101] V. V. Begun, Mark I. Gorenstein, M. Hauer, V. P. Konchakovski, and O. S. Zozulya. *Multiplicity fluctuations in hadron-resonance gas.* Phys. Rev., **C74**:044903, 2006.

[102] V. V. Begun and Mark I. Gorenstein. *Bose-Einstein condensation of pions in high multiplicity events.* Phys. Lett., **B653**:190–195, 2007.

[103] V. V. Begun *et al. Multiplicity fluctuations in relativistic nuclear collisions: statistical model versus experimental data.* Phys. Rev., **C76**:024902, 2007.

[104] M. I. Gorenstein, M. Hauer, and D. O. Nikolajenko. *Particle number fluctuations in nuclear collisions within excluded volume hadron gas model.* Phys. Rev., **C76**:024901, 2007.

[105] M. Hauer, V. V. Begun, and M. I. Gorenstein. *Multiplicity Distributions in Canonical and Microcanonical Statistical Ensembles.* Eur. Phys. J., **C58**:83–110, 2008.

[106] Michael Hauer. *Multiplicity Fluctuations in Limited Segments of Momentum Space in Statistical Models*. Phys. Rev., **C77**:034909, 2008.

[107] U. Fano. *Ionization Yield of Radiations. 2. The Fluctuations of the Number of Ions*. Phys. Rev., **72**:26–29, 1947.

[108] R. M. Ziff, G. E. Uhlenbeck, and M. Kac. *The ideal Bose-Einstein gas, revisited*. Phys. Rep., **32**:169–248, 1977.

[109] Siegfried Grossmann and Martin Holthaus. *Microcanonical fluctuations of a Bose system's ground state occupation number*. Phys. Rev. E, **54**(4):3495–3498, Oct 1996.

[110] W. Greiner, L. Neise, and H. Stöcker. *Thermodynamics and Statistical Mechanics*. Springer, New York, 1997.

[111] L. E. Patriha. *A modern course in statistical physics*. Wiley, New York, 1998.

[112] L. D. Landau and E. M. Lifschitz. *Statistical Physics*. Fizmatlit, Moscow, 2001.

[113] F. Becattini and L. Ferroni. *Statistical hadronization and hadronic microcanonical ensemble. I.* Eur. Phys. J., **C35**:243–258, 2004.

[114] F. Becattini and L. Ferroni. *Statistical hadronization and hadronic microcanonical ensemble. II.* Eur. Phys. J., **C38**:225–246, 2004.

[115] Francesco Becattini, Antti Keränen, Lorenzo Ferroni, and Tommaso Gabbriellini. *Multiplicity fluctuations in the hadron gas with exact conservation laws*. Phys. Rev., **C72**:064904, 2005.

[116] P. Koch, Berndt Müller, and Johann Rafelski. *Strangeness in Relativistic Heavy Ion Collisions*. Phys. Rept., **142**:167–262, 1986.

[117] Jean Letessier, Ahmed Tounsi, and Johann Rafelski. *Low-m(t) pi+ pi- asymmetry and pion enhancement from hadronization of QGP*. Phys. Lett., **B475**:213–219, 2000.

[118] Johann Rafelski and Jean Letessier. *Sudden hadronization in relativistic nuclear collisions*. Phys. Rev. Lett., **85**:4695–4698, 2000.

[119] M. Abramowitz and I. A. Stegun. *Handbook of Mathematical Functions with Formulas, Graphs, and Mathematical Tables*. New York, Dover, 1965.

[120] W. Feller. *An Introduction to Probability Theory and Its Applications Vol. I*. Wiley, New York, 1968.

[121] W. Feller. *An Introduction to Probability Theory and Its Applications Vol. II*. Wiley, New York, 1970.

[122] B. Hughes. *Random Walks and Random Environments Vol. I*. Clarendon Press, Oxford, 1995.

[123] B. Hughes. *Random Walks and Random Environments Vol. II*. Clarendon Press, Oxford, 1996.

[124] I.S. Gradshteyn and I. N. Ryzhik. *Table of Integrals, Series, and Products*. Academic Press, San Diego, 2000.

[125] R. K. Pathria. *On the (relativistic) statistical thermodynamics of an assembly in mass-motion*. Proc. Natl. Inst. Sci. (India), **23**:168–177, 1957.

[126] B. Touschek. *Covariant statistical mechanics*. Il Nuovo Cimento, **B58**:295–307, 1968.

[127] Michael Hauer, Giorgio Torrieri, and Spencer Wheaton. *Multiplicity Fluctuations and Correlations in Limited Momentum Space Bins in Relativistic Gases*. Phys. Rev., **C80**:014907, 2009.

[128] J. Randrup. *Microcanonical sampling of momenta in simulations of many-partilce systems*. Comput. Phys. Commun., **59**:439, 1990.

[129] J. Randrup. *Microcanonical sampling of momenta*. Nucl. Phys., **A522**:651, 1991.

[130] Adam Kisiel, Tomasz Taluc, Wojciech Broniowski, and Wojciech Florkowski. *THERMINATOR: Thermal heavy-ion generator*. Comput. Phys. Commun., **174**:669–687, 2006.

[131] Benjamin Lungwitz and Marcus Bleicher. *Searching for the Critical Point of QCD: Theoretical Benchmark Calculations*. Phys. Rev., **C76**:044904, 2007.

[132] Josef Sollfrank, Peter Koch, and Ulrich W. Heinz. *The Influence of resonance decays on the P(t) spectra from heavy ion collisions.* Phys. Lett., **B252**:256–264, 1990.

[133] Josef Sollfrank, Peter Koch, and Ulrich W. Heinz. *Is there a low p(T) 'anomaly' in the pion momentum spectra from relativistic nuclear collisions?* Z. Phys., **C52**:593–610, 1991.

[134] Ekkard Schnedermann, Josef Sollfrank, and Ulrich W. Heinz. *Thermal phenomenology of hadrons from 200-A/GeV S+S collisions.* Phys. Rev., **C48**:2462–2475, 1993.

[135] F. Becattini and J. Cleymans. *Chemical equilibrium in heavy ion collisions: Rapidity dependence.* J. Phys., **G34**:S959–964, 2007.

[136] R. V. Gavai and Sourendu Gupta. *Fluctuations, strangeness and quasiquarks in heavy-ion collisions from lattice QCD.* Phys. Rev., **D73**:014004, 2006.

[137] Claudia Ratti, Simon Roessner, and Wolfram Weise. *Quark number susceptibilities: Lattice QCD versus PNJL model.* Phys. Lett., **B649**:57–60, 2007.

[138] Stephane Häussler, Marcus Bleicher, and Horst Stöcker. *Susceptibilities and fluctuations in a Quark-Hadron System with Dynamical Recombination.* arXiv:0803.2846 [hep-ph], 2008.

[139] V. Koch, A. Majumder, and J. Randrup. *Baryon-strangeness correlations: A diagnostic of strongly interacting matter.* Phys. Rev. Lett., **95**:182301, 2005.

[140] Rajiv V. Gavai and Sourendu Gupta. *Valence quarks in the QCD plasma: Quark number susceptibilities and screening.* Phys. Rev., **D67**:034501, 2003.

[141] M. I. Gorenstein, M. Hauer, V. P. Konchakovski, and E. L. Bratkovskaya. *Fluctuations of the K/π Ratio in Nucleus-Nucleus Collisions: Statistical and Transport Models.* Phys. Rev., **C79**:024907, 2009.

[142] V. P. Konchakovski, M. Hauer, M. I. Gorenstein, and E. L. Bratkovskaya. *Particle Number Fluctuations and Correlations in Nucleus- Nucleus Collisions.* J. Phys., **G36**:125106, 2009.

[143] Fred Cooper and Graham Frye. *Comment on the Single Particle Distribution in the Hydrodynamic and Statistical Thermodynamic Models of Multiparticle Production.* Phys. Rev., **D10**:186, 1974.

[144] Giorgio Torrieri, Boris Tomasik, and Igor Mishustin. *Bulk Viscosity driven clusterization of quark-gluon plasma and early freeze-out in relativistic heavy-ion collisions.* Phys. Rev., **C77**:034903, 2008.

[145] A. Bialas and Robert B. Peschanski. *Moments of Rapidity Distributions as a Measure of Short Range Fluctuations in High-Energy Collisions.* Nucl. Phys., **B273**:703, 1986.

[146] I. Arsene *et al. Quark Gluon Plasma an Color Glass Condensate at RHIC? The perspective from the BRAHMS experiment.* Nucl. Phys., **A757**:1–27, 2005.

[147] B. B. Back *et al. The PHOBOS perspective on discoveries at RHIC.* Nucl. Phys., **A757**:28–101, 2005.

[148] K. Adcox *et al. Formation of dense partonic matter in relativistic nucleus nucleus collisions at RHIC: Experimental evaluation by the PHENIX collaboration.* Nucl. Phys., **A757**:184–283, 2005.

[149] A. Andronic, P. Braun-Munzinger, and J. Stachel. *Thermal hadron production in relativistic nuclear collisions: the sigma meson, the horn, and the QCD phase transition.* Erratum-ibid., **B678**:516, 2009.

[150] J. Noronha-Hostler, C. Greiner, and I. A. Shovkovy. *Fast Equilibration of Hadrons in an Expanding Fireball.* Phys. Rev. Lett., **100**:252301, 2008.

[151] Marek Gaździcki and Mark I. Gorenstein. *On the early stage of nucleus nucleus collisions.* Acta Phys. Polon., **B30**:2705, 1999.

[152] L. Ferroni and V. Koch. *Crossover transition in bag-like models.* Phys. Rev., **C79**:034905, 2009.

[153] J. Cleymans, H. Oeschler, K. Redlich, and S. Wheaton. *The thermal model and the transition from baryonic to mesonic freeze-out.* Eur. Phys. J., **A29**:119–121, 2006.

[154] Roger Dashen, Shang-Keng Ma, and Herbert J. Bernstein. *S Matrix formulation of statistical mechanics.* Phys. Rev., **187**:345–370, 1969.

[155] Roger F. Dashen, Shang-keng Ma, and R. Rajaraman. *Finite Temperature Behavior of a Relativistic Field Theory with Dynamical Symmetry Breaking.* Phys. Rev., **D11**:1499, 1975.

[156] V. P. Konchakovski *et al. Particle Number Fluctuations in High Energy Nucleus- Nucleus Collisions from Microscopic Transport Approaches.* Phys. Rev., **C73**:034902, 2006.

[157] V. P. Konchakovski, Mark I. Gorenstein, E. L. Bratkovskaya, and Horst Stöcker. *Baryon Number and Electric Charge Fluctuations in Pb+Pb Collisions at SPS energies.* Phys. Rev., **C74**:064911, 2006.

[158] Marek Gaździcki and Mark I. Gorenstein. *Transparency, Mixing and Reflection of Initial Flows in Relativistic Nuclear Collisions.* Phys. Lett., **B640**:155–161, 2006.

[159] J. Cleymans, K. Redlich, and L. Turko. *Probability distributions in statistical ensembles with conserved charges.* Phys. Rev., **C71**:047902, 2005.

[160] J. Cleymans, K. Redlich, and L. Turko. *Thermodynamic limit and semi-intensive quantities.* J. Phys., **G31**:1421–1435, 2005.

[161] A. Keränen, F. Becattini, V. V. Begun, Mark I. Gorenstein, and O. S. Zozulya. *Particle number fluctuations in statistical model with exact charge conservation laws.* J. Phys., **G31**:S1095–S1100, 2005.

[162] K. Hagiwara *et al. Review of Particle Properties.* Phys. Rev. D, **66**(1):010001, Jul 2002.